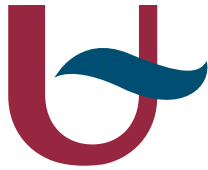




Universidade Federal do Ceará
CENTRO DE CIÊNCIAS
DEPARTAMENTO DE FÍSICA
PROGRAMA DE PÓS-GRADUAÇÃO EM FÍSICA



Universiteit
Antwerpen

UNIVERSITEIT ANTWERPEN
FACULTEIT WETENSCHAPPEN
DEPARTEMENT FYSICA

Ariel Adorno de Sousa

VAZAMENTOS DE CORRENTES E INEFICIÊNCIA DE
CORRENTE DE TRANSPORTE EM NANOESTRUTURAS
SEMICONDUCTORAS INVESTIGADAS ATRAVÉS DE
PROPAGAÇÃO DE PACOTES DE ONDA

CURRENT LEAKAGE AND TRANSPORT INEFFICIENCY
IN SEMICONDUCTOR NANOSTRUCTURES
INVESTIGATED BY QUANTUM WAVE PACKET

STUDIE VAN STROOM LEKKAGE EN TRANSPORT
INEFFICIËNTIE IN HALFGELEIDER NANOSTRUCTUREN
DOORMIDDEL VAN QUANTUM GOLF PAKKETTEN

Fortaleza - May 8th 2015



Universidade Federal do Ceará
CENTRO DE CIÊNCIAS
DEPARTAMENTO DE FÍSICA
PROGRAMA DE PÓS-GRADUAÇÃO EM FÍSICA



Universiteit
Antwerpen

UNIVERSITEIT ANTWERPEN
FACULTEIT WETENSCHAPPEN
DEPARTEMENT FYSICA

VAZAMENTOS DE CORRENTES E INEFICIÊNCIA DE
CORRENTE DE TRANSPORTE EM NANOESTRUTURAS
SEMICONDUCTORAS INVESTIGADAS ATRAVÉS DE
PROPAGAÇÃO DE PACOTES DE ONDA

CURRENT LEAKAGE AND TRANSPORT INEFFICIENCY
IN SEMICONDUCTOR NANOSTRUCTURES
INVESTIGATED BY QUANTUM WAVE PACKET

STUDIE VAN STROOM LEKKAGE EN TRANSPORT
INEFFICIËNTIE IN HALFGELEIDER NANOSTRUCTUREN
DOORMIDDEL VAN QUANTUM GOLF PAKKETTEN

Thesis presented within the pos-graduation at the
Department of Physics of the Federal University
of Ceará, as part of the requisites necessary to
obtain the title of Ph.D. in Physics.

Promoter: *Prof. Dr. Andrey Chaves*

Co-Promoter: *Prof. Dr. Gil de Aquino Farias*

Co-Promoter: *Prof. Dr. François M. Peeters*

Fortaleza - May 8th 2015

Dados Internacionais de Catalogação na publicação
Universidade Federal do Ceará
Biblioteca do Curso de Física

S696v Sousa, Ariel Adorno de

Vazamentos de correntes e ineficiência de corrente de transporte em nanoestruturas semicondutoras investigadas através de propagação de pacotes de onda / Ariel Adorno de Sousa. – Fortaleza, 2015.

150 F: il. algumas color. enc.; 30 cm.

Tese (Doutorado em Física) - Universidade Federal do Ceará, Centro de Ciências, Departamento de Física, Programa de Pós-Graduação em Física, Fortaleza, 2014.

Orientador: Prof. Dr. Andrey Chaves.

Coorientação: Prof. Dr. Gil de Aquino Farias.

Coorientação: Prof. Dr. François M. Peeters.

Área de concentração: Física da Matéria Condensada.

Inclui índice.

1. Nanotecnologia. 2. Semicondutores intrínseco. 3. Sistemas de Poços Quânticos. 4. Tunelamento quântico. 5. Pacote de ondas.

I. Chaves, Andrey (Orient.). II. Farias, Gil de Aquino (Coorient.).

III. Peeters, François (Coorient.). M. IV. Título.

CDD 620.5

ARIEL ADORNO DE SOUSA

**VAZAMENTOS DE CORRENTE E INEFICIÊNCIA DE TRANSPORTE EM
NANOESTRUTURAS SEMICONDUTORAS INVESTIGADAS ATRAVÉS DE
PROPAGAÇÃO DE PACOTES DE ONDA**

Tese de Doutorado apresentada ao Programa de Pós-Graduação em Física da Universidade Federal do Ceará, como requisito parcial para obtenção do Título de Doutor em Física. Área de Concentração: Física da Matéria Condensada.

Aprovada em 08 / 05 / 2015

BANCA EXAMINADORA

Dr. Andrey Chaves (Orientador)

Universidade Federal do Ceará (UFC)

Dr. Gil de Aquino Farias

Universidade Federal do Ceará (UFC)

Dr. François Maria Leopold Peeters

University of Antwerp

Dr. Teldo Anderson da Silva Pereira

Universidade Federal do Mato Grosso (UFMT)

Dr. Nilson Sena de Almeida

Universidade do Estado do Rio Grande do Norte (UERN)

*To my wife Juliana Lemes, my Daughter Thamyres Adorno and my Parents, Cleide
Adorno and Ary Iza.*

"A human being is a part of the whole called by us universe, a part limited in time and space. He experiences himself, his thoughts and feeling as something separated from the rest, a kind of optical delusion of his consciousness. This delusion is a kind of prison for us, restricting us to our personal desires and to affection for a few persons nearest to us. Our task must be to free ourselves from this prison by widening our circle of compassion to embrace all living creatures and the whole of nature in its beauty"

Albert Einstein (1876 - 1955)

Acknowledgments

First, I thank my family, especially my parents Ary Izá and Cleide Adorno. I would like to express my sincere gratitude to them for everything that they did for me, giving me the opportunity to study, supporting me and helping me during my whole life. I thank my wife, Juliana Lemes, for being by my side for the last 5 years. I can not imagine my life without her. I thank her for the good moments and also for the bad ones that we stayed together. Based on these years, I can say that the best choice in my life was you. Thank you so much for everything that you did for me.

I thank Professor Andrey Chaves for being my promoter the long time of the my Ph.D. It has been hard to work with completely different tools, but you have always tried to direct me to the right path. I thank you for being sincere in all the stages of my academic trajectory.

I thank Professor Gil de Aquino Farias for the motivation that he gave me. I had some tough moments during my the academic path, but the few words I heard from him during these times were enough to make me confident that I could get over the problems and make a good job at the end.

I thank Professor François M. Peeters by the support that he gave me in Antwerp along the time of the my sandwich Ph.D.

I thank Professor Teldo Anderson da Silva Pereira for kindly helping me every time I had trouble solving the problem he suggested, and for positively encouraging me to keep going.

I thank the other member of the jury, Prof. Nilson Almeida, for the time spent reviewing this work, as well as for their very important comments, corrections and suggestions that made possible to improve the quality of the final version of this thesis. In view of my academic background, I appreciate the discussions and exchanges of this thesis.

I thank my undergraduate friends in mathematics at Universidade Estadual de Goiás: Airton, Prof. Arnaldo, Prof. Carlos Santos, Delma, Edimeire, Edson, Emerson, Prof. Jair Jr., Jorge, Prof. Lucelene, Prof. Massako, Prof. Nilcyneia, Prof. Paulo Henrique, Sandra, Welligton, and my undergraduate friends in Physics at Universidade Federal do Mato Grosso: Prof. Alberto, Alessandro Henrique, Adriana Dussel, Ana Paula, Celso Ferst, Edson Ferreira, Prof. Denilton, Prof. Fabio Ramos, Fernanda Royo, Gideão, Prof. Harold, Heloisa, Prof. Hulk, Izabela, João Valim, José Divino, José Filho, Jones Queiroz, Júlio Cesar, Layane, Lucas Jorge, Marcelo Machado, Marcelo Pastor, Prof. Mauricio Godoy, Regiana, Prof. Ricardo, Rodrigo químico, Prof. Romildo, Tarsila, Welton, Wesley. I also thank my friends of the Universidade Federal do Ceará and University Antwerp where I made my Ph.D: Alan, Bruno Goldim, Cristiano Balbino, Davi Soares, David Figueiredo, Davoud, Diego Lucena (maluco), Yierpan, Esterfferson, Gardenia, Gustavo Gusmão, Hasan, Prof. Jeanlex, Joel Castro, Jonas Nascimento, Jorge Capuan, José

Gadelha, Khosrow, Levi Leite, Lucian Covaci, Massoud Masir, Mehdi, Rebeca de Holanda, Rodrigo Almeida, Silvia Helena, Slavisa Milovanovic, Vagner Bessa, Victor Fernández, Willian Muñoz. I can not forget my several friends out of the university: Angélica Silva, Derivânia, Dulce, Eduardo, Eliezel, Everaldo, Luciano Guerra, Ricardo, Rosa Pereira, Rosana, Taciana and my close relatives.

In special, I thank my close friends Diego Rabelo, Thiago de Melo and Thiago Bonelli. Diego Rabelo and I worked together for three years and half, where I faced the challenges of science with a very good friend that he was and I thank him for all his support. Thiago de Melo is a great person with admirable personality, and Thiago Bonelli is a good boy, he is “Palmeirense”.

I would like to thank all the agencies that gave me financial support like: Brazilian agency CAPES for the financial support during my stay in Belgium through the sandwich program fellowship, under agreement number, BEX-7177/13-5, the Flemish Science Foundation (FWO-VI), the Bilateral programme between CNPq and FWO-VI, and Brazilian Science Without Borders (CsF).

Finally, I thank all those who helped me directly or indirectly, for the preparation and conclusion of this work.

Resumo

Os avanços nas técnicas de crescimento tornaram possível a fabricação de estruturas semicondutoras quase-unidimensionais em escalas nanométricas, chamadas pontos, fios, poços e anéis quânticos. Interesse nessas estruturas tem crescido consideravelmente, não só devido às suas possíveis aplicações em dispositivos eletrônicos e à sua manipulação química fácil, mas também porque eles oferecem a possibilidade de explorar experimentalmente vários aspectos de confinamento quântico, espalhamento e fenômenos de interferência. Em particular, neste trabalho, investigamos as propriedades eletrônicas e de transporte em poços quânticos, fios e anéis, cujas dimensões podem ser alcançadas experimentalmente. Para isto, resolvemos a equação de Schrödinger dependente do tempo utilizando o método *Split-operator* em duas dimensões.

Nesta tese, abordamos quatro trabalhos, sendo o primeiro uma analogia ao Paradoxo de Braess para um sistema mesoscópico. Para isso, utilizamos um anel quântico com um canal adicional na região central, alinhado com os canais de entrada e saída. Este canal extra faz o papel do caminho adicional em uma rede de tráfego na teoria dos jogos, similar ao caso do paradoxo de Braess. Calculamos as auto-energias e a evolução temporal para o anel quântico. Surpreendentemente, o coeficiente de transmissão para algumas larguras do canal extra diminuiu, semelhante ao que acontece com redes de tráfego, onde a presença de uma via extra não necessariamente melhora o fluxo total. Com a análise dos resultados obtidos, foi possível determinar que neste sistema o paradoxo ocorre devido a efeitos de interferência e de espalhamento quântico.

No segundo trabalho, foi feita uma extensão do primeiro, (i) aplicando-se um campo magnético, onde foi possível obter o efeito Aharonov-Bohm para pequenos valores do canal extra e controlar efeitos de interferência responsáveis pelo paradoxo mencionado, e (ii) fazendo também a aplicação de um potencial que simula a ponta de um microscópio de força atômica (AFM) interagindo com a amostra - este potencial é repulsivo e simula um possível fechamento do caminho em que o pacote de onda se propaga. Assim, neste trabalho, realizamos uma contra-prova do primeiro, onde observamos que com o posicionamento da ponta do AFM sobre canal extra, se diminui o efeito de redução de corrente devido ao paradoxo de Braess.

No terceiro trabalho, realizamos uma análise de tunelamento entre dois fios quânticos separados por uma certa distância e calculamos qual a menor distância para qual ocorre tunelamento significativo nesse sistema eletrônico. Este trabalho é de fundamental importância para o manufaturamento de dispositivos nanoestruturados, porque nos permite investigar qual a distância mínima para a construção de um circuito eletrônico sem que haja interferências nas transmissões das informações.

No quarto e último trabalho desta tese, investigamos a energia de ligação do elétron-impureza em GaN/HfO₂ para um poço quântico. Consideramos simultaneamente as con-

tribuições de todas as interações das auto-energias devido ao descasamento das constantes dielétricas entre os materiais. Foram estudados poços largos e estreitos, comparando os resultados para diferentes posições da impureza e a contribuição da auto-energia para o sistema.

Abstract

Advances in growth techniques have made possible the fabrication of quasi one-dimensional semiconductor structures on nanometric scales, called quantum dots, wires, wells and rings. Interest in these structures has grown considerably not only due to their possible applications in electronic devices and to their easy chemical manipulation, but also because they offer the possibility of experimentally exploring several aspects of quantum confinement, scattering and interference phenomena. In particular, in this work, we investigate the electronic and transport properties in quantum wells, wires and rings, whose dimensions can be achieved experimentally. For this purpose, we solve the time-dependent Schrödinger equation using the split-operator method in two dimensions.

We address four different problems: in the first one, the electronic transport properties of a mesoscopic branched out quantum ring are discussed in analogy to the Braess Paradox of game theory, which, in simple words, states that adding an extra path to a traffic network does not necessarily improves its overall flow. In this case, we consider a quantum ring with an extra channel in its central region, aligned with the input and output leads. This extra channel plays the role of an additional path in a similar way as the extra roads in the classical Braess paradox. Our results show that in this system, surprisingly the transmission coefficient decreases for some values of the extra channel width, similarly to the case of traffic networks in the original Braess problem. We demonstrate that such transmission reduction in our case originates from both quantum scattering and interference effects, and is closely related to recent experimental results in a similar mesoscopic system.

In the second work of this thesis, we extend the first system by considering different ring geometries, and by investigating the effects of an external perpendicular magnetic field and of obstructions to the electrons pathways on the transport properties of the system. For narrow widths of the extra channel, it is possible to observe Aharonov-Bohm oscillations in the transmission probability. More importantly, the Aharonov-Bohm phase acquired by the wave function in the presence of the magnetic field allows one to verify in which situations the transmission reduction induced by the extra channel is purely due to interference. We simulate a possible closure of one of the paths by applying a local electrostatic potential, which can be seen as a model for the charged tip of an atomic force microscope (AFM). We show that positioning the AFM tip in the extra channel suppresses the transmission reduction due to the Braess paradox, thus demonstrating that closing the extra path improves the overall transport properties of the system.

In the third work, we analyze the tunneling of wave packets between two semiconductor quantum wires separated by a short distance. We investigate the smallest distance at which a significant tunneling between the semiconducting wires still occur. This work is of fundamental importance for the manufacturing of future nanostructured devices,

since it provides information on the minimum reasonable distances between the electron channels in miniaturized electronic circuits, where quantum tunnelling and interference effects will start to play a major role.

In the last work of this thesis, we investigate the binding energy of the electron-impurity pair in a GaN/HfO₂ quantum well. We consider simultaneously the contributions of all interactions in the self-energy due to the dielectric constant mismatch between materials. We investigate the electron-impurity bound states in quantum wells of several widths, and compared the results for different impurity positions.

Abstracte

Vooruitgang in groeitechnieken heeft het mogelijk gemaakt de vervaardiging van quasi-ééndimensionale halfgeleiderstructuren op nanometer schaal, genaamd quantum dots, draden en ringen. De interesse in deze structuren is aanzienlijk gegroeid niet alleen vanwege hun mogelijke toepassingen in elektronische apparaten en hun gemakkelijke chemische manipulatie, maar ook omdat ze de mogelijkheid bieden voor experimenteel onderzoek van verschillende aspecten van kwantumopsluiting, verstrooiing en interferentie verschijnselen. In het bijzonder, in dit werk onderzoeken we de elektronische en transport eigenschappen van kwantumputten, draden en ringen, met afmetingen die experimenteel kunnen worden gerealiseerd. Voor dit doel, lossen we de tijdsafhankelijke Schrödingervergelijking op met behulp van de split-operator methode in twee dimensies.

We beschouwen vier projecten: in de eerste, werden de transport eigenschappen van een mesoscopisch vertakte quantum ring bestudeerd in analogie met de Braess Paradox van speltheorie, die, in eenvoudige woorden, stelt dat het toevoegen van een extra pad naar een verkeersnetwerk niet per se een verbetering geeft van de totale stroom. In dit geval beschouwen we een quantum ring met een extra kanaal in het centrale gebied, dat een verbinding geeft tussen de input en output kanalen. Dit extra kanaal speelt de rol van een extra geleidingspad op soortgelijke wijze als de extra wegen in de klassieke Braess paradox. Onze resultaten tonen aan dat in dit systeem, de transmissie coëfficiënt verrassend vermindert voor sommige waarden van de extra kanaalbreedte, vergelijkbaar met het geval van verkeersnetwerken in het oorspronkelijke Braess probleem. We tonen aan dat zulke transmissie vermindering een gevolg is van zowel quantum verstrooiing als interferentie effecten, en dit resultaat is nauw verwant met recente experimenten aan vergelijkbare mesoscopische systemen.

Het tweede deel van dit proefschrift is een uitbreiding van het eerste deel waarbij verschillende ring geometrieën worden onderzocht en het effect van een extern loodrecht magnetisch veld. Voor smalle breedtes van het extra kanaal, vinden we dat het mogelijk is om Aharonov-Bohm oscillaties waar te nemen in de transmissie waarschijnlijkheid. Belangrijker, met behulp van de Aharonov-Bohm fase van de golffunctie verkregen in aanwezigheid van het magnetische veld is het mogelijk om na te gaan in welke situaties de verlaging van de transmissie zoals geïnduceerd door het extra kanaal louter een gevolg is van interferentie. We simuleren de mogelijke sluiting van één van de paden doormiddel van een lokaal elektrostatische potentiaal, die kan worden beschouwd als een model voor de tip van een geladen atomaire kracht microscoop (AFM). Wanneer de AFM tip gepositioneerd is in het extra kanaal onderdrukt het de transmissie vermindering vanwege de Braess paradox, waaruit blijkt dat het sluiten van het extra pad een verbetering geeft van de algehele transport eigenschappen van het systeem.

In het derde deel, analyseren we de tunneling van golfpakketten tussen twee halfgelei-

der quantumdraden die gescheiden zijn door een eindige korte afstand. In deze studie onderzoeken we de minimale afstand waarbij een aanzienlijke tunneling tussen de halfgeleiderdraden optreedt. Dit is van fundamenteel belang voor de productie van toekomstige nanostructuur apparaten, want het geeft informatie over de minimale toegestane afstand tussen elektronkanalen in geminiaturiseerde elektronische schakelingen, waarbij quantum tunneling en interferentie-effecten een belangrijke rol gaan spelen.

In het laatste deel van dit proefschrift onderzoeken we de bindingsenergie van het elektron-onzuiverheidspaar in een GaN / HfO₂ quantumput. We beschouwen tegelijkertijd de bijdragen van alle interacties tot de zelf-energie vanwege de mismatch in diëlektrische constante tussen de materialen. We onderzoeken de elektron-onzuiverheid gebonden toestanden in kwantumputten van verschillende breedtes, en vergelijken de resultaten voor verschillende onzuiverheidsposities.

Contents

Acknowledgments	vii
Resumo	ix
Abstract	xi
Abstracte	xiii
List of Figure	xvii
List of Tables	xxii
1 Introduction	23
1.1 Brief Historical Overview	23
1.2 Energy Bands	24
1.3 Adiabatic Approximation and Effective Mass	25
1.4 The Envelope-Function Approximation	30
1.5 Low-Dimensional Semiconductor Systems	30
1.5.1 Quantum Dot	31
1.5.2 Quantum Wires	32
1.5.3 Quantum Wells	33
1.5.4 Quantum Rings	34
1.6 The Aharonov-Bohm Effect	35
1.7 Braess paradox and game theory	37
1.8 Quantum wire devices	40
1.9 Outline of this thesis	41
2 Theoretical Model	43
2.1 The split-operator technique	44
2.2 Real-time Evolution	49

2.3	Imaginary-time evolution	51
3	Braess paradox at the mesoscopic scale	53
3.1	Theoretical model	54
3.2	Results and discussion	55
4	Wave packet propagation through branched quantum rings	64
4.1	Theoretical model	65
4.2	Results and Discussion	67
4.2.1	Influence of an external magnetic field	71
4.2.2	Effect of extra (obstructing) potentials	73
5	Quantum tunneling between bent semiconductor nanowires	78
5.1	Theoretical model	80
5.2	Transport properties	82
6	Dielectric mismatch and shallow donor impurities in GaN/HfO₂ quantum wells	91
6.1	Theoretical Model	93
6.2	Results and Discussion	96
7	Summary	102
7.1	Concluding remarks of the thesis	102
7.2	Future prospects	103
	Bibliographical References	105
	Publications related to this thesis	114
	Publications not related to this thesis	142
	Index	147
	Curriculum Vitae	149

List of Figures

- 1.1 (a) Scientists John Bardeen (standing left), Walter Houser Brattain (standing right) and William Bradford Shockley (seated); (b) first transistor in history based on semiconductors, manufactured by Bardeen, Brattain and Houser; and (c) first integrated circuit, produced and developed by Jack S. Kilby. Both were invented in the last century [6]. 23
- 1.2 (a) Formation of energy bands due to the approach of a large number of atoms in a solid semiconductor (b) Electron's energy bands (el), light hole (lh), heavy hole (hh) and *split-off* (so) in a semiconductor with gap E_g . The hatched regions illustrate the occupation of electrons with $T > 0$ K [20]. 25
- 1.3 Micrograph image obtained by scanning an electron to three types of quantum dots: circular, square and triangular, manufactured by self-assembly method [36]. 32
- 1.4 Quantum wires (a) SEM's image for the GaAs material with wire radius 50 nm grown with LCG techniques, [37](b)SEM image for the GaP material with radius 50 nm grown with LGC techniques, [37] (c) TSEM Image for AlGaAs nanowire perpendicular growth of Al, Ga, As and O, respectively, reference bar equals 50 nm grown with techniques MBE, [38] and (d)AFM image of a Si nanowire on the Au substrate with radius 10 nm grown with techniques VLS, [47] 33
- 1.5 Physical structure of a quantum well of AlGaAs/GaAs and representation of the potential profile of this heterostructure. In the right side, (I) represents the alloy AlGaAs and (II) represents the GaAs. 34
- 1.6 (a) Image obtained by atomic force microscopy (AFM) of a quantum ring grown with the anodic oxidation technique, (b) experiment the potential profile, where the dark curves represent the oxides lines [55]. 35

1.7	Illustration of experience proposed by Aharonov-Bohm. Between two slits a magnetic field B is applied. It is different from zero only in the inner region of the applied field, but the vector potential (shown by solid lines) is different from zero in all space, with cylindrical symmetry causing opposite effects on the path 1 and 2.	35
1.8	Scheme to the paradox of Braess (a) A network paths systems starting at point A and ends at point B and (b) Systems paths adding an extra path in the central region with fixed time in extra path.	39
1.9	(a) A scanning electron micrograph of a $2 \mu m \times 2 \mu m$ silicon nitride paddle. The supporting rods are 230 nm wide and $3 \mu m$ long, and the thickness of the device layer is 240 nm. (b) A scanning electron micrograph of silicon nitride suspended wires. The length of the wires varies form 1 to $8 \mu m$. Adapted from [78].	40
3.1	(a) Sketch of the system under investigation: a quantum ring with average radius R , attached to input (left) and output (right) channels with the same width as the ring ($W = 10 \text{ nm}$), and to an extra horizontal channel of width W_c . (b) Contour plots of the transmission probabilities as a function of the extra channel width and ring radius. The solid, dashed and dotted lines indicate seven minima that are discussed in the text. A zoom of the $4 \text{ nm} < W_c < 16 \text{ nm}$ region with the logarithm of the transmission is shown in (c).	55
3.2	Snapshot of the propagating wave function at $t = 900 \text{ fs}$ for two values of the extra channel width: 19 nm (a) and 20 nm (b).	57
3.3	Probability density currents as a function of time, calculated (a) in the input lead and (b) in the extra channel, for different values of the extra channel width W_c , for wave packet energy $\epsilon = 70 \text{ meV}$	58
3.4	(a) Eigenstates of a finite quantum well as a function of its width. (b) Diagram representing the energy sub-bands in the input lead and in the extra channel. The horizontal dotted line is the average energy of the wave packet used in Figs. 3.1 and 3.3, and the shaded area in (a) illustrates the FWHM of the energy distribution of this wave packet.	60
3.5	(a) Transmission probabilities as a function of the extra channel width in the vicinity of the minimum labeled as M in Fig. 3.1(a), for several values of the wave packet energy $\epsilon = 70$ (bottom curve), 80, ... 180 meV (top curve). The curves were shifted 0.1 up from each other, in order to help visualization. (b) Energy levels (solid) as a function of the channel width, plotted in a log scale, along with two fitting functions (dashed curves), for large (f_1) and small (f_2) values of the channel width. (c) Numerically obtained (symbols) positions of the M minima as a function of the wave packet energy, along with the results (solid curve) of the analytical model, given by Eq. (3.5).	61

3.6	Transmission probabilities for a $\epsilon = 70$ meV wave packet scattered by two kinds of defects in the lead-ring junction: a Gaussian attractive potential of depth V_G (solid, bottom axis) and width $\sigma_G = 5$ nm, and a circular bump of radius R_b (dashed, top axis), which are schematically illustrated in the lower and upper insets, respectively.	62
4.1	Sketch of the systems under investigation. (a) Half quantum ring with leads and channel aligned, (b) circular quantum ring with an extra channel in the perpendicular direction, (c) square ring with non-aligned leads and channel, and (d) circular quantum ring with leads and channel aligned. . .	65
4.2	Transmission probability as function of channel width W_c . The frames (a), (b), (c) and (d) refer collectively as the corresponding systems presented in Fig. 4.1. The WP have kinetic energies ϵ_1 (black, dotted line), ϵ_2 (red, dashed line), ϵ_3 (blue, solid line), propagating in the subband ground state, while the other is in the first excited state with kinetic energy ϵ_3 (green dash-dotted line).	67
4.3	Time-dependent probability current through the extra channel, calculated for kinetic energy ϵ_1 . The different frames refer to the systems in Fig. 4.1.	69
4.4	Snapshots of the squared wave function at $t = 460$ fs, for different channel width W_c and kinetic energy ϵ_1	70
4.5	Projection of the wave function on the ground state (top graphics) and first-excited subbands (bottom graphics) as function of channel width W_c , calculated at the output lead. Kinetic energy ϵ_1 (black dotted line), ϵ_2 (red short-dot line), and ϵ_3 (blue solid line). This figure is ordered in the same sequence Fig. 4.1.	71
4.6	Contour plots of the transmission probabilities as a function of the extra channel width W_c and magnetic field \mathbf{B} . This figure is ordered in the same sequence as Fig. 4.1.	72
4.7	Transmission probability as function of the channel width W_c for quantum rings depicted in (a) Fig. 4.1(c) and (b) Fig. 4.1(d), respectively. The kinetic energy used was ϵ_1 and each color curve represents a transmission probability for a specific magnetic field, ranging from 0 (purple) to 1 T (red).	74
4.8	Schematic diagram for an AFM tip potential over quantum rings represented by the dots (1), (2) and (3). The solid arrows indicate the direction of the tip displacement, while the dash line arrows indicate the final position of the tip. Tip (1) is fixed in the central region for each system.	75
4.9	Transmission as a function of (1) intensity of the Gaussian potential, (2) and (3) tip position. The order of the figures refer to the form different depicted in Fig. 4.1. The curves width black color are for $W_c = 10$ nm, while the curves width red colors are for the minima of the transmission shown in Fig. 4.2. The WP kinetic energy is ϵ_1	76

5.1	Potential profile scheme for the QWs studied in this work. The two QWs are separated from each other by a distance W_2 , ranging from 0 to 4.8 nm. The smooth connections between vertical and horizontal wire are described by circles of radius $R_W = W_1/2$ and $R_L = L/2$	80
5.2	(a)-(c) Wave packet transmissions (T) and reflexion (R) probabilities as function of W_2 for a well width of $L = W_1$. The transmissions are calculated in three different points in the QWs: bottom T_1 (green, dash dot line), top T_3 (red, dash line) right T_2 (black, solid line), while the reflexion R (blue, dash dot dot line) is calculated at the left side, as shown in (d). The wave packet energies used are (a) ε_1 , (b) ε_2 and (c) ε_3 . (d) Snapshot of the wave function calculated at $t = 160$ fs for $L = W_1$ and $W_2 = 1.2$ nm as depicted by the vertical dash line in (b).	82
5.3	The same result as shows in Fig. 5.2, but now for $L = 2W_1$	83
5.4	Transmission coefficient ($T_2 + T_3$) as function of the well width L , for wave packet energies (a) ε_1 and (b) ε_3 . Three W_2 distance were considered: 0 nm (black, solid line), 1.2 nm (red, dash line) and 2.4 nm (blue, dotted line).	84
5.5	(a) Bottom energy of the different subbands as function of the quantum well width L . Schematic diagrams that represents the subband energies as function of the wave vector k_x in the x direction, for output width of (b) $L = 5$ nm, (c) $L = 10$ nm, and (d) $L = 20$ nm. The horizontal dashed-dot lines represents the average energy of the wave packet, ε_1 and ε_3	85
5.6	Projection of the wave function on the ground state P_1 , first-excited P_2 and second-excited subbands P_3 integrated in time, for the output width $L = W_1$, panels column (a) and $L = 2W_1$, panels column (b), as function of the distance W_2 calculated at position 158 nm in the right-lead.	86
5.7	The total time-dependent probability current for wave packet energy of ε_1 (black, solid line), ε_2 (red, dash line) and ε_3 (blue, dotted line). Results for different distances W_2 are plotted in column (a) $W_2 = 0$ nm, and column (b) $W_2 = 2.4$ nm. The output width L is in the first row $L = W_1/2$, second row $L = W_1$, and third row $L = 2W_1$	87
5.8	Conductance in the output quantum wire as a function of the distance W_2 . Wavepacket energy is ε_1 (black, solid lines), ε_2 (red, dashed lines) and ε_3 (blue, dotted lines) for quantum well L width of (a) 10 nm and (b) 20 nm.	88
5.9	(Color online) Conductance of the quantum wire as a function of kinetic energy wave packet for the three possible output leads G_1 (dotted), G_2 (solid) and G_3 (dashed), with well widths $L = 5$ nm (blue), $L = 10$ nm (black) and $L = 20$ nm (red). The W_2 distance is given by (a) 0 nm, (b) 1.2 nm and (c) 2.4 nm.	89

6.1	(a) Energy potential $\Delta E_e(z_e)$ due to conduction band edge discontinuity (red dashed line) and the potential $\Sigma_e(z_e)$ due to self-energy corrections (black solid line). (b) Total potential $V(r) = \Delta E_e(z_e) + \Sigma_e(z_e) + V_{e-im}(r)$ in the z direction (black solid line) and electron ground state wave function (blue dashed line). (c) Coulomb potential $V_{e-m}(r)$ of electron-impurity interaction in 3D plot. (d) Total potential $V(r)$ in 3D plot.	94
6.2	(Color online) Waves functions projection in the (yz) plane for the ground state, first and second excited states. In (a) the impurity is located in $z_{im} = 0$ nm and in (b) the impurity is $z_{im} = 5$ nm far from the center of the QW. The z -projection of the total potential $V(z)$, in eV, are depicted for QWs with width of $L = 5$ nm.	96
6.3	(Color online) Left panels: Electron energy for ground state (black solid line), first (blue dashed line) and second (red dotted line) excited state in QW for (a) narrow $L = 5$ nm QW width and (b) wide $L = 10$ nm HfO ₂ /GaN QW width. Right panels: Electron-impurity binding energy for ground state (black solid line), first (blue dashed line) and second (red dotted line) excited state energy as function of impurity position for a (c) narrow ($L = 5$ nm) QW and (d) wide $L = 10$ nm HfO ₂ /GaN QW. The dark yellow line-sphere depict the electron energy (left) and electron-impurity binding energy (right) in narrow (top) and wide (bottom) AlN/GaN QW, and the green dash-dot line shows the effect of the image charges in GaN/HfO ₂ QW.	97
6.4	Schematic diagram of different interactions between electron and their image charges, electron and impurity as well as electron and impurity image charges for GaN/AlN (a)-(c) and in GaN/HfO ₂ (b)-(d) QWs. In (a)-(b) the impurity is located in the well region while in (c)-(d) the impurity is located in the barrier region.	98
6.5	Electron center-of-mass as function of the impurity position (z_{im}) for (a) narrow ($L = 5$ nm) and (b) wide ($L = 10$ nm) QWs. The ground state, first and second excited states are represented by black solid, blue dashed and red dotted lines, respectively. The gray line-sphere depict the standard deviation in position σ_x for narrow and wide QWs.	99
6.6	Stark shift of the ground state energy (solid lines), first excited state energy (dashed lines) and second excited state energy in (a) narrow (5 nm) and (b) wide (10 nm) QWs.	101

List of Tables

1.1	- Number and degree of confinement for different degrees of freedom of heterostructures [30]	31
5.1	- Exponential fitting to transmission probabilities T_2 shown in Figs. 5.2 and 5.3, for different energies ϵ and widths of the second wire L	84

1.1 Brief Historical Overview

In recent decades, technical advances have enabled a large number of experimental studies of semiconductor heterostructures [1, 2, 3, 4, 5]. The pioneers in manufacturing devices based on semiconductors were John Bardeen, William Shockley and Walter H. Brattain, and the transistor they produced is known as the point-contact transistor [6]. Figure 1.1 shows the three researchers (a), the first transistor they developed (b), and the first integrated circuit (c). Through these and other technological advances, we now have extremely efficient electronic devices. Semiconductor devices presents very interesting optical and transport properties, which lead to several technological application and represent the vanguard of the electronic devices manufacturing.

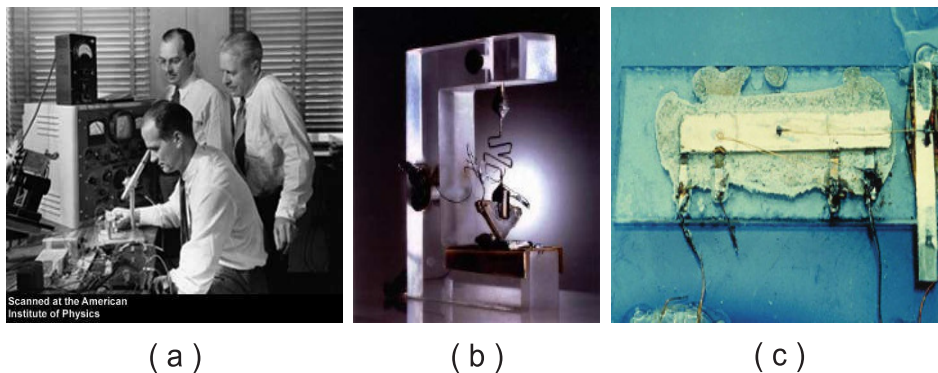


Figure 1.1: (a) Scientists John Bardeen (standing left), Walter Houser Brattain (standing right) and William Bradford Shockley (seated); (b) first transistor in history based on semiconductors, manufactured by Bardeen, Brattain and Houser; and (c) first integrated circuit, produced and developed by Jack S. Kilby. Both were invented in the last century [6].

At the end of the 1960s, researchers Tsu and Esaki[7, 8] proposed an innovative theoretical work in the study of heterostructured systems composed of different materials. They

proposed the fabrication of an artificial periodic structure consisting of alternate layers of two dissimilar semiconductors with layer thickness of the order of nanometers nowadays known as *Superlattices*. This work enabled numerous subsequent studies that continue to bring great technological advances.

Techniques such as MBE [2] (molecular beam epitaxy), MOCVD [3] (metalorganic chemical vapor deposition), CVD [4] (chemical vapor deposition) in addition to VLS [5] (vapor-liquid-solid) constitute the vanguard of growth of semiconductor devices, allowing not only the fabrication of Tsu and Esaki's *superlattices*, but also artificial lattices of quantum dots, nanowires and rings [9, 10, 11, 12]. This brought the possibility to observe and control the optical and electronic properties of these semiconductor nanostructures [13, 14, 15, 16]. Theoretical *Ab initio* works have also successfully described properties by ab initial calculations, tight-binding models, $\mathbf{k} \cdot \mathbf{p}$ Hamiltonians and effective mass approximation, based on the envelope function [17, 18, 19].

1.2 Energy Bands

In order to understand the mechanism responsible for the electrical current in semiconductor materials and their applications in nanotechnology, a study of energy bands in these materials is necessary. Electrons in an isolated atom are characterized by discrete and quantized energy levels, which correspond to the atomic orbitals 1s, 2s, 2p, 3p, 3d, ... and satisfy the Pauli exclusion principle. In an isolated atom, the calculation is based on the Schrödinger equation, and the solution is exact for low atomic number elements. In a solid, where there is a large number of atoms close to each other, the exact calculation becomes very complicated. This is because the electrons and nucleus of each atom interact with the electrons and the nuclei of neighboring atoms. An electron in level 1s in one of these atoms can also occupy this same level in another atom: it will have two distinct wave functions that describe the two possible states, but sharing the same energy, i.e., have a double degeneracy. The degeneracy is "broken" when several atoms are proximate, thereby forming an almost continuous energy band.

Because there are a lot of atoms ($N \sim 10^{23} \text{cm}^{-3}$) disposed periodically in the crystal lattice, energy states are distributed through continuous energy bands, which are separated from each other by a prohibited zone. The allowed energy states are defined as **energy bands** and the forbidden zone is the **gap**, as shown in Fig. 1.2.

Semiconductors at 0 K temperature behave as insulators, having all allowed energy states occupied below the Fermi level, while all allowed energy states above the Fermi level are unoccupied ¹. The lowest energy states are in the so called **valence band**, while the states with the highest energy are in the **conduction band**. The semiconductor gap is the energy corresponding to the difference between the top of the valence band and the

¹The Fermi wavelength is given by: $\lambda_F = 2\pi / (3\pi^2 n)^{1/3}$, where n is electronic density.

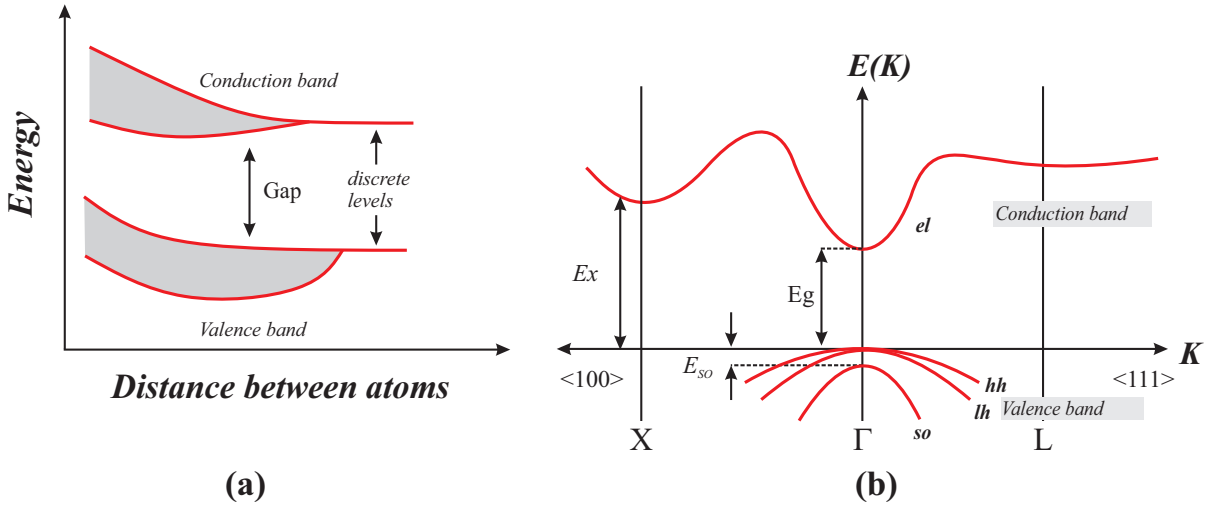


Figure 1.2: (a) Formation of energy bands due to the approach of a large number of atoms in a solid semiconductor (b) Electron's energy bands (el), light hole (lh), heavy hole (hh) and *split-off* (so) in a semiconductor with gap E_g . The hatched regions illustrate the occupation of electrons with $T > 0$ K [20].

minimum of the conduction band, and the Fermi energy in an intrinsic semiconductor² is the center of the energy gap [20].

Figure 1.2 (a) illustrates the allowed energy states that fills the bands in a semiconductor when a large number of ions are made closer. Figure 1.2 (b) represents the energy bands as a function of the k wave vector.

1.3 Adiabatic Approximation and Effective Mass

In order to understand the electronic properties of semiconductor materials, it is necessary to investigate the behavior of their electrons when subjected to external fields. To describe such many bodies system, we will initially neglect the *spin-orbit* interaction and other relativistic contributions [20, 21].

An ideal crystal consists of an infinite set of ions located near the sites a lattice, forming an electron gas that move in the ion field. The basic properties of the crystal depend on the electron dynamics in this lattice and the understanding of this problem depends on the solution of the Schrödinger equation, including electron-electron, electron-ion and ion-ion interactions. That allows us to study different aspects of the crystal such as its electronic and ionic dynamics and their interactions with various perturbations, including impurities and external fields.

The complete Schrödinger equation for \mathbf{n} electrons and \mathbf{N} ions, written in terms of the electronic coordinates, $r_1, r_2, r_3, \dots, r_n$ and ionic coordinates $R_1, R_2, R_3, \dots, R_N$ are:

²An intrinsic semiconductor is a pure semiconductor, free of doping.

$$\left[-\sum_{i=1}^n \frac{\hbar^2}{2m_i} \nabla_i^2 - \sum_{k=1}^N \frac{\hbar^2}{2M_k} \nabla_k^2 + \sum_{i<j=1}^n \frac{1}{4\pi\epsilon_0} \frac{e^2}{|\mathbf{r}_i - \mathbf{r}_j|} + \sum_{I<J}^N \frac{1}{4\pi\epsilon_0} \frac{Z_I Z_J e^2}{|\mathbf{R}_I - \mathbf{R}_J|} - \sum_{i,I}^{n,N} \frac{1}{4\pi\epsilon_0} \frac{Z_I e^2}{|\mathbf{R}_I - \mathbf{r}_i|} \right] \Psi(\mathbf{r}_1, \dots, \mathbf{r}_n, R_1, \dots, R_N) = E \Psi(\mathbf{r}_1, \dots, \mathbf{r}_n, R_1, \dots, R_N), \quad (1.1)$$

where the first term is the electrons kinetic energy, the second is the kinetic energy of ions, the third is the electron-electron Coulomb interaction potential, the fourth term is the ion-ion Coulomb interaction potential, and the fifth is the potential energy of Coulomb interaction between the electron and the ions. $|\mathbf{r}_i - \mathbf{r}_j|$, $|\mathbf{R}_I - \mathbf{R}_J|$, $|\mathbf{R}_I - \mathbf{r}_i|$ are, respectively the distances between the electron i and the electron j , ion I and ion J , and between the ion I and the electron i .

As the electron mass is less than the ion mass by a factor of approximately 1/1800 ($m_i \approx 1.8 \times 10^{-3} M_I$), the electron's kinetic energy is much higher than that of the ions. The electronic distribution continually adjusts itself with the positions of the ions, which at any time can be considered the same. This suggests that the ions remain approximately at rest. This hypothesis is called adiabatic approximation (Born and Oppenheimer 1927) [22]. It can be expressed by writing the wave function $\Psi(\mathbf{r}_1, \dots, \mathbf{r}_n, R_1, \dots, R_N)$, where electron coordinates are collectively represented by \mathbf{r} and the ionic coordinates collectively represented by \mathbf{R} :

$$\Psi(\mathbf{r}, \mathbf{R}) = \psi(\mathbf{r}, \mathbf{R}) \varphi(\mathbf{R}), \quad (1.2)$$

where $\psi(\mathbf{r}, \mathbf{R})$ is the electronic eigenfunction, which depends on the coordinated \mathbf{r} of electrons and coordinate \mathbf{R} of ions, appearing as a fixed parameter. This eigenfunction satisfies the Schrödinger equation :

$$\left[-\sum_{i=1}^n \frac{\hbar^2}{2m_i} \nabla_i^2 - \sum_{i<j=1}^n \frac{1}{4\pi\epsilon_0} \frac{e^2}{|\mathbf{r}_i - \mathbf{r}_j|} - \sum_{i,I}^{n,N} \frac{Z_I}{4\pi\epsilon_0} \frac{e^2}{|\mathbf{R}_I - \mathbf{r}_i|} \right] \psi(\mathbf{r}, \mathbf{R}) = E_e(\mathbf{R}) \psi(\mathbf{r}, \mathbf{R}), \quad (1.3)$$

where $E_e(\mathbf{R})$ is the electronic eigenvalues, which depend on the coordinate \mathbf{R} . The function $\varphi(\mathbf{R})$ is the ionic eigenfunction and satisfies

$$\left[-\sum_{I=1}^N \frac{\hbar^2}{2M_I} \nabla_I^2 + \Phi(\mathbf{R}) \right] \varphi(\mathbf{R}) = E \varphi(\mathbf{R}), \quad (1.4)$$

where

$$\Phi(\mathbf{R}) = E_e + \sum_{I < J}^N \frac{Z_I Z_J}{4\pi\epsilon_0} \frac{e^2}{|\mathbf{R}_I - \mathbf{R}_J|} \quad (1.5)$$

is the effective potential energy of the ions and E is the total energy. Eq. 1.4 is the ionic Schrödinger equation and arises from the substitution of eq. 1.2 in eq. 1.1.

The ionic coordinates \mathbf{R} in eq. 1.4 are arbitrary. Nevertheless, if ions occupy the equilibrium position R_0 of the crystal structure, the electron-ion interaction potential becomes periodic, with the same periodicity as the crystal lattice. The number of terms in eq. 1.4 is much smaller than in Eq. 1.1; however, even with the adiabatic approximation, the exact solution of eq. 1.3 is not possible. We then consider that electrons are indistinguishable and independent particles and that each electron moves under the influence of an average potential $V_{cr}(\mathbf{r})$, which describes the electron-ion interactions. Thus, the motion of a single electron can be described by the Schrödinger equation:

$$\left(\frac{p^2}{2m_0} + V_{cr}(\mathbf{r}) \right) \psi_{n,k}(\mathbf{r}) = E_{n,k} \psi_{n,k}(\mathbf{r}). \quad (1.6)$$

In an ideal crystal structure, the potential $V_{cr}(\mathbf{r})$ is periodic, and the wave function describes a Bloch state:

$$\psi_{n,k}(\mathbf{r}) = e^{i\mathbf{k}\cdot\mathbf{r}} u_{n,k}(\mathbf{r}), \quad (1.7)$$

where $e^{i\mathbf{k}\cdot\mathbf{r}}$ is a plane wave function, and $u_{n,k}(\mathbf{r})$ is a Bloch function, which has periodicity of the crystal lattice ($u_{n,k}(\mathbf{r}) = u_{n,k}(\mathbf{r} + \mathbf{R})$) and describes the behavior of the wave function within a unit cell. Substituting eq. 1.4 in eq. 1.3, we have:

$$\mathcal{H} u_{n,k}(\mathbf{r}) = E_{n,k} u_{n,k}(\mathbf{r}), \quad (1.8)$$

where we identify the Hamiltonian as

$$\mathcal{H} = \left(-\frac{\hbar^2}{2m_0} \nabla^2 + V_{cr}(\mathbf{r}) + \frac{\hbar^2 k^2}{2m_0} + \frac{\hbar}{m_0} \mathbf{k}\cdot\mathbf{p} \right). \quad (1.9)$$

If we take the center of the Brillouin zone, at the point Γ ($k = 0$), the solution to eq. 1.8 forms a complete set of functions $u_{n,0}(\mathbf{r})$ (for $n=1,2,3,\dots$) which allows us to calculate the wave function for any $\mathbf{k} \neq 0$ as a linear combination of Bloch functions.

$$u_{n,k}(\mathbf{r}) = \sum_{n'}^{\infty} c_{n,n'} u_{n',0}(\mathbf{r}), \quad (1.10)$$

where the coefficient $c_{n,n'}$, is known as the envelope function [23].

As our interest is focused on the study of electrons that are located in the conduction band, which is quite far from the valence band (except for narrow gap semiconductors which are not investigated here) we can simplify the model by considering a single of a band. The wave function of an excited state of an electron in the conduction band is formed by a Bloch function and the corresponding envelope function. In this way the $\mathbf{k} \cdot \mathbf{p}$ Hamiltonian is expanded into a basic element given by eq. 1.10

$$\langle u_{n,0} | \mathcal{H}_{kp} | u_{n,0} \rangle = E_{n,0} + \frac{\hbar^2 k^2}{2m_i^*}, \quad (1.11)$$

This model leads to a form of energy dispersion occurring in the equivalent model of free electrons, or conduction band region near the point $k=0$ is approximately parabolic shape. However, the curvature differs from that of the parabolic free electrons dispersion, and depends on the specific composition and structure of the semiconductor. This curvature is introduced by means of an empirical parameter called effective mass (m_e^*), which can be calculated by applying perturbation theory to the $\mathbf{k} \cdot \mathbf{p}$ Hamiltonian. In this sense, the unperturbed Hamiltonian and the perturbative term are defined, respectively, as

$$\mathcal{H}_0 = -\frac{\hbar}{2m_0} \nabla^2 + V_{cr}(\mathbf{r}), \quad (1.12)$$

and

$$\mathcal{H}' = \frac{\hbar^2}{2m_0} |\mathbf{k}^2| + \frac{\hbar}{m_0} \mathbf{k} \cdot \mathbf{p}, \quad (1.13)$$

The energy $E_{n,k}$, corrected up to the second order, is given by:

$$E_{n,k} = E_{n,0} + \sum_{\alpha=x,y,z} \frac{\hbar^2 k_\alpha^2}{2} \left[\frac{1}{m_0} + \frac{2}{m_0^2} \sum_{n'} \frac{|P_{n,n'}^\alpha|^2}{E_{n,0} - E_{n',0}} \right], \quad (1.14)$$

where the term $P_{n,n'}^\alpha$ is an empirical parameter determined either experimentally or by first principles calculating, and the term in brackets, identified as the inverse of the effective mass, can be condensed as

$$\frac{1}{m^*} = \frac{1}{m_0} + \frac{2}{m_0^2} \sum_{n'} \frac{|P_{n,n'}^\alpha|^2}{E_{n,0} - E_{n',0}}. \quad (1.15)$$

Thus, the energy obeys

$$E(k) = E_{n,0} + \frac{\hbar^2 k^2}{2m^*}. \quad (1.16)$$

Therefore, in the case of an infinite periodic crystal, which has no confining direction (Bulk), the envelope function of the conduction band is a plane wave, according to the Bloch theorem, eq. 1.7. From the point of view of kinematics, a Bloch electron, has acceleration given by:

$$\begin{aligned}\mathbf{a}_{\mathbf{k}} &= \frac{\partial \mathbf{v}_{\mathbf{k}}}{\partial t} = \frac{1}{\hbar} \frac{\partial}{\partial t} [\nabla_{\mathbf{k}} E(\mathbf{k})], \\ \mathbf{a}_{\mathbf{k}} &= \frac{1}{\hbar} \frac{\partial}{\partial t} \frac{\partial E(\mathbf{k})}{\partial \mathbf{p}},\end{aligned}\quad (1.17)$$

where we use the relation $v_k = \nabla_k \omega_k = \frac{1}{\hbar} \nabla_k E(\mathbf{k})$, that is, the electron velocity in the state \mathbf{k} is equal to the gradient of the energy band in reciprocal space. The acceleration can be rewritten as:

$$\mathbf{a}_{\mathbf{k}} = \frac{1}{\hbar} \frac{\partial}{\partial t} \frac{\partial E(\mathbf{k})}{\partial k} \frac{dk}{dt} = \frac{1}{\hbar^2} \frac{\partial^2}{\partial k_i \partial k_j} \cdot \mathbf{F}, \quad (1.18)$$

where we use $\mathbf{p} = \hbar \mathbf{k}$ and $\mathbf{F} = d\mathbf{p}/dt = \hbar d\mathbf{k}/dt$. Comparing the latter equation with Newton's second law, we have:

$$\mathbf{F} = \hbar^2 \left[\frac{\partial^2 E(\mathbf{k})}{\partial k_i \partial k_j} \right]^{-1} \mathbf{a}. \quad (1.19)$$

so that the effective mass can be expressed as:

$$m_{i,j}^* = \hbar^2 \left[\frac{\partial^2 E(k)}{\partial k_i \partial k_j} \right]^{-1}. \quad (1.20)$$

Eq. 1.20 is the effective mass tensor for an electron band, whose components are:

$$\frac{1}{m_{i,j}} = \frac{1}{\hbar^2} \frac{\partial^2 E(\mathbf{k})}{\partial k_i \partial k_j}, \quad (1.21)$$

Thus, a Bloch electron excited by an external force field behaves as if it had an anisotropic mass, that differs from the free electron mass m_e . The effective mass implicitly incorporates all the information about the lattice structure that leads to the energy band $E(\mathbf{k})$. For some crystals, non-diagonal components of the effective mass tensor are nonzero. Thus, an applied electric field in a certain direction of the crystal can cause electron acceleration in a different direction. In most semiconductors the effective mass tensor is diagonal and in isotropic crystals in particular, the tensor reduces to a scalar:

$$m^* = \frac{\hbar^2}{\left(\partial^2 E(\mathbf{k}) / \partial k^2 \right)}. \quad (1.22)$$

Note that the valence band normally has three branches, called light hole, heavy hole and split-off, due to their different effective masses, as one can see in Fig. 1.2(b). The theoretical expressions found for the electrons effective mass are also valid for holes, and in general, their values change as the crystal structure, periodicity of the lattice and the chemical composition of the material. Within the so-called effective mass approximation, the electrons (holes) in the conduction (valence) band of a material are considered as free moving particles, where the influence of any external potential is added to the effective continuum model Hamiltonian, and interactions with other electrons and lattice ions are all taken into account by introducing of the effective mass ³

1.4 The Envelope-Function Approximation

The envelope-function approximation is a mathematical formalism which allows the use of the effective mass approximation to study heterostructures materials, through the Hamiltonian

$$\mathcal{H} = \frac{p^2}{2m^*} + V(\mathbf{r}). \quad (1.23)$$

The method assumes as an approximation that all materials constituting the heterostructure have similar type of crystalline lattice and similar network structure so that we can assign the same Bloch function on the entire system.

In this work, we use the effective-mass approach, which considers a crystal infinite size. For calculation purposes, we will now consider limited heterostructures nanoscale sizes, because when we consider that the system is limited by the crystal size, the electron is also confined within the limits of this heterostructure. This is what divides the quantized energy spectrum into discrete levels at the bottom of the conduction band. The spatial confinement potential is defined by $V(\mathbf{r})$, which in turn is defined by the energy bands mismatch between materials forming the heterostructure.

A great advantage of using these approximations is in the fact that they simplify the inclusion additional perturbations, such as electric or magnetic fields, in the theoretical description of the charge carriers dynamics. This task often resorts simply to the introduction of an extra potential term in the Hamiltonian of eq. 1.23 [22, 23, 24].

1.5 Low-Dimensional Semiconductor Systems

It is impossible to think of modern physics or solid state physics and not to refer semiconductor heterostructures, particularly quantum wells, wires and dots [25]. The

³For a different approach to the effective mass, the reader should refer to References [26, 27, 28, 29, 30].

possibility of nanomanufacturing these devices was the fundamental piece for numerous articles published since the 70's [7, 8].

The carriers confinement potential in these systems arises from the mismatch between the energy bands in the heterostructures, since the heterostructure materials are separated by different gaps and different electronic properties, such mismatch attracts carriers to the region where the potential is lower. The fraction of the difference between the gaps which is responsible for confining electrons, is called conduction band-offset. The band-offset is a parameter usually obtained from experimental results, but it can also be calculated by means of the electron affinity, using the vacuum level as reference[20].

The carriers confinement can occur in one, two or three dimensions, as shown in Table 1.1 where the mathematical rule $G_{conf} + G_{freedom} = 3$ is kept. In one dimensional confinement, the system has two degrees of freedom (2-D), as in quantum wells; in two dimensional confinement, electrons are free to move only in 1-D, such as in quantum wires, or nanowires. Finally, when there is confinement in all directions, the carriers have zero degrees of the freedom, 0-D, as in quantum dots, which are sometimes called artificial atoms [31].

Table 1.1: - Number and degree of confinement for different degrees of freedom of heterostructures [30]

System	G_{conf}	$G_{freedom}$
Bulk	0	3
Quantum Wells	1	2
Quantum Wires	2	1
Quantum Dots	3	0

1.5.1 Quantum Dot

Quantum dot is a semiconductor structure with a size comparable to the Fermi wavelength. Its charge carriers are confined in all directions, so that electronic states are fully quantized [32]. Quantum dots are also known as artificial atoms because their electronic behavior is similar to that of an atom, but differs regarding the potential: in the the case of a quantum dot, the potential is step-like, while for the atom, the potential is Coulombic [30]. Recently, self-organized quantum dots have been grown by the Stranski-Krastanow method [33]. Quantum dots grown using this technique have the symmetry of a semi-ellipsoid, where the deposited materials are grown from the bottom up. Fig. 1.3 shows three quantum dots grown by the self-assembly process.

A self-grown quantum dot has at its base dimensions much greater than its height, enabling us to make an approach to a disk contained in the (x, y) -plane. This approach is

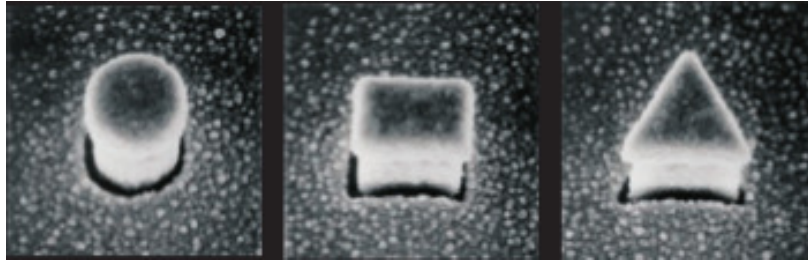


Figure 1.3: Micrograph image obtained by scanning an electron to three types of quantum dots: circular, square and triangular, manufactured by self-assembly method [36].

widely used in theoretical works [34, 35]. This implies that the energy spectrum in the z direction have energy levels transitions with higher energy than those in the (x, y) -plane. In this way, we justify the study of the electronic behavior only in the (x, y) -plane, saving considerable computational time to obtain results.

1.5.2 Quantum Wires

Wires with diameters of a few nanometers, which can be considered effectively as 1-D structures have been recently manufactured [37, 38] and studies of carriers (electrons and holes) confinement effects have been demonstrated with different levels of sophistication [15, 18, 39, 40]. For application as non-volatile memories, Zhu et al [13] have recently shown that silicon nanowires (Si) surrounded by a dielectric with high constant dielectric (high-k dielectric), as shown in Figure 1.4, exhibit excellent recording operations and good resistance. This shows that materials with high dielectric constant, growing around low-dimensional structures continues to attract the attention of researchers in order to extend Moore's Law [41].

Silva et al [15] presented a study of excitons properties in cylindrical nanowires $Si_{1-x}Ge_x$ surrounded by a silicon matrix, assuming the two known forms of band alignments, namely type-I and type-II⁴. The method used by the authors is based on the effective mass and envelope function approximations. Actually in general, theoretical studies on this subject are based on: (i) the use of the effective mass approximation, (ii) self-consistent solution of the Schrödinger and Poisson equations in cylindrical coordinates, providing theoretical descriptions of electronic and optical properties of the quantum wires [15]; (iii) methods based on first principles calculations (ab-initio methods) [45], which require high computational cost and, therefore, are limited for studies of nanowires with diameters between

⁴Regarding the type of quantum wires, they may be classified as type-I or type-II. When the alignment of the bands occurs in such way that in the same layer we have a quantum well both for electrons and for holes, this configuration presents features of type-I. But in case that we do not have this type of alignment, i.e. when the electrons and holes are confined in different semiconductor layers, the potential structure is characterized by a semiconductor of type-II. see more in Refs. [42, 43, 44]

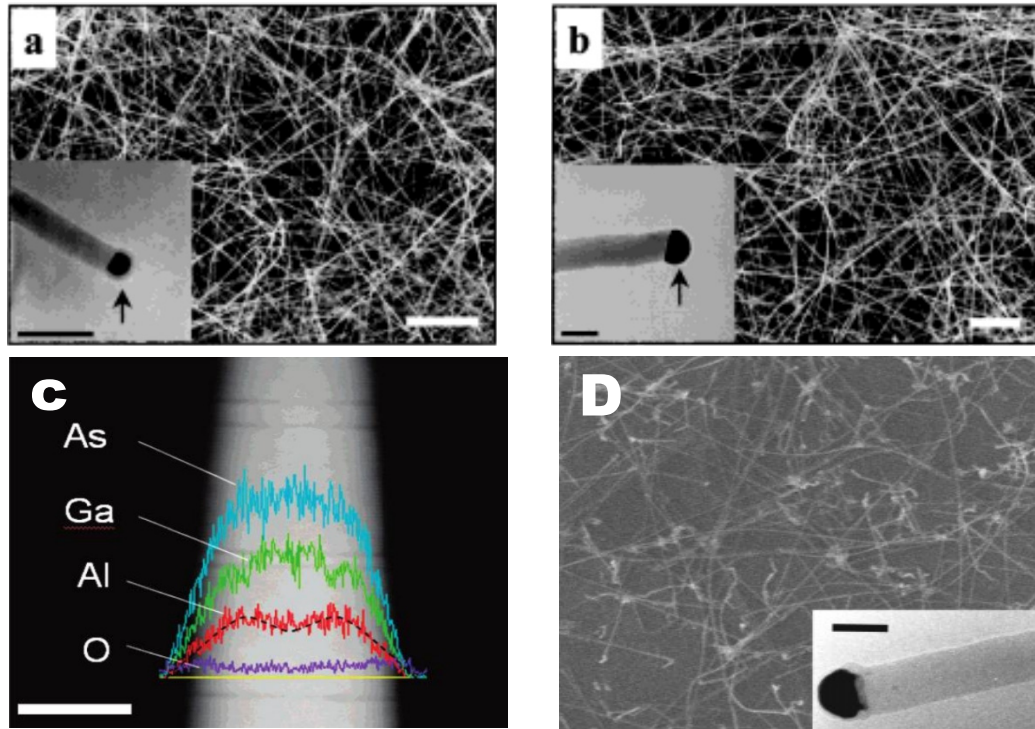


Figure 1.4: Quantum wires (a) SEM's image for the GaAs material with wire radius 50 nm grown with LCG techniques, [37](b)SEM image for the GaP material with radius 50 nm grown with LGC techniques, [37] (c) TSEM Image for AlGaAs nanowire perpendicular growth of Al, Ga, As and O, respectively, reference bar equals 50 nm grown with techniques MBE, [38] and (d)AFM image of a Si nanowire on the Au substrate with radius 10 nm grown with techniques VLS, [47]

1 and 2 nm; (iv) tight-binding, Approximating the electronic wave functions in the solid by linear combinations of the atomic wave function, this approach is known as the tight-binding approximation or Linear Combination of Atomic Orbitals (LCAO) approach [46], and (v) $\mathbf{k} \cdot \mathbf{p}$, the pseudopotential method is not the only method of band structure calculation which requires a small number of input parameters obtainable from experimental results. In the empirical pseudopotential method the inputs are usually energy gaps. The $\mathbf{k} \cdot \mathbf{p}$ method can be derived from the one-electron Schrodinger equation. Using the Bloch theorem the solutions are expressed, in the reduced zone scheme [46]

1.5.3 Quantum Wells

If the nanostructure is composed of a thin semiconductor layer, grown by epitaxy between two layers of different alloy, a confining potential ΔE appears in only one direction, as shown in Fig. 1.5, due to the bands mismatch between the materials. This formed nanostructure is called quantum well.

Quantum wells are one of the most investigated semiconductor based structures, after

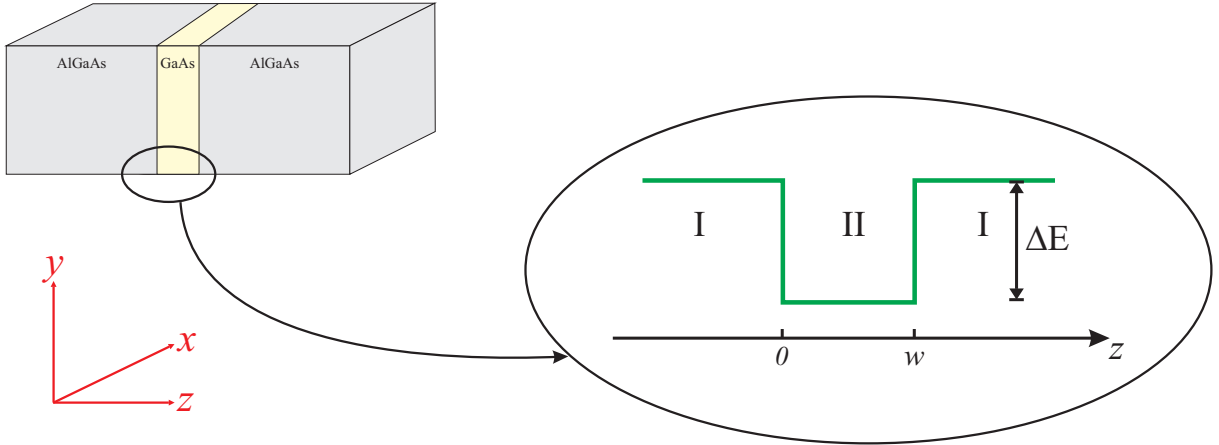


Figure 1.5: Physical structure of a quantum well of AlGaAs/GaAs and representation of the potential profile of this heterostructure. In the right side, (I) represents the alloy AlGaAs and (II) represents the GaAs.

the development of the heterostructures by Esaki and Tsu. This is due to their great potential for technological application and the countless physical properties they can provide, such as interband electronic transmission, excitonic properties, electron correlation of the charge carriers, strain-induced properties, among other various possibilities [48, 49, 50]. Besides, quantum well heterostructures require one of the less complex growth procedure, facilitating research in experimental laboratories [51, 52]

The achievement of a sharp interface imposes very stringent requirements on the growth conditions, such as purity of the source materials, substrate temperature and many others too numerous two dissimilar materials A and B, known as a heterojunction, is determined by their chemical and physical properties [46].

1.5.4 Quantum Rings

Quantum ring nanostructures regarding confinement dimensions are similar to quantum dots, but they have very interesting properties coming from their topology that allow, for example, experimental observation of the Aharonov-Bohm effect [53]. One method of growing quantum rings is through anodic oxidation. (See Fig 1.6). The anodic oxidation is oxidation by applying a potential difference between the probe of an atomic force microscope and the sample [54]. Another way of fabricating a quantum ring consists of quantum annealing (annealing) of a self-grown quantum dot, which causes a slippage from its center, thus forming the ring.

One of the systems that we will investigate further on in this thesis consists of planar quantum rings, with an input channel and one or two output channels so that the electronic motion occurs in the two-dimensional (x, y) -plane.

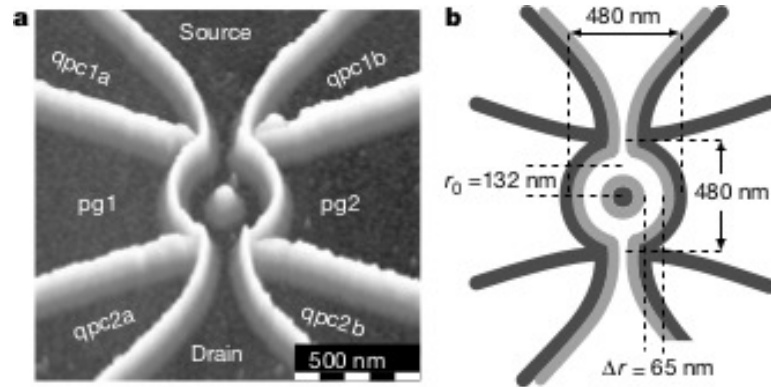


Figure 1.6: (a) Image obtained by atomic force microscopy (AFM) of a quantum ring grown with the anodic oxidation technique, (b) experiment the potential profile, where the dark curves represent the oxides lines [55].

1.6 The Aharonov-Bohm Effect

We will discuss in our work the problem of an electron in a quantum ring under the influence of an external magnetic field, so it is necessary to briefly overview the Aharonov-Bohm effect, which has been discussed widely in recent years for systems with cylindrical symmetry [56, 57, 58].

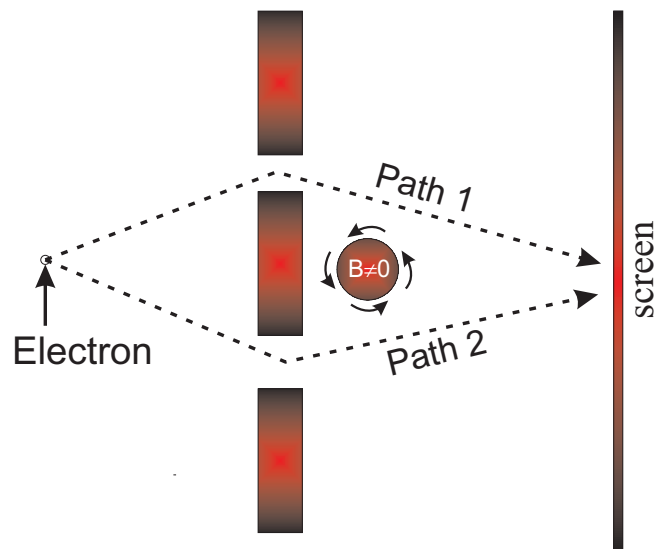


Figure 1.7: Illustration of experience proposed by Aharonov-Bohm. Between two slits a magnetic field B is applied. It is different from zero only in the inner region of the applied field, but the vector potential (shown by solid lines) is different from zero in all space, with cylindrical symmetry causing opposite effects on the path 1 and 2.

Figure 1.7 illustrates a scheme of the Aharonov-Bohm *gedanken* experiment. The electron beam can take two possible paths to reach the screen generating an interference

pattern. Between the two slits is placed a cylindrical coil (permanent magnet or solenoid), that generates a magnetic field \mathbf{B} only inside it. The possible electron paths are in the region where the field is zero.

Even in the absence of magnetic field in the path where the electrons pass, there is a potential vector \mathbf{A} in this region given by: $\mathbf{B} = \nabla \times \mathbf{A} = 0$, causing the momentum of the electron to assume $\mathbf{p} \rightarrow \mathbf{p} - q\mathbf{A}$. Taking the magnetic field of the material as $\mathbf{B} = B\hat{k}$, the vector potential can be expressed by a symmetric gauge $\mathbf{A} = \frac{1}{2}B\rho\hat{e}_\theta$. Observing Fig. 1.7, the vector potential points to the same direction as path 2, and in the opposite direction to path 1. This implies that the electrons that pass by 1 will have their momentum \mathbf{p} different from electrons that pass by 2; this fact changes the interference pattern generated in the screen. This difference observed in the screen due to the application of the external magnetic field is known as Aharonov-Bohm effect (AB) [59, 60].

In this approach, we have chosen a potential vector with a specific gauge; however, more extensive descriptions show that this effect does not depend on the choice of the gauge, for the vector potential [27, 29, 46, 60].

Further in this thesis, we will investigate fluctuations in transmission probabilities of an electron in a quantum ring under an external magnetic field applied perpendicular to its plane direction (x, y), where such AB effect is expected to occur. When the magnetic flux located between paths 1 and 2 reaches the value of $\phi = (n + 0.5)\phi_0$, where n is an integer and $\phi_0 = h/e$ is the elementary flux, wave functions following different paths interfere in the area of the ring-leads junctions and undergo a destructive interference, causing a lower electronic transmission. Thus we can see that the transmission in terms of the magnetic flux has a frequency ϕ_0 , presented here as AB oscillations [61]. In an actual nanodevice, at low temperatures, the inelastic scattering length is much larger than the sample dimensions and, as a result, the transport is completely phase coherent, i.e., it is dominated by quantum interference effects, allowing for experimental observation of the AB oscillations. On the other hand, at very high temperatures, the inelastic scattering length is much smaller than the sample size, which brings the system back to the classical behavior, thus losing the interference effects. [62, 63]

Interestingly, the AB phase also has strong influence in the energy spectrum of a quantum ring. Let us consider an electron in a planar ring system, which is infinitesimally small in the z-direction, so that only one bound state in this direction plays a role. We can write the Hamiltonian of this system as

$$\mathcal{H} = \frac{\mathbf{P}^2}{2m^*}, \quad (1.24)$$

as previously defined using the momentum modified by the magnetic field: $\mathbf{P} - q\mathbf{A}$ we have:

$$\mathcal{H} = (\mathbf{P} - q\mathbf{A}) \frac{1}{2m^*} (\mathbf{P} - q\mathbf{A}), \quad (1.25)$$

where we take $q = -e$, so we can write the Hamiltonian as:

$$\mathcal{H} = \frac{1}{2m^*} (\mathbf{P}^2 + 2e\mathbf{A} \cdot \mathbf{P} + e^2\mathbf{A} \cdot \mathbf{A}), \quad (1.26)$$

taking a symmetric gauge for the vector potential $\mathbf{A} = 0.5\mathbf{B}\rho e_\theta$, we have for each term of eq. 1.26:

$$\frac{\mathbf{P}^2}{2m^*(R)} = -\frac{\hbar^2}{2R} \frac{\partial}{\partial R} \left(\frac{R}{m^*(R)} \frac{\partial}{\partial R} \right) - \frac{\hbar^2}{2m^*(R)R^2} \frac{\partial^2}{\partial R^2} \quad (1.27)$$

$$\frac{1}{2m^*(R)} (2e\mathbf{A} \cdot \mathbf{P}) = \frac{\hbar}{i} \frac{eB}{2m^*(R)} \frac{\partial}{\partial \theta} \quad (1.28)$$

and finally:

$$\frac{e^2\mathbf{A} \cdot \mathbf{A}}{2m^*(R)} = \frac{e^2B^2}{8m^*(R)} R^2 \quad (1.29)$$

Replacing the eqs. 1.27, 1.28 and 1.29 in 1.26 and taking only the radial terms, we have:

$$\mathcal{H} = -\frac{\hbar^2}{2m^*(R)R^2} \frac{\partial^2}{\partial \theta^2} + \frac{\hbar\omega_c}{2i} \frac{\partial}{\partial \theta} + \frac{1}{8}m\omega_c^2 R^2, \quad (1.30)$$

where $\omega_c = e\mathbf{B}/m^*$ is defined as frequency cyclotron and m^* is effective mass of electron. Using the definition of elementary magnetic flux and magnetic flux, we write the Hamiltonian of eq. 1.30 as:

$$\mathcal{H} = -\frac{\hbar^2}{2m^*R^2} \left[-i\frac{\partial}{\partial \theta} + \frac{\phi}{\phi_0} \right]^2. \quad (1.31)$$

The eigenfunctions for the Hamiltonian of eq. 1.31 are written as:

$$\psi(\theta) = \frac{\exp(in\theta)}{2\sqrt{2\pi}}, \quad (1.32)$$

where $n = 0, \pm 1, \pm 2, \dots$ and eigenstates are obtained:

$$E_n(\phi) = \frac{\hbar^2}{2m^*R^2} \left[n + \frac{\phi}{\phi_0} \right]^2 \quad (1.33)$$

from eq. 1.33 we can see that energy is a function of magnetic flux and has a parabolic shape having minimum at $\phi = -n\phi_0$. Thus, we can conclude that there are fluctuations AB with period ϕ_0 , and that there is an exchange of angular momentum in the ground state to flow in $\phi = (n + 0.5)\phi_0$.

1.7 Braess paradox and game theory

In the following chapters of this thesis, we present results concerning the transport inefficiency caused by the addition of an extra path to a mesoscopic network, observed in recent experiments with semiconductor nanostructures [64, 65]. This is in contrast to the

common sense that adding extra paths should always improve the flow, and appear to be similar to the Braess paradox in game theory. In order to understand this paradox, it is necessary to review some concepts of game theory.

John Nash, in the mid 1950s, proposed a theory for n players, each with i possible moves, in which there is at least one equilibrium point satisfying all players. This point is known as Nash equilibrium, and presents applications in economic science and game theory[66]. Conceptually, the ideal game is one where no player receives incentive to change strategy after the opponents have made their choices, so that no other strategy taken by any player after this point will result in benefit. Even for players that do not cooperate, it is possible to individually find the best strategy for the game, leading to stability, provided there is no incentive for players to change their behavior. This possibility stems from the predictions that the players can make about the behavior of their opponents. Thus, the Nash equilibrium corresponds to a combination of strategies so that each player makes the best possible move for him(her)self, taking into account the strategy chosen by the opponents. In this context, the result pleases all players, so that none of them have an incentive to change the initiated strategy [66]. In general, the Nash equilibrium is achieved when the system is in a Pareto optimal. The Pareto optimal occurs when there is no way to improve the payoff of one of the players without reducing the payoff of another player; for example, when Companies A and B sell different products on the market in a way that the sale of each of their products do not affect the final corporate profits [67, 68].

The Braess paradox is credited to German mathematician Dietrich Braess. In his publication in 1968s, he concludes that the addition of an extra path in a traffic network can, in some situations, reduce the overall flow. This is a situation where the system can be in a Nash equilibrium, but out of Pareto optimality [69].

As an example, suppose that people have to travel in a road from point A to point B, with two possibilities to perform this activity, see Figure 1.8. Each individual chooses a route minimizing the traffic time between the inlet and the outlet, which, of course, depend on the number of people going through a given route. Equilibrium occurs when time is equal for both routes. This case would be the one where there is the same amount of people passing through each path. Let us now discuss this situation in terms of game theory. In the case of Figure 1.8, defining f as the relative frequency of people who decided to go by a given path, we can take a fixed time t , representing the time required to pass through the parts of the roads where flow does not depend on the amount of players who pass through it, and $t' = ft$ and $t'' = (1 - f)t$, representing the times necessary to go through the parts of the road where flow depends on the amount people passing through it. Total travel time for the upper (lower) path is $T_u = t + t'$ ($T_l = t + t''$). Thus, the individuals on the network can be seen as players of a non-cooperative game, where each one seeks to minimize the time traffic between the inlet and the outlet of the pathway. We now reason about it: (i) upper path is the best if $t + f \leq t + (1 - f)$, *i.e.* if $f \leq 1/2$;

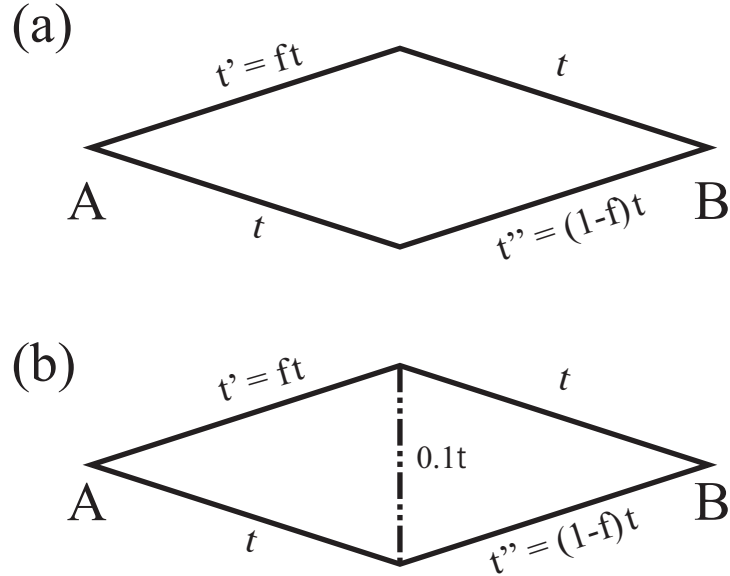


Figure 1.8: Scheme to the paradox of Braess (a) A network paths systems starting at point A and ends at point B and (b) Systems paths adding an extra path in the central region with fixed time in extra path.

(ii) lower path is the best if $t + ft \geq t + (1 - f)t$, i.e. if $f \geq 1/2$. But if $f < 1/2$, everybody will seek for the upper path (supposed to be the best), so $f \rightarrow 1$, leading to $T_u = t + t = 2t$ and $T_l = t < T_u$, which is inconsistent with the idea that the upper path is the best. Similar conclusion is drawn for $f > 1/2$, were $f \rightarrow 0$. Therefore, equilibrium situation is attained only if $f = 1/2$ and everybody gets a delay $T_u = T_l = t + 0.5t = 1.5t$.

Now, let us add an extra road with fixed time $0.1t$ connecting the pathways in the central region, which would allow an escape route between upper and lower paths. Common sense would say that more options means better results. However, taking upper path until the end, one gets $ft + t$ delay; but taking the extra path, one gets $T_{extra} = ft + f_l t + 0.1t = 1.1t$ (f_l is the fraction of players that change to the lower path) or even a bit less, if not everybody takes the extra path. It turns out this is always better than T_u or T_l , since, if one takes first the upper path, one is left with a variable component $f_l t + 0.1t$, which is, at most, $1t + 0.1t = 1.1t < 1.5t$. But then, everybody will take this path, since this is a dominant strategy - it will *always* lead to better results for each individual than the other options. In this way, everybody makes the same move, $f = f_l = 1$ and finally $T_{extra} = 2.1t$, which is larger than the $1.5t$ we had before the extra path was added! Thus, the addition of this path would clearly change the Nash equilibrium point. In Ref. [70], this is demonstrated with computational simulation of a data collection, obtaining the optimal of the system where Nash equilibrium and the real equilibrium (from Braess theory) points are compared. In summary, depending on the strategy taken by the majority of players, this extra path can reduce the overall flow. This effect has been verified a number of times in traffic systems.[71] We note then that

the overall flow depends on the strategy of players and not just the addition of an extra route [70, 72].

1.8 Quantum wire devices

Modern technology is characterized by its on miniaturization. These reductions in the size are made up to the nanoscale, which is useful in the development of modern transistors. With that, it is possible to increase the number of transistors that fit into a chip-set. Gordon Moore, co-founder and current director emeritus of Intel, made a prediction in 1965 that every two years, the increase in computer processing power would double, this led him to predict that this trend should be continued over the years. This fact became known as Moore's law. Today, we observe that these values are doubling (in average) every eighteen months [41, 73]

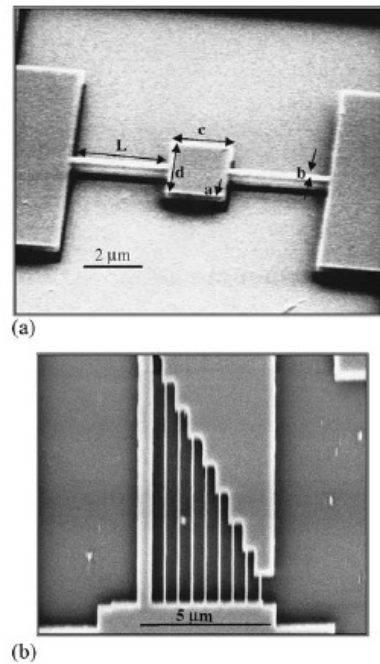


Figure 1.9: (a) A scanning electron micrograph of a $2\ \mu\text{m} \times 2\ \mu\text{m}$ silicon nitride paddle. The supporting rods are $230\ \text{nm}$ wide and $3\ \mu\text{m}$ long, and the thickness of the device layer is $240\ \text{nm}$. (b) A scanning electron micrograph of silicon nitride suspended wires. The length of the wires varies from 1 to $8\ \mu\text{m}$. Adapted from [78].

Nowadays, manufacturing of nano-devices is fundamentally based in semiconductor heterostructures, such as quantum wires and quantum dots - specifically, the former have electrons free to move in one-direction and is especially important on the field of medical, optoelectronic applications, di-electrophoretic manipulation and photovoltaics devices [74, 75, 76, 77]. Figure 1.9 shows a semiconductor quantum wire device, where $400\ \text{nm}$ of silicon dioxide were grown by thermal oxidation, then $230\text{-}250\ \text{nm}$ of silicon-rich amorphous

silicon nitride was deposited on it, by low-pressure chemical vapor deposition (LPCVD) [78]. In this context of smaller and smaller semiconductor devices, quantum tunnelling between electronic pathways becomes an important topic of discussion, which can be investigated by wave packet propagation and scattering, as we will demonstrate further in this thesis.

1.9 Outline of this thesis

In **chapter 1** we have introduced briefly some historical facts about the discovery and manufacturing of semiconductor nanostructures and their relevance in condensed matter physics and new technological applications. We discussed about energy bands and the approximations used in this thesis. We described the most important low-dimensional semiconductor systems, such as, quantum dots, quantum wires, quantum wells and quantum rings.

In the **chapter 2** we give a brief introduction to the calculation tools used in this thesis, specially the so called Split-operator technique. In this chapter, we show how to calculate the propagation using this method and how it is adapted for computational codes. Using real time propagation, we calculated the transmission probabilities and the currents on system. Finally, we discuss over imaginary time evolution, the technique that was used on the fourth work of this thesis.

In the **chapter 3** we theoretically demonstrate that the transport inefficiency recently found experimentally for branched-out mesoscopic networks can also be observed in a quantum ring of finite width with an attached central horizontal branch. This is done by investigating the time evolution of an electron wave packet in such a system. Our numerical results show that the conductivity of the ring does not necessarily improve if one adds an extra channel. This ensures that there exists a quantum analogue of the Braess Paradox, originating from quantum scattering and interference.

In the **chapter 4** We theoretically investigate the effect of opening and closing pathways on the dynamics of electron wave packets in semiconductor quantum rings with semi-circular, circular, and squared geometries. Our analysis is based on the time evolution of an electron wave packet, within the effective-mass approximation. We demonstrate that opening an extra channel in the quantum ring does not necessarily improve the electron transmission and, depending on the extra channel width, may even reduce it, either due to enhancement of quantum scattering or due to interference. In the latter case, transmission reduction can be controlled through the Aharonov-Bohm phase of the wave function, adjusted by an applied magnetic field. On the other hand, closing one of the channels of the branched out quantum ring systems surprisingly improves the transmission probability under specific conditions.

In the **chapter 5** we theoretically investigate the electronic transport properties of two closely spaced L-shaped semiconductor quantum wires, for different configurations

of the output channel widths as well as the distance between the wires. Within the effective-mass approximation, we solve the time-dependent Schrödinger equation using the split-operator technique that allows us to calculate the transmission probability, the total probability current, the conductance and the wave function scattering between the energy subbands. We determine the maximum distance between the quantum wires below which a relevant non-zero transmission is still found. The transmission probability and the conductance show a strong dependence on the width of the output channel for small distances between the wires.

In the **chapter 6** in this work, we investigate electron-impurity binding energy in GaN/HfO₂ quantum wells. The calculation considers simultaneously all energy contributions caused by the dielectric mismatch: (i) image self-energy (i.e., interaction between electron and its image charge), (ii) the direct Coulomb interaction between the electron-impurity and (iii) the interactions among electron and impurity image charges. The theoretical model involves for the solution of the time-dependent Schrödinger equation and the results show how the magnitude of the electron-impurity binding energy depends on the position of impurity in the well-barrier system. The role of the large dielectric constant in the barrier region is exposed with the comparison of the results for GaN/HfO₂ with those of a more typical GaN/AlN system, for two different confinement regimes: narrow and wide quantum wells.

In **chapter 7**, we provide our conclusions and future perspective for new works using the same theoretical techniques described in this thesis.

Theoretical Model

In this chapter, we will discuss in greater details the split-operator method, which will be widely used in the present thesis to solve the time-dependent Schrödinger equation

$$i\hbar \frac{\partial}{\partial t} \Psi(\mathbf{r}, t) = \mathcal{H} \Psi(\mathbf{r}, t). \quad (2.1)$$

Here, $\Psi(\mathbf{r}, t)$ is the wave function that solves the Schrödinger equation at the instant t . Within initial conditions $\Psi(\mathbf{r}, t_0)$, the wave function at any later time t can be given by using a time-evolution operator $\hat{U}(t, t_0)$

$$\Psi(\mathbf{r}, t) = \hat{U}(t, t_0) \Psi(\mathbf{r}, t_0). \quad (2.2)$$

This time-evolution operator can be represented in three different ways [60]:

1. If the Hamiltonian is a time-independent operator, which means $V = V(\mathbf{r})$, the time-evolution operator is defined as

$$\hat{U}(t, t_0) = \exp \left[-\frac{i}{\hbar} \hat{\mathcal{H}}(t - t_0) \right]. \quad (2.3)$$

2. If the Hamiltonian H is a time-dependent operator and the initial and final time Hamiltonian commute $[\hat{\mathcal{H}}(t), \hat{\mathcal{H}}(t')] = 0$, for any t and t' , the time-evolution operator is defined as

$$\hat{U}(t, t_0) = \exp \left[-\frac{i}{\hbar} \int_{t_0}^t \mathcal{H}(t') dt' \right]. \quad (2.4)$$

3. If the Hamiltonian does not commute with itself in a different time $[\hat{\mathcal{H}}(t), \hat{\mathcal{H}}(t')] \neq 0$, then

$$\hat{U}(t, t_0) = 1 + \sum_{n=1}^{\infty} \left(-\frac{i}{\hbar} \right)^n \int_{t_0}^t dt_1 \int_{t_0}^{t_1} dt_2 \dots \int_{t_0}^{t_{n-1}} dt_n \hat{\mathcal{H}}(t_1) \hat{\mathcal{H}}(t_2) \dots \hat{\mathcal{H}}(t_n). \quad (2.5)$$

For all systems investigated in this work, the potential is time-independent $V = V(r)$. We thus use the time-evolution operator given by eq. 2.3 and solve eq. 2.2 numerically through the split-operator method, which will be discussed in detail in the following section.

2.1 The split-operator technique

The split-operator method consists in writing the time-evolution operator as a product between exponential. This method was investigated by Feit *et. al.* [79] to determine the eigenvalues and eigenfunctions of the Schrödinger equation for a one-dimensional asymmetric double quantum well potential and for the two-dimensional Henon-Heiles potential, and improve in several papers in order to investigate finite semiconductor superlattice in the presence of an external static electric field [80, 81]. The main problem is: *how to compute an exponential operator given by a sum of two operators that do not commute?*, once that

$$\exp[\hat{A} + \hat{B}] = \exp(\hat{A})\exp(\hat{B}), \quad (2.6)$$

if, and just if $[\hat{A}, \hat{B}] = 0$. M. Suzuki [82] proposed a scheme to compute the exponential operators of a sum of that do not commute, by using an approximant $f_m(\hat{A}_1, \hat{A}_2, \dots, \hat{A}_q)$ as

$$\exp\left[\varepsilon \sum_{j=1}^q \hat{A}_j\right] = f_m(\hat{A}_1, \hat{A}_2, \dots, \hat{A}_q) + \mathcal{O}(\varepsilon^{m+1}), \quad (2.7)$$

with $\mathcal{O}(\varepsilon^{m+1})$ as an error of order $(m+1)$. The functions $f_m(\hat{A}_1, \hat{A}_2)$ and $f_m(\hat{A}_1, \hat{A}_2, \hat{A}_3)$, for $m = 1, 2$ can be expanded as [83]

$$f_1(\hat{A}_1, \hat{A}_2) = \exp[\varepsilon \hat{A}_1] \exp[\varepsilon \hat{A}_2], \quad (2.8)$$

$$f_2(\hat{A}_1, \hat{A}_2) = \exp\left[\frac{\varepsilon}{2}\hat{A}_1\right] \exp[\varepsilon \hat{A}_2] \exp\left[\frac{\varepsilon}{2}\hat{A}_1\right], \quad (2.9)$$

$$f_1(\hat{A}_1, \hat{A}_2, \hat{A}_3) = \exp[\varepsilon \hat{A}_1] \exp[\varepsilon \hat{A}_2] \exp[\varepsilon \hat{A}_3], \quad (2.10)$$

$$f_2(\hat{A}_1, \hat{A}_2, \hat{A}_3) = \exp\left[\frac{\varepsilon}{2}\hat{A}_1\right] \exp\left[\frac{\varepsilon}{2}\hat{A}_3\right] \exp[\varepsilon \hat{A}_2] \exp\left[\frac{\varepsilon}{2}\hat{A}_3\right] \exp\left[\frac{\varepsilon}{2}\hat{A}_1\right]. \quad (2.11)$$

This process writes the function in terms of linear combinations of the exponential $\exp \sum \hat{A}_j$. This makes it possible to reduce the solution process for the time-dependent

Schrödinger equation to a successive applications of exponential multiplication of these operators as we will demonstrate as follows. For the problems proposed here, the time-evolution operator $U(t + \Delta t, t)$ is expressed as

$$\widehat{U}(t + \Delta t, t) = \exp\left[-\frac{i}{2\hbar}V(\mathbf{r})\Delta t\right] \exp\left[-\frac{i}{2m\hbar}\widehat{P}^2\Delta t\right] \exp\left[-\frac{i}{2\hbar}V(\mathbf{r})\Delta t\right] + \mathcal{O}(\Delta t^3). \quad (2.12)$$

Numerically performing this process, we obtain the wave function for any instant of time. The error $\mathcal{O}(\Delta t^3)$ is on the order of Δt^3 , where $\Delta t = 0.2$ fs. By applying the eq. 2.12, the wave function in eq. 2.2 can be written as

$$\Psi(\mathbf{r}, t_0 + \Delta t) = \exp\left[-\frac{iV(\mathbf{r})}{2\hbar}\Delta t\right] \exp\left[-\frac{i\widehat{P}^2}{2m\hbar}\Delta t\right] \exp\left[-\frac{iV(\mathbf{r})}{2\hbar}\Delta t\right] \Psi(\mathbf{r}, t) + \mathcal{O}(\Delta t^3). \quad (2.13)$$

Here, eq. 2.13 can be solved by acting separately each operator over the wave function. First, we define a function $\Theta(\mathbf{r}, t_0 + \Delta t)$ as the solution for the first part,

$$\Theta(\mathbf{r}, t_0 + \Delta t) = \exp\left[-\frac{iV(\mathbf{r})}{2\hbar}\Delta t\right] \Psi(\mathbf{r}, t), \quad (2.14)$$

and as result, we have

$$\Psi(\mathbf{r}, t_0 + \Delta t) \simeq \exp\left[-\frac{iV(\mathbf{r})}{2\hbar}\Delta t\right] \exp\left[-\frac{i\widehat{P}^2}{2m\hbar}\Delta t\right] \Theta(\mathbf{r}, t_0 + \Delta t). \quad (2.15)$$

Second, we define a function $\Xi(\mathbf{r}, t_0 + \Delta t)$ as the solution for the kinetic energy operator over the function $\Theta(\mathbf{r}, t_0 + \Delta t)$,

$$\Xi(\mathbf{r}, t_0 + \Delta t) = \exp\left[-\frac{i\widehat{P}^2}{2m\hbar}\Delta t\right] \Theta(\mathbf{r}, t_0 + \Delta t). \quad (2.16)$$

By defining the momentum operator \widehat{P} in Cartesian coordinates $\widehat{P}^2 = \widehat{P}_x^2 + \widehat{P}_y^2 + \widehat{P}_z^2$, as components of the momentum operator commute $[\widehat{P}_x, \widehat{P}_y] = [\widehat{P}_x, \widehat{P}_z] = [\widehat{P}_z, \widehat{P}_y] = 0$, we can write

$$\Xi(\mathbf{r}, t_0 + \Delta t) = \exp\left[-i\frac{\widehat{P}_x^2}{2m\hbar}\Delta t\right] \exp\left[-i\frac{\widehat{P}_y^2}{2m\hbar}\Delta t\right] \exp\left[-i\frac{\widehat{P}_z^2}{2m\hbar}\Delta t\right] \Theta(\mathbf{r}, t_0 + \Delta t). \quad (2.17)$$

or

$$\Xi(\mathbf{r}, t_0 + \Delta t) = \exp\left[\frac{i\hbar}{2m}\frac{\partial^2}{\partial x^2}\Delta t\right] \exp\left[\frac{i\hbar}{2m}\frac{\partial^2}{\partial y^2}\Delta t\right] \exp\left[\frac{i\hbar}{2m}\frac{\partial^2}{\partial z^2}\Delta t\right] \Theta(\mathbf{r}, t_0 + \Delta t). \quad (2.18)$$

Solving eq. 2.18 by three parts, we obtain

$$\vartheta(\mathbf{r}, t_0 + \Delta t) = \exp\left[\frac{i\hbar}{2m} \frac{\partial^2}{\partial z^2} \Delta t\right] \Theta(\mathbf{r}, t_0 + \Delta t), \quad (2.19)$$

$$v(\mathbf{r}, t_0 + \Delta t) = \exp\left[\frac{i\hbar}{2m} \frac{\partial^2}{\partial y^2} \Delta t\right] \vartheta(\mathbf{r}, t_0 + \Delta t), \quad (2.20)$$

$$\zeta(\mathbf{r}, t_0 + \Delta t) = \exp\left[\frac{i\hbar}{2m} \frac{\partial^2}{\partial x^2} \Delta t\right] v(\mathbf{r}, t_0 + \Delta t). \quad (2.21)$$

The exponential function can be approximated as¹, we obtain

$$\exp\left[\frac{i\hbar\Delta t}{2m} \frac{\partial^2}{\partial z^2}\right] = \left[1 - \frac{i\hbar\Delta t}{4m} \frac{\partial^2}{\partial z^2}\right]^{-1} \left[1 + \frac{i\hbar\Delta t}{4m} \frac{\partial^2}{\partial z^2}\right] + \mathcal{O}(\Delta t^4). \quad (2.22)$$

Replacing eq. 2.22 in eq. 2.19, gives ²

$$\vartheta(\mathbf{r}, t_0 + \Delta t) = \left[1 - \frac{i\hbar\Delta t}{4m} \frac{\partial^2}{\partial z^2}\right]^{-1} \left[1 + \frac{i\hbar\Delta t}{4m} \frac{\partial^2}{\partial z^2}\right] \Theta(\mathbf{r}, t_0 + \Delta t) + \mathcal{O}(\Delta t^4), \quad (2.23)$$

and after a reorganizing some terms,

$$\left[1 - \frac{i\hbar\Delta t}{4m} \frac{\partial^2}{\partial z^2}\right] \vartheta(\mathbf{r}, t_0 + \Delta t) = \left[1 + \frac{i\hbar\Delta t}{4m} \frac{\partial^2}{\partial z^2}\right] \Theta(\mathbf{r}, t_0 + \Delta t) + \mathcal{O}(\Delta t^4), \quad (2.24)$$

or

$$\vartheta(\mathbf{r}, t_0 + \Delta t) - \frac{i\hbar\Delta t}{4m} \frac{\partial^2}{\partial z^2} \vartheta(\mathbf{r}, t_0 + \Delta t) = \Theta(\mathbf{r}, t_0 + \Delta t) + \frac{i\hbar\Delta t}{4m} \frac{\partial^2}{\partial z^2} \Theta(\mathbf{r}, t_0 + \Delta t). \quad (2.25)$$

From the last equation, on wards the error term is omitted, since Δt is considered to be small enough to have no significant improve in accuracy by adding these terms.

1

Given the exponential function

$$\exp[A\hat{B}] = \left[\exp\left(-\frac{A\hat{B}}{2}\right)\right]^{-1} \left[\exp\left(-\frac{A\hat{B}}{2}\right)\right] \exp(A\hat{B})$$

such that we can rewrite it as

$$\exp[A\hat{B}] = \left[\exp\left(-\frac{A\hat{B}}{2}\right)\right]^{-1} \exp\left(\frac{A\hat{B}}{2}\right)$$

and using a relationship for an exponential expansion $\exp[J] = \sum_{n=0}^{\infty} \frac{J^n}{n!}$, we can rewrite the above expression as

$$\exp[A\hat{B}] = \left[1 - \frac{A\hat{B}}{2} + \mathcal{O}(A^2)\right]^{-1} \left[1 + \frac{A\hat{B}}{2} + \mathcal{O}(A^2)\right]$$

and finally we obtain:

$$\exp[A\hat{B}] = \left[1 - \frac{A\hat{B}}{2}\right]^{-1} \left[1 + \frac{A\hat{B}}{2}\right] + \mathcal{O}(A^4)$$

²We used $A = \Delta t$ and $\hat{B} = \frac{i\hbar}{2m} \frac{\partial^2}{\partial z^2}$.

Since $\Theta(\mathbf{r}, t_0 + \Delta t)$ comes from an arbitrary wave function which we imposed on the system, we proceed by calculating eq. 2.25 within a numerical discretization technique to evaluate the function $\vartheta(\mathbf{r}, t_0 + \Delta t)$. The physical system can be considered three dimensional, and the space is discretized in steps in each direction

$$\Delta x = \frac{L_x}{N_x}, \quad (2.26a)$$

$$\Delta y = \frac{L_y}{N_t}, \quad (2.26b)$$

$$\Delta z = \frac{L_z}{N_z}. \quad (2.26c)$$

Given a function $G(x, y, z)$, the definition of derivative in the continuum case can be used to approximate the derivative in the discrete case

$$\frac{\partial}{\partial z} G_{i,j,k}(x, y, z) = \frac{G_{i,j,k+1} - G_{i,j,k-1}}{2\Delta z} + \mathcal{O}(\Delta z^2), \quad (2.27)$$

which represent a finite differences approximation for first derivative and

$$\frac{\partial^2}{\partial z^2} G_{i,j,k}(x, y, z) = \frac{G_{i,j,k+1} - 2G_{i,j,k} + G_{i,j,k-1}}{2\Delta z^2} + \mathcal{O}(\Delta z^2), \quad (2.28)$$

for second derivative. Using the finite difference scheme in the eq. 2.25 we obtain

$$\begin{aligned} & -\frac{i\hbar\Delta t}{4m\Delta z^2} \vartheta_{i,j,k-1}(\mathbf{r}, t_0 + \Delta t) + \left(1 + \frac{i\hbar\Delta t}{2m\Delta z^2}\right) \vartheta_{i,j,k}(\mathbf{r}, t_0 + \Delta t) + \\ & -\frac{i\hbar\Delta t}{4m\Delta z^2} \vartheta_{i,j,k+1}(\mathbf{r}, t_0 + \Delta t) = \frac{i\hbar\Delta t}{4m\Delta z^2} \Theta_{i,j,k-1}(\mathbf{r}, t_0 + \Delta t) + \\ & \left(1 + \frac{i\hbar\Delta t}{2m\Delta z^2}\right) \Theta_{i,j,k}(\mathbf{r}, t_0 + \Delta t) + \frac{i\hbar\Delta t}{4m\Delta z^2} \Theta_{i,j,k+1}(\mathbf{r}, t_0 + \Delta t) \end{aligned} \quad (2.29)$$

Taking the finite boundary conditions, $\Psi(\mathbf{r}, t_0 + \Delta t)|_{z=0} = \Psi(\mathbf{r}, t_0 + \Delta t)|_{z=l_z} = 0$, or periodic boundary conditions, $\Psi(\mathbf{r}, t_0 + \Delta t)|_{z=0} = \Psi(\mathbf{r}, t_0 + \Delta t)|_{z=l_z}$ we can rewrite the eq. 2.29 for the n -th z term ($k = n_z$), as

$$\begin{aligned} & -\frac{i\hbar\Delta t}{4m\Delta z^2} \vartheta_{i,j,1}(\mathbf{r}, t_0 + \Delta t) - \frac{i\hbar\Delta t}{4m\Delta z^2} \vartheta_{i,j,N_z-1}(\mathbf{r}, t_0 + \Delta t) + \\ & + \left(1 + \frac{i\hbar\Delta t}{2m\Delta z^2}\right) \vartheta_{i,j,N_z}(\mathbf{r}, t_0 + \Delta t) = \frac{i\hbar\Delta t}{4m\Delta z^2} \Theta_{i,j,1}(\mathbf{r}, t_0 + \Delta t) + \\ & \frac{i\hbar\Delta t}{4m\Delta z^2} \Theta_{i,j,N_z-1}(\mathbf{r}, t_0 + \Delta t) + \left(1 - \frac{i\hbar\Delta t}{2m\Delta z^2}\right) \Theta_{i,j,N_z}(\mathbf{r}, t_0 + \Delta t), \end{aligned} \quad (2.30)$$

likewise we can represent this equation system, eq. 2.30, as matrix product

$$\begin{pmatrix} \alpha & \beta & 0 & \cdots & \cdots & \delta_z \beta \\ \beta & \alpha & \beta & \ddots & \cdots & 0 \\ 0 & \beta & \alpha & \ddots & \ddots & \vdots \\ \vdots & 0 & \ddots & \ddots & \ddots & \ddots \\ \vdots & \vdots & \vdots & \ddots & \ddots & \beta \\ \delta_z \beta & 0 & \cdots & \cdots & \beta & \alpha \end{pmatrix} \begin{pmatrix} \vartheta_{i,j,1} \\ \vartheta_{i,j,2} \\ \vdots \\ \vdots \\ \vartheta_{i,j,N_z-1} \\ \vartheta_{i,j,N_z} \end{pmatrix} = \begin{pmatrix} \gamma & -\beta & 0 & \cdots & \cdots & -\delta_z \beta \\ -\beta & \gamma & -\beta & \ddots & \cdots & 0 \\ 0 & -\beta & \gamma & \ddots & \ddots & \vdots \\ \vdots & 0 & \ddots & \ddots & \ddots & \ddots \\ \vdots & \vdots & \vdots & \ddots & \ddots & -\beta \\ -\delta_z \beta & 0 & \cdots & \cdots & -\beta & \gamma \end{pmatrix} \begin{pmatrix} \Theta_{i,j,1} \\ \Theta_{i,j,2} \\ \vdots \\ \vdots \\ \Theta_{i,j,N_z-1} \\ \Theta_{i,j,N_z} \end{pmatrix}, \quad (2.31)$$

where we define

$$\alpha = 1 + \frac{i\hbar\Delta t}{2m\Delta z^2}, \quad (2.32a)$$

$$\beta = -\frac{i\hbar\Delta t}{4m\Delta z^2}, \quad (2.32b)$$

$$\gamma = 1 - \frac{i\hbar\Delta t}{2m\Delta z^2}, \quad (2.32c)$$

$$\delta_z = \begin{cases} 0, & \text{for a finit system} \\ 1, & \text{for a periodic system} \end{cases}, \quad (2.32d)$$

the index ranging as $i = 1, 2, 3, \dots, N_x$ and $j = 1, 2, 3, \dots, N_y$. The solution is a tridiagonal matrix equation, which can be solved by various available and easily accessible subroutines. For periodic systems, the matrix described in eq. 2.31 requires the numerical routine CYCLIC, available on *Numerical Recipes*. In cases where the system is, the finite more convenient routine is TRIDAG, also available on *Numerical Recipes* [84]. Both routines are based on lower and upper (LU) decomposition method.

Repeating previous steps to obtain $\vartheta(\mathbf{r}, t_0 + \Delta t)$ in eq. 2.19, we can obtain the results for $v(\mathbf{r}, t_0 + \Delta t)$, eq. 2.20 and $\zeta(\mathbf{r}, t_0 + \Delta t)$, eq. 2.21 and finally to obtain the final wave function applying the last operator in the function $\zeta(\mathbf{r}, t_0 + \Delta t)$, *i.e.*

$$\Psi(\mathbf{r}, t_0 + \Delta t) = \exp\left[-\frac{i\widehat{V}(\mathbf{r})\Delta t}{2\hbar}\right] \zeta(\mathbf{r}, t_0 + \Delta t). \quad (2.33)$$

The dynamics of one electron wave packet in quantum system can be investigated by proceeding with above explained numerical method, implemented with a previously cited

subroutines, and looking to the time evolution of the wave function with a time step Δt . The advantages of using the split-operator method are due to its simplicity, computation speed and because it is easy to adapt for solving problems related to dynamics of electrons in low dimensional systems, allowing the use of imaginary absorbing potentials and the calculus of eigenstates through the evolution in imaginary time. Instead of using split-operator method, to study the dynamics of wave functions, it is possible to use the Cayley formula to solve a seven diagonal matrix, which is more complicated and requires a long computational time [85], whereas the split operator technique requires only a solution of linear systems with tridiagonal matrices leading to short computational time.

2.2 Real-time Evolution

The description of electrons transports can be started through the probability current, directly extracted from the wave functions

$$J_x = \frac{\hbar}{2im_e} \left(\Psi^* \frac{\partial \Psi}{\partial x} - \frac{\partial \Psi^*}{\partial x} \Psi \right), \quad (2.34)$$

written here for x -direction. The transmission T and reflection R coefficients are determined by integrating the current at a specific point: the transmission coefficient is calculated usually in the output region (most of cases considered to be at right side of the system), and reflection coefficient is calculated in the input region (left side of the system), by respectively using

$$T = \int_0^\infty \int_{-\infty}^{+\infty} J_x(x_R, y, t) dy dt, \quad (2.35)$$

and

$$R = - \int_0^\infty \int_{-\infty}^{+\infty} J_x(x_L, y, t) dy dt. \quad (2.36)$$

The errors observed in the sum $R + T$, presented by the numerical results is $\sim 0.1\%$ which demonstrate that there is a good precision in the results. If a magnetic field is applied in the system, the probability current receives an additional term $(e/m_e \mathbf{A}_x |\psi|^2)$, related to the potential vector \mathbf{A}_x . For the systems that we are investigating in this work, the external magnetic field is applied perpendicular to the (x, y) plane, and the potential vector is given by a Coulomb gauge $\mathbf{A} = (-y, x, 0)B/2$. If the energy of the propagation wave packet is high enough, it can be scattered to more energetic sub-bands. The probability current will then present contribution from more energetic states in the

output leads [53]. It is possible to investigate the projections of the j – th output wave function on the initial wave packet by fixing a point in the output lead and performing the integral

$$P_j(x_i, t) = \langle \Psi | \varphi_j \rangle = \int_{-\infty}^{+\infty} \Psi(x_i, y, t) \varphi_j dy. \quad (2.37)$$

which gives the contribution of the wave packet at each sub-band. The current calculation localized will help us to understand the wave packet propagation

$$J_T(x_i, y, t) = \int_{-\infty}^{\infty} J_x(x_i, y, t) dy, \quad (2.38)$$

within a appropriated boundary conditions.

When a wave packet is propagating on a finite system with a discrete grid, for any point outside the grid, or located on its edges, the wave function must vanish. One possibility to circumvent this problem is to ensure that the wave function never reaches the system's edge. On the other hand, in some systems, like quantum rings, the wave packet propagates in loops leading to a lost of information as time evolves, due to spurious transmissions and reflections at the grid's edge. In this case, the regions outside the grid works as infinite potentials for wave packet propagation. Among the several existing techniques to work around this boundary condition [86, 87, 88], in this work we apply an imaginary potential [89] at the edges of the input and output channels and, therefore, absorb the transmitted and reflected packets, in order to prevent these spurious reflections at the boundaries of the computational box. The imaginary potential used in this work reads

$$V_{im} = -iE_{min} \left(a\bar{x} - b\bar{x}^3 + \frac{4}{(c - \bar{x})^2} - \frac{4}{(c + \bar{x})^2} \right), \quad (2.39)$$

where

$$a = 1 - \frac{1}{c^3}, \quad (2.40a)$$

$$b = \left(1 - \frac{1}{c^3} \right) / c^2, \quad (2.40b)$$

$$c = \int_0^{\infty} \frac{dz}{(1 + z^2)^{3/4}} = \sqrt{2}K(1/\sqrt{2}), \quad (2.40c)$$

K is defined as an elliptic integral with arguments $K(k) = F(\pi/2, k)$ [90], resulting in $c = 2.62206$. E_{min} is the minimum energy that can be considered for the electron, and may be written as [53, 89]

$$E_{min} = \frac{\hbar^2}{2m_e} \left[\frac{c}{2(x_2 - x_1)\delta} \right]^2, \quad (2.41)$$

for the points located between x_1 e x_2 . The parameter δ account for the accuracy of the absorbent potential. Here, we use $\delta = 0.2$ in order to obtain a small reflections at x_1 . The variable \bar{x} , in eq. 2.39, has dependence in x , and can be written as

$$\bar{x} = 2k_{min}\delta/(x - x_1), \quad (2.42)$$

where $k_{min} = \sqrt{2m^*E_{min}/\hbar^2}$. The eq. 2.42 gives the point where the absorbing potential begins. The systems investigated in this thesis consists of a planar quantum structures in which the electron motion is constrained to be in (x, y) plane, whose dimension is 4200 x 4200 Å. The absorbing potential has width of 420 Å, fixed at the left and right edges of the grid. This width gives a minimum energy in eq. 2.41 of ~ 25 meV [91].

2.3 Imaginary-time evolution

The imaginary-time evolution technique will be used to calculate the eigenstates of a given Hamiltonian. For a time-independent potential, the eigenstates are obtained with good accuracy by using the propagation in imaginary time. The propagation of all states of interest can be obtained simultaneously using the ortho-normalization modified algorithm of Gram-Schmidt, which guarantee the ortho-normalization of all eigenstates. A wave function can be expressed as a linear combination of its eigenstates of a Hamiltonian, since it forms a complete orthogonal basis

$$|\Psi\rangle_t = \sum_{n=0}^{\infty} a_n e^{-\frac{iE_n t}{\hbar}} |\Phi_n\rangle, \quad (2.43)$$

or,

$$|\Psi\rangle_t = a_0 e^{-\frac{iE_0 t}{\hbar}} |\Phi_0\rangle + \sum_{n=1}^{\infty} a_n e^{-\frac{iE_n t}{\hbar}} |\Phi_n\rangle, \quad (2.44)$$

where ϕ_n and E_n are the n -th eigenfunctions and eigenenergies, respectively. Defining $\tau = it$, we get

$$|\Psi\rangle_t = e^{-\frac{E_0 \tau}{\hbar}} \left[a_0 |\Phi_0\rangle + \sum_{n=1}^{\infty} a_n e^{-\frac{(E_n - E_0)\tau}{\hbar}} |\Phi_n\rangle \right]. \quad (2.45)$$

After several imaginary-time steps of propagation ($\tau \rightarrow \infty$), the term of the ground state, $e^{-\frac{E_0 \tau}{\hbar}} a_0 |\varphi_0\rangle$, becomes strongly dominant over the other terms of the sum, since $E_n - E_0 > 0$ for $n > 0$. Therefore, starting with any wave function, this function should converge to the ground state of the system as τ increases. We can consider as a very long time those in which $\tau \gg \hbar/(E_n - E_0)$. The excited states are obtained

adding to the algorithm the Gram-Schmidt orthonormalization method which will assure orthonormality between all states in each time step

$$|\Phi_1\rangle = \frac{|\Psi\rangle - b_0 |\Phi_0\rangle}{\| |\Psi\rangle - b_0 |\Phi_0\rangle \|}, \quad (2.46)$$

where

$$b_0 = \langle \Phi_0 | \Psi \rangle. \quad (2.47)$$

The first state ϕ_1 will be excited if

$$b_1 = \langle \Phi_1 | \Psi \rangle \neq 0. \quad (2.48)$$

Taking a new propagation on imaginary time, and using a new initial wave function, perpendicular to Φ_0 and ϕ_1 we have

$$|\Phi_2\rangle = \frac{|\Psi\rangle - b_0 |\Phi_0\rangle - b_1 |\Phi_1\rangle}{\| |\Psi\rangle - b_0 |\Phi_0\rangle - b_1 |\Phi_1\rangle \|} \quad (2.49)$$

where

$$b_1 = \langle \Phi_1 | \Psi \rangle. \quad (2.50)$$

The second excited state Φ_2 will be obtained if

$$b_2 = \langle \Phi_2 | \Psi \rangle \neq 0. \quad (2.51)$$

Thus, we can get all the accessible states of the system, retracing the propagation in imaginary time again and again, since the propagated wave function for the n -th state is orthonormal to auto previous functions.

Braess paradox at the mesoscopic scale

Suppose that two points A and B of a network are connected only by two possible paths (e.g. roads in a traffic network, or wires in an electricity network). One would intuitively expect that adding to the network a third path connecting these two points would lead to an improvement of the flux through the pre-existing roads and, consequently, to a transmission enhancement. However, the so-called Braess paradox [66, 67, 68, 69, 70, 72, 92] of games theory states that this is not necessarily the case: under specific conditions, [93] adding a third path to a network may lead to transport inefficiency instead. This effect has been even observed in traffic networks in big cities, where *closing* roads *improves* the flux in traffic jams, [71] or in electricity networks, where it has been demonstrated that adding extra power lines may lead to power outage, due to desynchronization. [94, 95, 96]

A recent paper [65] showed both experimental and theoretical evidence of a very similar effect, but on a mesoscopic scale: they observed that branching out a mesoscopic network does not always improve the electrons conductance through the system. As they were dealing with a system consisting of wide transmission channels, quantum interference effects are not expected to be relevant. [97]

In this chapter, we demonstrate that the transport inefficiency in branched out devices also occurs on a nano scale, when only few sub-bands are involved, and transport is strongly influenced by quantum effects. For this purpose, we investigate wave packet propagation through a circular quantum ring attached to input (left) and output (right) leads, [53] in the presence of an extra channel passing diametrically through the ring. Our results demonstrate that increasing the extra channel width does not necessarily improve the overall current. The fundamental reasons behind this effect, which are related to quantum scattering and interference, are discussed in details in the following Sections.

3.1 Theoretical model

We consider an electron confined in a circular quantum ring attached to input (left) and output (right) leads, [53] in the presence of an extra channel passing diametrically through the ring, as sketched in Fig. 3.1(a). Both the ring and the leads are assumed to have the same width $W = 10$ nm, whereas different values of the extra channel width W_c are considered.

As initial wave packet, we consider a plane wave with wave vector $k_0 = \sqrt{2m_e\epsilon}/\hbar$, where ϵ is the energy and m_e is the electron effective mass, multiplied by a Gaussian function in the x -direction, and by the ground state $\phi_0(y)$ of the input channel in the y -direction,

$$\Psi(x, y, 0) = \exp \left[ik_0x - \frac{(x - x_0)^2}{2\sigma_x^2} \right] \phi_0(y). \quad (3.1)$$

Several papers have reported calculations on wave packet propagation in nanostructured systems, [98, 99, 100, 101] hence, a number of numerical techniques for this kind of calculation is available in the literature, such as the expansion of the time evolution operator in Chebyshev polynomials, [102] and Crank-Nicolson based techniques. [103] In the present work, the propagation of the wave packet in Eq. (3.1) is calculated by using the split-operator technique [53, 104, 105] to perform successive applications of the time-evolution operator, i.e. $\Psi(x, y, t + \Delta t) = \exp[-iH\Delta t/\hbar] \Psi(x, y, t)$, where Δt is the time step. The Hamiltonian H is written within the effective mass approximation, describing an electron constrained to move in the (x, y) -plane and confined, by external potential barriers of height V_0 , to move inside the nanostructured region represented in gray in Fig. 3.1(a), where the potential is set to zero. The interface between the confinement region and the potential barrier is assumed to be abrupt. Nevertheless, considering smooth potential barriers would not affect the qualitative behavior of the results to be presented here, since the effect of such smooth interfaces has been demonstrated to be mainly a shift on the eigenenergies of the system. [106, 107] The (x, y) -plane is discretized in a $\Delta x = \Delta y = 0.4$ nm grid, and the finite differences technique is used to perform the derivatives coming from the kinetic energy terms of the Hamiltonian. Imaginary potentials [89] are placed on the edges of the input and output channels, in order to absorb the propagated wave packet and avoid spurious reflection at the boundaries of the computational box. As the wave packet propagates, we compute the probability density currents at the input and output leads, which, when integrated in time, gives us the reflection and transmission probabilities, respectively, from which the conductance can be calculated.

As the fabrication of InGaAs quantum ring structures have already been reported in the literature, [108] we assume that the ring, channel and leads in our model are made out of this material, so that the electron effective mass is taken as $m_e = 0.041m_0$. Nevertheless, the qualitative features of the results presented in the following Section does not depend on specific material parameters.

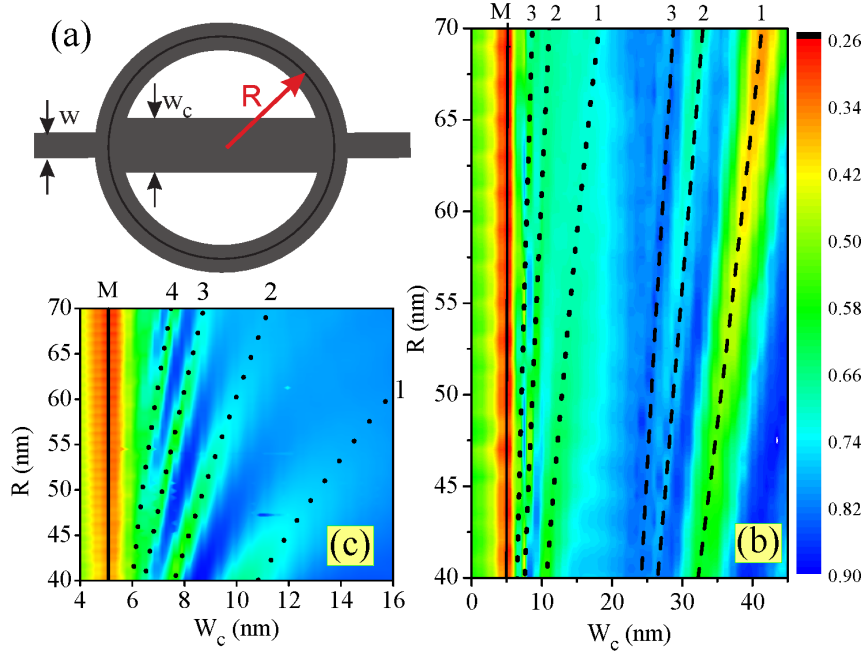


Figure 3.1: (a) Sketch of the system under investigation: a quantum ring with average radius R , attached to input (left) and output (right) channels with the same width as the ring ($W = 10 \text{ nm}$), and to an extra horizontal channel of width W_c . (b) Contour plots of the transmission probabilities as a function of the extra channel width and ring radius. The solid, dashed and dotted lines indicate seven minima that are discussed in the text. A zoom of the $4 \text{ nm} < W_c < 16 \text{ nm}$ region with the logarithm of the transmission is shown in (c).

3.2 Results and discussion

Contour plots of the calculated transmission probabilities are shown in Fig. 3.1(b) as a function of the ring radius R and the width W_c of the extra channel. Notice that the extra channel in the system is opened in the horizontal direction, namely, parallel to the input and output leads, being practically just a continuation of these leads. Even so, instead of improving the transmission, the existence of such a channel surprisingly *reduces* the transmission probability for specific values of W_c , leading to several minima in each curve. In what follows, we discuss the origin of several of these minima, indicated by the solid, dashed and dotted curves in Fig. 1(b).

The position of the minima labeled as 1, 2 and 3 in Figs. 3.1 (b,c) changes with the ring radius, which indicates that these minima are related to a path difference, i.e. to an interference effect. Let us provide other arguments to support this indication: in a very simplistic model, consider that part of the wave packet travels through the central channel, while the other part passes through the ring arms. The latter runs a length $\approx \pi R$ while going from the input to output leads, whereas the former runs through the

$2R$ diameter of the ring. The condition for destructive interference is:

$$\gamma \frac{\pi R}{\lambda} - \frac{2R}{\bar{\lambda}} = n + \frac{1}{2}, \quad (3.2)$$

where $\lambda = 2\pi/\sqrt{2m_e\epsilon/\hbar^2}$ ($\bar{\lambda} = 2\pi/\sqrt{2m_e(E - \bar{E}_j)/\hbar^2}$) is the wave length in the ring arms (extra channel), E_i (\bar{E}_j) is the energy of the i -th (j -th) eigenstate of the input lead (extra channel), and $E = \epsilon + E_i$ is the total energy of the wave packet. The parameter γ is close to one and accounts for the fact that the effective arm length may be slightly different from πR [see Fig. 1(a)]. By substituting these expressions for λ and $\bar{\lambda}$ in Eq. (3.2), one obtains

$$\bar{E}_j = E - \frac{\hbar^2\pi^2}{2m_e} \left[\frac{\gamma}{2} \sqrt{\frac{2m_e}{\hbar^2}} \epsilon - \left(n + \frac{1}{2} \right) \frac{1}{R} \right]^2, \quad (3.3)$$

Hence, this equation gives the condition for the interference related minima in the transmission probability. The extra channel eigenstates \bar{E}_j depend on W_c - which can be fairly well approximated by $\bar{E}_j \simeq \beta/W_c^{1.85}$ for large W_c (notice that the structure has finite potential barriers, therefore, the infinite square well relation $\bar{E}_j \propto 1/W_c^2$, is no longer valid). Therefore, the minima for large W_c are expected to occur for

$$W_c^{(n)} = \left\{ \frac{\beta}{E - \frac{\hbar^2\pi^2}{2m_e} \left[\frac{\gamma}{2} \sqrt{\frac{2m_e}{\hbar^2}} \epsilon - \left(n + \frac{1}{2} \right) \frac{1}{R} \right]^2} \right\}^{1/1.85}, \quad (3.4)$$

which are shown in Fig. 3.1(b) by black dashed lines for $n = 1, 2$ and 3 . The model fits very well the numerically obtained positions for these minima for $\gamma = 0.865$. The $n = 0$ minimum occurs outside of the investigated range W_c . The wave packet in this case has total energy $E = 124$ meV, with $\epsilon = 70$ meV and $E_0 = 54$ meV (ground state of the $W = 10$ nm input lead). For the $26 \text{ nm} < W_c < 42 \text{ nm}$ range in Fig. 3.1(b), the eigenstates of the channel, which are accessible by the electron with this energy, are the ground state and the second excited state. The first and third excited states, although still having energy lower than 124 meV for this range of W_c , are not accessible by the wave packet because of the even symmetry of the initial wave packet with respect to the x -axis, while these excited states of the channel are odd. Therefore, the part of the wave packet that goes through the central channel under these conditions populates mostly the second excited state, but has also some projection on the ground state and none on the other states. The fitting of \bar{E}_j for the second excited state ($j = 2$) has $\beta \approx 3000$ meV nm^{1.85}, which is the value used in Eq. (3.4) to obtain the dashed curves in Fig. 3.1(b).

The $n = 1, 2$ and 3 minima occurring for $7 \text{ nm} < W_c < 15 \text{ nm}$ in Fig. 3.1(b) can also be obtained from Eq. (3.4) but, since this is a lower W_c range, the dependence of \bar{E}_j on W_c will have a different exponent, one needs to replace 1.85 by 1.50 in Eq. (3.4). Besides, for such low W_c , the wave function travels predominantly through the ground state sub-band of the extra channel, so that one must consider the $j = 0$ state of this

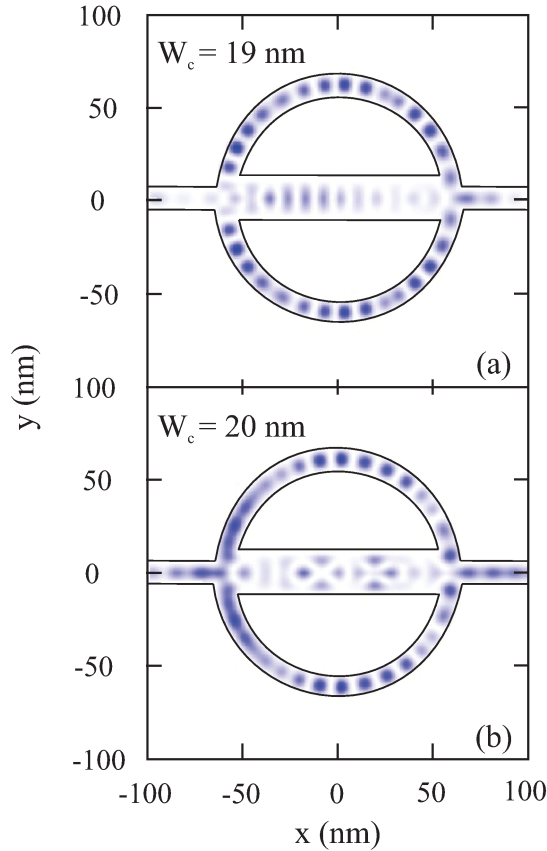


Figure 3.2: Snapshot of the propagating wave function at $t = 900$ fs for two values of the extra channel width: 19 nm (a) and 20 nm (b).

channel, which has $\beta \approx 56.99$ meV nm^{1.50} in this range. The results for this model are shown as black dotted lines in Fig. 3.1(b). To show these minima more clearly, we present in Fig. 3.1 (c), a magnification of the logarithm of the probability in the low W_c region. The numerically obtained minima are well fitted by the model of Eq. (3.4) for $\gamma = 0.925$ with $n = 1, 2, \dots, 4$ (see dotted lines).

In order to demonstrate that for lower (higher) values of W_c the wave function inside the extra channel is predominantly in its ground (second excited) state, Fig. 3.2 shows a snapshot of the propagating wave function at $t = 900$ fs for two values of the extra channel width: $W_c = 19$ nm (a) and 20 nm (b). In the former case, the wave function inside the extra channel exhibits predominantly a single maximum peak around $y = 0$, which suggests a large contribution of the ground state eigenfunction in the wave packet within this region. Similar results are obtained for lower values of the channel width W_c . However, the results for a slightly larger $W_c = 20$ nm are qualitatively different, exhibiting three peaks along the y -direction inside the extra channel, which implies a higher contribution of the second excited state on the wave function in this region.

Differently from the other minima, the position of the first minimum M in Fig. 3.1(b) appears around $W_c = 5$ nm and does not change with the radius R . Therefore, this mini-

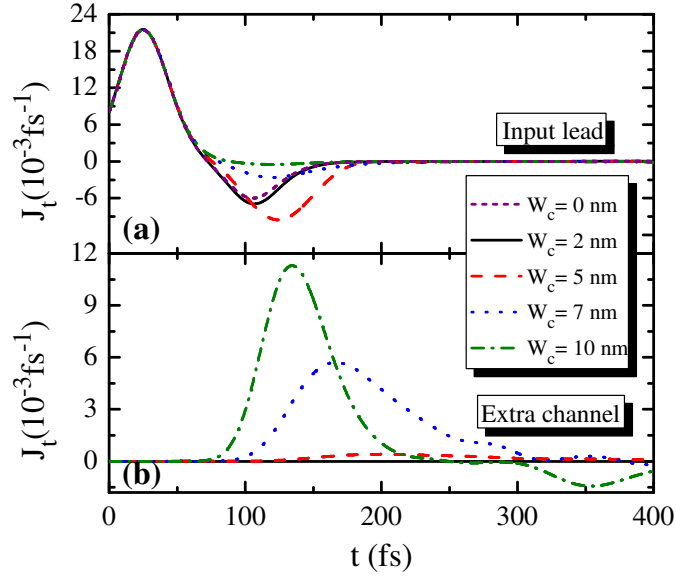


Figure 3.3: Probability density currents as a function of time, calculated (a) in the input lead and (b) in the extra channel, for different values of the extra channel width W_c , for wave packet energy $\epsilon = 70$ meV.

mum cannot be related to the above discussed interference effect. In order to understand the origin of the M minima, we show in Fig. 3.3 the integrated current J_t in the input lead and the extra channel. Fig. 3.3(a) exhibits a high negative peak for $W_c = 2$ nm and 5 nm at ≈ 100 fs and ≈ 140 fs, respectively, which represents a strong reflection of the wave packet at the ring - channel junction¹. This is confirmed by the very low currents observed for these cases inside the extra channel, in Fig. 3.3(b). On the other hand, for $W_c = 7$ nm the reflection peak in the input lead becomes very weak, while for $W_c = 10$ nm, almost no reflection is observed. For the latter two cases instead, large current peaks are observed inside the extra channel. This is a clear indication that the transmission inefficiency in the low W_c case is not related to interference effects, but rather to scattering at the ring-channel junction, since the wave packet barely enters the extra channel when it is too narrow.

We discuss now the possibility of having part of the incoming wave packet passing through a narrow extra channel. Both the leads and the extra channel have discrete eigenstates due to the quantum well confinement in the y -direction, whose energy levels are shown in Fig. 3.3(a) as a function of the well width. In the x -direction, parabolic sub-bands stem from these eigenstates, as illustrated in Fig. 3.3(b). The incoming wave packet considered in Figs. 3.1 - 3.3 has $\epsilon = 70$ meV on top of its ground state energy in the input lead, $E_0 = 54$ meV (for $W = 10$ nm). This energy is represented by the dotted horizontal lines in Figs. 3.3(a) and (b). The wave packet has a Gaussian distribution

¹The high positive peak in the input channel is just the incoming wave packet.

of energies of width $\Delta E = \hbar^2/m_e k_0 \Delta k$, where $\Delta k = 2\sqrt{\ln 2}/\sigma_x$ is the full width at half maximum (FWHM) of the wave vector distribution, which is represented by the shaded area around the dotted line in Fig. 3.3(a). A narrow extra channel has a very high ground state sub-band energy, so that no component of the incoming wave packet energy has enough energy to pass through the channel. As the extra channel width W_c increases, its sub-band energies decrease, allowing the incoming wave packet to travel through this channel. These two situations are illustrated in the upper and lower figures of Fig. 3.3(b), respectively. Notice that the upper boundary of the energy distribution (shaded area) in Fig. 3.3(a) is crossed by the second excited state energy curve (blue triangles) approximately at $W = 20$ nm. This explains the drastic difference between the wave functions within the extra channel with $W_c = 19$ nm and 20 nm, observed in Fig. 3.2: in the latter case, the wave function has a significantly larger part of its energy distribution above the second excited state energy, allowing it to have a larger projection on this state.

Therefore, the counter-intuitive result observed in Figs. 3.1, namely, the transmission reduction as the extra channel width increases for lower values of W_c , is a pure quantum scattering effect. For classical particles, such an extra channel with any width would allow the passage of the particles and, consequently, improve the transmission. However, a quantum channel has a confinement energy (ground state) and, if the energy of the incoming particle is lower than this minimum, the particle is not allowed to pass through the channel. Therefore, adding a narrow extra channel to the system, which effectively also adds extra scattering, does not add an extra path for the wave packet, because of the very high ground state energy of the narrow channel. This mechanism, which is illustrated by the band diagrams in Fig. 3.3(b), leads to the strong reflections observed in Fig. 3.3 for $W_c = 2$ nm and 5 nm. For $W_c > 5$ nm, a significant part of the $E = 70$ meV wave packet has enough energy to go through the extra channel, explaining the increasing transmission as W_c increases above 5 nm. This also suggests that incoming wave packets with higher energy would need lower extra channel widths to pass, which is indeed observed, as we will discuss further on.

In fact, the position of M strongly depends on the wave packet energy, as shown in Fig. 3.5(a), where the transmission probability in the vicinity of M is plotted as a function of the channel width W_c for several values of the energy, ranging from 70 meV (bottom curve) to 120 meV (top curve), with 10 meV intervals. The ring radius is fixed as $R = 60$ nm, and each consecutive curve in this figure is shifted by 0.1. If the energy dependence of the position of M is due to the above discussed quantum effect, it should be possible to predict the position of these minima from the following argument: the highest energy components of the wave packet have energy around $\approx E + \Delta E/2$. These components would be allowed to pass through the extra channel, consequently improving the current, provided the channel width is wide enough to have a ground state energy as low as their energy, i.e. if $\bar{E}_0 < E + \Delta E/2$. For low values of W_c , the ground state energy of the

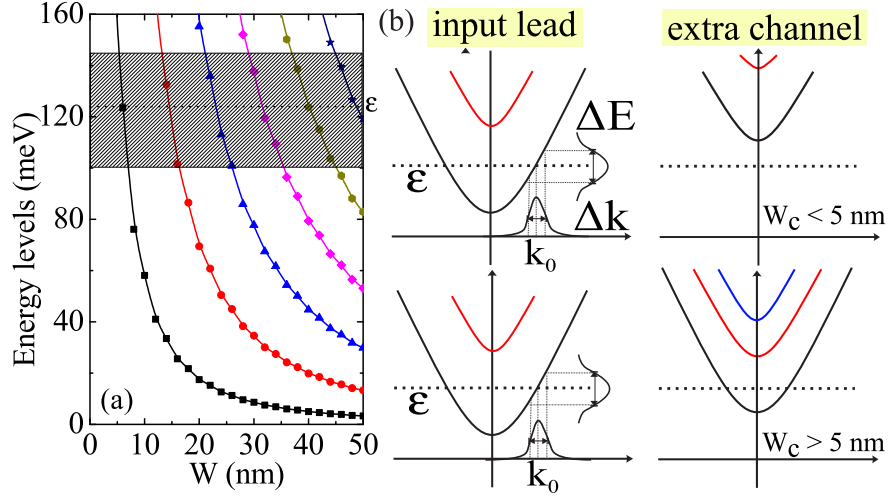


Figure 3.4: (a) Eigenstates of a finite quantum well as a function of its width. (b) Diagram representing the energy sub-bands in the input lead and in the extra channel. The horizontal dotted line is the average energy of the wave packet used in Figs. 3.1 and 3.3, and the shaded area in (a) illustrates the FWHM of the energy distribution of this wave packet.

channel is well approximated by $\bar{E}_0 = \alpha/W_c^{1.04}$, for $\alpha = 8.65$ eV, as shown by the green dashed line ($f_2(W)$ function) in Fig. 3.5(b). Notice it is a different power from the one used in Eq. (3.4), which is valid only for higher W_c values. The red dotted line ($f_1(W)$ function) in Fig. 3.5(b) is an example of fitting for high values of W_c , which was used in Eq. (3.4). Figure 3.5(b) is in log-log scale, so that the power laws in $f_1(W)$ and $f_2(W)$ are shown as straight curves, whose slopes are the functions' exponents. Using this expression for \bar{E}_j , one obtains the following approximate expression for the position of the M minima

$$W_c^{(M)} = \frac{6103}{\left(\epsilon + E_0 + \hbar\sqrt{\frac{\epsilon}{2m_e}}\Delta k\right)^{1/1.04}}, \quad (3.5)$$

which is shown by the solid curve in Fig. 3.5(c). Notice the rather good agreement with the numerically obtained positions of the M minima, represented by the symbols.

It is important to point out that the exponents 1.85, 1.50 and 1.04, as well as the values of α and β , found for the fitting functions for the eigenstate energies as a function of the well width and used in Eqs. (3.4) and (3.5), were obtained for an abrupt interface between the potential barriers and the confining region. These values must be slightly modified in the case of smooth potential barriers.

Our results, therefore, demonstrate that the M minima in Figs. 3.1 and 3.5 are a consequence of a competition between two effects: (i) the quantum scattering in the ring-channel junction, which increases the reflection when a narrow extra channel is added, and (ii) the improvement in the transmission resulting from the part of the wave packet that has enough energy to propagate through the sub-bands of the extra channel. The for-

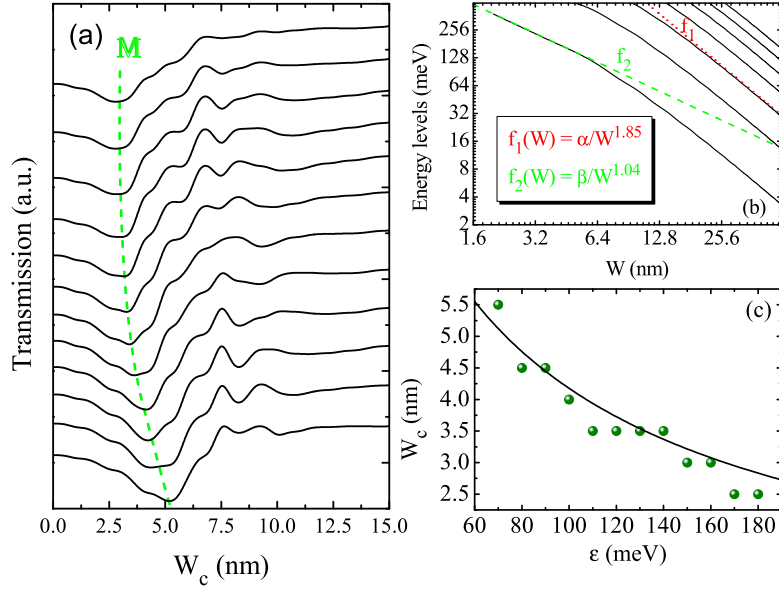


Figure 3.5: (a) Transmission probabilities as a function of the extra channel width in the vicinity of the minimum labeled as M in Fig. 3.1(a), for several values of the wave packet energy $\epsilon = 70$ (bottom curve), 80, ... 180 meV (top curve). The curves were shifted 0.1 up from each other, in order to help visualization. (b) Energy levels (solid) as a function of the channel width, plotted in a log scale, along with two fitting functions (dashed curves), for large (f_1) and small (f_2) values of the channel width. (c) Numerically obtained (symbols) positions of the M minima as a function of the wave packet energy, along with the results (solid curve) of the analytical model, given by Eq. (3.5).

mer suggests that adding extra scatterers at the input lead-ring junction leads to a larger reflection back into the input lead. In order to verify this, we consider two situations that mimic the appearance of an extra “blind” channel (see insets of Fig. 3.6): one is the presence of an attractive Gaussian potential [53] $V_a(x, y) = -V_G \exp \{[(x - x_g)^2 + y^2]/2\sigma_G^2\}$ close to the lead-ring junction, and the other is a circular bump of radius R_b in the inner boundary of the ring. Fig. 3.6 shows the transmission probabilities for $\epsilon = 70$ meV as a function of the Gaussian potential depth V_G (bottom axis) and the radius R_b (top axis) of the circular bump. In both cases, the transmission is reduced in the presence of the extra scatterer, which supports the idea that the transmission reduction in the low W_c range in Figs. 3.1 and 3.5 is indeed a consequence of extra scattering created by the opening of the extra channel, which is however effectively blind, since the bottom of the ground state sub-band of the a narrow channel has energy higher than that of the incoming electron wave packet.

All the results in this work were calculated for sharp connections between the ring, the extra channel, and the input and output leads. However, qualitatively similar results are also obtained for smooth junctions [53] between these parts of the system. Moreover, different ring geometries would shift the high W_c minima, which are related to quantum

interference, by effectively changing the electronic paths, while impurities in the ring could suppress these minima, by destroying phase coherence. However, neither impurities nor different ring geometries can affect the low W_c minimum (M), since it is related only to quantum scattering in the input lead-ring junction, which does not depend on these features.

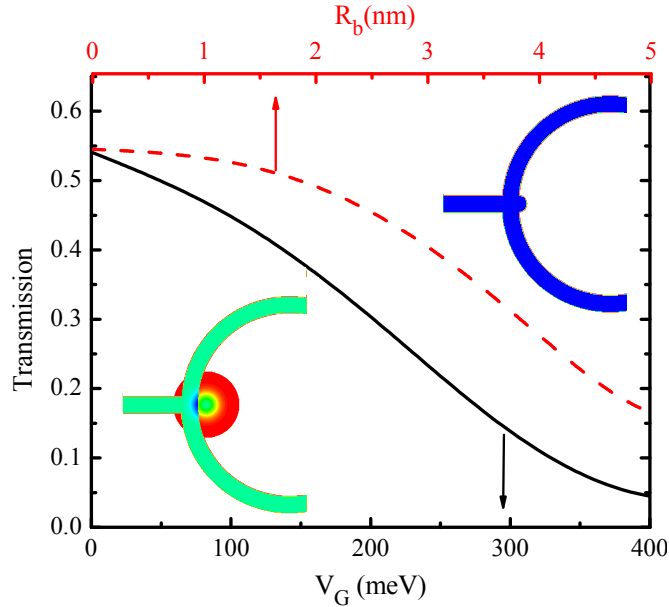


Figure 3.6: Transmission probabilities for a $\epsilon = 70$ meV wave packet scattered by two kinds of defects in the lead-ring junction: a Gaussian attractive potential of depth V_G (solid, bottom axis) and width $\sigma_G = 5$ nm, and a circular bump of radius R_b (dashed, top axis), which are schematically illustrated in the lower and upper insets, respectively.

The original version of the Braess paradox, described in details in Ref. [69], discusses how the travel time between two points connected by only two possible roads, A and B, changes if these two roads are inter-connected by a third road C. If one considers that the traffic at specific parts of A and B depend on the number of drivers in these roads, then, depending on the (partial) travel time through this new connection C, the dominant strategy turns out to consist in starting in one road and changing to the other road through the connection C, and therefore, all players (drivers) would take this path. This strategy, though leading to the Nash equilibrium situation of this system, represents an increase in the travel time - lower travel times could even be reached if the drivers agree not to use the connection C *a priori*, but in a scenario of selfish drivers, they would switch roads until the equilibrium is reached, despite the reduction in overall performance. Therefore, the classical Braess paradox is closely related to an unsuccessful attempt to optimize the travel time through a traffic network by the drivers. The transport properties of the branched out mesoscopic network investigated in Refs. [65, 97] is reminiscent of those of the roads network in the original Braess paper just in the sense that it exhibits a

reduced overall current when an extra channel is added to the network, depending on the channel width. However, the fundamental reason behind this phenomenon is not clear in Refs. [65, 97] - it cannot be an interference effect, since this is not a coherent system, but it is not also due to an optimization of the currents, as in the classical paradox, since the model in these papers does not involve non-linear equations or iterative calculations of the overall current flow. On the other hand, for the quantum case investigated here, where such a transmission reduction in the presence of an extra channel is also observed, the main reason behind this Braess-like paradoxical behavior is quite clear: for small values of the channel width, it is due to quantum scattering effects at the ring-channel junction, whereas for larger widths, it is due to interference effects. Therefore, if one includes the transmission reduction phenomena described here into the category of analogs of Braess paradox, one must keep in mind that, just like most of the other analogs suggested in the literature [69, 94, 95, 96], although presenting results similar to those of the original Braess network, in the sense that more paths leads to reduced performance, the reason behind this reduction is not related to an attempt to optimize the flux, but to other fundamental physical properties of the investigated system.

Wave packet propagation through branched quantum rings

In the previous chapter, we demonstrated that transport inefficiency in branched out devices also occurs on a quantum scale, when few subbands are involved in the transport. [64] The transport properties are strongly influenced by quantum scattering and interference, so that a similar reduction in transmission can be found in a quantum ring with a central branch. In this chapter, we extend the previous one [64] and investigate: (i) the effect of the geometry of the quantum ring, by considering, semi-circular, circular and squared rings, (ii) the effect of an Aharonov-Bohm (AB) phase, induced by an external magnetic field, and (iii) the effect of the position of an AFM tip potential which is able to obstruct one of the system channels. For this purpose, we investigate wave packet propagation through these branched quantum rings, attached to input and output leads, by numerically solving the time-dependent Schrödinger equation. Our results show that the so-called quantum analog of the Braess paradox is robust in these nano scale devices and that it is a correspondence of effects related to a combination between quantum interference and scattering events. We also shown here the Braess effect can be tuned by magnetic and electric fields.

4.1 Theoretical model

We consider here four different planar quantum rings, attached to input (left) and output (right) leads for electrons injection, in the presence of an extra channel. We assume that the rings and the leads have the same width $W = 10$ nm, while the width of the extra branch W_c , will be varied from 0 to 50 nm. Figure 4.1 shows a schematic view of our systems under investigation: in (a), (b) and (d) the ring has a circular symmetry with average radius $R_{ave} = 60$ nm, while in (c) the ring has a rectangular symmetry with width and height given by 60 nm and 30 nm, respectively. From now onwards, we will refer to these systems by their labels (a-d).

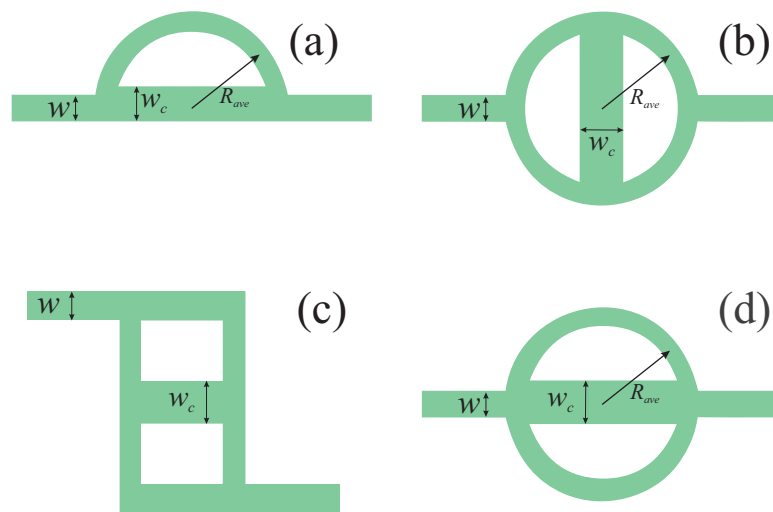


Figure 4.1: Sketch of the systems under investigation. (a) Half quantum ring with leads and channel aligned, (b) circular quantum ring with an extra channel in the perpendicular direction, (c) square ring with non-aligned leads and channel, and (d) circular quantum ring with leads and channel aligned.

An electron confined in such a quasi-one-dimensional channel with width W has sub-band energy given by

$$E_n(k_x) = E_n^{(y)} + \frac{\hbar^2 k_x^2}{2m_e}. \quad (4.1)$$

Here m_e is the electron effective mass and eigenenergies of the confining well $E_n^{(y)}$ are numerically calculated for a finite potential V_e . For the initial wave packet (WP), we assumed a plane wave with wave vector $k_0 = \sqrt{2m_e \varepsilon}/\hbar$, where ε is the average kinetic energy, multiplied by a Gaussian function with width σ_x in the x direction and by the ground state wave function $\phi_0(y)$ of the input lead in the y -direction

$$\Psi(x, y, t = 0) = \exp \left[ik_0 x - \frac{(x - x_0)^2}{2\sigma_x^2} \right] \phi_0(y). \quad (4.2)$$

There are several techniques to numerically solve the time dependent Schrödinger equation.[98, 99, 100, 102, 103, 109] In this work we opted for the split-operator technique, which consists in separating the time evolution [53, 104, 105] operator as

$$\begin{aligned}\Psi(x, y, t + \Delta t) &= \exp[-iH\Delta t/\hbar] \Psi(x, y, t) \\ &= \exp[-iV\Delta t/2\hbar] \exp[-iT_x\Delta t/\hbar] \\ &\times \exp[-iT_y\Delta t/\hbar] \exp[-iV\Delta t/2\hbar] \\ &\times \Psi(x, y, t) + \mathcal{O}(\Delta t^3),\end{aligned}\tag{4.3}$$

where Δt is the time step, $T_{x(y)}$ is the kinetic-energy operator for the $x(y)$ -direction, and the error $\mathcal{O}(\Delta t^3)$ is due to the noncommutativity of the potential and kinetic terms. [82] Nevertheless, this error can be neglected provided we use a very small time step, that in our case is $\Delta t = 0.1$ fs. The Hamiltonian \mathcal{H} is written within the effective mass approximation, describing an electron constrained to move in the (x, y) -plane and confined by an external in-plane potential of height V_0 , which allows the electron to move only within the leads, arms and channels regions, illustrated by shaded areas in Fig. 4.1, where the potential is zero. The potential step is assumed here to be abrupt, but smooth interfaces will not qualitatively affect the results. [106, 107] The (x, y) -plane is discretized in $\Delta x = \Delta y = 0.4$ nm steps, and the finite difference scheme is used to write the derivatives coming from the kinetic energy terms of the Hamiltonian. We apply an imaginary potential at the edges of the input and output channels and, in order to, absorb the transmitted and reflected packets, and to prevent spurious reflections at the boundaries of the computational box. [89]

The transmission and reflection probabilities are calculated by integrating the probability density current at specific points of the system, namely, at the output lead ($x_R = 158$ nm), for the former, and at the input lead ($x_L = -158$ nm), for the latter. Thus, the expressions for transmission and reflection are, respectively,

$$T = \int_0^\infty dt \int_{-\infty}^{+\infty} dy J_x(x_R, y, t)\tag{4.4}$$

and

$$R = - \int_0^\infty dt \int_{-\infty}^{+\infty} dy J_x(x_L, y, t).\tag{4.5}$$

The component of the probability current in the x -direction is given by

$$\begin{aligned}J_x(x, y, t) &= \frac{\hbar}{2m_e i} \left(\Psi^* \frac{\partial}{\partial x} \Psi - \Psi \frac{\partial}{\partial x} \Psi^* \right) \\ &+ \frac{e}{m_e} A_x |\Psi|^2.\end{aligned}\tag{4.6}$$

For a magnetic field applied perpendicularly to the ring plane, *i.e.* in the z direction, the vector potential is taken in the Coulomb gauge $\mathbf{A} = (-y, x, 0)B/2$. In order to quantify the scattering of the electron into different subbands, we project the wave function on the

j -th subband at a fixed point x_i of the quantum well,

$$\begin{aligned} P_j(x_i, t) &= |\langle \Psi | \varphi_j \rangle|^2 \\ &= \left| \int_{-\infty}^{+\infty} dy \Psi(x_i, y, t) \varphi_j(y) \right|^2. \end{aligned} \quad (4.7)$$

Equation (5.7) gives the probabilities to find an electron in the j -th subband at position x_i at time t . The contribution from each subband to the total probability current is given by

$$\begin{aligned} J_x^{(j)}(x) &= \int \frac{\hbar}{2m_e i} \left(\bar{P}_j^* \frac{\partial}{\partial x} \bar{P}_j - \bar{P}_j \frac{\partial}{\partial x} \bar{P}_j^* \right) \\ &\quad + \frac{e}{m_e} A_x |\bar{P}_j|^2 dt. \end{aligned} \quad (4.8)$$

Notice that Eq. (5.7) is not normalized, and therefore the values assumed by $J_x^{(j)}$ can be larger than one. We assume ballistic transport and, for the sake of simplicity, all kinds of disorder are neglected.

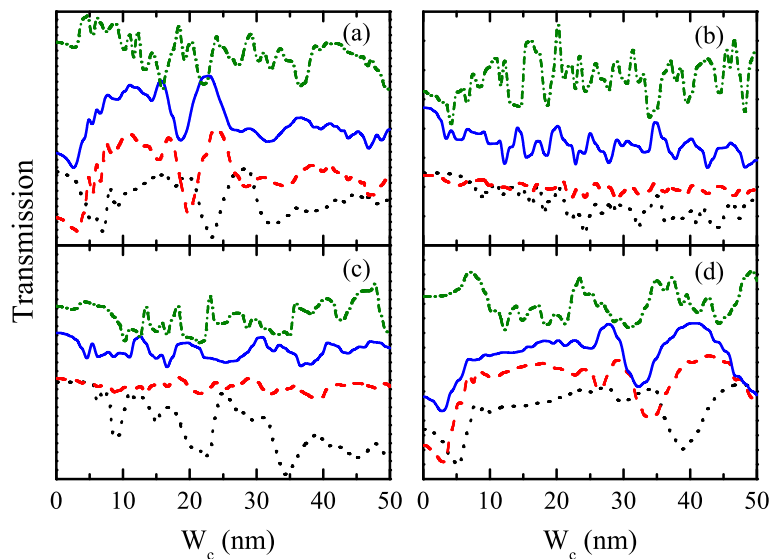


Figure 4.2: Transmission probability as function of channel width W_c . The frames (a), (b), (c) and (d) refer collectively as the corresponding systems presented in Fig. 4.1. The WP have kinetic energies ε_1 (black, dotted line), ε_2 (red, dashed line), ε_3 (blue, solid line), propagating in the subband ground state, while the other is in the first excited state with kinetic energy ε_3 (green dash-dotted line).

4.2 Results and Discussion

We consider materials parameters for InGaAs and InAlAs, in which the band-offset and electron effective mass are taken as $V_e = 600$ meV and $m_e = 0.041m_0$, respectively.

Three values of kinetic energy for the WP are used: $\varepsilon_1 = 70$, $\varepsilon_2 = 140$ and $\varepsilon_3 = 180$ meV. These WP were propagated in the ground state $E_0^{(y)} \simeq 58$ meV and, specifically for ε_3 , we also propagated it in the first excited state of the channel, $E_1^{(y)} \simeq 226$ meV.

Figure 4.2 shows the transmission probabilities as function of the channel width W_c for kinetic energies ε_1 (black, dotted line), ε_2 (red, dashed line), and ε_3 (blue, solid curve), for the initial WP in the ground state, and ε_3 in the first excited state (green, dash-dotted line). Each curve shown in Fig. 4.2 is vertically shifted up by 0.2. The disposition of the frames (a), (b), (c) and (d) presented in Fig. 4.2 follows one of Fig. 4.1. For all systems investigated, the existence of an extra channel surprisingly reduces the transmission probability for some width W_c , instead of improving it. This decreasing is either an effect of quantum scattering at the channel-ring junctions, or a WP interference effect. Both possibilities will be discussed now in more detail.

Notice that the extra channels for the profiles in Figs. 4.1(b) and (c) are not aligned with respect to input and output leads, as in Figs. 4.1(a) and (d). Thus, transmission probabilities in Figs. 4.2(a) and (d) present some similarities in their patterns, and the same is observed in Figs. 4.2(b) and (c). The curves clearly exhibit minima for all kinetic energies, and transmission probability always start decreasing as the extra channel width increases for WP propagating in the ground state subband, although the extra channel represents an alternative for the electron to bypass through the central region which should, in principle, improve the transmission. The positions of most of the minima in W_c strongly depend on of WP energy. In Figs. 4.2(b) and (c), besides the minima, transmission probabilities also exhibit an overall decreasing trend with increasing of channel width W_c , specifically for low kinetic energy. Moreover, transmission probability patterns are strongly dependent on the geometry of the ring, which indicates that there are numerous possibilities of WP interference in these cases, where the system geometry is more complex than that in Fig. 4.2(a) and (d).

For a better understanding of WP dynamics in these systems, Fig. 4.3 shows the time-dependent probability current through the extra channel as a function of time. The WP propagates in the lowest subband from left to right with kinetic energy given by ε_1 . Three different values for channel width W_c are considered: 5, 10, and 20 nm. In all studied cases we observe initially a positive peak of current followed by a negative peak, which is more acute in Figs. 4.3(b) and (c). In these cases, a sequence of positive and negative peaks clearly demonstrates that the WP is repeatedly reflected at the extra channel-ring junctions, propagating back and forth within the extra channel. Thus, the time that electrons are kept in the structure is increased, contributing to an overall reduction of the electric current. For $W_c = 5$ nm, only a a small part of the WP propagates through the extra channel, because the average value of the kinetic energy is lower than the ground state of this channel. In addition, the input and output leads are not aligned, which also harness the WP propagation through this channel. For cases in which the extra channel is aligned with input and output leads, as in Fig. 4.3 a) and (d), a somewhat larger part

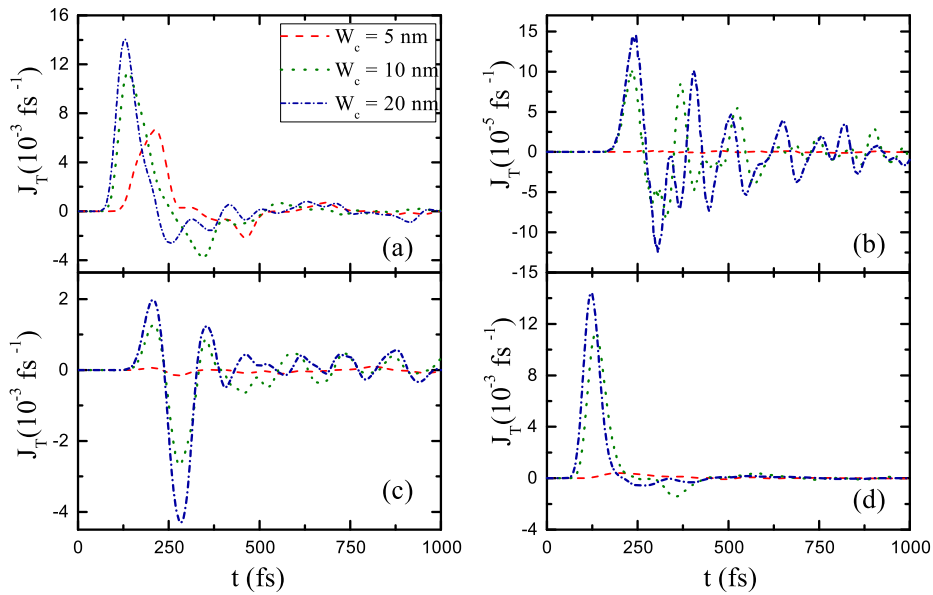


Figure 4.3: Time-dependent probability current through the extra channel, calculated for kinetic energy ε_1 . The different frames refer to the systems in Fig. 4.1.

of the WP can propagate through the extra channel even in the $W_c = 5$ nm case.

Figure 4.4 shows snapshots of the squared modulus of the wave functions at $t = 460$ fs, for kinetic energy ε_1 , and $W_c = 0, 5, 7, 10,$ and 20 nm, respectively, in each column. The wave function presents just one peak in the confinement direction within the ring arms, input and output leads, which indicates that the propagation is kept in the ground state subband in all these regions. Along the extra channel, however, the wave function propagates in the ground state subband only for $W_c = 5$ nm, while for larger W_c , it is scattered to excited states and exhibits multiples peaks and even different parities, due to the lower confinement energies in this channel.

The contributions of each subband to the total transmission probability is shown in Fig. 4.5, where $J_x^{(1)}$ (top) and $J_x^{(2)}$ (bottom) calculated in the output lead (at $x = 158$ nm), are depicted as function of W_c . Other states were omitted because they do not significantly contribute for the WP energies considered here. The systems sequence used here is the same as in previous figures. The projected density current exhibits minima with patterns similar to those in Fig. 4.2. As mentioned above, the output lead has a width of $w = 10$ nm and the energy difference between the first two states, $E_1^{(y)} - E_0^{(y)} = 168$ meV, is higher than the kinetic energy ε_1 . For this reason, in all systems, the contribution $J_x^{(2)}$ in Fig. 4.5 is zero when the kinetic energy is ε_1 (black, dotted line). Moreover, the WP is a gaussian distribution in energy space, whose width allows for non-zero projection on P_2 with energy the ε_2 . We observe in Figs. 4.5(b) and (d) that the WP in output lead does not propagate in the subband excited states in these systems, regardless of the kinetic energy or channel width W_c , even when the wave function projections are non-zero for

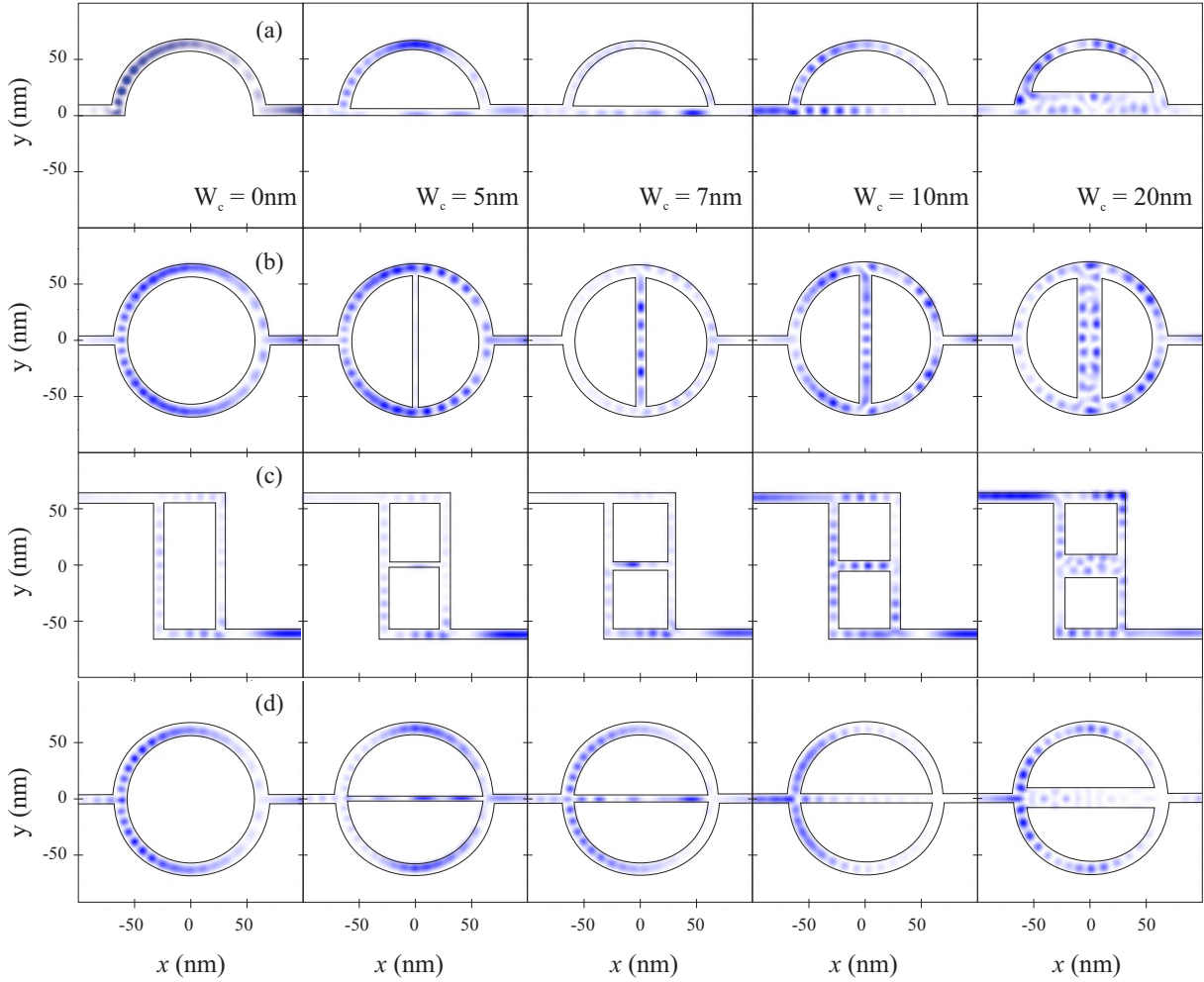


Figure 4.4: Snapshots of the squared wave function at $t = 460$ fs, for different channel width W_c and kinetic energy ε_1 .

excited states in the extra channel, as shown in Fig. 4.4. In these systems, the quantum ring has a circular symmetry and the WP propagate in subbands of the top and bottom arms with a phase difference given by π , which leads to an interference that cancels the projection P_2 on the output lead.[53]

The contribution $J_x^{(2)}$ of the second subband to the probability density current in Figs. 5.5(a) and (c) does not vanish, despite of the interference, due to the asymmetry in the potential of these systems. They lead to additional peaks and valleys in the transmission probabilities as a function of the extra channel width for these systems in Fig. 4.2(a) and (c). Notice that the position of these peaks and valleys are completely independent of the WP energy, whereas the minima observed for $J_x^{(1)}$ are significantly shifted as the energy varies. Therefore, the former minima cannot be interpreted in terms of quantum scattering and interference as done here for the latter, as they are just a consequence of inter-subband scattering by the channel-junctions.

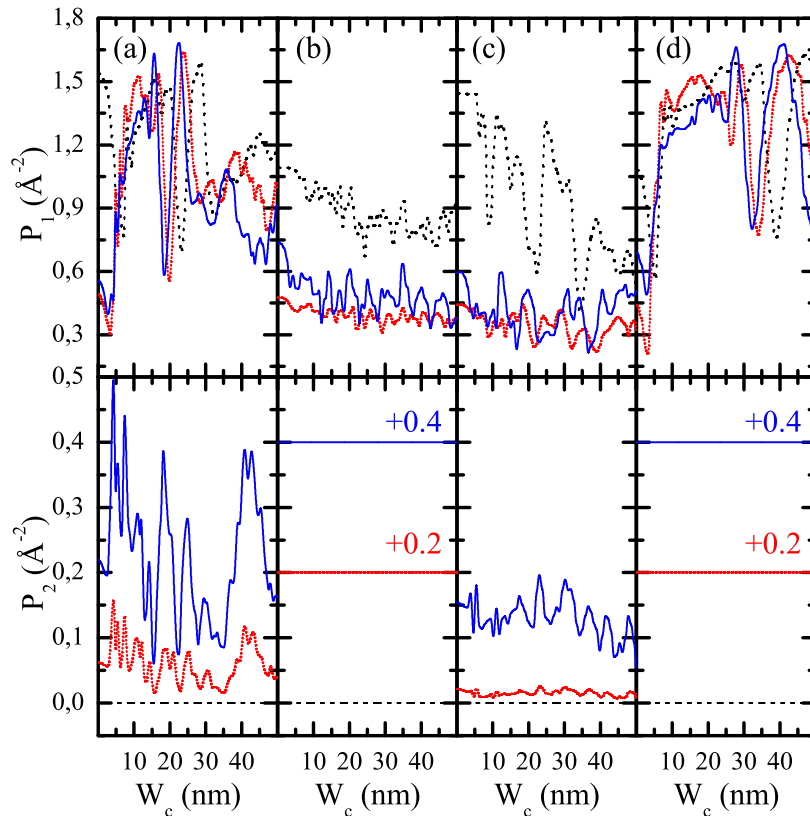


Figure 4.5: Projection of the wave function on the ground state (top graphics) and first-excited subbands (bottom graphics) as function of channel width W_c , calculated at the output lead. Kinetic energy ε_1 (black dotted line), ε_2 (red short-dot line), and ε_3 (blue solid line). This figure is ordered in the same sequence Fig. 4.1.

4.2.1 Influence of an external magnetic field

Let us now turn our attention to the minima in the transmission probabilities shown in Fig. 4.2. One may expect that these minima come from interference, and therefore we should be able to change the position of the minima not only by changing the kinetic energy, but also by applying an external magnetic field. This magnetic field adds a phase in the wave function through the vector potential \mathbf{A} . If the minima are due to interference, their position will change in the presence of the field, since the vector potential induces an additional phase to the wave function. Fig. 4.6 displays a color map of transmission probabilities as function of channel width W_c and magnetic field \mathbf{B} . In Fig. 4.6(a), for $B = 0$, as W_c increases, minima (red and yellow regions) are observed around $W_c = 5$ nm and some intermediate values of $W_c \approx 23$ nm. In these cases, then, enlarging the extra channel reduces the current. As the magnetic field increases, the minima positions are not significantly affected, which indicates that these minima are not related to interference, but rather to pure quantum scattering. For W_c between 5 and 10 nm, there are also other minima (green regions), equally spaced in B , that are affected by the magnetic field, due

to the AB effect. In this case, the WP passes through both channels, now connected as a semi-circular ring-like path, which explains the observed AB oscillations. For $W_c < 5$ nm, subband energies are higher than the kinetic energy, and the WP can not propagate through the extra channel. The W_c width and the magnetic field can change the AB period. The system in (a) thus proves to be a good example of the quantum analog of the Braess paradox, where more channels (surprisingly) means less current, and which is not simply due to quantum interference effects.

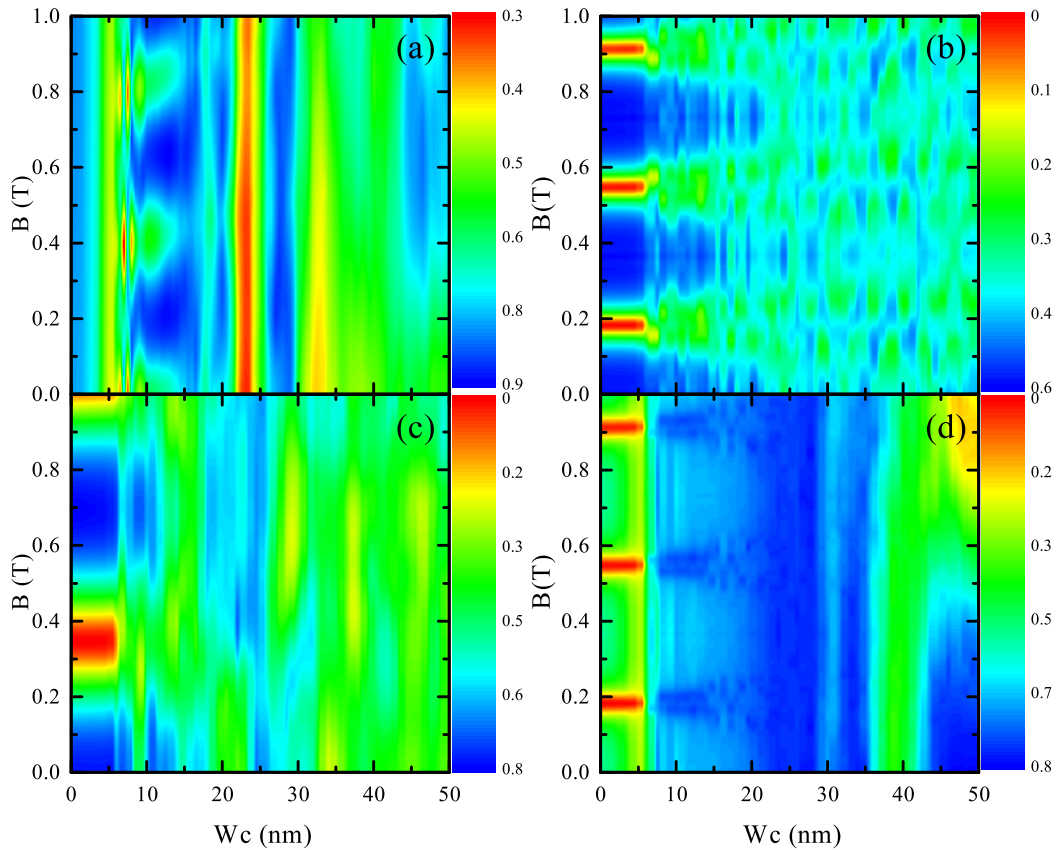


Figure 4.6: Contour plots of the transmission probabilities as a function of the extra channel width W_c and magnetic field \mathbf{B} . This figure is ordered in the same sequence as Fig. 4.1.

AB oscillations are evident in Figs. 4.6(b), (c) and (d), as B increases in the range of small W_c width. As W_c increases, two rings are effectively formed in system (b), and this yields a reduction in the AB period in Fig. 4.6 (b). In Fig. 4.6 (c), the minima observed for $B = 0$ are strongly affected by the magnetic field, which indicates that these minima are a result of destructive interference. In Fig. 4.6 (d) the minima around $W_c \sim 5$ nm for $B = 0$ do not change with the magnetic field, whereas the next minima, around $W_c \sim 35$ nm, shift to the right as the magnetic field increases, showing that the first minima is due to scattering while the latter is due to WP interference. In order

to improve the visualisation of the transmission in Fig. 4.6(c) and (d), we show the respective transmission as function of W_c width in Fig. 4.7(a) and (b), corresponding to the systems of Figs. 4.1(c) and (d), respectively. Each contour (or on-line color) represents a transmission for a specific applied magnetic field, ranging from 0 to 1 T, and reproduce the behaviour of the minima, as discussed above.

4.2.2 Effect of extra (obstructing) potentials

In order to test the robustness of the Braess paradox analog, observed here in the context of quantum mechanics, we add a perturbing potential, which can be seen as a model for an AFM tip [108], we consider three different configurations for each of the systems of Fig. 4.1 to analyse the behaviour of the transmissions, see Fig. 4.8: the tip potential (1) is fixed at the central region $(x, y) = (0, 0)$; the tip potential (2) is placed at $x = 0$ and moved from bottom to top along the y -axis, and the tip potential (3) is placed at $y = 0$ and moved from left to right along the x -axis. This perturbative potential, which depends on the tip position and is assumed to be isotropic, is expressed as a Gaussian distribution centered at (x_p, y_p) ,

$$V_{gau} = V_G \exp \left\{ -\frac{1}{2\sigma_G^2} [(x - x_p)^2 + (y - y_p)^2] \right\}, \quad (4.9)$$

where, V_G is the potential intensity and σ_G ($= 5$ nm) represents the width of the Gaussian potential.

Figure 4.9 shows transmission probabilities for a WP with kinetic energy ε_1 propagating in the first subband. This figure is spatially arranged in four groups, in the same sequence of geometries as in Figs. 4.1(a-d), with three panels each: panel (1) shows the transmission probability as function of the tip potential intensity V_G , with the tip potential fixed at the central region of the system; whereas panels (2) and (3) are the transmission probabilities for the tip potential moving from bottom to top side, at $x = 0$, and from left to right at $y = 0$, respectively, as mentioned above. The black solid line represents the transmission calculated for a system with a central channel width $W_c = 10$ nm. The red dotted line represents the transmission probability calculated with W_c given by the respective minima of the transmission, depicted in Fig. 4.2, *i.e.*, the W_c width is 23 nm in Fig. 4.9(a), 24 nm in (b), 22 nm in (c), 5.5 nm (related to the minima due to WP quantum scattering), and 39 nm (related to the minima due to WP quantum interference) in (d). For (2) and (3) tips, we use $V_G = 300$ meV, because the red curves (minima) present a large transmission probability for this potential, as we can see in Figs. 4.9 (1) for all four systems investigated.

For all systems investigated here, increasing V_G for the tip in situation (1), *i.e.* closing the path in the central channel, improves the transmission probability when W_c is chosen as one of the minima mentioned above, as one can see by the red curves in any of the panels labelled as (1) of Fig. 4.9. In Fig. 4.9 (a)(1), the minimum of the transmission

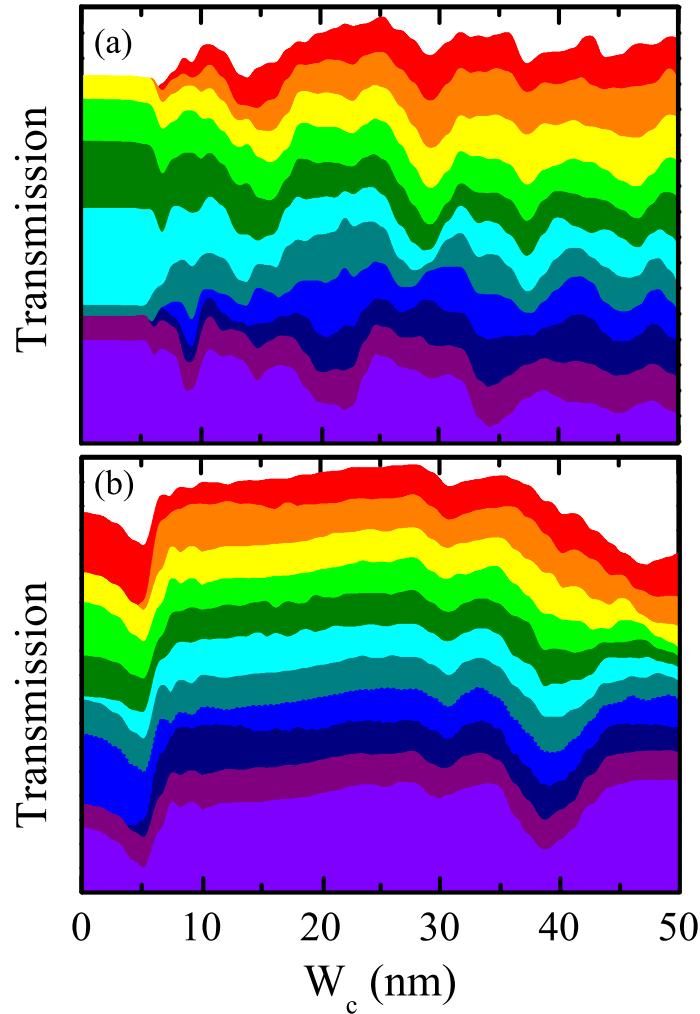


Figure 4.7: Transmission probability as function of the channel width W_c for quantum rings depicted in (a) Fig. 4.1(c) and (b) Fig. 4.1(d), respectively. The kinetic energy used was ε_1 and each color curve represents a transmission probability for a specific magnetic field, ranging from 0 (purple) to 1 T (red).

(red, dotted line) increases as the potential intensity V_G increases, raising from 0.3 at $V_G = 0$ to around 0.6 at $V_G = 100$ meV and 300 meV. On the other hand, for the solid black line, except for the oscillations around $V_G = 250$ and 500 meV, the transmission has no significant changes. This result reflects the fact that when the transmission in system (a) is in its minimum at $W_c = 23$ nm, a larger part of the WP moves through the extra channel, while for $W_c = 10$ nm, the WP has a large part propagating through the upper arm of the ring, therefore, the tip potential in situation (1) cannot affect much the transport in the latter case. Moreover, this result brings even closer resemblance with the Braess paradox: counter intuitively, the presence of the tip potential, which in practice shuts down the extra channel, raises the overall transmission back to the higher value it

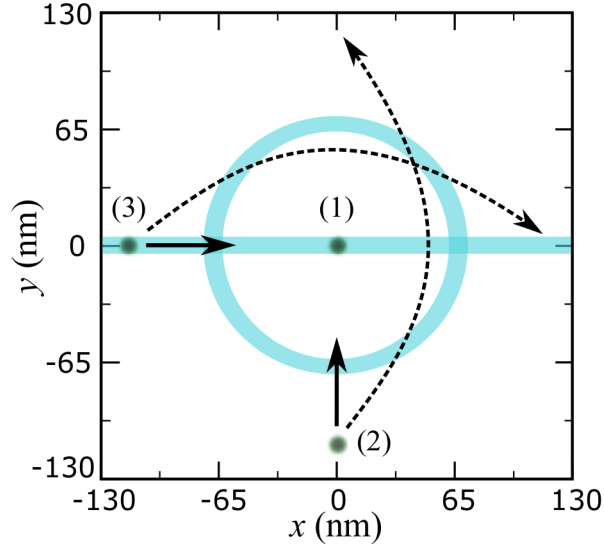


Figure 4.8: Schematic diagram for an AFM tip potential over quantum rings represented by the dots (1), (2) and (3). The solid arrows indicate the direction of the tip displacement, while the dash line arrows indicate the final position of the tip. Tip (1) is fixed in the central region for each system.

had without this channel in the $W_c = 23$ nm (minimum) case. In other words, for this value of channel width, having an extra channel is worse, in terms of conductivity. In Fig. 4.9 (a)(2) a significant change occurs when the tip is over the bottom edge of the channel, at $(x, y) = (0, 0)$: the minimum of the transmission increases from 0.3 to 0.6, while for $W_c = 10$ nm, the transmission decreases from 0.6 to 0.4. Therefore, if $W_c = 10$ nm, shutting the extra channel decreases the transmission, as expected from a classical point of view, and in contrast with the behaviour observed for $W_c = 23$ nm. Notice that as the tip moves up, the transmission probability minimum for $W_c = 23$ nm (red dotted) decreases to 0.3 at the center of the channel and increases back to 0.6 as the tip moves to the upper edge of the channel. This is due to the fact that, for such larger W_c , the wave packet enters the extra channel through its first excited state subband, whose eigenfunction is zero at $y = 0$, which is not the case for $W_c = 10$ nm (black solid). Out of the central channel, even when the tip is over the upper arm, the potential has no significant effects on the minima transmission, since the largest part of the WP propagates through the extra channel for large W_c . In Fig. 4.9(a)(3) when the tip potential is over the input or output leads there is no transmission in the ring. Nevertheless, the transmission minimum increases to 0.6 when the tip potential is over the central channel, in accordance with the results discussed above for Fig. 4.9 (a)(2) and (1).

The time-dependent probability current through the extra channel of the system in Fig. 4.1 (b) is very small, as depicted in Fig. 4.3 (b). Therefore, when the tip potential is over the extra channel in this system, the transmission probability has no significant change, as it can be seen in Fig. 4.9 (b) where the oscillations in the transmission probability exhibit

a rather small amplitude ~ 0.2 in the extra channel region. In Fig. 4.9(b)(3), when the tip is over the extra channel, the transmission presents a small oscillation around $(x, y) = (0, 0)$. The displacement of the tip (2) over the system (c) closes the arm of the squared ring at $y \approx \pm 60$ nm and closes the extra channel at $y \approx 0$ nm. Over the ring arms, the tip potential reduces the transmission probability to 0.2 for the minimum $W_c = 24$ nm, and to 0.4, for the channel width $W_c = 10$ nm, whereas over the extra channel, the tip potential increase the transmission to 0.3 for the minimum and more than 0.1 for $W_c = 10$ nm, when compared to the case where the tip potential is absent in the system. The displacement of the tip (3) closes the extra channel and the ring arms at $x \approx \pm 30$ nm. When the tip is over the extra channel, the minimum transmission increases, while it decreases when the tip is over the ring arms, as was discussed for the tip (2).

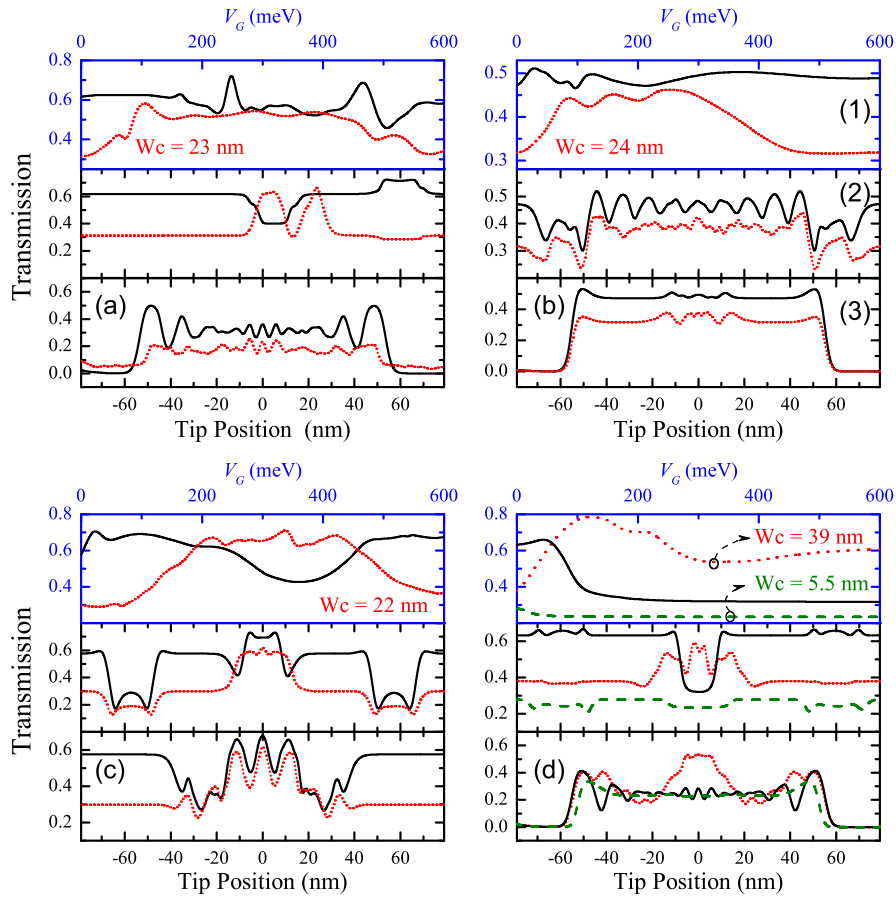


Figure 4.9: Transmission as a function of (1) intensity of the Gaussian potential, (2) and (3) tip position. The order of the figures refer to the form different depicted in Fig. 4.1. The curves width black color are for $W_c = 10$ nm, while the curves width red colors are for the minima of the transmission shown in Fig. 4.2. The WP kinetic energy is ε_1 .

In Fig. 4.9(d) two minima of the transmission probability are investigated: the first

one, red dotted line, is for an extra channel width $W_c = 39$ nm, and the second one, green dashed line, for an extra channel width $W_c = 5$ nm. These minima have their origins in quantum interference and scattering, respectively, as previously discussed. For the minimum coming from interference, the tip potential (1) strongly affects the transmission probability, which changes from ~ 0.4 to ~ 0.8 . On the other hand, for the minimum due to quantum scattering, the tip potential (1) does not significantly change the transmission. For $W_c = 10$ nm, when the tip potential closes the extra channel, it produces interference of the WP that propagate through the ring arms, decreasing the transmission probability. The tip (2) does not affect the transmission when it is moving over the bottom or top ring arms. When the tip potential is over the extra channel, the minima which came from interference increase to 0.2, while for $W_c = 10$ nm, the transmission decreases from ~ 0.6 to ~ 0.3 . Moreover, when closing the extra channel, the tip (3) increases the minimum 0.6 which comes from interference, but it does not affect either the other transmission minimum, which is due to scattering, and or transmission for $W_c = 10$ nm.

Quantum tunneling between bent semiconductor nanowires

Advances in the fabrication and nanostructuring of semiconductor compounds opens up opportunities for combination of different shapes of devices on a nanometric scale [110, 111, 112]. There are numerous experimental methods and techniques of fabricating these semiconductor nanostructures, such as self-organized growth in a MBE chamber [113, 114, 115], split-gate technique used to fabricate narrow quantum channels for electrons [116], and AFM lithography, which can be used to create different nanostructures. [55, 117] On a nanometric scale, transport properties of one-dimensional structures are of great interest and a large number of novel phenomena have been predicted and observed in recent years. [118, 119] Here, we shall mention for example investigations on the transport properties through confined states in a 1D wire were performed by Auslaender *et al.* [120] Tserkovnyak *et al.* [121] gave a detailed experimental investigation and theoretical explanation of a set of interference patterns in the nonlinear tunneling conductance between two parallel wires that were first reported by Auslaender in 2002. [122]

From a theoretical point of view, the attempt to model increasingly smaller semiconductor systems that is driven by the miniaturization of technological devices has led to more systematic studies with the aim to describe in more detail the different physical effects, such as tunneling in transistor gate oxides [123, 124] and energy quantization in nanometer scale MOSFETs. [125, 126] In addition, different systems used to calculate the scattering probabilities per unit of time under the effect of perturbative potentials have been proposed and investigated. Some cases of interest here are those when adding an extra path in the system [64], an effective potential simulating a Scanning Gate Microscopy tip [109, 127] as well as the effect of a smooth potential in path's connections. [53]

In this chapter, we investigate the wave packet scattering in two L-shaped quantum wires (QW) separated by a distance W_2 , see Fig. 5.1. The aim is to find the minimum separation distance between two bent wires with acceptable values for tunneling. For this purpose, we inject a Gaussian wave packet in the left-lead and calculate the transmission into the bottom lead and the tunnelling into the second wire. Our theoretical model is

based on the solution of the time dependent Schrödinger equation within the effective mass approach using the split-operator technique. [53, 128] We consider different values of the wave packet kinetic energy and W_2 distances between the quantum wires as well as different width values for the second wire L . We then analyse how the conductivity depends on these parameters (W_2 and L).

5.1 Theoretical model

Our model describes electrons in the (x, y) plane moving from left to right in a region with a L-shaped wire (see left side of Fig. 5.1). The effective-mass approximation was considered and all electrons are confined by a step like potential, i.e., $V(x, y) = 0$ inside the QW and $V(x, y) = V_0$ otherwise. Abrupt interfaces between the confinement region and the potential barrier are assumed. Similarly, in the right side of our set up, another L-shaped QW is considered. The left QW is assumed to have fixed width $W_1 = 10$ nm, whereas for right QW, three different widths L ($= W_1/2, W_1$ and $2W_1$). The smooth edges of the QWs are draw by circles of radius $R_W = W_1/2$ and $R_L = L/2$ for the left and right wire, respectively, in order to approach more realistic systems. The left side is separated from the right by a distance W_2 which ranges from 0 nm to 4.8 nm in this work. In the transverse cross section, the QW behaves as a quasi-one-dimensional channel where an electron confined in this region has a subband energy

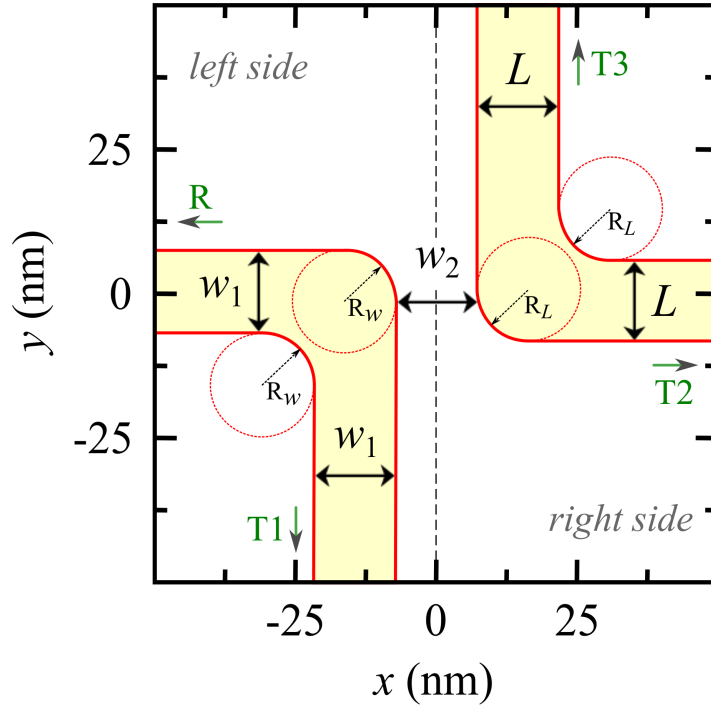


Figure 5.1: Potential profile scheme for the QWs studied in this work. The two QWs are separated from each other by a distance W_2 , ranging from 0 to 4.8 nm. The smooth connections between vertical and horizontal wire are described by circles of radius $R_W = W_1/2$ and $R_L = L/2$.

$$E_n(k_x) = E_n^{(y)} + \frac{\hbar^2 k_x^2}{2m_e}, \quad (5.1)$$

where $E_n^{(y)}$ are the y components of the eigenvalues which were obtained numerically for a potential of $V_0 = 600$ meV. These eigenvalues are lower than the corresponding

eigenvalues calculated for an infinite potential, $E_n^{(y)} = n^2\pi^2\hbar^2/2m_eW_1^2$, although this analytical expression can be used for an estimate of energies in a quantum well of W_1 width. A combination of a Gaussian function with a plane wave is injected from the left to the right along the x direction, so that at $t = 0$ the wave packet is given by

$$\Psi(x, y) = \exp \left[ik_0x - \frac{(x - x_0)^2}{2\sigma_x^2} \right] \phi_0(y). \quad (5.2)$$

Here, $k_0 = \sqrt{2m_e\epsilon}/\hbar$ is a wave vector corresponding to the kinetic energy ϵ , and $\phi_0(y)$ is the ground state wave function of the quantum well in the y direction. The width of the wave packet in the x direction is fixed by σ . The time evolution of the wave packet is studied with the split-operator technique, which allows to separate the kinetic terms for each direction. This separation is important for systems with many degrees of freedom. We follow the approach of Refs. [53] and [128], the details of which will not be reproduced here.

The (x, y) -plane is discretized by a squared grid $\Delta x = \Delta y = 0.4$ nm, and the finite difference scheme is used to solve the derivatives in the kinetic energy terms of the Hamiltonian. To avoid spurious reflection when the wave packet reaches the edges of our set up, we applied an imaginary potential, as discussed in Ref. [53] and suggested by Manolopoulos. [89] The current of the system is given by

$$\mathbf{J} = -\frac{i\hbar}{2m_e} (\Psi^*\nabla\Psi - \Psi\nabla\Psi^*). \quad (5.3)$$

The transmission T probabilities are calculated in three different positions at vertical (T_1 and T_3) and horizontal (T_2) axis, as shown in Fig. 5.1. For horizontal axis we fixed a point x_r , localized in the right side and the transmission T_2 is calculated as

$$T = \int_0^\infty dt \int_{-\infty}^\infty dy J_x(x_r, y, t). \quad (5.4)$$

For vertical axis we fixed a point y_B in the bottom wire and a point y_T in the top wire and calculated the transmission T_1 and T_3 through Eq. (5.4), changing $J_x(x_r, y, t)$ for $J_y(x, y_T, t)$ and $J_y(x, y_B, t)$, respectively, and the above spatial integral is now evaluated along x -direction. The reflection probability R is calculated in the left side by fixing a point x_l in the left side and evaluating the integrals in dt and dy . More precisely

$$R = -\int_0^\infty dt \int_{-\infty}^\infty dy J_x(x_l, y, t), \quad (5.5)$$

where J_x is the x component of the probability current.

In order to investigate the scattering of an electron into different subbands of the wires, we project the wave function on the j th eigenstate of the quantum well at a fixed point x_i , using the relation

$$P_j(x_i, t) = |\langle \Psi | \phi_j \rangle|^2 = \left| \int_{-\infty}^{+\infty} dy \Psi(x_i, y, t) \phi_j(y) \right|^2. \quad (5.6)$$

Eq. (5.6) is the probability density of finding an electron in the j th subband at position x_i per length in the x direction. Moreover, the contribution of each subband state to the probability current can be calculated by

$$j_x^{(j)}(x, t) = \frac{\hbar}{2m_e i} \left(\bar{P}_j^* \frac{\partial}{\partial x} \bar{P}_j - \bar{P}_j \frac{\partial}{\partial x} \bar{P}_j^* \right), \quad (5.7)$$

where $\bar{P}_j(x, t) = \langle \phi_j | \Psi \rangle$ gives the time-dependent wave function within the j th subband. Notice that, since $\bar{P}_j(x, t)$ is not normalized, its value can be larger than one. Finally, the time-dependent probability current at x_i is given by

$$J_t(x_i, t) = \int_{-\infty}^{+\infty} J_x(x_i, y, t) dy. \quad (5.8)$$

Solution of Eqs. (5.6-5.8) form the basis to understand the conductivity and the trajectory of the wave packet through the wires.

5.2 Transport properties

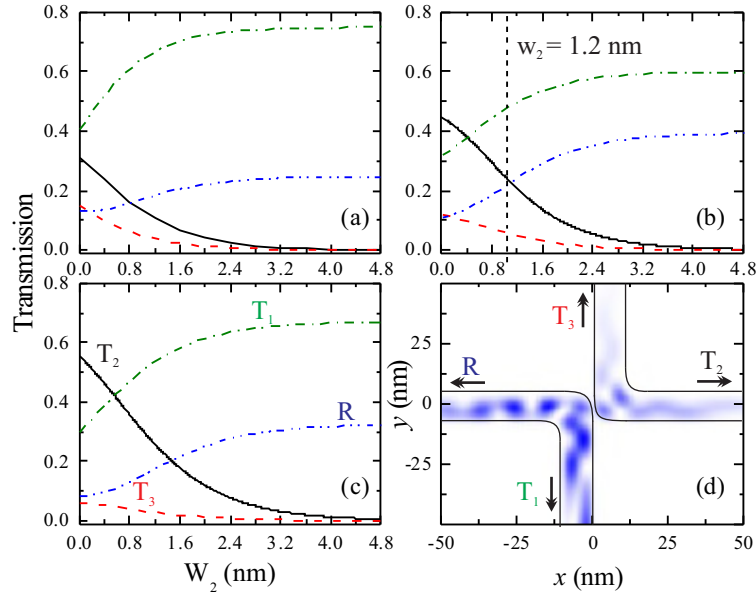


Figure 5.2: (a)-(c) Wave packet transmissions (T) and reflexion (R) probabilities as function of W_2 for a well width of $L = W_1$. The transmissions are calculated in three different points in the QWs: bottom T_1 (green, dash dot line), top T_3 (red, dash line) right T_2 (black, solid line), while the reflexion R (blue, dash dot dot line) is calculated at the left side, as shown in (d). The wave packet energies used are (a) ε_1 , (b) ε_2 and (c) ε_3 . (d) Snapshot of the wave function calculated at $t = 160$ fs for $L = W_1$ and $W_2 = 1.2$ nm as depicted by the vertical dash line in (b).

For all cases considered in this work, we consider material parameters for InGaAs (wire) and GaAs (barrier material), in which the conduction band of the InGaAs/GaAs heterostructure has a band-offset of 600 meV. Moreover, for InGaAs the electron effective mass is $m_e = 0.041 m_0$. [108] The wave packets are injected from left to right at $t = 0$, in the lowest subband $\phi_{n=1}(y)$. Three different values of the kinetic energy of the wave packets are considered: $\varepsilon_1 = 70$ meV, $\varepsilon_2 = 140$ meV and $\varepsilon_3 = 200$ meV.

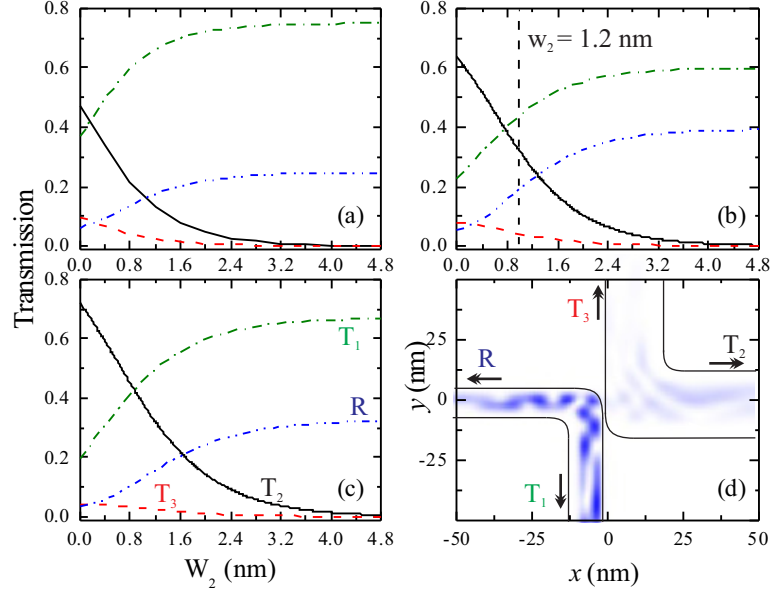


Figure 5.3: The same result as shows in Fig. 5.2, but now for $L = 2W_1$.

Transmission and reflection probabilities obtained with our method are presented in Fig. 5.2 and Fig. 5.3 as function of the distance W_2 for $L = W_1$ and $L = 2W_1$, respectively. The transmission probabilities are calculated on the left-bottom wire T_1 (green, dash dot line), right-output wire T_2 (black, solid line) and right-top wire T_3 (red, dash line). The reflection R (blue, dash dot dot line) is calculated on the input left-wire. We checked numerically that the sum $R + \sum T_i = 1$ is satisfied up to a maximum error of 0.1 %. Figs. 5.2(d) and 5.3(d) are snapshots of the wave function with kinetic energy 70 meV, calculated at $t = 160$ fs for $W_2 = 1.2$ nm, as indicated by the vertical dashed-gray line in Fig. 5.2(b) and Fig. 5.3(b), respectively. For a wave packet with kinetic energy ε_1 (Figs. 5.2(a) and 5.3(a)) the transmission coefficient T_2 decreases faster than the one with kinetic energy ε_3 , (Figs. 5.2(c) and 5.3 (c)), i.e., the tunnelling through the barrier W_2 is in general larger for higher kinetic energy. Furthermore, the transmission T_2 decreases towards zero with increasing width W_2 , and as a consequence, the transmission T_1 and reflection R increase such that $T_1 + R \simeq 1$ for wide W_2 . The tunnelling T_3 through the top-right side is less than 10%, but nonzero even for high kinetic energy of the wave packet and for different W_2 distance. This behavior is shown in Figs. 5.2 and 5.3 by dashed red lines for $L = W_1$ and $L = 2W_1$, respectively, and occurs because the quantum wire shape

spreads the wave function around the position $x = 0$, specially for $W_2 = 0$, where the transmission is about 70 % through T_1 and the other 30 % are reflected R or tunnel through T_2 and T_3 , as shown in Fig. 5.3(c). The transmission probability T_2 in Figs. 5.2 and 5.3 is perfectly fitted by an exponential function $f(W_2) = A_0 \exp(-W_2/\tau) - A_1$, where τ , A_0 and A_1 are fitting parameters given in Table 5.1.

Table 5.1: - Exponential fitting to transmission probabilities T_2 shown in Figs. 5.2 and 5.3, for different energies ϵ and widths of the second wire L .

ϵ	$L = 10$ nm			$L = 20$ nm		
	A_0	A_1	τ	A_0	A_1	τ
ϵ_1	0.33	11.46	0.01	0.49	9.89	0.01
ϵ_2	0.512	15.108	0.035	0.70	13.32	0.03
ϵ_3	0.620	15.384	0.038	0.80	14.65	0.04

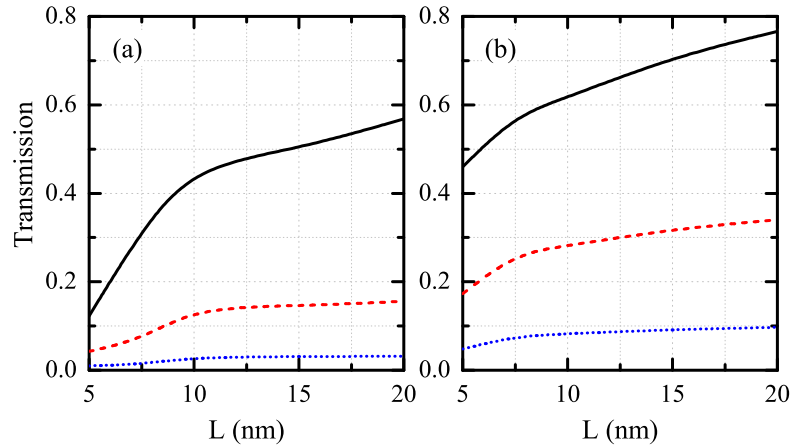


Figure 5.4: Transmission coefficient ($T_2 + T_3$) as function of the well width L , for wave packet energies (a) ϵ_1 and (b) ϵ_3 . Three W_2 distance were considered: 0 nm (black, solid line), 1.2 nm (red, dash line) and 2.4 nm (blue, dotted line).

In order to clarify the role of the well width L in the output lead on the transmission probabilities in Fig. 5.4 we display the transmission coefficient on the right side ($T_2 + T_3$) as function of L for two different wave packet kinetic energies ϵ_1 (a) and ϵ_3 (b). Three different W_2 distances were considered namely, 0 nm (black, solid line), 1.2 nm (red, dash line) and 2.4 (blue, dotted line). The transmission increase with increasing L which is a consequence of the lowering of the subband energy states in the right side over which the tunnelled wave function can be distributed. For a lower wave packet kinetic energy ϵ_1 the

transmission stays below 20 % for W_2 distance above 1.2 nm, and for ε_3 the transmission keep below 40 %.

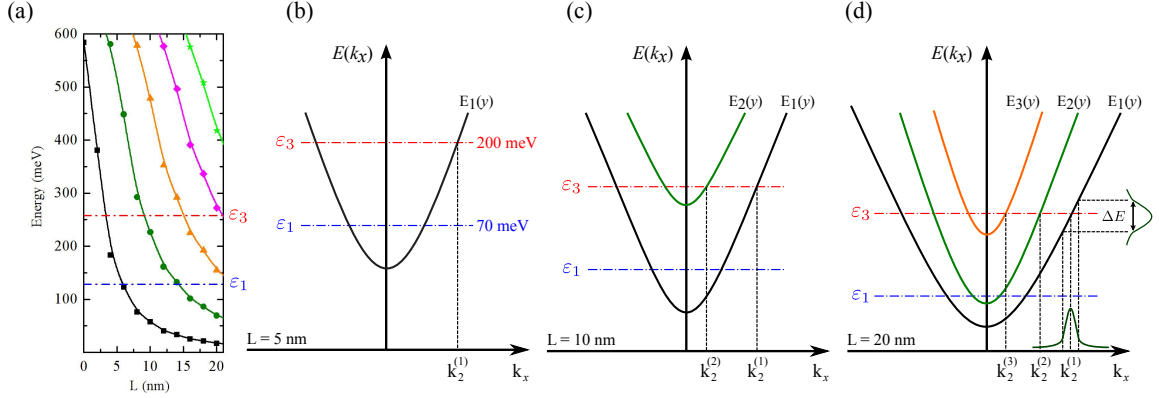


Figure 5.5: (a) Bottom energy of the different subbands as function of the quantum well width L . Schematic diagrams that represents the subband energies as function of the wave vector k_x in the x direction, for output width of (b) $L = 5$ nm, (c) $L = 10$ nm, and (d) $L = 20$ nm. The horizontal dashed-dot lines represents the average energy of the wave packet, ε_1 and ε_3 .

Let us now discuss the contribution of each subband of the output lead to its overall current. In order to have a better understanding of this problem, we display in Fig. 5.5(a) the eigenenergies of the output lead as a function of its width. The average wave vector k_x^i of the wave packet is schematically shown in Figs. 5.5(b) for $L = W_1/2$, 5.5(c) for $L = W_1$, and in 5.5(d) for $L = 2W_1$. Here, the highest kinetic energy was chosen to cover the first three subbands in the output lead, where the bottom of the subband is found to be around ε_3 , for an output width of $L = 2W_1$. This kinetic energy allows us to calculate the influence of the subbands on the scattering of the wave packet. The number of k_x values allowed for each kinetic energy ε , at each subband, depends on the width L , which in the case illustrated in Fig. 5.5 (b) is $k_2^{(1)}$ when $L = W_1/2$. However, it take values $k_2^{(1)}$, $k_2^{(2)}$, and $k_2^{(3)}$ for ε_2 with $L = 2W_1$ (see Fig. 5.5(d)). As for our Gaussian wave packet, the initial wave functions with distributions of k_x 's around $k_x^{(i)}$, that yields an energy distribution ΔE as illustrated in Figs. 5.5(d). More details regarding the initial wave package width in k_x -space can be obtained by Fourier transform and this is explained in details in Ref. [53]. In the case proposed here, where the wave function is also Gaussian in reciprocal space, it is possible to determine the energy distribution of the wave packet as $\Delta E = \hbar^2 \Delta k / m_e k_0$, where $\Delta k = 2\sqrt{\ln 2} / \sigma_x$ is the full width at half maximum (FWHM).[53]

In Fig. 5.6 we show the projection of the time-dependent wave packet on the ground (P_1), first-excited (P_2), and second-excited state subband (P_3) of the right-lead. The projections are calculated numerically as function of W_2 at the point $x = 158$ nm in the right side, for output widths $L = W_1$ (a) and $L = 2W_1$ the (b). The results are shown for wave packet kinetic energies of ε_1 (black, solid line), ε_2 (red, dash line) and ε_3 (blue,

dotted line). Initially the wave packet propagates in the lowest subband. As expected, all projections decrease towards zero as W_2 increases, since the overall current also exhibits this decreasing behavior. For narrow wells, the packets with kinetic energies ε_2 and ε_3 scatter to the first excited state, while for energy ε_1 this projection is almost zero for any W_2 value. The projection for the second excited state is only possible for wave packets with an energy of ε_3 , as shown in Fig. 5.5(c). For quantum wells with $L = 2W_1$, the subbands energies get closer to each other such that the wave packet scatter to excited states even for energy ε_1 , Fig. 5.6(b).

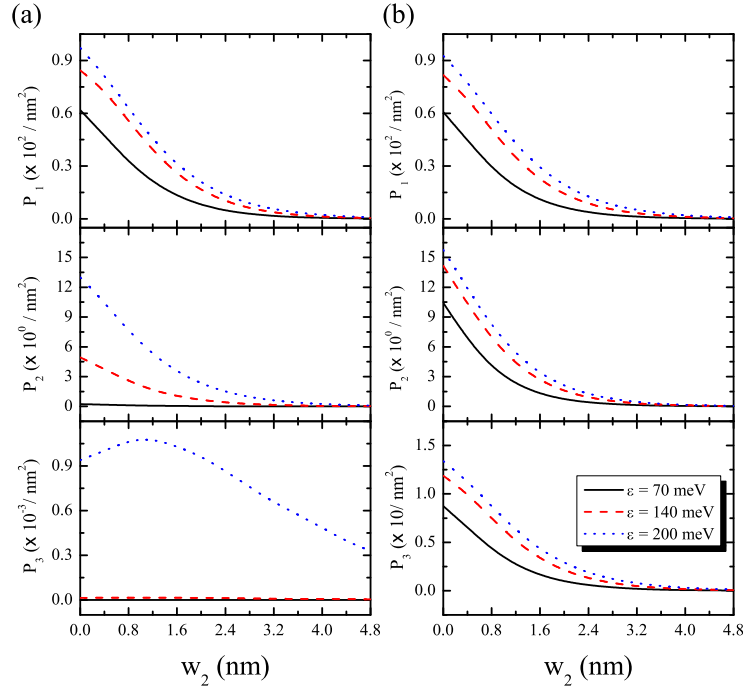


Figure 5.6: Projection of the wave function on the ground state P_1 , first-excited P_2 and second-excited subbands P_3 integrated in time, for the output width $L = W_1$, panels column (a) and $L = 2W_1$, panels column (b), as function of the distance W_2 calculated at position 158 nm in the right-lead.

An analysis of the time-dependent current probability for the wave packet as a function of time is illustrated in Fig. 5.7. The wave packet propagates in the lowest subband from the left to the right side with kinetic energy given by ε_1 (blue, dotted line), ε_2 (red, dash line) and ε_3 (black, solid line). Around $y = 0$ and along the x -axis, the potential is similar to a simple quantum barrier with height of 600 meV. Calculated at $x = 158$ nm across the potential barrier, the time-dependent current probability is a tunnelling current that can give an estimate about the leakage current through the barrier. In Fig. 5.7 we plot the tunnelling current probabilities for two different W_2 distances: (a) $W_2 = 0$ nm and (b) 2.4 nm. For each W_2 distance we consider three different output widths L , from top to bottom $L = W_1/2$ in the first row, $L = W_1$ in the second, and $L = 2W_1$ in the third row. Clearly, the peak in the probability current is lower at low energies, and it also

decreases (increases) with increasing distance (width) W_2 (L). Particularly, in the case of $L = W_1$, Fig. 5.7 emphasizes the oscillatory behaviour of the probability current for the two distances W_2 used in our calculations. This probability current oscillation is due to wave function scattering in the central region of the wires, as illustrated in Figs. 5.2 and 5.3 (d). It is easy to see that the current peak occurs faster as the energy increases, as a consequence of the higher Fermi velocity in this case. Besides, increasing L for fixed W_2 slightly shift the peaks to lower times, which is due to the fact that larger widths lead to lower subband energies and consequently, higher momentum for fixed wave packet energy.

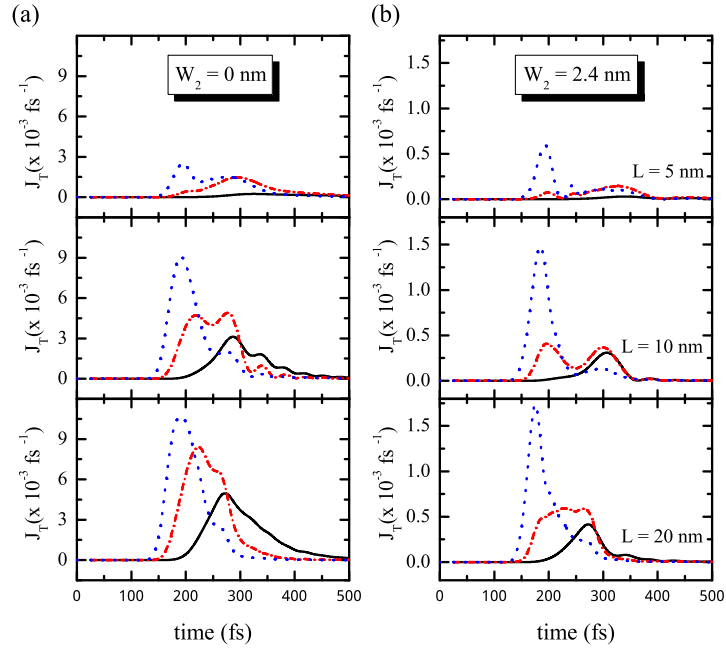


Figure 5.7: The total time-dependent probability current for wave packet energy of ε_1 (black, solid line), ε_2 (red, dash line) and ε_3 (blue, dotted line). Results for different distances W_2 are plotted in column (a) $W_2 = 0$ nm, and column (b) $W_2 = 2.4$ nm. The output width L is in the first row $L = W_1/2$, second row $L = W_1$, and third row $L = 2W_1$.

Finally, from a practical point of view, it is important to investigate the behaviour of the conductance for different values of the kinetic energy, W_2 distance and output width L . With this in mind, we express the conductance as a particular case of the multiband Landauer formalism [129, 130]

$$G(x_t, y_t) = \frac{2e^2}{h} \sum_n T_n(x_t, y_t), \quad (5.9)$$

where the output lead index l is 1, 2 or 3 for conductance calculated with T_1 , T_2 and T_3 , respectively, and the index n account for different occupied subbands in the input lead. The quantum conductance ($G_0 = 2e^2/h$) is used here as unit of electrical conductance, and the transmission coefficients $T_{(x_t, y_t)}^{(n)}(\varepsilon)$ are calculate by setting the wave packet at the

initial time in a given subband n , with average energy ε , and integrating the probability current at the axis defined by (x_t, y_t) , as in Eq. (5.4).

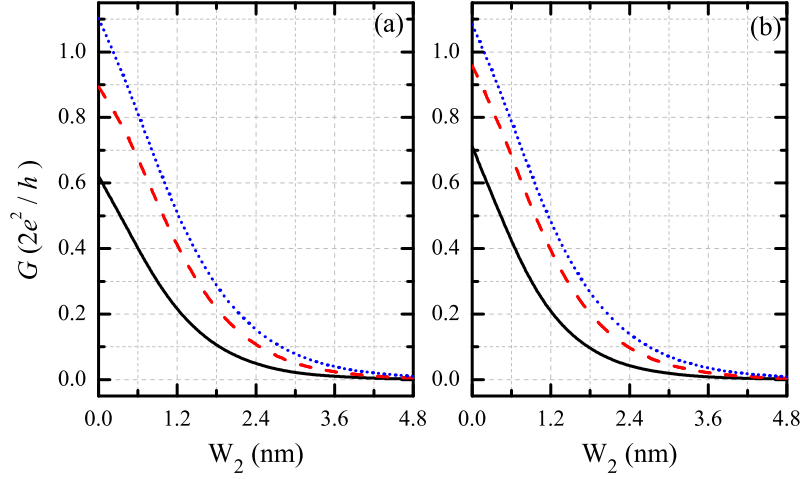


Figure 5.8: Conductance in the output quantum wire as a function of the distance W_2 . Wavepacket energy is ε_1 (black, solid lines), ε_2 (red, dashed lines) and ε_3 (blue, dotted lines) for quantum well L width of (a) 10 nm and (b) 20 nm.

Figure 5.8 displays the conductance versus the distance W_2 calculated for three wave packet kinetic energies ε_1 (solid black), ε_2 (dashed red) and ε_3 (dotted blue). The conductance was computed by taking into account the transmission probability of the first three subbands for the T_2 coefficient at $x = 158$ nm on the output lead, with output width $L = W_1$ in Fig. 5.8(a) and $L = 2W_1$ in Fig. 5.8(b). The conductance depends strongly on the distance W_2 . We observe that when the distance W_2 increases the transmission probability decreases, hence decreasing the conductance in the output region. The wave packet scattering is larger for the case where $L = W_1$, resulting in a larger reflection probability, as can be seen in Figs. 5.2 and 5.3, which explains why G is higher in 5.8(b), as compared to Fig. 5.8(a). Also, the conductance changes with the kinetic energy of the wave function even for $W_2 = 0$ nm, as observed in Fig. 5.8(a), as a consequence of quantum scattering at the junction between the wires.

All results presented so far were made for fixed wave packet average energies $\varepsilon = \varepsilon_1$, ε_2 or ε_3 . It is important to discuss how these results relate to possible future experiments aiming to verify the quantum tunnelling effects investigated here. In fact, at temperature $T = 0$ K, Landauer formula for conductance is exactly given by Eq. (5.9), but with transmission probabilities calculated for a plane wave with energy ε_3 . For non-zero temperature, however, the transmission probability must be multiplied by the derivative of the Fermi's energy distribution and then integrated in energy, so that there will be

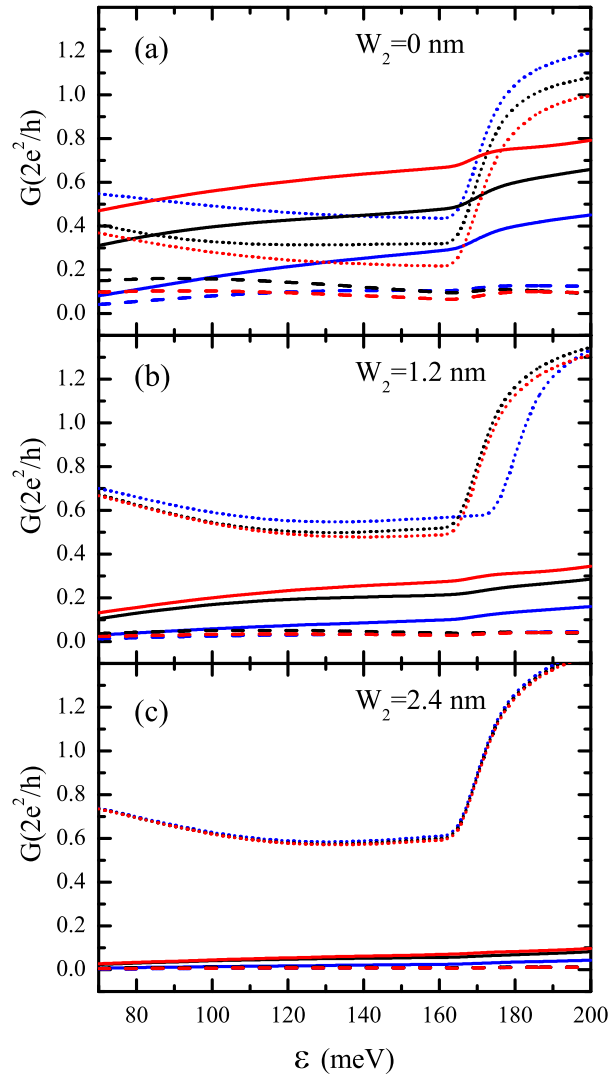


Figure 5.9: (Color online) Conductance of the quantum wire as a function of kinetic energy wave packet for the three possible output leads G_1 (dotted), G_2 (solid) and G_3 (dashed), with well widths $L = 5$ nm (blue), $L = 10$ nm (black) and $L = 20$ nm (red). The W_2 distance is given by (a) 0 nm, (b) 1.2 nm and (c) 2.4 nm.

a temperature dependent range of energies around the Fermi level that effectively contribute to the overall conduction. Notice that in our calculations, since we do not consider plane waves, results are never for a single ε_3 and, consequently, they do not describe a zero-temperature situation. Actually, the Gaussian wave packet considered here yields a Gaussian distribution of momenta or, equivalently, a combination of plane waves with different energies. Therefore, in a sense, our results for conductance are closely related to those for non-zero temperature, where the width of the Gaussian wave packet in reciprocal space is related to the width of the energy distribution and, consequently, plays the role of the temperature. Finding the exact relation between temperature and the wave packet width is, however, a difficult task, which is left for future works, whereas here we restrict ourselves to a more qualitative discussion of this matter.

Having stated that, we now use our method to calculate the steps in conductance as a function of the electron energy, as expected for a quantum channel such as the one considered here. These steps cannot be sharp, since we are dealing with a non-zero temperature simulation. This is shown in Fig. 5.9 for energies ranging from ε_1 to ε_3 , for three different W_2 width: (a) 0 nm, (b) 1.2 nm, and (c) 2.4 nm. The conductance is calculated between the input lead and the three possible output leads, namely, with T_1 (dotted), T_2 (solid) and T_3 (dashed). Well widths are $L = 5$ nm (blue), 10 nm (black), and 20 nm (red). Conductance to the upper lead G_3 (dashed) is always close to zero and reaches, at most, ≈ 0.15 for $W_2 = 0$, as expected from the low transmission probabilities for this lead observed in previous results in Figs. 5.2 and 5.3. Notice that for the widest L width, three subbands are involved in the output lead for a wave packet kinetic energy around ε_3 , as shown in Fig. 5.5 (d). On the other hand, for narrow widths, one subband is involved for $L = 5$ nm, Fig. 5.5 (b), and two subbands are involved for $L = 10$ nm, Fig. 5.5 (c). For this reason, the conductances G_2 in Fig. 5.9 (a) and (b) are clearly spaced for different values of L . Since G_2 is directly related to the current leak, it is responsible for reducing the conductance through the original channel G_1 . For lower values of energy ϵ , conductance G_1 is reduced as the energy increases, due to the increasing current leakage G_2 . This effect is reduced either as the distance between wires increases or as the second wire width L is made narrower, thus hindering the quantum tunnelling between wires. Furthermore, the differences between conductance G_1 (dotted) for different values of L become negligible as the W_2 distance becomes too large, see Fig. 5.9 (c). The quantized steps of conductance are also observed in the leakage current G_2 , but much lower than those for G_1 , which suggests that states in the first excited subband of the input lead have lower contribution for the leakage current as compared to those coming from the first subband.

Dielectric mismatch and shallow donor impurities in GaN/HfO₂ quantum wells

When an impurity is introduced into a low dimensional structure, such as quantum wells (QW), nano wires (NW) and quantum dots (QD) the calculation of the electronic properties in this structures becomes considerably more complex if compared to that of a doped three-dimensional crystal [131, 132, 133, 134, 135, 136]. This occurs because of the restricted movement in the structure growth direction, which is imposed by the potential due to band edges discontinuities ΔE . First, the binding energy of the carrier-impurity in the structure depends on the confinement potential ΔE , and second, both the binding energy and wave function of the carrier and impurity depends on the impurity position in the structure growth direction. On the other hand, due to recent progress in epitaxial crystal growth techniques, such as molecular beam epitaxy (MBE), research focusing on impurity and electronic states in nano-structures has attracted great attention [137, 138]. However, effects caused by image charges due to the dielectric mismatch at the structure interface have been overlooked. Indeed, donor binding energy can be significantly modified by additional confinement effects that image charges distribution produce [139, 140]. Thus, recent research focusing on high-k dielectrics based QWs and NWs reveals interesting results related to carrier confinement [17, 141, 142, 143]. We recently demonstrate that the interaction between carriers and their image charge, induced by the dielectric mismatch ($\epsilon_r = \epsilon_{\text{GaN}}/\epsilon_{\text{HfO}_2} = 9.5 / 25 = 0.38$), strongly modifies the electronic structure in GaN/HfO₂ QWs (and NWs) and for wide QWs (wide radii NWs) heavy holes are confined in interfacial regions, similar to that observed in type-II heterostructures [17, 143]. Such interfacial confinement leads to drastic modification on the electronic properties of the QWs and NWs. Particularly, for NWs under an applied magnetic field, where angular momentum transitions occur in the ground state due to the Aharonov-Bohm effect [143]. A decrease in the oscillator strength of electron-hole pairs in $\epsilon_r < 1$ QWs and NWs is also predicted for wide QW and larger wire radii, which directly affects their recombination rates [17, 143].

In this chapter, we investigate electron-impurity binding energy in GaN/HfO₂ Qws.

As for illustration we compared this results with those of a more typical AlN/GaN system. The presence of a point charge in a region where the dielectric constant is discontinuous induces polarization charges at the QW interfaces, and this problem can be solved by the image charges method [144]. As shown here, The electron energy, electron wave function and the electron-impurity binding energy can change significantly due to additional confinement effects produced by the image charge distribution. Our calculation considers simultaneously all energy contributions caused by the dielectric mismatch: (i) image self-energy (interaction between electron and its image charges), (ii) the direct Coulomb interaction between electron and the actual impurity, as well as (iii) the interactions among electron and impurity image charges. Moreover, from practical means, we also investigate Stark effect and electron-impurity binding energy for two different confinement regimes: narrow (5 nm) and wide (10 nm) QWs. When compared to the effective Bohr's radius for the GaN bulk a_B^* ($= a_B \varepsilon_{\text{GaN}} / m_e^* = 2.65$ nm; where $a_B = 0.53$ is the Bohr's radius) narrow and wide QWs used in this work are twice and four times the effective Bohr's radius, respectively. The binding energy of an electron bound to a hydrogenic impurity is obtained as function of the impurity position, by solving a fully three-dimensional time dependent Schrödinger equation using a method with neither adjustable parameters nor restrictive basis expansions as employed by almost all theoretical approaches in the literature [104, 105, 145]. For simplicity, we address zinc blende GaN instead of its wurtzite crystalline structure in order to avoid more complicated polarizations effects observed in this phase [146].

6.1 Theoretical Model

1. Time-dependent Schrödinger equation

The theoretical method used to calculate the binding energy of an electron bound to a hydrogenic impurity is based on the adiabatic approximation. The time-dependent Schrödinger equation [53, 128, 147, 148] is consistent with the effective mass approach and the envelope function formalism

$$i\hbar \frac{\partial}{\partial t} \psi(r, t) = H \psi(r, t), \quad (6.1)$$

and describes the quantized states of a single particle coupled to a quantum well under the effect of impurity Coulomb potential and potential due to image charges. The Hamiltonian H is given by

$$H = \frac{1}{2} P \frac{1}{m^*(r)} P + V(r), \quad (6.2)$$

where $P = -i\hbar \nabla$ is the kinetic energy operator and $V(r)$ is the potential energy operator. The initial solution $\Psi(r, t)$ given by the method is

$$\Psi(r, t) = \exp \left(-\frac{i}{\hbar} \int_0^t H dt \right) \Psi(r, 0). \quad (6.3)$$

The Hamiltonian of Equation (6.2) does not depend on time, so the integral in Equation (6.3), solved in the range between t and $t + \Delta t$ is given by

$$\Psi(r, t + \Delta t) = \exp \left(-\frac{i}{\hbar} H \Delta t \right) \Psi(r, t), \quad (6.4)$$

which is approximated by the expression

$$\begin{aligned} \Psi(r, t + \Delta t) &= \exp[-iV(r) \Delta t / 2\hbar] \\ &\quad \times \exp[-ip^2 \Delta t / 2\hbar m^*] \\ &\quad \times \exp[-iV(r) \Delta t / 2\hbar] + O(\Delta t^3). \end{aligned} \quad (6.5)$$

The error introduced in this expression, when we drop the term $O(\Delta t^3)$, results from the noncommutability of the kinetic and potential operators. The potential operator $V(r)$, with $r = (\rho_e, z_e, z_{im})$ and $\rho = \sqrt{x^2 + y^2}$, is given by

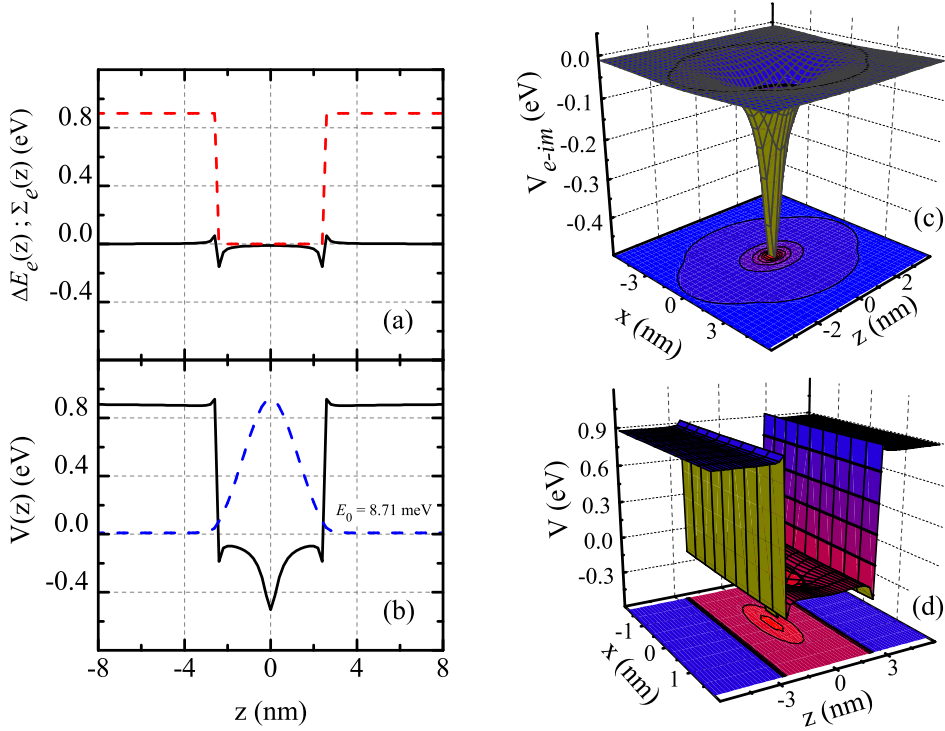


Figure 6.1: (a) Energy potential $\Delta E_e(z_e)$ due to conduction band edge discontinuity (red dashed line) and the potential $\Sigma_e(z_e)$ due to self-energy corrections (black solid line). (b) Total potential $V(r) = \Delta E_e(z_e) + \Sigma_e(z_e) + V_{e-im}(r)$ in the z direction (black solid line) and electron ground state wave function (blue dashed line). (c) Coulomb potential $V_{e-im}(r)$ of electron-impurity interaction in 3D plot. (d) Total potential $V(r)$ in 3D plot.

$$V(r) = \Delta E_e(z_e) + \Sigma_e(z_e) + V_{e-im}(r), \quad (6.6)$$

where $\Delta E_e(z_e)$ is the heterostructure band edge confinement, $\Sigma_e(z_e)$ is the self-energy potential and $V_{e-im}(r)$ is the direct electron-impurity Coulomb interaction. The last term includes direct electron-impurity Coulomb interaction and the interactions between electron and impurity image charges. This contribution to the total potential was deduced from solutions of the Poisson equation in 2D quantum structures, as shown in Eqs. (A21)-(A25) of Reference [149]. Fig. 6.1 shows each potential given by Equation (6.6), for a 5 nm QW: Fig. 6.1(a) shows the potential due to band edges confinement $\Delta E_e(z_e)$ (red dashed line) and the self-energy potential $\Sigma_e(z_e)$ (black solid line), which is attractive (repulsive) for charge on the low (high) dielectric constant side ($\varepsilon_{\text{GaN}} < \varepsilon_{\text{HfO}_2}$). The attractive potential on the well region produce cusps that appears near the edges of the interface transition layers, shown in the total potential depicted in Fig. 6.1(b). For the purpose of our analyses, we plot in Fig. 6.1(c) and 6.1(d) the potential $V_{e-im}(r)$, due to direct electron-impurity Coulomb interaction, and the total potential $V(r)$ in a three-dimensional space, respectively.

The eigenstates of the Hamiltonian are calculated by using a propagation scheme in the imaginary time domain. [148] Any wave function can be written as a linear combination of the eigenstates of a Hamiltonian, since it forms a complete orthogonal basis

$$|\Psi\rangle_t = \sum_{n=0}^{\infty} a_n e^{-\frac{iE_n t}{\hbar}} |\varphi_n\rangle, \quad (6.7)$$

where φ_n and E_n are the eigenfunction and eigenenergy of the n th eigenstate, respectively. Using $\tau = it$,

$$\begin{aligned} |\Psi\rangle_t &= \sum_{n=0}^{\infty} a_n e^{-\frac{E_n \tau}{\hbar}} |\varphi_n\rangle \\ &= e^{-\frac{E_0 \tau}{\hbar}} \left[a_0 |\varphi_0\rangle + \sum_{n=1}^{\infty} a_n e^{-\frac{(E_n - E_0) \tau}{\hbar}} |\varphi_n\rangle \right]. \end{aligned} \quad (6.8)$$

After several imaginary-time steps of propagation ($\tau \rightarrow \infty$), the term of the ground state, $e^{-\frac{E_0 \tau}{\hbar}} a_0 |\varphi_0\rangle$, becomes strongly dominant over the terms of the sum, since $E_n - E_0 > 0$ for $n > 0$. Therefore, starting with any wave function, this function should converge to the ground state of the system as τ increases. We can consider as a very long time those in which $\tau \gg \hbar / (E_n - E_0)$. The excited states are obtained adding to the algorithm the Gram-Schmidt orthonormalization method which will assure orthonormality between all states in each time step.

2. Self-energy potential

In order to calculate the effects of the self-energy potential $\Sigma_e(z_e)$, shown in Fig. 6.1(a) (black solid line), on the electron energy we use the method based on image charges. The electrostatic potential due to a charge Q located at $r = (0, 0, z_0)$, in a medium where the dielectric constant $\varepsilon(z)$ depends on the position is given by

$$\nabla \cdot [\varepsilon(z) \nabla \phi(r)] = -Q \delta(r - r_0). \quad (6.9)$$

The solution in cylindrical coordinates is independent of the azimuth angle (see detail in References [17, 144]). In this case, we can write $\phi(r)$ in the general series as

$$\phi(r) = \int_0^{\infty} q J_0(qR) A_q(z) dq, \quad (6.10)$$

where $J_0(qR)$ is the Bessel function of the zeroth order, $A_q(z)$ is a function determined by the boundary conditions of $\phi(r)$ at the interfaces. The solution for the image self-energy potential $\Sigma_e(z_e)$ is

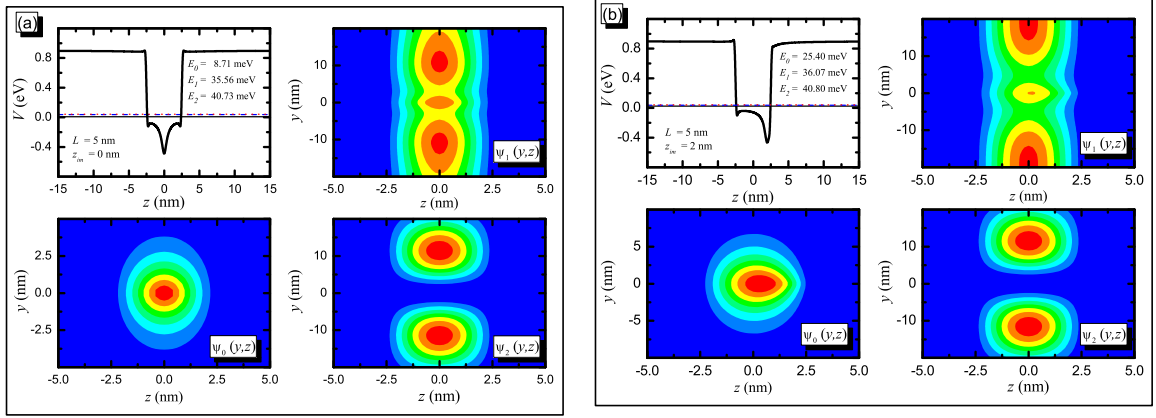


Figure 6.2: (Color online) Waves functions projection in the (yz) plane for the ground state, first and second excited states. In (a) the impurity is located in $z_{im} = 0$ nm and in (b) the impurity is $z_{im} = 5$ nm far from the center of the QW. The z -projection of the total potential $V(z)$, in eV, are depicted for QWs with width of $L = 5$ nm.

$$\Sigma_e(z_e) = \frac{Q}{2} \int_0^{\infty} q [A_q(z_0) - A_q^0(z_0)] dq, \quad (6.11)$$

where $A_q^0(z_0)$ is solution of Equation (6.10) if ε is z independent. Without loss of generality, we shall here consider QWs with abrupt interface. The self energy potential $\Sigma_e(z_e)$ diverges at the interface $z = \pm L/2$ and we employ a numerical grid such that the coordinate in $z = \pm L/2$ does not sit at a grid point in order to avoid the divergence problem. The major results for $\Sigma_e(z_e)$ can be seen in the Reference [17] and will not be repeat here.

6.2 Results and Discussion

As in the case of a model structure, QWs are formed by a zinc blende GaN layer ranging in the region $|z| \leq a$ between two HfO₂ layers in the region $|z| \geq a$. Between these materials, we consider the existence of abrupt interfaces at a position along the z axis. The GaN electron effective mass were taken from experiments ($m_e^* = 0.19$) [146], and for simplicity, we have considered the electron effective mass invariable along z . Although photoemission spectroscopy experiments demonstrated that $\Delta E_e = 2.1$ eV for wurtzite GaN/HfO₂ interfaces [150], the absence of this information for the zinc blende heterojunction leads us to estimate these quantities through the simple electron affinity model [151, 152], for which we obtain $\Delta E_e = 0.9$ eV. As shown in Fig. 6.1, the quantum well has mirror symmetry from the origin in the z direction, at $z = 0$, and the reference of the total potential $V(z)$ in Equation (6.6) is taken with respect to the zero level of the potential $\Delta E_e(z)$, as shown in Fig. 6.1(a).

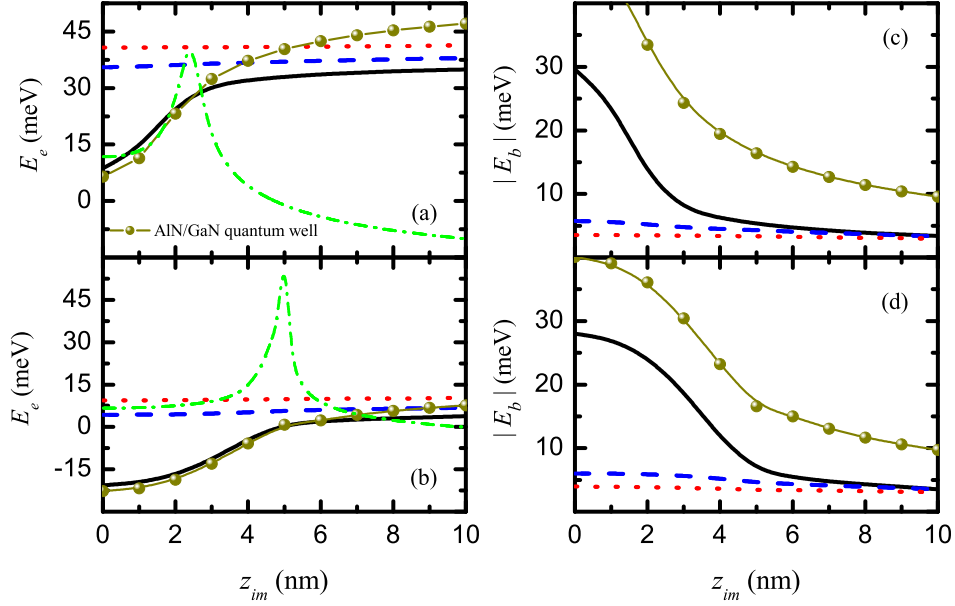


Figure 6.3: (Color online) Left panels: Electron energy for ground state (black solid line), first (blue dashed line) and second (red dotted line) excited state in QW for (a) narrow $L = 5$ nm QW width and (b) wide $L = 10$ nm HfO_2/GaN QW width. Right panels: Electron-impurity binding energy for ground state (black solid line), first (blue dashed line) and second (red dotted line) excited state energy as function of impurity position for a (c) narrow ($L = 5$ nm) QW and (d) wide $L = 10$ nm HfO_2/GaN QW. The dark yellow line-sphere depict the electron energy (left) and electron-impurity binding energy (right) in narrow (top) and wide (bottom) AlN/GaN QW, and the green dash-dot line shows the effect of the image charges in GaN/HfO_2 QW.

The impurity can be placed at any position along z direction, and two particular positions are shown in the Fig. 6.2. Fig. 6.2(a) depicted the total potential $V(z)$ projected along z direction, where the impurity is located at the center of the QW in $(x_{im}, y_{im}, z_{im}) = (0.0, 0.0, 0.0)$ nm. Fig. 6.2(b) shows the total potential $V(z)$ with the impurity located at the interface in $(x_{im}, y_{im}, z_{im}) = (0.0, 0.0, 2.5)$ nm. These figures also display the energy and the projection of the electron wave function in the (y, z) plane, for ground state $\psi_0(y, z)$, first $\psi_1(y, z)$ and second $\psi_2(y, z)$ excited states, confined in a 5 nm QW. For example, when the impurity is located in the center of the QW the ground state energy is about 8.71 meV upward of potential energy reference, and goes up to 25.40 meV when the impurity is placed at the interface of the QW. Noteworthy the potential energy $V(z)$ is attractive in the well region due to both electron-impurity interaction and attractive behavior of the image self-energy. This potential move the electron to the center of the QW and the wave function is concentrated in that region, as depicted in Fig. 6.2(a). When the impurity is located at the interface, for a 5 nm QW, the electron is pushed towards to the right interface, as shown by the ground state $\psi_0(y, z)$ and first excited state

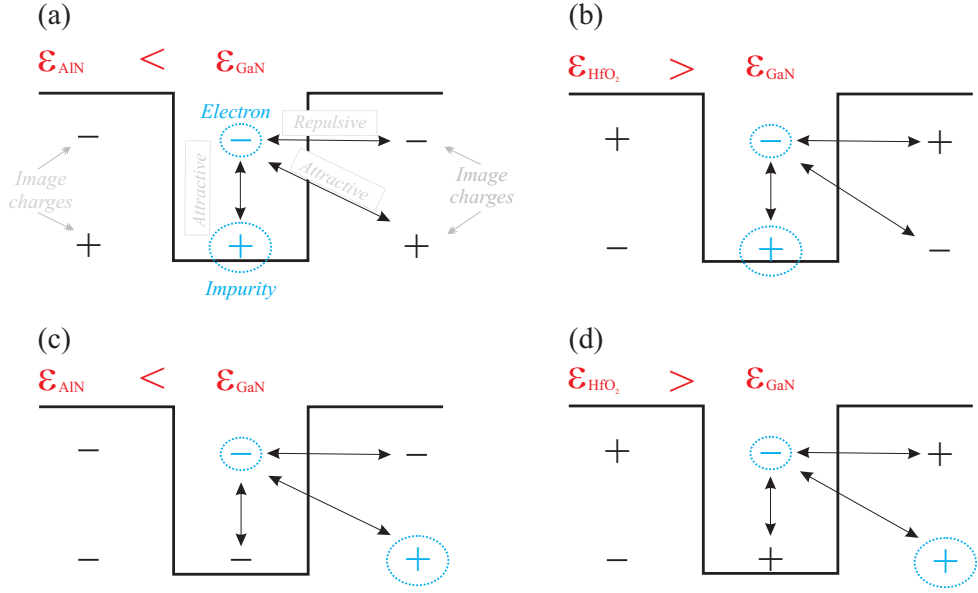


Figure 6.4: Schematic diagram of different interactions between electron and their image charges, electron and impurity as well as electron and impurity image charges for GaN/AlN (a)-(c) and in GaN/HfO₂ (b)-(d) QWs. In (a)-(b) the impurity is located in the well region while in (c)-(d) the impurity is located in the barrier region.

$\psi_1(y, z)$ wave function. Interestingly, the second excited state $\psi_2(y, z)$ is weakly attracted by the impurity.

Figures 6.3(a) and 6.3(b) illustrate the electron energy as function of the impurity position along z axis, in narrow ($L = 5$ nm) and wide ($L = 10$ nm) QWs, respectively, for the ground state energy (solid lines), first (dashed lines) and second (dotted lines) excited states. Our result shows that the ground state energy increases asymptotically until the point where it reaches values with less pronounced variations from $z_{im} \approx 2$ nm in narrow QW and from $z_{im} \approx 5$ nm in wide QW. For $z_{im} > 2$ nm in narrow QW and $z_{im} > 5$ nm in wide QW the ground state energy is invariant with z_{im} position, which indicates that the effect of the impurity potential is small when the impurity is located in the region of the barrier. Excited states are, on the other hand, weakly affected by the impurity position.

The n -th electron-impurity binding energy level is calculated, with appropriate image charge contribution take into consideration, by the difference

$$E_{n,b} = E_n(V_{e-im} \neq 0) - E_n(V_{e-im} = 0), \quad (6.12)$$

where the term $E_n(V_{e-im} \neq 0)$ means the n -th electron energy level calculated considering $V_{e-im} \neq 0$ and $E_n(V_{e-im} = 0)$ is the n -th electron energy level calculated considering $V_{e-im} = 0$, in Equation (6.4). The absolute value of the electron-impurity binding energy, as function of the impurity position, is depicted in Fig. 6.3(c) and Fig. 6.3(d) for narrow ($L = 5$ nm) and wide ($L = 10$ nm) QWs, respectively. The curves are shown for

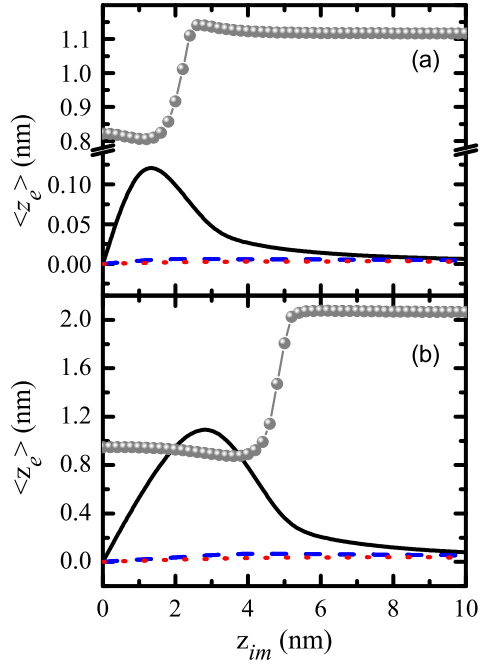


Figure 6.5: Electron center-of-mass as function of the impurity position (z_{im}) for (a) narrow ($L = 5$ nm) and (b) wide ($L = 10$ nm) QWs. The ground state, first and second excited states are represented by black solid, blue dashed and red dotted lines, respectively. The gray line-sphere depict the standard deviation in position σ_x for narrow and wide QWs.

the ground state (black solid line), first excited state (blue dashed line) and second excited state (red dotted line). As seen, the binding energy changes with impurity position in the QW structure. The maximum ground state electron-impurity binding energy value occurs in the center of the QW, for $z_{im} = 0$ nm and decreases when the impurity moves towards the interface (in both cases $L = 5$ nm and $L = 10$ nm) of the well region. For impurity at the interface region, the electron is weakly bound and the binding energy is about 5 meV, for the z_{im} values investigated in this work. Excited states are always weakly bound to impurities, independent of the z_{im} position.

In order to help us to understand the role of the large dielectric constant in the barrier region we compare the results for GaN/HfO₂ with those of a more typical GaN/AlN system, where we have $\epsilon_r = \epsilon_{\text{GaN}}/\epsilon_{\text{AlN}} = 9.5 / 8.5 = 1.12$. Figure 6.3 show in dark yellow line-sphere the electron energy and electron-impurity binding energy in narrow and wide AlN/GaN QWs. Different from GaN/HfO₂ ($\epsilon_r < 1$) in a GaN/AlN ($\epsilon_r > 1$) quantum well the electron fell a repulsive potential in the well region due to the dielectric mismatch. To elucidate the results presented in Figure 6.3(a) and (b) we show in Figure 6.4 a schematic diagram of different interactions between electron, impurity and image charges for GaN/AlN (a)-(c) and GaN/HfO₂ (b)-(d) QWs. For the impurity at the well region, this picture clearly shows that the coulomb potential of impurity and image charges is

more attractive in GaN/AlN QW compared to that in GaN/HfO₂ QW. For the impurity located at barrier region the coulomb potential becomes more attractive in GaN/HfO₂. This explains why the electron energy is smaller (larger) at the GaN/AlN system when the impurity is located in the well (barrier) region, as shown in Fig. 6.3(a) and (b). Without dielectric mismatch, or even for $\varepsilon_r > 1$, the confinement energy is always positive since the reference of confinement potential $V(z)$ is always either zero or larger. The energy $E_n(V_{e-im} = 0)$ shown in the equation 6.12 is bigger in GaN/AlN than that in GaN/HfO₂, giving rise to a difference in the binding energy as it is shown in Fig. 6.3(c) and (d). Aside from this difference this energy is essentially due to the band offset and the self energy potential, as it is shown in the Fig. 6.1(a). Further more, as the impurity position z_{im} increase to the barrier region, the stationary states inside the well tends to discrete states analogous to the case of a quantum well without impurity, as we can see in Fig. 6.3(a) and (b) for $z_{im} > 5$ nm. In the binding energy $E_{n,b}$ both contribution band offset and self energy potentials are not take into account and the states collapse near to $z_{im} = 10$ nm, as shown in Fig. 6.3(c) and (d).

To clarify the role played by the high dielectric mismatch at the interfaces we add in the Fig. 6.3 (a) and (b), in dash-dot green lines the difference in the electron energy take into account image charges and does not take into account the image charges contributions for a GaN/HfO₂ quantum well. This results show essentially the contribution due to image self-energy (interaction between electron and its image charges) as well as the interactions among electron and impurity image charges. As the impurity position increase this difference increase asymptotically until reach the maximum value around the interface position and decrease toward negative values in narrow quantum wells due to the attractive character of the self energy in systems with $\varepsilon_r < 1$, as it can see on the Reference [141] and [142].

To further elucidate here, the expectation value of the electron position $\langle z_e \rangle$, along of z axis, is plotted as function of the impurity position z_{im} , for narrow ($L = 5$ nm) and wide ($L = 10$ nm) QWs in Fig. 6.5(a) and Fig. 6.5(b), respectively. For wells with $L = 5$ nm ($L = 10$ nm), the $\langle z_e \rangle$ of the ground state (solid lines) has maximum displacement around 0.12 nm (1.0 nm) when the impurity is located in $z_{im} = 1$ nm ($z_{im} = 3$ nm). Moving the impurity towards the barrier region, $\langle z_e \rangle$ tends to return to the QW center. In this case $\langle z_e \rangle$ of the excited states are also weakly affected by the impurity position. We also present in the Fig. 6.5 in gray line-sphere the standard deviation in the position, namely the square root of the variance $\sigma_x = \sqrt{\langle z^2 \rangle - \langle z \rangle^2}$. This quantity illustrate better the transition from strong binding to weak binding as z_{in} goes into the barrier, illustrating the big variance at the interface position.

Finally, from practical point of view, it is important to investigate the effects of external electric fields on the electronic structure of GaN/HfO₂ QWs. In Fig. 6.6, we show the stark shift $\Delta E_e = E_e(F \neq 0) - E_e(F = 0)$ of the three first electron energy states, for (a) narrow and (b) wide QWs. The electron energy $E_e(F \neq 0)$ is calculated by considering

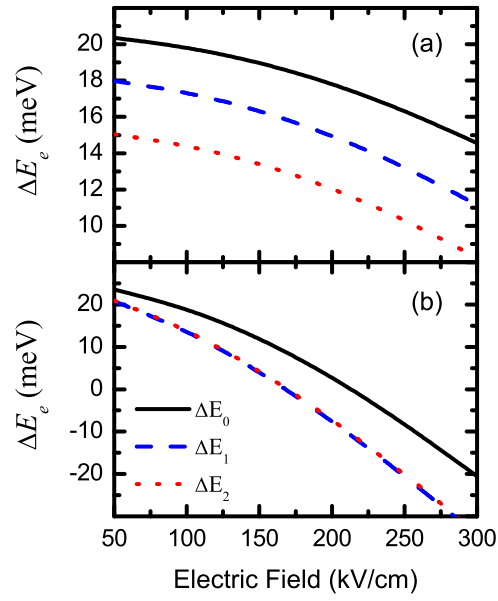


Figure 6.6: Stark shift of the ground state energy (solid lines), first excited state energy (dashed lines) and second excited state energy in (a) narrow (5 nm) and (b) wide (10 nm) QWs.

an electric field \mathbf{F} , pointing along the z direction, by including the term eFz on Equation (6.6). Here, it is important to notice that the shift on the electron energy ΔE_e can be underestimated by several meV with the applied electric field, i.e., $\simeq 6$ meV for narrow QWs and $\simeq 50$ meV for wide QWs.

7.1 Concluding remarks of the thesis

In this thesis, we studied and computationally developed the Split-operator technique for time dependent Schrödinger equation in order to investigate transport and electronic properties of semiconductor nanostructures. These nanostructures consist of quantum rings, with different geometries (circular, semi-circular and squared) with central branches, and under applied of magnetic field; L-shaped quantum wires and quantum wells with external static electric field and impurities.

In first work, we investigated the propagation of a wave packet through a quantum ring with an extra channel along its diameter. Surprisingly, our results demonstrate that even when an extra channel is added in the horizontal direction, as a continuation of the input and output leads, the transmission through the whole system can be lower than in the absence of such an extra current path. This is evidence of the "Braess paradox analog" observed recently for mesoscopic networks. Nevertheless, while the original Braess paradox in games theory is explained in terms of an attempt to optimize the flux, which eventually leads to transport inefficiency in the equilibrium situation, the transport inefficiency observed for the wave packet propagation in quantum systems originates from two possible effects: (i) the quantum scattering of the wave packet in the input channel-ring junction, along with the absence of an allowed energy sub-band for propagation in the central channel when it is too narrow, and (ii) the quantum interference between parts of the wave packets that passed through the central channel and those that propagated through the rings arms.

In second work, we investigated the WP propagation through rings with different circular and squared shapes, adding an extra channel along their respective diameters, and calculated the transmission probabilities as function of parameters like magnetic field and extra channel width W_c . In the presence of an external magnetic field, the position of the transmission probability minima owing to quantum interference are clearly shifted, and Aharonov-Bohm oscillations are observed as well. Moreover, a charged AFM tip placed over the systems, acts as an obstruction to some of the quantum pathways, is

found to favor enhancement of the transmission probability in its minima under specific conditions. Results shown here, therefore, not only allow us to discuss transport properties of a branched out quantum ring in close resemblance with the Braess paradox, but also provides tools to control the transmission probability minima in such systems.

In the third work, we presented a theoretical investigation of the electron tunneling and the consequent current leakage between two bent quantum wires, based on the propagation of a Gaussian wave packet. The two L-shaped semiconductor quantum wires are separated by a distance W_2 . We discussed how changes in the distance between the two QWs W_2 affect the tunneling probability and current for different values of kinetic energy wave packet. The wave packet scattered by the potential is reflected and transmitted through the barrier. The tunneling current provides an estimate of the leakage current in the system, which becomes larger as W_2 is reduced. It is of fundamental and practical importance to control these undesired leakage currents in miniaturized electronic devices and circuits, thus, we believe the results presented here might contribute to help future experimental investigations of carrier transport in low dimensional circuits and their future applications in nanotechnology.

In the last work, we studied impurity states with image charges effects in GaN/HfO₂ quantum wells. Our results show that the electron-impurity binding energy is highest when the impurity is located at the center of the quantum well and decreases when the impurity moves towards the interface. When the impurity is located on the barrier region the binding energy has a smaller intensity. Moreover, when a electric field is applied perpendicularly to the QW plane the electron energy can be shifted by about 50 meV in wide quantum wells. These results are lacking experimental confirmation, and we expect that our predictions induce the realization of such experiments.

7.2 Future prospects

Regarding the study of charge carriers dynamics in semiconductor nanostructure, using the wave packet propagation, we propose several interesting problems to be investigate near future. So, as a short-term perspective, we intend to address a study about the following problems:

- The wave packet propagation through a quantum dot with a localized magnetic field, simulating a “Scanning Gate Microscopy” (SGM) experiment, where we hope to calculate the transmission probabilities map as a function a magnetic field for different positions of the magnetic tip;
- Investigate infrared photocurrent with one and two -photon absorptions in a quantum dot: in this case, the wave packet propagation is in imaginary time, in order to obtain the eigenstates of the system, and after that propagation in real time, to calculate the interaction between the electron and the photon.

-
- Investigate a quantum channel with impurities in order to obtain the interaction of a photon with series of eigenstates of the system. We hope to obtain results to compare with current experiments and help news works in this subject.
 - As a last proposal, we suggest a multi terminals system, in order to observe which channel will be preferential by the Gaussian wave packet, in the presence of an uniform magnetic field. The to the system field will add a phase in the wave function, changing the trajectory when compared to the system without magnetic field.

Bibliography

- [1] N. R. Wilson and D. H. Cobden, *Nano Lett.* **8** 2161 (2008);
- [2] V. G. Dubrovskii, N. V. Sibirev, G. E. Cirlin, I. P. Soshnikov, W. H. Chen, R. Larde, E. Cadel, P. Pareige, T. Xu, B. Grandidier, J.-P. Nys, D. Stievenard, M. Moewe, L. C. Chuang and C. Chang-Hasnain, *Phys. Rev. B.* **79**, 205316 (2009);
- [3] J. Y. Chung, H. D. Li, Chang, W. H. Chang. T. C. Leung, and D. S. Lin, *Phys. Rev. B.* **83**, 085305 (2011);
- [4] N. N. Ha, K. Dohnalová, T. Gregorkiewicz, and J. Valenta *Phys. Rev. B.* **81**, 195206 (2010);
- [5] F. Villalpando-Paez, L. G. Moura, C. Fantini, H. Muramatsu, T. Hayashi, Y. A. Kim, M. Endo, M. Terrones, M. A. Pimenta, and M. S. Dresselhaus *Phys. Rev. B.* **82**, 155416 (2010);
- [6] W. Shockley, "Circuit element utilizing semiconductor material," U.S. Patent Office 2,569,347, September 1951;
- [7] L. Esaki and R. Tsu, *IBM Res. Note*, RC- 2418 (1969);
- [8] L. Esaki and R. Tsu, *IBM J. Res. Dev.* **14**, 61 (1970);
- [9] K.-D. Hof, C. Rossler, S. Manus, J. P. Kotthaus, A. W. Holleitner, D. Schuh, and W. Wegscheider, *Phys. Rev. B*, **78**, 115325 (2008);
- [10] R. R. Cooney, S. L. Sewall, K. E. H. Anderson, E. A. Dias, and P. Kambhampati, *Phys. Rev. Lett.* **98**, 177403 (2007);
- [11] S. Sanguinetti, M. Abbarchi, A. Vinattieri, M. Zamfirescu, M. Gurioli, T. Mano, T. Kuroda, and N. Koguchi, *Phys. Rev. B* **77**, 125404 (2008);
- [12] S. Fafard, Y. H. Zhang, and J. L. Merz, *Phys. Rev. B*, **48**, 12308 (1993);

-
- [13] X. Zhu, Q. Li, D. E. Ioannou, D. Gu, J. E. Bonevich, H. Baumgart, J. S. Suehle, and C. A. Richter, *Nanotechnology* **22**, 254020 (2011);
- [14] Y. Zhao, J. T. Smith, J. Appenzeller, and C. Yang, *Nano Letters* **11**, 1406 (2011);
- [15] J. C. Silva, A. Chaves, J. A. K. Freire, V. N. Freire, and G.A. Farias, *Phys. Rev. B.* **74**, 085317 (2006);
- [16] R. Stefano , N. Kristian , A. Gvidas, S. Lars, W. Lars-Erik , K. Olov, and W. Andreas, *appl. phys. lett.* **92**, 253509 (2008);
- [17] T. A. S. Pereira, J. S. de Sousa, J. A. K. Freire, and G. A. Farias, *Jour. Appl. Phys.*, **108**, 054311 (2010);
- [18] A. F. Slachmuylders, B. Partoens, W. Magnus and F.M. Peeters, *Phys. Rev. B.* **74**, 235321 (2006);
- [19] T. Ogawa, and T. Takagahara, *Phys. Rev. B.* **43**, 14325 (1991);
- [20] S. M. Rezende, *A Física de materiais e dispositivos eletrônicos*, Editora da UFPE (1996);
- [21] R. J. Le Roy and Y. Huang, *Journal of Mol. Struc.* 591, 175 (2002);
- [22] M. Born and J. R. Oppenheimer, *Ann. Phys.* 84, 457 (1927);
- [23] N. W. Ashcroft, and N. D. Mermin, *Solid State Physics*, publishing Thomson Learning (1976);
- [24] M. R. Valls, *Theoretical Modelling of electrons and holes in semiconductor nanostructures*, thesis PHD. Universitat Jaume I, Spain (2010);
- [25] Z. I. Alferov, *Rev. Of Mod. Phys.* **73**, 767 (2001);
- [26] T. A. S. Pereira, *Confinamento Dielétrico Versus Quântico em nanoestruturas*, Tese de Doutorado, Universidade Federal do Ceará (2006);
- [27] S.M. Sze, K. K. Ng, *Physics of Semiconductor Devices*, Third Edition, Editor: Wiley (2007);
- [28] M. Balkanski, and R.F. Wallis, *Semiconductor Physics and Applications*, publishing Oxford University Press, (2000);
- [29] J. Singh, *Physics of Semiconductors and their Heterostructures*, publishing McGraw Hill (1993);
- [30] P. Harrison, *Quantum Wells, Wire and Dots*, publishing Wiley (2004);

-
- [31] C. L. N. Oliveira, Excitons em sistemas quânticos 0-2D, Dissertação de Mestrado, Universidade Federal do Ceará, UFC(2005);
- [32] T. Mlakar, Conductive Atomic Force Microscopy of Quantum Dots and Quantum Rings, Master's Thesis, University of Nova Gorica (2011);
- [33] C. H. Chiu, Z. Huang, and C. T. Poh, Phys. Rev. Lett., **93**, 136105 (2004);
- [34] F. M. Peeters, and V. A. Schweigert, Phys. Rev. B, **53**, 1468 (1996);
- [35] M. Ramezani Masir, A. Matulis, and F. M. Peeters, Phys. Rev. B, **79**, 155451 (2009);
- [36] L. P. Kouwenhoven, D. G. Austin, and S. Tarucha, Rep. Prog. Phys. **64**, 701-736 (2001);
- [37] X. Duan, C. M. Lieber, Adv. Mater. **12**, 298 (2000);
- [38] C. Chen, S. Shehata, C. Fradin, R. LaPierre, C. Couteau, G. Weihs, Nano Lett. **7**, 2584 (2007);
- [39] B. Li, B. Partoens, F. M. Peeters, and W. Magnus Phys. Rev. B **79**, 085306 (2009);
- [40] A. Chaves, J. C. Silva, J. A. K. Freire, and G. A. Farias, J. Appl. Phys. **101**, 113703 (2007);
- [41] G. E. Moore, Electronics **38**, 8 (1965);
- [42] G. Grimbom, M. Saraf, S. Sagy, A. Bartnik, F. Wise, E. Lifshitz, Phys. Rev. B, **81**, 245301 (2010).
- [43] O. Ruth, C. Dima, K. Viki, S. Aldona, K. Martin, and E. Lifshitz, Phys. Rev. Lett. **102**, 197401 (2009);
- [44] D. R. Costa, "Anéis quânticos semicondutores ideais", Master's thesis, Federal University of Ceará, defense (2011).
- [45] L. Zhang, and H. Huang, Appl. Phys. Lett. **90**, 023115 (2007);
- [46] M. Cardona and Y. P. Yu, Fundamentals of Semiconductor, Physics and materials properties, Editor: Springer (2001);
- [47] Cui, Y., Lauhon, L. J., Gudiksen, M. S., Wang, J. F. and Lieber, C. M., Appl. Phys. Lett. **78**, 2214 (2001);
- [48] A. H. Cabrera, and P. Aceituno, Phys. E, **70**, 5-10 (2015);
- [49] Z. Geng, H. Dai, X. Chen, S. Wei, and C. Xia Superlatt. and Microstruc., **58**, 81 (2013);

- [50] T.V. Torchynska, R. C. Tamayo, G. Polupan, A. Stints, and L. Shcherbyna, *Jour. of Luminescence*, **163**, 40 (2015);
- [51] M. P. Halsall, P. Harrison, J. P. R. Wells, I. V. Bradley, and H. Pellemans, *Phys. Rev. B*, **63**, 155314 (2001);
- [52] D. O. Kundys, J. P. R. Wells, A. D. Andreev, S. A. Hashemizadeh, T. Wang, P. J. Parbrook, A. M. Fox, D. J. Mowbray, and M. S. Skolnick, *Phys. Rev. B*, **73**, 165309 (2006);
- [53] A. Chaves, G. A. Farias, F. M. Peeters, and B. Szafran, *Phys. Rev. B* **80**, 125331 (2009);
- [54] B. S. Archanjo, *Sensores de Gás e memristores fabricados por oxidação anódica local utilizando microscopia de varredura por sonda*, Tese de doutorado, Universidade Federal de Minas Gerais (2009);
- [55] A. Fuhrer, S. Lüscher, T. Ihn, T. Heinzl, K. Ensslin, W. Wegscheider, and M. Bichler, *Nature*, **413**, 822 (2001);
- [56] L. G. Dias da Silva, S. E. Ulloa and A. O. Govorov, *Phys. Rev. B*. **70**, 155318 (2004);
- [57] B. Szafran, F. M. Peeters and S. Bednarek, *Phys. Rev. Lett.* **70**, 125310 (2004);
- [58] J. Liu, A. Zaslavsky and L. B. Freund, *Phys. Rev. Lett.* **89**, 096804 (2002);
- [59] Y. Aharonov and D. Bohm, *The Phys. Rev.* **115**, 485 (1959);
- [60] J. J. Sakurai, *Modern Quantum Mechanics*, Editor: Addison Wesley Longman, New York, (1994);
- [61] A. J. M. Giesbers, U. Zeitler, D. Reuter, A. D. Wieck, G. Biasiol, L. Sorba and J. C. Maan, *Phys. E*. **40**, 1470, (2008);
- [62] A. M. Jayannavar, *Pramana - Jour. Phys.*, **58**, 173-181 (2002);
- [63] D. Sprinzak, E. Buks, M. Heiblum, and H. Shtrikman, *Phys. Rev. Lett.*, **84**, 5820 (2000);
- [64] A.A.Sousa, A.Chaves, G.A.Farias and F.M.Peeters, *Phys. Rev. B* **88**, 245417 (2013).
- [65] M. G. Pala, S. Baltazar, P. Liu, H. Sellier, B. Hackens, F. Martins, V. Martins, V. Bayot, X. Wallart, L. Desplanque, and S. Huant, *Phys. Rev. Lett.*, **108**, 076802 (2012).
- [66] J. Nash, *Non-Cooperative Games*, Doctoral Thesis, Princeton University, 1950;

- [67] G. Issac and A. O. Bahya, *Appl. Math. Lett.* **15**, 633 (2002);
- [68] J. M. Courtault, B. Crettez, and N. Hayek, *Math. Soc. Sci.* **56**, 439 (2008);
- [69] D. Braess, *Unternehmensberatung* **12**, 258 (1968); D. Braess, A. Nagurney, and T. Wakolbinger, *Transp. Sci.* **39**, 446 (2005);
- [70] J. N. Hagstrom, R. A. Abrams, *IEEE Intelligent Transport System Conference Proceedings*, “*Characterizing Braess’s Paradox for Traffic Networks*”, 836 (2001);
- [71] V. Zverovich and E. Avineri, arXiv:1207.3251 (2012); See also G. Kolata, *What if they closed 42nd street and nobody noticed?*, *New York Times*, p. 38, 25/12/1990.
- [72] J. E. Cohen and F. P. Kelly, *Journ. Appl. Probab.* **27**, 730 (1990);
- [73] Marc Baldo. 6.701 Introduction to Nanoelectronics, Spring 2010. (Massachusetts Institute of Technology: MIT OpenCourseWare), <http://ocw.mit.edu> (Accessed 21 Apr, 2015). License: Creative Commons BY-NC-SA
- [74] C. Dekker, *Phys. Today* **52**, 5, 22 (1999)
- [75] S. Bhattacharya, D. Deb, S. M. Adhikaric, S. Sahad, K. M. Chatterjeed, S. Choudhurye, and K. P. Ghatak, *Superlattices and Microstructures*, **50**, 609-627 (2010)
- [76] K. J. Kang, *Progress in Materials Science*, **69**, 213-307 (2015).
- [77] M. Grätzel, *Nature*, **414**, 338-344 (2001).
- [78] L. Sekaric, D. W. Carr, S. Evoy, J. M. Parpia and H. G. Craighead, *Sensors and Actuators A*, **101**, 215-219 (2002). **26**, 0644008 (2011).
- [79] M. D. Feit, J. A. Fleck, *Jour. Comput. Phys.* **47**, 412-433 (1982);
- [80] M. H. Degani, *Appl Phys. Letters*, **59**, 57-59 (1991);
- [81] J. M. Pereira, F. M. Peeters, A. Chaves, and G. A. Farias, *Semicond. Sci. Technol.* **25**, 033002 (2010);
- [82] M. Suzuki, *Phys. Rev. A*, **146**, 319-323 (1990);
- [83] J. P. M. Braga, *Técnica Split-operator em coordenadas generalizadas*, Dissertação de mestrado, UFC (2010);
- [84] W. A. Press, S. A. Teukolsky, W. T. Vetterling and B. P. Flannery, *Numerical Recipes in Fortran 77: The Art of Scientific Computing* (Cambridge University Press, Cambridge) (1992);
- [85] M. H. Degani, G. A. Farias, and P. F. Farinas, *Appl. Phys. Lett.*, **89**, 152109 (2006);

- [86] S. Mahapatra and N. Sathyamurthy, *J. Chem. Soc.* **93**, 773 (1997).
- [87] R. Kosloff and D. Kosloff, *Jour. Comp. Phys.*, **63**, 363 (1986);
- [88] D. Neuhauser and M. Baer, *Jour. Chem. Phys.*, **90**, 4351 (1988);
- [89] D. E. Manolopoulos, *Jour. Chem. Phys.*, **117**, 9552 (2002);
- [90] I. S. Gradshteyn and I. M. Ryzhik, *Table of integrals, series, and products*, 7th ed. (Academic, San Diego), Sec 8.1 eq. 8.112 (2007);
- [91] A. Chaves, *Dinâmica de pacotes de onda em semicondutores e grafeno e de vórtices em supercondutores*, Tese de Doutorado, Universidade Federal do Ceará (2010);
- [92] H. Lin, T. Roughgarden, É. Tardos, and A. Walkover, *Siam J. Discrete Math.* **25**, 1667 (2011);
- [93] Y. Xia and D. J. Hill, *IEEE Trans. Circuits and Systems-II: Express Briefs* **60**, 172 (2013).
- [94] J. E. Cohen and P. Horowitz, *Nature (London)* **352**, 699 (1991).
- [95] D. Witthaut and M. Timme, *New J. Phys.* **14**, 083036 (2012).
- [96] M. Rohden, A. Sorge, M. Timme, and D. Witthaut, *Phys. Rev. Lett.* **109**, 064101 (2012).
- [97] M. G. Pala, H. Sellier, B. Hackens, F. Martins, V. Bayot, and S. Huant, *Nanoscale Res. Lett.* **7**, 472 (2012).
- [98] S. S. Buchholz, S. F. Fischer, U. Kunze, D. Reuter, and A. D. Wieck, *Appl. Phys. Lett.* **94**, 022107 (2009).
- [99] C. Kreisbeck, T. Kramer, S. S. Buchholz, S. F. Fischer, U. Kunze, D. Reuter, A. D. Wieck, *Phys. Rev. B* **82**, 165329 (2010).
- [100] H. Fehske, J. Schleede, G. Schubert, G. Wellein, V. S. Filinov, and A. R. Bishop, *Phys. Lett. A* **373**, 2182 (2009).
- [101] B. Szafran and F. M. Peeters, *Phys. Rev. B* **72**, 165301 (2005).
- [102] A. Alvermann and H. Fehske, *Phys. Rev. B* **77**, 045125 (2008).
- [103] M. R. Poniedzialek and B. Szafran, *J. Phys.: Condens. Matter* **24**, 085801 (2012).
- [104] M. H. Degani, *Appl. Phys. Lett.* **59**, 57 (1991).
- [105] M. H. Degani and M. Z. Maialle, *J. Comp. Theor. Nanosci.* **7**, 454 (2010).

- [106] H. Wang, G. A. Farias, and V. N. Freire, *Superlatt. Microstruct.* **25**, 307 (1999).
- [107] J. A. K. Freire, G. A. Farias, and V. N. Freire, *Sol. Stat. Comm.* **106**, 559 (1998).
- [108] B. Hackens, F. Martins, T. Ouisse, H. Sellier, S. Bollaert, X. Wallart, A. Cappy, J. Chevrier, V. Bayot and S. Huant, *Nature Phys.* **2**, 826 (2006);
- [109] B. Szafran, *Phys. Rev. B* **84**, 075336 (2011).
- [110] R. J. Warburton, C. Schäflein, D. Haft, F. Bickel, A. Lorke, K. Karrai, J. M. Garcia, W. Schoenfeld, and P. M. Petroff, *Nature*, **405**, 926 (2000).
- [111] S. S. Mao, *Int. Jour. Nanot.* **1** 42 (2004).
- [112] C. Y. Hou, A. Rahmani, A. E. Feiguin, and C. Chamon, *Phys. Rev. B* **86**, 075451 (2012).
- [113] J. J. Ramsey, E. Pan, P. W. Chung and Z. M. Wang, *NanoScale Res. Lett.* **5**, 1272 (2010).
- [114] Y. Cohin, O. Mauguin, L. Largeau, G. Patriarche, F. Glas, E. Sondergard, and J. C. Harmand, *Nano Lett.* **13**, 2743 (2013).
- [115] T. Ihn, *Quantum states and electronic transport* (Oxford University press, Oxford, 2010).
- [116] H. U. Baranger, and A. D. Stone, *Phys. Rev. Lett.* **63**, 414 (1989).
- [117] M. D. Seta, G. Capellini, and F. Evangelisti, *Phys. Rev. B* **77**, 045431 (2008).
- [118] M. T. Björk, B. J. Ohlsson, C. Thelander, A. I. Persson, K. Deppert, L. R. Wallenberg, and L. Samuelson, *Appl. Phys. Lett.* **81**, 4458 (2002).
- [119] T. D. Stanescu, R. M. Lutchyn, S. Das Sarma, *Phys. Rev. B* **90**, 085302 (2014).
- [120] O. M. Auslaender, A. Yacoby, R. de Picciotto, K. W. Baldwin, L. N. Pfeiffer, and K. W. West, *Phys. Rev. Lett.* **84**, 1764 (2000).
- [121] Y. Tserkovnyak, B. I. Halperin, O. M. Auslaender, and A. Yacoby, *Phys. Rev. Lett.* **89**, 136805 (2002).
- [122] O. M. Auslaender, A. Yacoby, R. de Picciotto, K. W. Baldwin, L. N. Pfeiffer, and K. W. West, *Science* **295**, 825 (2002).
- [123] Y. T. Hou, M. F. Li, Y. Jin, and W. H. Lai, *Jour. Appl. Phys.* **91**, 258 (2002).
- [124] W. C. Lee and C. Hu, *Trans. Elect. Dev.* **48**, 1366 (2001).
- [125] A. Chaudhry and J. N. Roy, *Journ. Elect. Scien. Tech.* **9**, 51 (2011).

- [126] A. Chaudhry and J. N. Roy, *Int. Jour. Nanoelect. Mater.* **5**, 1 (2012).
- [127] H. Sellier, B. Hackens, M. G. Pala, F. Martins, S. Baltazar, X. Wallart, L. Desplanque, V. Bayot, and S. Huant, *Semicond. Sci. Techno.* **26**, 064008 (2011);
- [128] M. H. Degani, *Phys. Rev. B*, **66**, 233306 (1997);
- [129] M. Büttiker, *Phys. Rev. Lett.* **57**, 1761 (1986);
- [130] R. Landauer, *IBM Journ. Res. Develop.* **1**, 223 (1957)
- [131] Bin Li, A. F. Slachmuylders, B. Partoens, W. Magnus, F. M. Peeters, *Phys. Rev. B* **77**, 115335 (2008).
- [132] N. C. Jarosik, B. D. McCombe, B. V. Shanabrook, J. Comas, John Ralston and G. Wicks, *Phys. Rev. Lett.* **54**, 1283 (1985).
- [133] G. Weber, *Phys. Rev. B* **41**, 10043 (1990).
- [134] S. Fraizzoli, F. Bassani, *Phys. Rev. B* **41**, 5096 (1990).
- [135] J. M. Ferreyra and C. R. Proetto, *Phys. Rev. B* **52** 2309 (1995).
- [136] B. Li, B. Partoens, F. M. Peeters and W. Magnus, *Phys. Rev. B* **79** 085306 (2009).
- [137] C. G. Morgan, P. Kratzer, and M. Scheffler, *Phys. Rev. Lett.* **82** 4886 (1999).
- [138] N. Q. Vinh, H. Przybylińska, Z. F. Krasil'nik, and T. Gregorkiewicz, *Phys. Rev. Lett.* **90**, 066401 (2003).
- [139] J. Cen and K. K. Bajaj, *Phys. Rev. B* **48**, 8061 (1993).
- [140] Z. Y. Deng, and S. W. Gu, *Phys. Rev. B* **48**, 8083 (1993).
- [141] T. A. S. Pereira, J. A. K. Freire, V. N. Freire, G. A. Farias, L. M. R. Scolfaro, J. R. Leite, and E. F. da Silva Jr., *Appl. Phys. Lett.* **88**, 242114 (2006).
- [142] T. A. S. Pereira, J. S. de Sousa, G. A. Farias, J. A. K. Freire, M. H. Degani, and V. N. Freire, *Appl. Phys. Lett.* **87**, 171904 (2005).
- [143] A. A. Sousa, T. A. S. Pereira, A. Chaves, J. S. de Sousa, and G. A. Farias, *Appl. Phys. Lett.* **100**, 211601 (2012).
- [144] F. Stern, *Phys. Rev. B* **17**, 5009 (1978); *ibid.*, *Solid State Commun.* **25**, 163 (1977).
- [145] M. Z. Maialle and M. H. Degani, *Phys. Rev. B* **83**, 155308, (2011).
- [146] I. Vurgaftman, J. R. Meyer, and L. R. Ram-Mohan, *J. Appl. Phys.* **89**, 5815 (2001).
- [147] R. Kosloff, *J. Phys. Chem.* **92**, 2087 (1988).

-
- [148] M. H. Degani and J. P. Leburton, *Phys. Rev. B* **44**, 10901 (1991)
- [149] M. Kumagai and T. Takagahara, *Phys. Rev. B* **40**, 12359 (1989).
- [150] T. E. Cook, Jr., C. C. Fulton, W. J. Mecoouch, R. F. Davis, G. Lucovsky, and R. J. Nemanich, *J. Appl. Phys.* **94**, 7155 (2003).
- [151] R. Y. Korotkov, J. M. Gregie, and B. W. Wessels, *Appl. Phys. Lett.* **80**, 1731 (2002).
- [152] C. I. Wu and A. Kahn, *J. Appl. Phys.* **86**, 3209 (1999).

Appendix A

Publications related to this thesis

- A. A. Sousa, Andrey Chaves, G. A. Farias, and F. M. Peeters, *Braess paradox at the mesoscopic scale*, Physical Review B, **88**, 245417 (2013), DOI:10.1103/PhysRevB.88.245417
- T. A. S. Pereira, A. A. Sousa, M. H. Degani, G. A. Farias, *Dielectric mismatch and shallow donor impurities in GaN/HfO₂ quantum wells*, Physica E, **66**, 81-86 (2015), DOI: <http://dx.doi.org/10.1016/j.physe.2014.10.005>
- A. A. Sousa, A. Chaves, T. A. S. Pereira, G. A. Farias, and F. M. Peeters, *Wave packet propagation through branched quantum rings*, Submitted at journal physics of condensed matter
- A. A. Sousa, A. Chaves, T. A. S. Pereira, G. A. Farias, and F. M. Peeters, *Quantum tunneling between bent semiconductor nanowires*, Submitted at Journal of Applied Physics

Braess paradox at the mesoscopic scaleA. A. Sousa,^{1,2,*} Andrey Chaves,^{1,†} G. A. Farias,¹ and F. M. Peeters^{2,1,‡}¹*Departamento de Física, Universidade Federal do Ceará, Caixa Postal 6030, Campus do Pici, 60455-900 Fortaleza, Ceará, Brazil*²*Department of Physics, University of Antwerp, Groenenborgerlaan 171, B-2020 Antwerp, Belgium*

(Received 24 June 2013; revised manuscript received 2 October 2013; published 11 December 2013)

We theoretically demonstrate that the transport inefficiency recently found experimentally for branched-out mesoscopic networks can also be observed in a quantum ring of finite width with an attached central horizontal branch. This is done by investigating the time evolution of an electron wave packet in such a system. Our numerical results show that the conductivity of the ring does not necessarily improve if one adds an extra channel. This ensures that there exists a quantum analog of the Braess paradox, originating from quantum scattering and interference.

DOI: [10.1103/PhysRevB.88.245417](https://doi.org/10.1103/PhysRevB.88.245417)

PACS number(s): 73.63.-b, 85.35.Ds

I. INTRODUCTION

Suppose that two points A and B of a network are connected only by two possible paths (e.g., roads in a traffic network, or wires in an electricity network). One would intuitively expect that adding a third path to the network that connects these two points would lead to an improvement of the flux through the preexisting roads and, consequently, to a transmission enhancement. However, the so-called Braess paradox¹⁻³ of game theory states that this is not necessarily the case: Under specific conditions,⁴ adding a third path to a network instead may lead to transport inefficiency. This effect has been observed even in traffic networks in big cities, where *closing* roads *improves* the flux in traffic jams,⁵ or in electricity networks, where it has been demonstrated that adding extra power lines may lead to power outages, due to desynchronization.⁶⁻⁸

A recent paper⁹ showed both experimental and theoretical evidence of a very similar effect, but on a mesoscopic scale: They observed that branching out a mesoscopic network does not always improve the electrons' conductance through the system. As they were dealing with a system consisting of wide transmission channels, quantum interference effects are not expected to be relevant.¹⁰

In this paper, we demonstrate that the transport inefficiency in branched-out devices also occurs on a nanoscale, when only a few subbands are involved, and transport is strongly influenced by quantum effects. For this purpose, we investigate wave packet propagation through a circular quantum ring attached to input (left) and output (right) leads,¹¹ in the presence of an extra channel passing diametrically through the ring. Our results demonstrate that increasing the extra channel width does not necessarily improve the overall current. The fundamental reasons behind this effect, which are related to quantum scattering and interference, are discussed in detail in the following sections.

II. THEORETICAL MODEL

We consider an electron confined in a circular quantum ring attached to input (left) and output (right) leads,¹¹ in the presence of an extra channel passing diametrically through the ring, as sketched in Fig. 1(a). Both the ring and the leads

are assumed to have the same width $W = 10$ nm, whereas different values of the extra channel width W_c are considered.

As the initial wave packet, we consider a plane wave with wave vector $k_0 = \sqrt{2m_e\epsilon}/\hbar$, where ϵ is the energy and m_e is the electron effective mass, multiplied by a Gaussian function in the x direction, and by the ground state $\phi_0(y)$ of the input channel in the y direction,

$$\Psi(x, y, 0) = \exp\left[ik_0x - \frac{(x - x_0)^2}{2\sigma_x^2}\right] \phi_0(y). \quad (1)$$

Several papers have reported calculations on wave packet propagation in nanostructured systems,¹²⁻¹⁵ hence, a number of numerical techniques for this kind of calculation is available in the literature, such as the expansion of the time-evolution operator in Chebyshev polynomials,¹⁶ and Crank-Nicolson based techniques.¹⁷ In the present work, the propagation of the wave packet in Eq. (1) is calculated by using the split-operator technique^{11,18,19} to perform successive applications of the time-evolution operator, i.e., $\Psi(x, y, t + \Delta t) = \exp[-iH\Delta t/\hbar]\Psi(x, y, t)$, where Δt is the time step. The Hamiltonian H is written within the effective mass approximation, describing an electron constrained to move in the (x, y) plane and confined, by external potential barriers of height V_0 , to move inside the nanostructured region represented in gray in Fig. 1(a), where the potential is set to zero. The interface between the confinement region and the potential barrier is assumed to be abrupt. Nevertheless, considering smooth potential barriers would not affect the qualitative behavior of the results to be presented here, since the effect of such smooth interfaces has been demonstrated to be mainly a shift on the eigenenergies of the system.^{20,21} The (x, y) plane is discretized in a $\Delta x = \Delta y = 0.4$ nm grid, and the finite difference technique is used to perform the derivatives coming from the kinetic energy terms of the Hamiltonian. Imaginary potentials²² are placed on the edges of the input and output channels in order to absorb the propagated wave packet and avoid spurious reflection at the boundaries of the computational box. As the wave packet propagates, we compute the probability density currents at the input and output leads, which, when integrated in time, gives us the reflection and transmission probabilities, respectively, from which the conductance can be calculated.

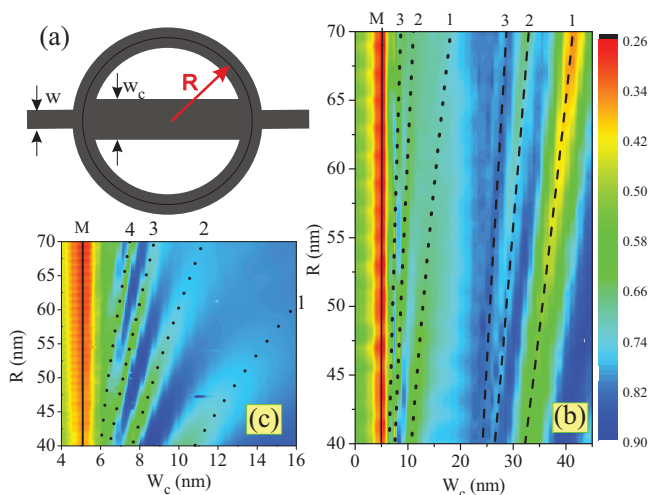


FIG. 1. (Color online) (a) Sketch of the system under investigation: A quantum ring with average radius R , attached to input (left) and output (right) channels with the same width as the ring ($W = 10$ nm), and to an extra horizontal channel of width W_c . (b) Contour plots of the transmission probabilities as a function of the extra channel width and ring radius. The solid, dashed, and dotted lines indicate seven minima that are discussed in the text. A zoom of the 4 nm $< W_c < 16$ nm region with the logarithm of the transmission is shown in (c).

As the fabrication of InGaAs quantum ring structures has already been reported in the literature,²³ we assume that the ring, channel, and leads in our model are made out of this material, so that the electron effective mass is taken as $m_e = 0.041m_0$. Nevertheless, the qualitative features of the results presented in the following section do not depend on specific material parameters.

III. RESULTS AND DISCUSSION

Contour plots of the calculated transmission probabilities are shown in Fig. 1(b) as a function of the ring radius R and the width W_c of the extra channel. Notice that the extra channel in the system is opened in the horizontal direction, namely, parallel to the input and output leads, being practically just a continuation of these leads. Even so, instead of improving the transmission, the existence of such a channel surprisingly *reduces* the transmission probability for specific values of W_c , leading to several minima in each curve. In what follows, we discuss the origin of several of these minima, indicated by the solid, dashed, and dotted curves in Fig. 1(b).

The position of the minima labeled as 1, 2, and 3 in Figs. 1(b) and 1(c) changes with the ring radius, which indicates that these minima are related to a path difference, i.e., to an interference effect. Let us provide other arguments to support this indication: In a very simplistic model, consider that part of the wave packet travels through the central channel, while the other part passes through the ring arms. The latter runs a length $\approx \pi R$ while going from the input to output leads, whereas the former runs through the $2R$ diameter of the ring. The condition for destructive interference is

$$\gamma \frac{\pi R}{\lambda} - \frac{2R}{\bar{\lambda}} = n + \frac{1}{2}, \quad (2)$$

where $\lambda = 2\pi/\sqrt{2m_e\epsilon/\hbar^2}$ [$\bar{\lambda} = 2\pi/\sqrt{2m_e(E - \bar{E}_j)/\hbar^2}$] is the wavelength in the ring arms (extra channel), E_i (\bar{E}_j) is the energy of the i th (j)th eigenstate of the input lead (extra channel), and $E = \epsilon + E_i$ is the total energy of the wave packet. The parameter γ is close to one and accounts for the fact that the effective arm length may be slightly different from πR [see Fig. 1(a)]. By substituting these expressions for λ and $\bar{\lambda}$ in Eq. (2), one obtains

$$\bar{E}_j = E - \frac{\hbar^2\pi^2}{2m_e} \left[\frac{\gamma}{2} \sqrt{\frac{2m_e}{\hbar^2}} \epsilon - \left(n + \frac{1}{2}\right) \frac{1}{R} \right]^2. \quad (3)$$

Hence, this equation gives the condition for the interference related minima in the transmission probability. The extra channel eigenstates \bar{E}_j depend on W_c —which can be fairly well approximated by $\bar{E}_j \simeq \beta/W_c^{1.85}$ for large W_c (notice that the structure has finite potential barriers, therefore, the infinite square well relation $\bar{E}_j \propto 1/W_c^2$ is no longer valid). Therefore, the minima for large W_c are expected to occur for

$$W_c^{(n)} = \left\{ \frac{\beta}{E - \frac{\hbar^2\pi^2}{2m_e} \left[\frac{\gamma}{2} \sqrt{\frac{2m_e}{\hbar^2}} \epsilon - \left(n + \frac{1}{2}\right) \frac{1}{R} \right]^2} \right\}^{1/1.85}, \quad (4)$$

which are shown in Fig. 1(b) by black dashed lines for $n = 1, 2$, and 3 . The model fits very well the numerically obtained positions for these minima for $\gamma = 0.865$. The $n = 0$ minimum occurs outside of the investigated range W_c . The wave packet in this case has a total energy $E = 124$ meV, with $\epsilon = 70$ meV and $E_0 = 54$ meV (ground state of the $W = 10$ nm input lead). For the 26 nm $< W_c < 42$ nm range in Fig. 1(b), the eigenstates of the channel, which are accessible by the electron with this energy, are the ground state and the second excited state. The first and third excited states, although still having energy lower than 124 meV for this range of W_c , are not accessible by the wave packet because of the even symmetry of the initial wave packet with respect to the x axis, while these excited states of the channel are odd. Therefore, the part of the wave packet that goes through the central channel under these conditions populates mostly the second excited state, but has also some projection on the ground state and none on the other states. The fitting of \bar{E}_j for the second excited state ($j = 2$) has $\beta \approx 3000$ meV nm^{1.85}, which is the value used in Eq. (4) to obtain the dashed curves in Fig. 1(b).

The $n = 1, 2$, and 3 minima occurring for 7 nm $< W_c < 15$ nm in Fig. 1(b) can also be obtained from Eq. (4) but, since this is a lower W_c range, the dependence of \bar{E}_j on W_c will have a different exponent, and one needs to replace 1.85 by 1.50 in Eq. (4). Besides, for such low W_c , the wave function travels predominantly through the ground state subband of the extra channel, so that one must consider the $j = 0$ state of this channel, which has $\beta \approx 56.99$ meV nm^{1.50} in this range. The results for this model are shown as black dotted lines in Fig. 1(b). To show these minima more clearly, we present in Fig. 1(c) a magnification of the logarithm of the probability in the low W_c region. The numerically obtained minima are well fitted by the model of Eq. (4) for $\gamma = 0.925$ with $n = 1, 2, \dots, 4$ (see dotted lines).

In order to demonstrate that for lower (higher) values of W_c the wave function inside the extra channel is predominantly

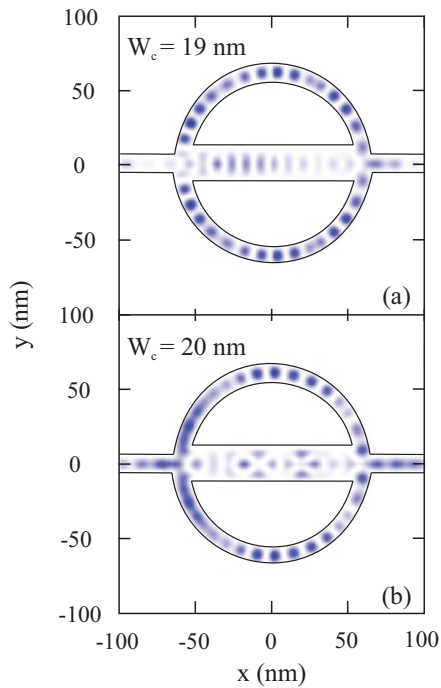


FIG. 2. (Color online) Snapshot of the propagating wave function at $t = 900$ fs for two values of the extra channel width: (a) 19 nm and (b) 20 nm.

in its ground (second excited) state, Fig. 2 shows a snapshot of the propagating wave function at $t = 900$ fs for two values of the extra channel width: $W_c = 19$ nm (a) and 20 nm (b). In the former case, the wave function inside the extra channel exhibits predominantly a single maximum peak around $y = 0$, which suggests a large contribution of the ground state eigenfunction in the wave packet within this region. Similar results are obtained for lower values of the channel width W_c . However, the results for a slightly larger $W_c = 20$ nm are qualitatively different, exhibiting three peaks along the y direction inside the extra channel, which implies a higher contribution of the second excited state on the wave function in this region.

Differently from the other minima, the position of the first minimum M in Fig. 1(b) appears around $W_c = 5$ nm and does not change with the radius R . Therefore, this minimum cannot be related to the above discussed interference effect. In order to understand the origin of the M minima, we show in Fig. 3 the integrated current J_t in the input lead and the extra channel. Figure 3(a) exhibits a high negative peak for $W_c = 2$ and 5 nm at ≈ 100 and ≈ 140 fs, respectively, which represents a strong reflection of the wave packet at the ring-channel junction.²⁴ This is confirmed by the very low currents observed for these cases inside the extra channel, in Fig. 3(b). On the other hand, for $W_c = 7$ nm the reflection peak in the input lead becomes very weak, while for $W_c = 10$ nm almost no reflection is observed. For the latter two cases instead, large current peaks are observed inside the extra channel. This is a clear indication that the transmission inefficiency in the low W_c case is not related to interference effects, but rather to scattering at the ring-channel junction, since the wave packet barely enters the extra channel when it is too narrow.

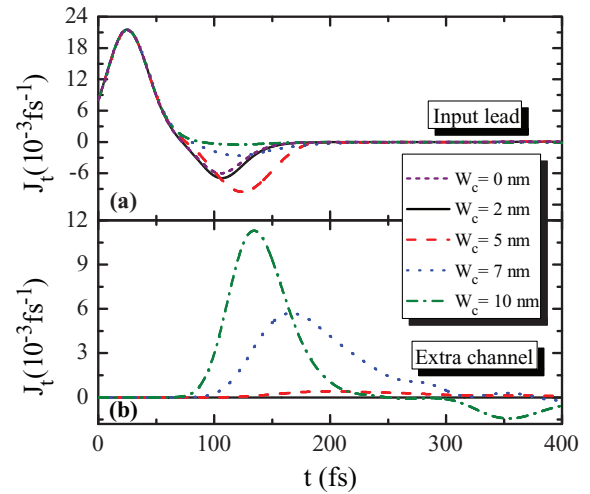


FIG. 3. (Color online) Probability density currents as a function of time, calculated (a) in the input lead and (b) in the extra channel, for different values of the extra channel width W_c , for wave packet energy $\epsilon = 70$ meV.

We discuss now the possibility of having part of the incoming wave packet pass through a narrow extra channel. Both the leads and the extra channel have discrete eigenstates due to the quantum well confinement in the y direction, whose energy levels are shown in Fig. 4(a) as a function of the well width. In the x direction, parabolic subbands stem from these eigenstates, as illustrated in Fig. 4(b). The incoming wave packet considered in Figs. 1–3 has $\epsilon = 70$ meV on top of its ground state energy in the input lead, $E_0 = 54$ meV (for $W = 10$ nm). This energy is represented by the dotted horizontal lines in Figs. 4(a) and 4(b). The wave packet has a Gaussian distribution of energies of width $\Delta E = \hbar^2/m_e k_0 \Delta k$, where $\Delta k = 2\sqrt{\ln 2}/\sigma_x$ is the full width at half maximum (FWHM) of the wave vector distribution, which is represented by the shaded area around the dotted line in Fig. 4(a). A narrow extra channel has a very high ground state subband energy, so that no component of the incoming wave packet energy has enough energy to pass through the channel. As

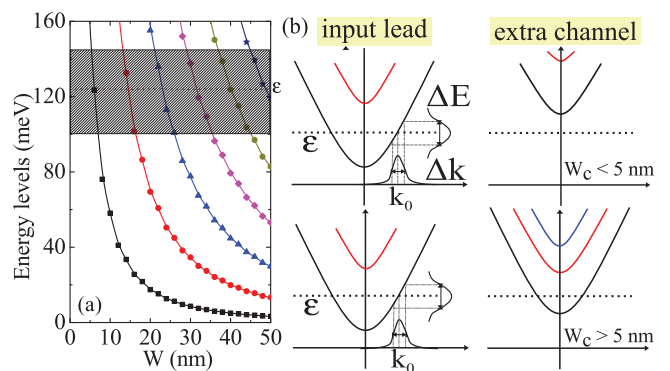


FIG. 4. (Color online) (a) Eigenstates of a finite quantum well as a function of its width. (b) Diagram representing the energy subbands in the input lead and in the extra channel. The horizontal dotted line is the average energy of the wave packet used in Figs. 1 and 3, and the shaded area in (a) illustrates the FWHM of the energy distribution of this wave packet.

the extra channel width W_c increases, its subband energies decrease, allowing the incoming wave packet to travel through this channel. These two situations are illustrated in the upper and lower figures of Fig. 4(b), respectively. Notice that the upper boundary of the energy distribution (shaded area) in Fig. 4(a) is crossed by the second excited state energy curve (blue triangles) approximately at $W = 20$ nm. This explains the drastic difference between the wave functions within the extra channel with $W_c = 19$ and 20 nm, observed in Fig. 2: In the latter case, the wave function has a significantly larger part of its energy distribution above the second excited state energy, allowing it to have a larger projection on this state.

Therefore, the counterintuitive result observed in Fig. 1, namely, the transmission reduction as the extra channel width increases for lower values of W_c , is a pure quantum scattering effect. For classical particles, such an extra channel with any width would allow the passage of the particles and, consequently, improve the transmission. However, a quantum channel has a confinement energy (ground state) and, if the energy of the incoming particle is lower than this minimum, the particle is not allowed to pass through the channel. Therefore, adding a narrow extra channel to the system, which effectively also adds extra scattering, does not add an extra path for the wave packet, because of the very high ground state energy of the narrow channel. This mechanism, which is illustrated by the band diagrams in Fig. 4(b), leads to the strong reflections observed in Fig. 3 for $W_c = 2$ and 5 nm. For $W_c > 5$ nm, a significant part of the $E = 70$ meV wave packet has enough energy to go through the extra channel, explaining the increasing transmission as W_c increases above 5 nm. This also suggests that incoming wave packets with higher energy would need lower extra channel widths to pass, which is indeed observed, as we will discuss further on.

In fact, the position of M strongly depends on the wave packet energy, as shown in Fig. 5(a), where the transmission probability in the vicinity of M is plotted as a function of the channel width W_c for several values of the energy, ranging from 70 meV (bottom curve) to 120 meV (top curve), with 10 meV intervals. The ring radius is fixed as $R = 60$ nm, and each consecutive curve in this figure is shifted by 0.1 . If the energy dependence of the position of M is due to the above discussed quantum effect, it should be possible to predict the position of these minima from the following argument: The highest energy components of the wave packet have energy around $\approx E + \Delta E/2$. These components would be allowed to pass through the extra channel, consequently improving the current, provided the channel width is wide enough to have a ground state energy as low as their energy, i.e., if $\bar{E}_0 < E + \Delta E/2$. For low values of W_c , the ground state energy of the channel is well approximated by $\bar{E}_0 = \alpha/W_c^{1.04}$, for $\alpha = 8.65$ eV, as shown by the green dashed line [$f_2(W)$ function] in Fig. 5(b). Notice it is a different power from the one used in Eq. (4), which is valid only for higher W_c values. The red dotted line [$f_1(W)$ function] in Fig. 5(b) is an example of fitting for high values of W_c , which was used in Eq. (4). Figure 5(b) is in log-log scale, so that the power laws in $f_1(W)$ and $f_2(W)$ are shown as straight curves, whose slopes are the functions' exponents. Using this expression for \bar{E}_j , one obtains the following approximate expression for the position

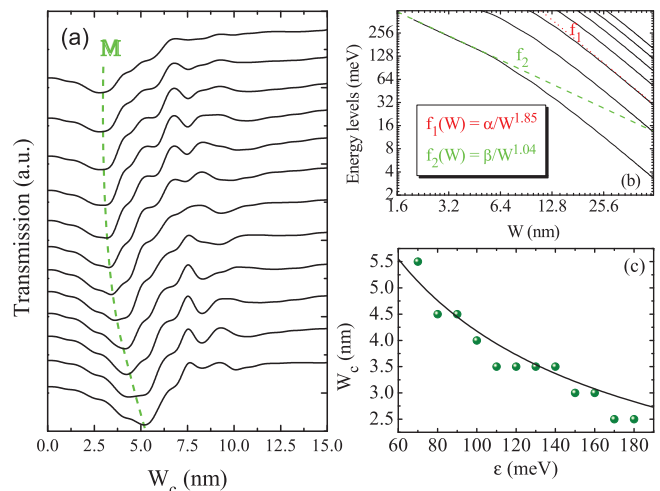


FIG. 5. (Color online) (a) Transmission probabilities as a function of the extra channel width in the vicinity of the minimum labeled as M in Fig. 1(a), for several values of the wave packet energy $\epsilon = 70$ (bottom curve), $80, \dots, 180$ meV (top curve). The curves were shifted 0.1 up from each other in order to help visualization. (b) Energy levels (solid) as a function of the channel width, plotted in a log scale, along with two fitting functions (dashed curves), for large (f_1) and small (f_2) values of the channel width. (c) Numerically obtained (symbols) positions of the M minima as a function of the wave packet energy, along with the results (solid curve) of the analytical model, given by Eq. (5).

of the M minima,

$$W_c^{(M)} = \frac{6103}{\left(\epsilon + E_0 + \hbar \sqrt{\frac{\epsilon}{2m_e}} \Delta k\right)^{1/1.04}}, \quad (5)$$

which is shown by the solid curve in Fig. 5(c). Notice the rather good agreement with the numerically obtained positions of the M minima, represented by the symbols.

It is important to point out that the exponents 1.85 , 1.50 , and 1.04 , as well as the values of α and β , found for the fitting functions for the eigenstate energies as a function of the well width and used in Eqs. (4) and (5) were obtained for an abrupt interface between the potential barriers and the confining region. These values must be slightly modified in the case of smooth potential barriers.

Our results, therefore, demonstrate that the M minima in Figs. 1 and 5 are a consequence of a competition between two effects: (i) the quantum scattering in the ring-channel junction, which increases the reflection when a narrow extra channel is added, and (ii) the improvement in the transmission resulting from the part of the wave packet that has enough energy to propagate through the subbands of the extra channel. The former suggests that adding extra scatterers at the input lead-ring junction leads to a larger reflection back into the input lead. In order to verify this, we consider two situations that mimic the appearance of an extra “blind” channel (see the insets of Fig. 6): One is the presence of an attractive Gaussian potential¹¹ $V_a(x, y) = -V_G \exp\{[(x - x_g)^2 + y^2]/2\sigma_G^2\}$ close to the lead-ring junction, and the other is a circular bump of radius R_b in the inner boundary of the ring. Figure 6 shows

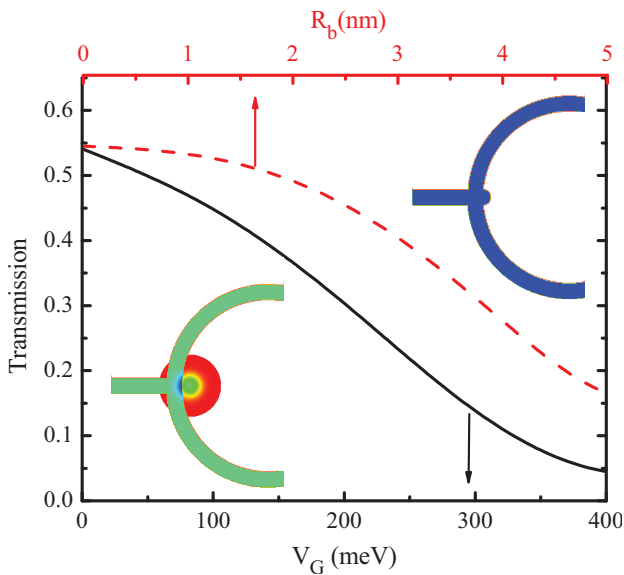


FIG. 6. (Color online) Transmission probabilities for a $\epsilon = 70$ meV wave packet scattered by two kinds of defects in the lead-ring junction: A Gaussian attractive potential of depth V_G (solid, bottom axis) and width $\sigma_G = 5$ nm, and a circular bump of radius R_b (dashed, top axis), which are schematically illustrated in the lower and upper insets, respectively.

the transmission probabilities for $\epsilon = 70$ meV as a function of the Gaussian potential depth V_G (bottom axis) and the radius R_b (top axis) of the circular bump. In both cases, the transmission is reduced in the presence of the extra scatterer, which supports the idea that the transmission reduction in the low W_c range in Figs. 1 and 5 is indeed a consequence of extra scattering created by the opening of the extra channel, which is, however, effectively blind, since the bottom of the ground state subband of the narrow channel has energy higher than that of the incoming electron wave packet.

All the results in this work were calculated for sharp connections between the ring, the extra channel, and the input and output leads. However, qualitatively similar results are also obtained for smooth junctions¹¹ between these parts of the system. Moreover, different ring geometries would shift the high W_c minima, which are related to quantum interference, by effectively changing the electronic paths, while impurities in the ring could suppress these minima by destroying phase coherence. However, neither impurities nor different ring geometries can affect the low W_c minimum (M), since it is related only to quantum scattering in the input lead-ring junction, which does not depend on these features.

The original version of the Braess paradox, described in detail in Ref. 1, discusses how the travel time between two points connected by only two possible roads, A and B, changes if these two roads are interconnected by a third road C. If one considers that the traffic at specific parts of A and B depends on the number of drivers on these roads, then, depending on the (partial) travel time through this new connection C, the dominant strategy turns out to consist in starting on one road and changing to the other road through the connection C,

and therefore all players (drivers) would take this path. This strategy, though leading to the Nash equilibrium situation of this system, represents an increase in the travel time—lower travel times could even be reached if the drivers agree not to use the connection C *a priori*, but in a scenario of selfish drivers, they would switch roads until the equilibrium is reached, despite the reduction in overall performance. Therefore, the classical Braess paradox is closely related to an unsuccessful attempt to optimize the travel time through a traffic network by the drivers. The transport properties of the branched-out mesoscopic network investigated in Refs. 9 and 10 is reminiscent of those of the road network in the original Braess paper just in the sense that it exhibits a reduced overall current when an extra channel is added to the network, depending on the channel width. However, the fundamental reason behind this phenomenon is not clear in Refs. 9 and 10—it cannot be an interference effect, since this is not a coherent system, but it is not also due to an optimization of the currents, as in the classical paradox, since the model in these papers does not involve nonlinear equations or iterative calculations of the overall current flow. On the other hand, for the quantum case investigated here, where such a transmission reduction in the presence of an extra channel is also observed, the main reason behind this Braess-like paradoxical behavior is quite clear: For small values of the channel width it is due to quantum scattering effects at the ring-channel junction, whereas for larger widths it is due to interference effects. Therefore, if one includes the transmission reduction phenomena described here into the category of analogs of the Braess paradox, one must keep in mind that, just as most of the other analogs suggested in the literature,^{6–9} although presenting results similar to those of the original Braess network, in the sense that more paths lead to reduced performance, the reason behind this reduction is not related to an attempt to optimize the flux, but to other fundamental physical properties of the investigated system.

IV. CONCLUSIONS

We have investigated the propagation of a wave packet through a quantum ring with an extra channel along its diameter. Surprisingly, our results demonstrate that even when an extra channel is added in the horizontal direction, as a continuation of the input and output leads, the transmission through the whole system can be lower than in the absence of such an extra current path. This is evidence of the “Braess paradox analog” observed recently for mesoscopic networks. Nevertheless, while the original Braess paradox in game theory is explained in terms of an attempt to optimize the flux, which eventually leads to transport inefficiency in the equilibrium situation, the transport inefficiency observed for the wave packet propagation in quantum systems originates from two possible effects: (i) the quantum scattering of the wave packet in the input channel-ring junction, along with the absence of an allowed energy subband for propagation in the central channel when it is too narrow, and (ii) the quantum interference between parts of the wave packets that passed through the central channel and those that propagated through the ring arms.

ACKNOWLEDGMENTS

This work was financially supported by PRONEX/CNPq/FUNCAP and the bilateral project CNPq-FWO.

Discussions with J. S. Andrade, Jr. are gratefully acknowledged. A.A.S. has been financially supported by CAPES, under PDSE Contract No. BEX 7177/13-5.

*ariel@fisica.ufc.br

†andrey@fisica.ufc.br

‡francois.peeters@ua.ac.be

¹D. Braess, A. Nagurney, and T. Wakolbinger, *Transp. Sci.* **39**, 446 (2005) [English translation of D. Braess, *Unternehmensforschung* **12**, 258 (1968) (in German)].

²J. E. Cohen and F. P. Kelly, *J. Appl. Probab.* **27**, 730 (1990).

³H. Lin, T. Roughgarden, É. Tardos, and A. Walkover, *SIAM J. Discrete Math.* **25**, 1667 (2011).

⁴Y. Xia and D. J. Hill, *IEEE Trans. Circuits Syst., II* **60**, 172 (2013).

⁵V. Zverovich and E. Avineri, arXiv:1207.3251; see also G. Kolata, "What if They Closed 42nd Street and Nobody Noticed?," *N. Y. Times* (N. Y. Ed.), 25 December 1990, p. 38, <http://www.nytimes.com/1990/12/25/health/what-if-they-closed-42d-street-and-nobody-noticed.html>

⁶J. E. Cohen and P. Horowitz, *Nature (London)* **352**, 699 (1991).

⁷D. Witthaut and M. Timme, *New J. Phys.* **14**, 083036 (2012); *Eur. Phys. J. B* **86**, 377 (2013).

⁸M. Rohden, A. Sorge, M. Timme, and D. Witthaut, *Phys. Rev. Lett.* **109**, 064101 (2012).

⁹M. G. Pala, S. Baltazar, P. Liu, H. Sellier, B. Hackens, F. Martins, V. Bayot, X. Wallart, L. Desplanque, and S. Huant, *Phys. Rev. Lett.* **108**, 076802 (2012).

¹⁰M. G. Pala, H. Sellier, B. Hackens, F. Martins, V. Bayot, and S. Huant, *Nanoscale Res. Lett.* **7**, 472 (2012).

¹¹A. Chaves, G. A. Farias, F. M. Peeters, and B. Szafran, *Phys. Rev. B* **80**, 125331 (2009).

¹²S. S. Buchholz, S. F. Fischer, U. Kunze, D. Reuter, and A. D. Wieck, *Appl. Phys. Lett.* **94**, 022107 (2009).

¹³C. Kreisbeck, T. Kramer, S. S. Buchholz, S. F. Fischer, U. Kunze, D. Reuter, and A. D. Wieck, *Phys. Rev. B* **82**, 165329 (2010).

¹⁴H. Fehske, J. Schleede, G. Schubert, G. Wellein, V. S. Filinov, and A. R. Bishop, *Phys. Lett. A* **373**, 2182 (2009).

¹⁵B. Szafran and F. M. Peeters, *Phys. Rev. B* **72**, 165301 (2005).

¹⁶A. Alvermann and H. Fehske, *Phys. Rev. B* **77**, 045125 (2008).

¹⁷M. R. Poniedzialek and B. Szafran, *J. Phys.: Condens. Matter* **24**, 085801 (2012).

¹⁸M. H. Degani, *Appl. Phys. Lett.* **59**, 57 (1991).

¹⁹M. H. Degani and M. Z. Maialle, *J. Comput. Theor. Nanosci.* **7**, 454 (2010).

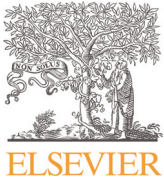
²⁰H. Wang, G. A. Farias, and V. N. Freire, *Superlattices Microstruct.* **25**, 307 (1999).

²¹J. A. K. Freire, G. A. Farias, and V. N. Freire, *Solid State Commun.* **106**, 559 (1998).

²²D. E. Manolopoulos, *J. Chem. Phys.* **117**, 9552 (2002).

²³B. Hackens, F. Martins, T. Ouisse, H. Sellier, S. Bollaert, X. Wallart, A. Cappy, J. Chevrier, V. Bayot, and S. Huant, *Nat. Phys.* **2**, 826 (2006).

²⁴The high positive peak in the input channel is just the incoming wave packet.



Dielectric mismatch and shallow donor impurities in GaN/HfO₂ quantum wells



T.A.S. Pereira^a, A.A. Sousa^{b,*}, M.H. Degani^c, G.A. Farias^b

^a Instituto de Física, Universidade Federal de Mato Grosso, 78060-900 Cuiabá, Mato Grosso, Brazil

^b Departamento de Física, Universidade Federal do Ceará, Caixa Postal 6030, 60455-900 Fortaleza, CE, Brazil

^c Faculdade de Ciências Aplicadas, Universidade Estadual de Campinas - UNICAMP, R. Pedro Zaccaria, 1300, 13484-350 Limeira, SP, Brazil

ARTICLE INFO

Article history:

Received 5 May 2014

Received in revised form

12 September 2014

Accepted 10 October 2014

Available online 16 October 2014

Keywords:

Quantum well

Hydrogenic impurity

Image potential

ABSTRACT

In this work we investigate electron–impurity binding energy in GaN/HfO₂ quantum wells. The calculation considers simultaneously all energy contributions caused by the dielectric mismatch: (i) image self-energy (i.e., interaction between electron and its image charge), (ii) the direct Coulomb interaction between the electron–impurity and (iii) the interactions among electron and impurity image charges. The theoretical model account for the solution of the time-dependent Schrödinger equation and the results shows how the magnitude of the electron–impurity binding energy depends on the position of impurity in the well–barrier system. The role of the large dielectric constant in the barrier region is exposed with the comparison of the results for GaN/HfO₂ with those of a more typical GaN/AlN system, for two different confinement regimes: narrow and wide quantum wells.

© Elsevier B.V. All rights reserved.

1. Introduction

When an impurity is introduced into a low dimensional structure, such as quantum wells (QW), nano wires (NW) and quantum dots (QD) the calculation of the electronic properties in this structures becomes considerably more complex if compared to that of a doped three-dimensional crystal [1–6]. This occurs because of the restricted movement in the structure growth direction, which is imposed by the potential due to band edges discontinuities ΔE . First, the binding energy of the carrier–impurity in the structure depends on the confinement potential ΔE , and second, both the binding energy and wave function of the carrier and impurity depends on the impurity position in the structure growth direction. On the other hand, due to recent progress in epitaxial crystal growth techniques, such as molecular beam epitaxy (MBE), research focusing on impurity and electronic states in nano-structures has attracted great attention [7,8]. However, effects caused by image charges due to the dielectric mismatch at the structure interface have been overlooked. Indeed, donor binding energy can be significantly modified by additional confinement effects that image charges distribution produce [9,10]. Thus, recent research focusing on high- k dielectrics based QWs and NWs reveals interesting results related to carrier confinement [11–14]. We recently demonstrate that the interaction between

carriers and their image charge, induced by the dielectric mismatch ($\epsilon_r = \epsilon_{\text{GaN}}/\epsilon_{\text{HfO}_2} = 9.5/25 = 0.38$), strongly modifies the electronic structure in GaN/HfO₂ QWs (and NWs) and for wide QWs (wide radii NWs) heavy holes are confined in interfacial regions, similar to that observed in type-II heterostructures [13,14]. Such interfacial confinement leads to drastic modifications on the electronic properties of the QWs and NWs. Particularly, for NWs under an applied magnetic field, where angular momentum transitions occur in the ground state due to the Aharonov–Bohr effect [14]. A decrease in the oscillator strength of electron–hole pairs in $\epsilon_r < 1$ QWs and NWs is also predicted for wide QW and larger wire radii, which directly affects their recombination rates [13,14].

In this work, we investigate electron–impurity binding energy in GaN/HfO₂ Qws. As for illustration we compared this results with those of a more typical AlN/GaN system. The presence of a point charge in a region where the dielectric constant is discontinuous induces polarization charges at the QW interfaces, and this problem can be solved by the image charges method [15]. As shown here, The electron energy, electron wave function and the electron–impurity binding energy can change significantly due to additional confinement effects produced by the image charge distribution. Our calculation considers simultaneously all energy contributions caused by the dielectric mismatch: (i) image self-energy (interaction between electron and its image charges), (ii) the direct Coulomb interaction between electron and the actual impurity, as well as (iii) the interactions among electron and impurity image charges. Moreover, from practical means, we also

* Corresponding author. Tel.: +55 85 33669018; fax: +55 85 33669450.

E-mail address: ariel@fisica.ufc.br (A.A. Sousa).

investigate stark effect and electron–impurity binding energy for two different confinement regimes: narrow (5 nm) and wide (10 nm) QWs. When compared to the effective Bohr's radius for the GaN bulk a_B^* ($= a_B \epsilon_{\text{GaN}} / m_e^* = 2.65$ nm; where $a_B = 0.53$ Å is the Bohr's radius) narrow and wide QWs used in this work are twice and four times the effective Bohr's radius, respectively. The binding energy of an electron bound to a hydrogenic impurity is obtained as function of the impurity position, by solving a fully three-dimensional time dependent Schrödinger equation using a method with neither adjustable parameters nor restrictive basis expansions as employed by almost all theoretical approaches in the literature [16–18]. For simplicity, we address zinc blende GaN instead of its wurtzite crystalline structure in order to avoid more complicated polarizations effects observed in this phase [19].

2. Theoretical model

2.1. Time-dependent Schrödinger equation

The theoretical method used to calculate the binding energy of an electron bound to a hydrogenic impurity is based on the adiabatic approximation. The time-dependent Schrödinger equation [20–23] is consistent with the effective mass approach and the envelope function formalism:

$$i\hbar \frac{\partial}{\partial t} \psi(r, t) = H\psi(r, t), \quad (1)$$

and describes the quantized states of a single particle coupled to a quantum well under the effect of impurity Coulomb potential and potential due to image charges. The Hamiltonian H is given by

$$H = \frac{1}{2} P \frac{1}{m^*(r)} P + V(r), \quad (2)$$

where $P = -i\hbar \nabla$ is the kinetic energy operator and $V(r)$ is the potential energy operator. The initial solution $\Psi(r, t)$ given by the method is

$$\Psi(r, t) = \exp\left(-\frac{i}{\hbar} \int_0^t H dt\right) \Psi(r, 0). \quad (3)$$

The Hamiltonian of Eq. (2) does not depend on time, so the integral in Eq. (3), solved in the range between t and $t + \Delta t$ is given by

$$\Psi(r, t + \Delta t) = \exp\left(-\frac{i}{\hbar} H \Delta t\right) \Psi(r, t), \quad (4)$$

which is approximated by the expression:

$$\Psi(r, t + \Delta t) = \exp[-iV(r)\Delta t/\hbar] \times \exp[-ip^2\Delta t/2m^*] \times \exp[-iV(r)\Delta t/\hbar] + O(\Delta t^3). \quad (5)$$

The error introduced in this expression, when we drop the term $O(\Delta t^3)$, results from the noncommutability of the kinetic and potential operators. The potential operator $V(r)$, with $r = (\rho_e, z_e, z_{im})$ and $\rho_e = \sqrt{x^2 + y^2}$, is given by

$$V(r) = \Delta E_e(z_e) + \Sigma_e(z_e) + V_{e-im}(r), \quad (6)$$

where $\Delta E_e(z_e)$ is the heterostructure band edge confinement, $\Sigma_e(z_e)$ is the self-energy potential and $V_{e-im}(r)$ is the direct electron–impurity Coulomb interaction. The last term includes direct electron–impurity Coulomb interaction and the interactions between electron and impurity image charges. This contribution to the total potential was deduced from solutions of the Poisson equation in 2D quantum structures, as shown in Eqs. (A21)–(A25) of Ref. [24]. Fig. 1 shows each potential given by Eq. (6), for a 5 nm QW: Fig. 1

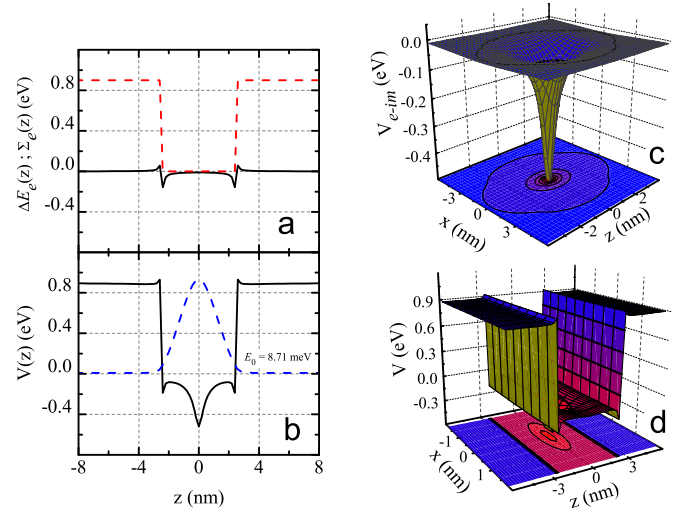


Fig. 1. (Color online) (a) Energy potential $\Delta E_e(z_e)$ due to conduction band edge discontinuity (red dashed line) and the potential $\Sigma_e(z_e)$ due to self-energy corrections (black solid line). (b) Total potential $V(r) = \Delta E_e(z_e) + \Sigma_e(z_e) + V_{e-im}(r)$ in the z direction (black solid line) and electron ground state wave function (blue dashed line). (c) Coulomb potential $V_{e-im}(r)$ of electron–impurity interaction in 3D plot. (d) Total potential $V(r)$ in 3D plot.

(a) shows the potential due to band edges confinement $\Delta E_e(z_e)$ (red dashed line) and the self-energy potential $\Sigma_e(z_e)$ (black solid line), which is attractive (repulsive) for charge on the low (high) dielectric constant side ($\epsilon_{\text{GaN}} < \epsilon_{\text{HfO}_2}$). The attractive potential on the well region produce cusps that appears near the edges of the interface transition layers, shown in the total potential depicted in Fig. 1(b). For the purpose of our analyses, we plot in Fig. 1(c) and (d) the potential $V_{e-im}(r)$, due to direct electron–impurity Coulomb interaction, and the total potential $V(r)$ in a three-dimensional space, respectively.

The eigenstates of the Hamiltonian are calculated by using a propagation scheme in the imaginary time domain. [22] Any wave function can be written as a linear combination of the eigenstates of a Hamiltonian, since it forms a complete orthogonal basis:

$$|\Psi\rangle_t = \sum_{n=0}^{\infty} a_n e^{-iE_n t/\hbar} |\varphi_n\rangle, \quad (7)$$

where φ_n and E_n are the eigenfunction and eigenenergy of the n th eigenstate, respectively. Using $\tau = it$,

$$|\Psi\rangle_t = \sum_{n=0}^{\infty} a_n e^{-E_n \tau/\hbar} |\varphi_n\rangle = e^{-E_0 \tau/\hbar} \left[a_0 |\varphi_0\rangle + \sum_{n=1}^{\infty} a_n e^{-(E_n - E_0)\tau/\hbar} |\varphi_n\rangle \right]. \quad (8)$$

After several imaginary-time steps of propagation ($\tau \rightarrow \infty$), the term of the ground state, $e^{-E_0 \tau/\hbar} a_0 |\varphi_0\rangle$, becomes strongly dominant over the terms of the sum, since $E_n - E_0 > 0$ for $n > 0$. Therefore, starting with any wave function, this function should converge to the ground state of the system as τ increases. We can consider as a very long time those in which $\tau \gg \hbar/(E_n - E_0)$. The excited states are obtained adding to the algorithm the Gram-Schmidt orthonormalization method which will assure orthonormality between all states in each time step.

2.2. Self-energy potential

In order to calculate the effects of the self-energy potential $\Sigma_e(z_e)$, shown in Fig. 1(a) (black solid line), on the electron energy we use the method based on image charges. The electrostatic potential due to a charge Q located at $r = (0, 0, z_0)$, in a medium

where the dielectric constant $\epsilon(z)$ depends on the position is given by

$$\nabla \cdot [\epsilon(z) \nabla \phi(r)] = -Q\delta(r - r_0). \quad (9)$$

The solution in cylindrical coordinates is independent of the azimuth angle (see detail in References [15,13]). In this case, we can write $\phi(r)$ in the general series as

$$\phi(r) = \int_0^\infty q J_0(qR) A_q(z) dq, \quad (10)$$

where $J_0(qR)$ is the Bessel function of the zeroth order, $A_q(z)$ is a function determined by the boundary conditions of $\phi(r)$ at the interfaces. The solution for the image self-energy potential $\Sigma_e(z_e)$ is

$$\Sigma_e(z_e) = \frac{Q}{2} \int_0^\infty q [A_q(z_0) - A_q^0(z_0)] dq, \quad (11)$$

where $A_q^0(z_0)$ is solution of Eq. (10) if ϵ is z independent. Without loss of generality, we shall here consider QWs with abrupt interface. The self-energy potential $\Sigma_e(z_e)$ diverges at the interface $z = \pm L/2$ and we employ a numerical grid such that the coordinate in $z = \pm L/2$ does not sit at a grid point in order to avoid the divergence problem. The major results for $\Sigma_e(z_e)$ can be seen in the Reference [13] and will not be repeat here.

3. Results and discussion

As in the case of a model structure, QWs are formed by a zinc blende GaN layer ranging in the region $|z| \leq a$ between two HfO₂ layers in the region $|z| \geq a$. Between these materials, we consider the existence of abrupt interfaces at a position along the z axis. The GaN electron effective mass were taken from experiments ($m_e^* = 0.19$) [19], and for simplicity, we have considered the electron effective mass invariable along z . Although photoemission spectroscopy experiments demonstrated that $\Delta E_e = 2.1$ eV for wurtzite GaN/HfO₂ interfaces [25], the absence of this information for the zinc blende heterojunction leads us to estimate these quantities through the simple electron affinity model [26,27], for which we obtain $\Delta E_e = 0.9$ eV. As shown in Fig. 1, the quantum well has mirror symmetry from the origin in the z direction, at $z=0$, and the reference of the total potential $V(z)$ in Eq. (6) is taken with respect to the zero level of the potential $\Delta E_e(z)$, as shown in Fig. 1(a).

The impurity can be placed at any position along z direction, and two particular positions are shown in Fig. 2. Fig. 2(a) depicted the total potential $V(z)$ projected along z direction, where the impurity is located at the center of the QW in $(x_{im}, y_{im}, z_{im}) = (0.0, 0.0, 0.0)$ nm. Fig. 2(b) shows the total potential $V(z)$ with the impurity located at the interface in $(x_{im}, y_{im}, z_{im}) = (0.0, 0.0, 2.5)$ nm. These figures also display the energy and the projection of the electron wave function in the (y, z) plane, for ground state $\psi_0(y, z)$, first $\psi_1(y, z)$ and second $\psi_2(y, z)$ excited states, confined in a 5 nm QW. For example, when the impurity is located in the center of the QW the ground state energy is about 8.71 meV upward of potential energy reference, and goes up to 25.40 meV when the impurity is placed at the interface of the QW. Noteworthy the potential energy $V(z)$ is attractive in the well region due to both electron-impurity interaction and attractive behavior of the image self-energy. This potential move the electron to the center of the QW and the wave function is concentrated in that region, as depicted in Fig. 2(a). When the impurity is located at the interface, for a 5 nm QW, the electron is pushed towards to the right interface, as shown by the ground state $\psi_0(y, z)$ and first excited state $\psi_1(y, z)$ wave function. Interestingly, the second excited state $\psi_2(y, z)$ is weakly attracted by the impurity.

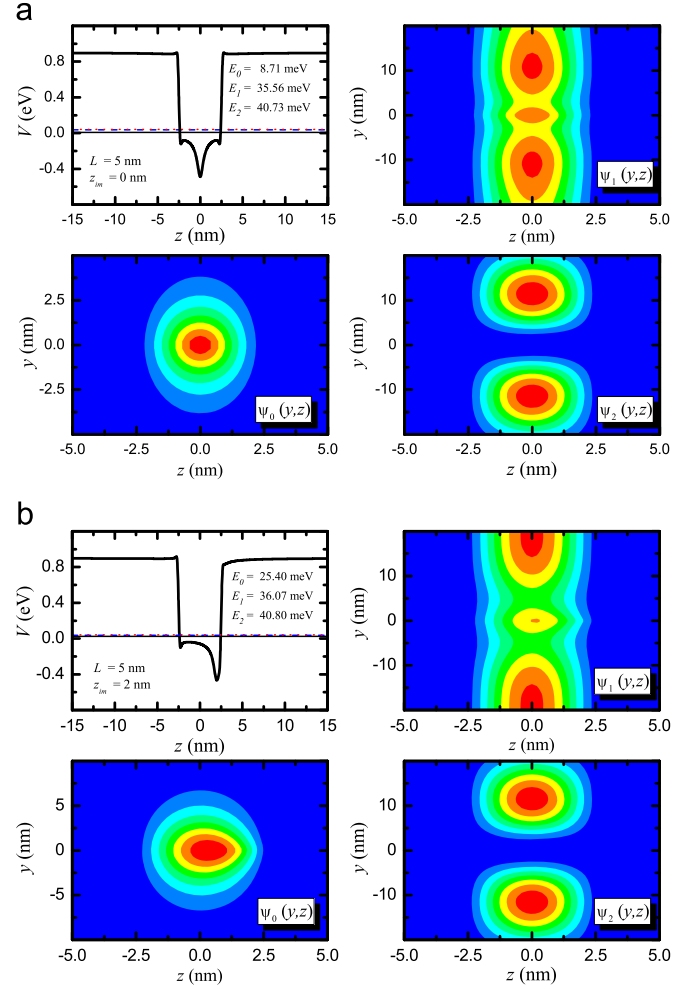


Fig. 2. (Color online) Waves functions projection in the (yz) plane for the ground state, first and second excited states. In (a) the impurity is located in $z_{im} = 0$ nm and in (b) the impurity is $z_{im} = 5$ nm far from the center of the QW. The z -projection of the total potential $V(z)$, in eV, are depicted for QWs with width of $L=5$ nm.

Fig. 3(a) and (b) illustrates the electron energy as function of the impurity position along z axis, in narrow ($L=5$ nm) and wide ($L=10$ nm) QWs, respectively, for the ground state energy (solid lines), first (dashed lines) and second (dotted lines) excited states. Our result shows that the ground state energy increases asymptotically until the point where it reaches values with less pronounced variations from $z_{im} \approx 2$ nm in narrow QW and from $z_{im} \approx 5$ nm in wide QW. For $z_{im} > 2$ nm in narrow QW and $z_{im} > 5$ nm in wide QW the ground state energy is invarient with z_{im} position, which indicates that the effect of the impurity potential is small when the impurity is located in the region of the barrier. Excited states are, on the other hand, weakly affected by the impurity position.

The n th electron-impurity binding energy level is calculated, with appropriate image charge contribution taken into consideration, by the difference

$$E_{n,b} = E_n(V_{e-im} \neq 0) - E_n(V_{e-im} = 0), \quad (12)$$

where the term $E_n(V_{e-im} \neq 0)$ means the n -th electron energy level calculated considering $V_{e-im} \neq 0$ and $E_n(V_{e-im} = 0)$ is the n -th electron energy level calculated considering $V_{e-im} = 0$, in Eq. (4). The absolute value of the electron-impurity binding energy, as function of the impurity position, is depicted in Fig. 3(c) and (d) for narrow ($L=5$ nm) and wide ($L=10$ nm) QWs, respectively. The

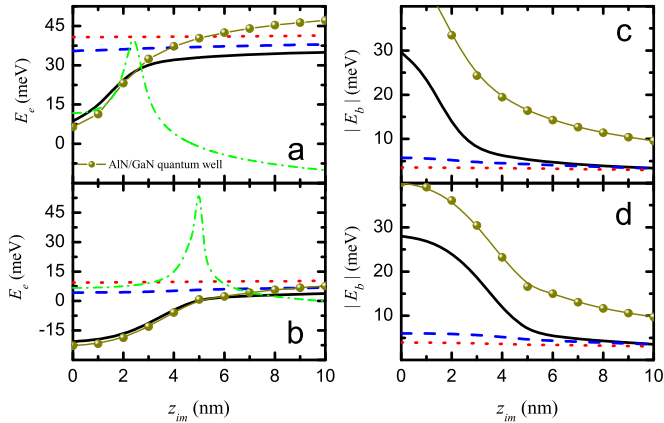


Fig. 3. (Color online) Left panels: Electron energy for ground state (black solid line), first (blue dashed line) and second (red dotted line) excited state in QW for (a) narrow $L=5$ nm QW width and (b) wide $L=10$ nm HfO_2/GaN QW width. Right panels: Electron-impurity binding energy for ground state (black solid line), first (blue dashed line) and second (red dotted line) excited state energy as function of impurity position for (c) narrow ($L=5$ nm) QW and (d) wide $L=10$ nm HfO_2/GaN QW. The dark yellow line-sphere depict the electron energy (left) and electron-impurity binding energy (right) in narrow (top) and wide (bottom) AlN/GaN QW, and the green dash-dot line shows the effect of the image charges in GaN/HfO₂ QW.

curves are shown for the ground state (black solid line), first excited state (blue dashed line) and second excited state (red dotted line). As seen, the binding energy changes with impurity position in the QW structure. The maximum ground state electron-impurity binding energy value occurs in the center of the QW, for $z_{im} = 0$ nm and decreases when the impurity moves towards the interface (in both cases $L=5$ nm and $L=10$ nm) of the well region. For impurity at the interface region, the electron is weakly bound and the binding energy is about 5 meV, for the z_{im} values investigated in this work. Excited states are always weakly bound to impurities, independent of the z_{im} position.

In order to help us to understand the role of the large dielectric constant in the barrier region we compare the results for GaN/HfO₂ with those of a more typical GaN/AlN system, where we have $\epsilon_r = \epsilon_{\text{GaN}}/\epsilon_{\text{AlN}} = 9.5/8.5 = 1.12$. Fig. 3 shows in dark yellow line-sphere the electron energy and electron-impurity binding

energy in narrow and wide AlN/GaN QWs. Different from GaN/HfO₂ ($\epsilon_r < 1$) in a GaN/AlN ($\epsilon_r > 1$) quantum well the electron felt a repulsive potential in the well region due to the dielectric mismatch. To elucidate the results presented in Fig. 3(a) and (b) we show in Fig. 4 a schematic diagram of different interactions between electron, impurity and image charges for GaN/AlN (a)–(c) and GaN/HfO₂ (b)–(d) QWs. For the impurity at the well region, this picture clearly shows that the coulomb potential of impurity and image charges is more attractive in GaN/AlN QW compared to that in GaN/HfO₂ QW. For the impurity located at barrier region the coulomb potential becomes more attractive in GaN/HfO₂. This explains why the electron energy is smaller (larger) at the GaN/AlN system when the impurity is located in the well (barrier) region, as shown in Fig. 3(a) and (b). Without dielectric mismatch, or even for $\epsilon_r > 1$, the confinement energy is always positive since the reference of confinement potential $V(z)$ is always either zero or larger. The energy $E_n(V_{e-im} = 0)$ shown in Eq. (12) is bigger in GaN/AlN than that in GaN/HfO₂, giving rise to a difference in the binding energy as it is shown in Fig. 3(c) and (d). Aside from this difference this energy is essentially due to the band offset and the self-energy potential, as it is shown in Fig. 1(a). Further more, as the impurity position z_{im} increase to the barrier region, the stationary states inside the well tends to discrete states analogous to the case of a quantum well without impurity, as we can see in Fig. 3(a) and (b) for $z_{im} > 5$ nm. In the binding energy $E_{n,b}$ both contribution band offset and self-energy potentials are not taken into account and the states collapse near to $z_{im} = 10$ nm, as shown in Fig. 3(c) and (d).

To clarify the role played by the high dielectric mismatch at the interfaces we add in the Fig. 3(a) and (b), in dash-dot green lines the difference in the electron energy taken into account image charges and does not taken into account the image charges contributions for a GaN/HfO₂ quantum well. This results show essentially the contribution due to image self-energy (interaction between electron and its image charges) as well as the interactions among electron and impurity image charges. As the impurity position increase this difference increase asymptotically until reach the maximum value around the interface position and decrease toward negative values in narrow quantum wells due to the attractive character of the self-energy in systems with $\epsilon_r < 1$, as it can see on the References [12] and [13].

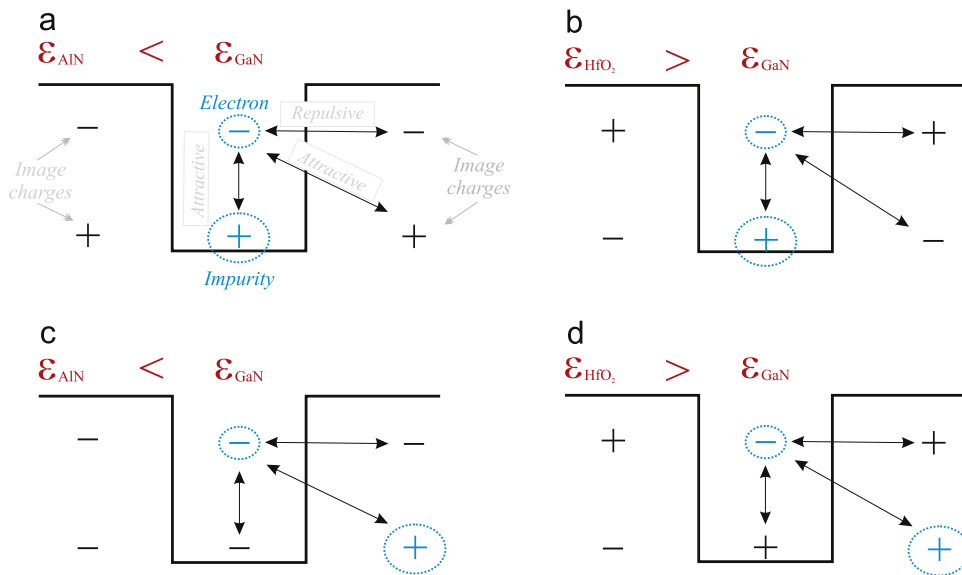


Fig. 4. (Color online) Schematic diagram of different interactions between electron and their image charges, electron and impurity as well as electron and impurity image charges for GaN/AlN (a)–(c) and in GaN/HfO₂ (b)–(d) QWs. In (a)–(b) the impurity is located in the well region while in (c)–(d) the impurity is located in the barrier region.

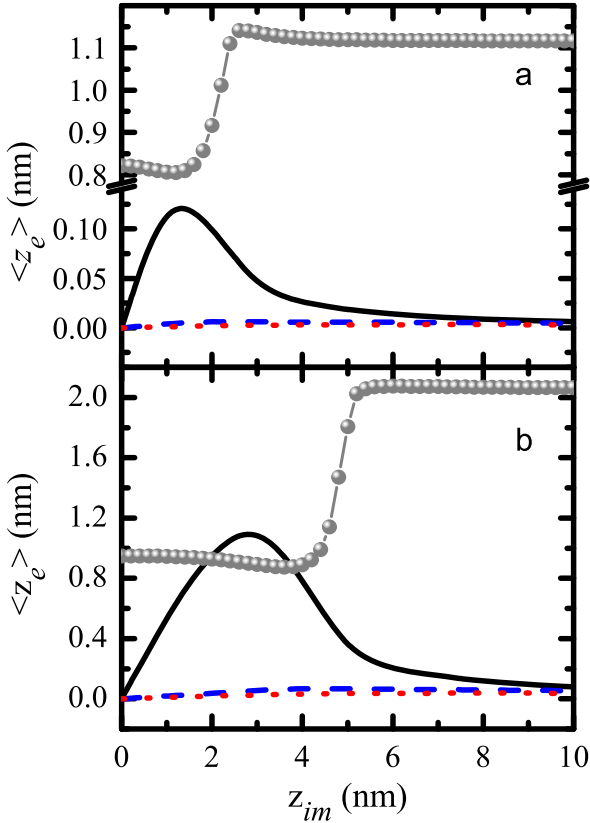


Fig. 5. (Color online) Electron center-of-mass as function of the impurity position (z_{im}) for (a) narrow ($L=5$ nm) and (b) wide ($L=10$ nm) QWs. The ground state, first and second excited states are represented by black solid, blue dashed and red dotted lines, respectively. The gray line-sphere depict the standard deviation in position σ_x for narrow and wide QWs.

To further elucidate here, the expectation value of the electron position $\langle z_e \rangle$, along of z axis, is plotted as function of the impurity position z_{im} , for narrow ($L=5$ nm) and wide ($L=10$ nm) QWs in Fig. 5(a) and (b), respectively. For wells with $L=5$ nm ($L=10$ nm), the $\langle z_e \rangle$ of the ground state (solid lines) has maximum displacement around 0.12 nm (1.0 nm) when the impurity is located in $z_{im} = 1$ nm ($z_{im} = 3$ nm). Moving the impurity towards the barrier region, $\langle z_e \rangle$ tends to return to the QW center. In this case $\langle z_e \rangle$ of the excited states are also weakly affected by the impurity position. We also present in the Fig. 5 in gray line-sphere the standard deviation in the position, namely the square root of the variance $\sigma_x = \sqrt{\langle z^2 \rangle - \langle z \rangle^2}$. This quantity illustrate better the transition from strong binding to weak binding as z_{im} goes into the barrier, illustrating the big variance at the interface position.

Finally, from practical point of view, it is important to investigate the effects of external electric fields on the electronic structure of GaN/HfO₂ QWs. In Fig. 6, we show the stark shift $\Delta E_e = E_e(F \neq 0) - E_e(F = 0)$ of the three first electron energy states, for (a) narrow and (b) wide QWs. The electron energy $E_e(F \neq 0)$ is calculated by considering an electric field \mathbf{F} , pointing along the z direction, by including the term eFz in Eq. (6). Here, it is important to notice that the shift on the electron energy ΔE_e can be underestimated by several meV with the applied electric field, i.e., ≈ 6 meV for narrow QWs and ≈ 50 meV for wide QWs.

4. Conclusions

In conclusion, we have studied impurity state with image charges effects in GaN/HfO₂ quantum wells. Our results show that

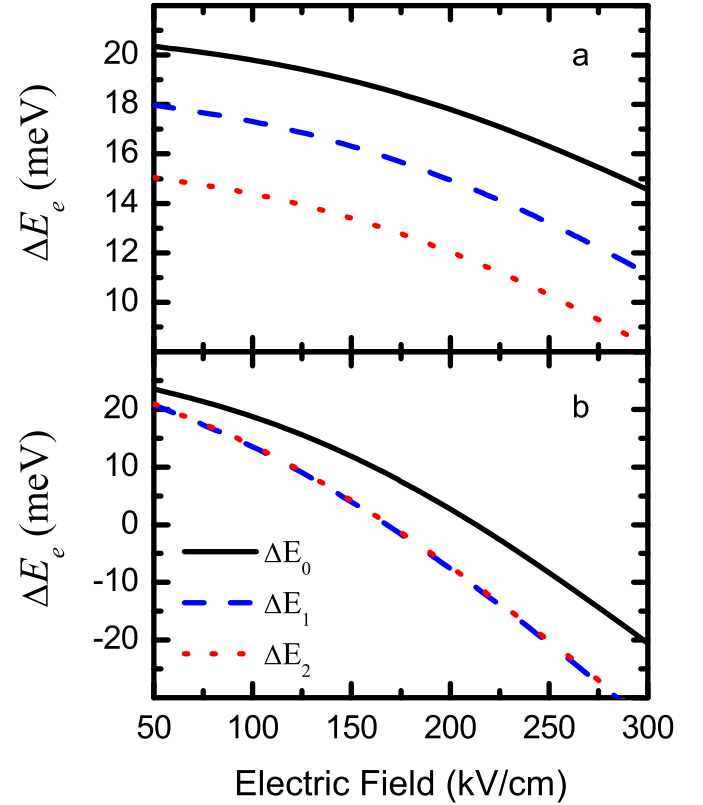


Fig. 6. (Color online) Stark shift of the ground state energy (solid lines), first excited state energy (dashed lines) and second excited state energy in (a) narrow (5 nm) and (b) wide (10 nm) QWs.

the electron–impurity binding energy is highest when the impurity is located at the center of the quantum well and decreases when the impurity moves towards the interface. When the impurity is located on the barrier region the binding energy has a smaller intensity. Moreover, when a electric field is applied on z direction the electron energy can be shifted by about 50 meV in wide quantum wells. These results are lacking experimental confirmation, and we expect that our predictions induce the realization of such experiments.

Acknowledgments

T.A.S. Pereira was financially supported by PRONEX/CNPq/FAPEMAT 850109/2009 and by CAPES under process 3299/13-9. A.A. Sousa has been financially supported by CAPES, under the PDSE contract BEX 7177/13-5. The authors also would like to acknowledge the CNPq, NanoBioEstruturas/CNPq, Pronex/FUNCAP/CNPq. Thanks to L. Craco for a careful reading of this manuscript.

References

- [1] Bin Li, A.F. Slachmuylders, B. Partoens, W. Magnus, F.M. Peeters, *Phys. Rev. B* 77 (2008) 115335.
- [2] N.C. Jarosik, B.D. McCombe, B.V. Shanabrook, J. Comas, John Ralston, G. Wicks, *Phys. Rev. Lett.* 54 (1985) 1283.
- [3] G. Weber, *Phys. Rev. B* 41 (1990) 10043.
- [4] S. Fraizzoli, F. Bassani, *Phys. Rev. B* 41 (1990) 5096.
- [5] J.M. Ferreyra, C.R. Proetto, *Phys. Rev. B* 52 (1995) 2309.
- [6] B. Li, B. Partoens, F.M. Peeters, W. Magnus, *Phys. Rev. B* 79 (2009) 085306.
- [7] C.G. Morgan, P. Kratzer, M. Schefer, *Phys. Rev. Lett.* 82 (1999) 4886.
- [8] N.Q. Vinh, H. Przybylińska, Z.F. Krasil'nik, T. Gregorkiewicz, *Phys. Rev. Lett.* 90 (2003) 066401.

- [9] J. Cen, K.K. Bajaj, *Phys. Rev. B* 48 (1993) 8061.
- [10] Z.Y. Deng, S.W. Gu, *Phys. Rev. B* 48 (1993) 8083.
- [11] T.A.S. Pereira, J.A.K. Freire, V.N. Freire, G.A. Farias, L.M.R. Scolfaro, J.R. Leite, E. F. da Silva Jr, *Appl. Phys. Lett.* 88 (2006) 242114.
- [12] T.A.S. Pereira, J.S. de Sousa, G.A. Farias, J.A.K. Freire, M.H. Degani, V.N. Freire, *Appl. Phys. Lett.* 87 (2005) 171904.
- [13] T.A.S. Pereira, J.S. de Sousa, J.A.K. Freire, G.A. Farias, *J. Appl. Phys.* 108 (2010) 054311.
- [14] A.A. Sousa, T.A.S. Pereira, A. Chaves, J.S. de Sousa, G.A. Farias, *Appl. Phys. Lett.* 100 (2012) 211601.
- [15] F. Stern, *Phys. Rev. B* 17 (1978) 5009;
F. Stern, *Solid State Commun.* 25 (1977) 163.
- [16] M.H. Degani, *Appl. Phys. Lett.* 59 (1991) 57.
- [17] M.H. Degani, M.Z. Maialle, *J. Comput. Theor. Nanosci.* 7 (2010) 454.
- [18] M.Z. Maialle, M.H. Degani, *Phys. Rev. B* 83 (2011) 155308.
- [19] I. Vurgaftman, J.R. Meyer, L.R. Ram-Mohan, *J. Appl. Phys.* 89 (2001) 5815.
- [20] R. Kosloff, *J. Phys. Chem.* 92 (1988) 2087.
- [21] M.H. Degani, *Phys. Rev. B* 66 (2002) 233306.
- [22] M.H. Degani, J.P. Leburton, *Phys. Rev. B* 44 (1991) 10901.
- [23] A. Chaves, G.A. Farias, F.M. Peeters, B. Szafran, *Phys. Rev. B* 80 (2009) 125331.
- [24] M. Kumagai, T. Takagahara, *Phys. Rev. B* 40 (1989) 12359.
- [25] T.E. Cook Jr., C.C. Fulton, W.J. Mecoouch, R.F. Davis, G. Lucovsky, R.J. Nemanich, *J. Appl. Phys.* 94 (2003) 7155.
- [26] R.Y. Korotkov, J.M. Gregie, B.W. Wessels, *Appl. Phys. Lett.* 80 (2002) 1731.
- [27] C.I. Wu, A. Kahn, *J. Appl. Phys.* 86 (1999) 3209.

Wave packet propagation through branched quantum rings

A. A. Sousa,^{1,2,*} A. Chaves,^{1,†} T. A. S. Pereira,^{3,‡} G. A. Farias,^{1,§} and F. M. Peeters^{2,1,¶}

¹*Departamento de Física, Universidade Federal do Ceará,*

Caixa Postal 6030, Campus do Pici, 60455-900 Fortaleza, Ceará, Brazil

²*Department of Physics, University of Antwerp, Groenenborgerlaan 171, B-2020 Antwerp, Belgium*

³*Instituto de Física, Universidade Federal de Mato Grosso, 78060-900 Cuiabá, Mato Grosso, Brazil*

(Dated: April 20, 2015)

We theoretically investigate the effect of opening and closing pathways on the dynamics of electron wave packets in semiconductor quantum rings with semi-circular, circular, and squared geometries. Our analysis is based on the time evolution of an electron wave packet, within the effective-mass approximation. We demonstrate that opening an extra channel in the quantum ring does not necessarily improve the electron transmission and, depending on the extra channel width, may even reduce it, either due to enhancement of quantum scattering or due to interference. In the latter case, transmission reduction can be controlled through the Aharonov-Bohm phase of the wave function, adjusted by an applied magnetic field. On the other hand, closing one of the channels of the branched out quantum ring systems surprisingly improves the transmission probability under specific conditions.

PACS numbers: 73.63.-b, 85.35.Ds, 73.63.Nm

I. INTRODUCTION

Carrier transport is a very important property of mesoscopic and nanoscopic physical systems, for both academic and technological applications. In particular, the transport inefficiency caused by the addition of an extra path to a network¹⁻³ have been subject of recent interest in the literature. This behaviour is in contrast to common sense and was both experimentally and theoretically demonstrated in a branched out mesoscopic network,⁴ and theoretically confirmed in a quantum dots system coupled by multi-leads in a mesoscopic setup.⁵ In the first case, the system under investigation was of micrometer scale with wide transmission channels and consequently quantum interference effects are expected not to be relevant.⁶ In the second case, the system consists of two quantum dots, each one coupled to ideal electronic leads with an independent number of open propagating channels. These effects appear to be similar to the Braess paradox of games theory,⁷ but now on a mesoscopic scale. The paradox lies in the fact that, as demonstrated in Ref. 7, adding an extra road in a traffic network does not necessarily improve the overall traffic flow. In a more general interpretation of the paradox, recent works have proposed further examples of systems where better conditions leads to worse performance.^{8,9}

From a nanoscopic point of view, the dynamics of waves in nanodevices with multiterminals is affected quantum effects.¹⁰ In a previous work, we demonstrated that transport inefficiency in branched out devices also occurs on a quantum scale, when few subbands are involved in the transport.¹¹ The transport properties are strongly influenced by quantum scattering and interference, so that a similar reduction in transmission can be found in a quantum ring with a central branch. In the present paper, we extend our previous work in Ref. [11] and investigate: (i) the effect of the geometry of the

quantum ring, by considering, semi-circular, circular and squared rings, (ii) the effect of an Aharonov-Bohm (AB) phase, induced by an external magnetic field, and (iii) an AFM tip potential which is able to the effect of the position of obstruct one of the system channels. For this purpose, we investigate wave packet propagation through these branched quantum rings, attached to input and output leads, by numerically solving the time-dependent Schrödinger equation. Our results show that the so-called quantum analog of the Braess paradox is robust in these nano scale devices and that it is a correspondence of effects related to a combination between quantum interference and scattering events. We also shown here the Braess effect can be tuned by magnetic field and electric fields

II. THEORETICAL MODEL

We consider here four different planar quantum rings, attached to input (left) and output (right) leads for electrons injection, in the presence of an extra channel. We assume that the rings and the leads have the same width $W = 10$ nm, while the width of the extra branch W_c , will be varied from 0 to 50 nm. Figure 1 shows a schematic view of our systems under investigation: in (a), (b) and (d) the ring has a circular symmetry with average radius $R_{ave} = 60$ nm, while in (c) the ring has a rectangular symmetry with width and height given by 60 nm and 30 nm, respectively. From now onwards, we will refer to these systems by their labels (a-d).

An electron confined in such a quasi-one-dimensional channel with width W has subband energy given by

$$E_n(k_x) = E_n^{(y)} + \frac{\hbar^2 k_x^2}{2m_e}. \quad (1)$$

Here m_e is the electron effective mass and eigenenergies

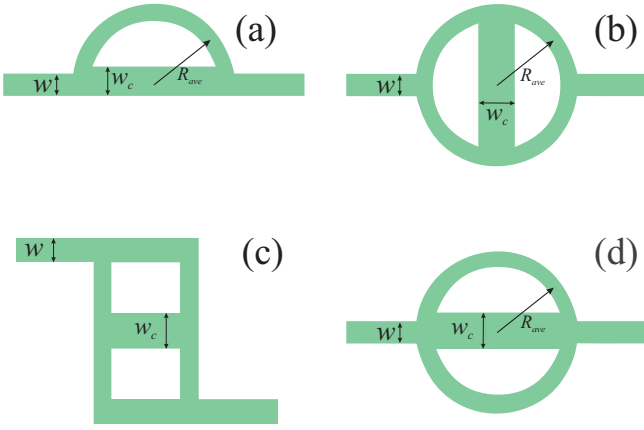


FIG. 1: Sketch of the systems under investigation. (a) Half quantum ring with leads and channel aligned, (b) circular quantum ring with an extra channel in the perpendicular direction, (c) square ring with non-aligned leads and channel, and (d) circular quantum ring with leads and channel aligned.

of the confining well $E_n^{(y)}$ are numerically calculated for a finite potential V_e . For the initial wave packet (WP), we assumed a plane wave with wave vector $k_0 = \sqrt{2m_e\varepsilon}/\hbar$, where ε is the average kinetic energy, multiplied by a Gaussian function with width σ_x in the x direction and by the ground state wave function $\phi_0(y)$ of the input lead in the y -direction

$$\Psi(x, y, t = 0) = \exp \left[ik_0x - \frac{(x - x_0)^2}{2\sigma_x^2} \right] \phi_0(y). \quad (2)$$

There are several techniques to numerically solve the time dependent Schrödinger equation.^{12–17} In this work we opted for the split-operator technique, which consists in separating the time evolution^{18–20} operator as

$$\begin{aligned} \Psi(x, y, t + \Delta t) &= \exp[-iH\Delta t/\hbar] \Psi(x, y, t) \\ &= \exp[-iV\Delta t/2\hbar] \exp[-iT_x\Delta t/\hbar] \\ &\times \exp[-iT_y\Delta t/\hbar] \exp[-iV\Delta t/2\hbar] \\ &\times \Psi(x, y, t) + \mathcal{O}(\Delta t^3), \end{aligned} \quad (3)$$

where Δt is the time step, $T_{x(y)}$ is the kinetic-energy operator for the $x(y)$ -direction, and the error $\mathcal{O}(\Delta t^3)$ is due to the noncommutativity of the potential and kinetic terms.²¹ Nevertheless, this error can be neglected provided we use a very small time step, that in our case is $\Delta t = 0.1$ fs. The Hamiltonian \mathcal{H} is written within the effective mass approximation, describing an electron constrained to move in the (x, y) -plane and confined by an external in-plane potential of height V_0 , which allows the electron to move only within the leads, arms and channels regions, illustrated by shaded areas in Fig. 1, where the potential is zero. The potential step is assumed

here to be abrupt, but smooth interfaces will not qualitatively affect the results.^{22,23} The (x, y) -plane is discretized in $\Delta x = \Delta y = 0.4$ nm steps, and the finite difference scheme is used to write the derivatives coming from the kinetic energy terms of the Hamiltonian. We apply an imaginary potential at the edges of the input and output channels and, in order to, absorb the transmitted and reflected packets, and to prevent spurious reflections at the boundaries of the computational box.²⁴

The transmission and reflection probabilities are calculated by integrating the probability density current at specific points of the system, namely, at the output lead ($x_R = 158$ nm), for the former, and at the input lead ($x_L = -158$ nm), for the latter. Thus, the expressions for transmission and reflection are, respectively,

$$T = \int_0^\infty dt \int_{-\infty}^{+\infty} dy J_x(x_R, y, t) \quad (4)$$

and

$$R = - \int_0^\infty dt \int_{-\infty}^{+\infty} dy J_x(x_L, y, t). \quad (5)$$

The component of the probability current in the x -direction is given by

$$\begin{aligned} J_x(x, y, t) &= \frac{\hbar}{2m_e i} \left(\Psi^* \frac{\partial}{\partial x} \Psi - \Psi \frac{\partial}{\partial x} \Psi^* \right) \\ &+ \frac{e}{m_e} A_x |\Psi|^2. \end{aligned} \quad (6)$$

For a magnetic field applied perpendicularly to the ring plane, *i.e.* in the z direction, the vector potential is taken in the Coulomb gauge $\mathbf{A} = (-y, x, 0)B/2$. In order to quantify the scattering of the electron into different subbands, we project the wave function on the j -th subband at a fixed point x_i of the quantum well,

$$\begin{aligned} P_j(x_i, t) &= |\langle \Psi | \varphi_j \rangle|^2 \\ &= \left| \int_{-\infty}^{+\infty} dy \Psi(x_i, y, t) \varphi_j(y) \right|^2. \end{aligned} \quad (7)$$

Equation (7) gives the probabilities to find an electron in the j -th subband at position x_i at time t . The contribution from each subband to the total probability current is given by

$$\begin{aligned} J_x^{(j)}(x) &= \int \frac{\hbar}{2m_e i} \left(\bar{P}_j^* \frac{\partial}{\partial x} \bar{P}_j - \bar{P}_j \frac{\partial}{\partial x} \bar{P}_j^* \right) \\ &+ \frac{e}{m_e} A_x |\bar{P}_j|^2 dt. \end{aligned} \quad (8)$$

Notice that Eq. (7) is not normalized, and therefore the values assumed by $J_x^{(j)}$ can be larger than one. We assume ballistic transport and, for the sake of simplicity, all kinds of disorder are neglected.

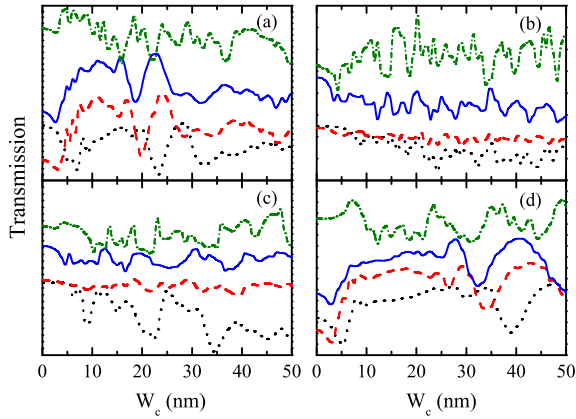


FIG. 2: (Online color) Transmission probability as function of channel width W_c . The frames (a), (b), (c) and (d) refer collectively as the corresponding systems presented in Fig. 1. The WP have kinetic energies ε_1 (black, dotted line), ε_2 (red, dashed line), ε_3 (blue, solid line), propagating in the subband ground state, while the other is in the first excited state with kinetic energy ε_3 (green dash-dotted line).

III. RESULTS AND DISCUSSION

We consider materials parameters for InGaAs and InAlAs, in which the band-offset and electron effective mass are taken as $V_e = 600$ meV and $m_e = 0.041m_0$, respectively. Three values of kinetic energy for the WP are used: $\varepsilon_1 = 70$, $\varepsilon_2 = 140$ and $\varepsilon_3 = 180$ meV. These WP were propagated in the ground state $E_0^{(y)} \simeq 58$ meV and, specifically for ε_3 , we also propagated it in the first excited state of the channel, $E_1^{(y)} \simeq 226$ meV.

Figure 2 shows the transmission probabilities as function of the channel width W_c for kinetic energies ε_1 (black, dotted line), ε_2 (red, dashed line), and ε_3 (blue, solid curve), for the initial WP in the ground state, and ε_3 in the first excited state (green, dash-dotted line). Each curve shown in Fig. 2 is vertically shifted up by 0.2. The disposition of the frames (a), (b), (c) and (d) presented in Fig. 2 follows one of Fig. 1. For all systems investigated, the existence of an extra channel surprisingly reduces the transmission probability for some width W_c , instead of improving it. This decreasing is either an effect of quantum scattering at the channel-ring junctions, or a WP interference effect. Both possibilities will be discussed now in more detail.

Notice that the extra channels for the profiles in Figs. 1(b) and (c) are not aligned with respect to input and output leads, as in Figs. 1(a) and (d). Thus, transmission probabilities in Figs. 2(a) and (d) present some similarities in their patterns, and the same is observed in Figs. 2(b) and (c). The curves clearly exhibit minima for all kinetic energies, and transmission probability always start decreasing as the extra channel width increases for WP propagating in the ground state subband, although

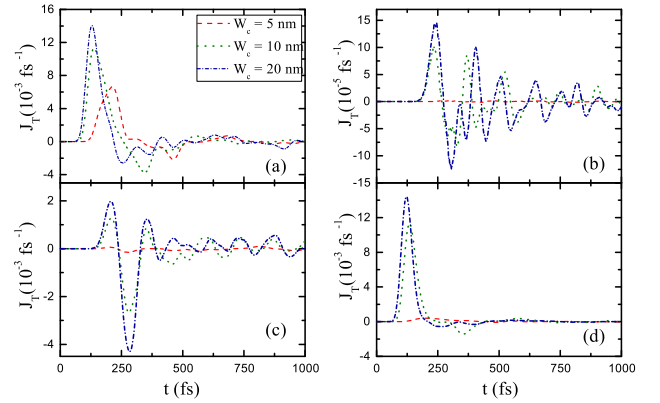


FIG. 3: (Online color) Time-dependent probability current through the extra channel, calculated for kinetic energy ε_1 . The different frames refer to the systems in Fig. 1.

the extra channel represents an alternative for the electron to bypass through the central region which should, in principle, improve the transmission. The positions of most of the minima in W_c strongly depend on of WP energy. In Figs. 2(b) and (c), besides the minima, transmission probabilities also exhibit an overall decreasing trend with increasing of channel width W_c , specifically for low kinetic energy. Moreover, transmission probability patterns are strongly dependent on the geometry of the ring, which indicates that there are numerous possibilities of WP interference in these cases, where the system geometry is more complex than that in Fig. 2(a) and (d).

For a better understanding of WP dynamics in these systems, Fig. 3 shows the time-dependent probability current through the extra channel as a function of time. The WP propagates in the lowest subband from left to right with kinetic energy given by ε_1 . Three different values for channel width W_c are considered: 5, 10, and 20 nm. In all studied cases we observe initially a positive peak of current followed by a negative peak, which is more acute in Figs. 3(b) and (c). In these cases, a sequence of positive and negative peaks clearly demonstrates that the WP is repeatedly reflected at the extra channel-ring junctions, propagating back and forth within the extra channel. Thus, the time that electrons are kept in the structure is increased, contributing to an overall reduction of the electric current. For $W_c = 5$ nm, only a small part of the WP propagates through the extra channel, because the average value of the kinetic energy is lower than the ground state of this channel. In addition, the input and output leads are not aligned, which also harness the WP propagation through this channel. For cases in which the extra channel is aligned with input and output leads, as in Fig. 3(a) and (d), a somewhat larger part of the WP can propagate through the extra channel even in the $W_c = 5$ nm case.

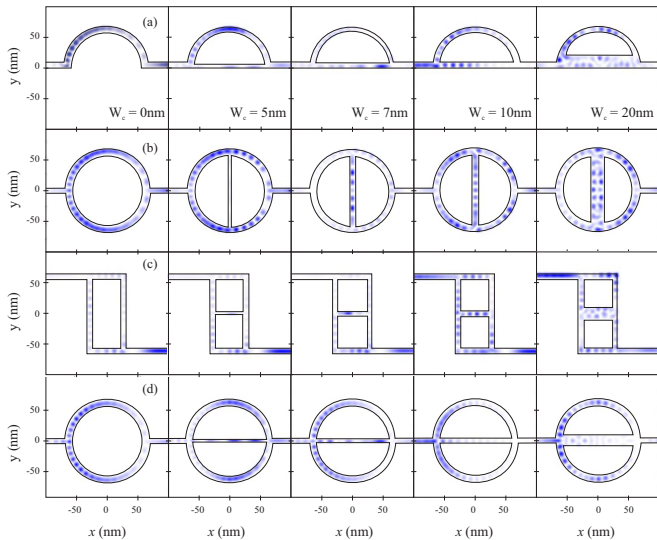


FIG. 4: (Online color) Snapshots of the squared wave function at $t = 460$ fs, for different channel width W_c and kinetic energy ε_1 .

Figure 4 shows snapshots of the squared modulus of the wave functions at $t = 460$ fs, for kinetic energy ε_1 , and $W_c = 0, 5, 7, 10,$ and 20 nm, respectively, in each column. The wave function presents just one peak in the confinement direction within the ring arms, input and output leads, which indicates that the propagation is kept in the ground state subband in all these regions. Along the extra channel, however, the wave function propagates in the ground state subband only for $W_c = 5$ nm, while for larger W_c , it is scattered to excited states and exhibits multiples peaks and even different parities, due to the lower confinement energies in this channel.

The contributions of each subband to the total transmission probability is shown in Fig. 5, where $J_x^{(1)}$ (top) and $J_x^{(2)}$ (bottom) calculated in the output lead (at $x = 158$ nm), are depicted as function of W_c . Other states were omitted because they do not significantly contribute for the WP energies considered here. The systems sequence used here is the same as in previous figures. The projected density current exhibits minima with patterns similar to those in Fig. 2. As mentioned above, the output lead has a width of $w = 10$ nm and the energy difference between the first two states, $E_1^{(y)} - E_0^{(y)} = 168$ meV, is higher than the kinetic energy ε_1 . For this reason, in all systems, the contribution $J_x^{(2)}$ in Fig. 5 is zero when the kinetic energy is ε_1 (black, dotted line). Moreover, the WP is a gaussian distribution in energy space, whose width allows for non-zero projection on P_2 with energy the ε_2 . We observe in Figs. 5(b) and (d) that the WP in output lead does not propagate in the subband excited states in these systems, regardless of the kinetic energy or channel width W_c , even when the wave function projections are non-zero for excited states in the extra channel, as shown in Fig. 4. In these systems, the quantum

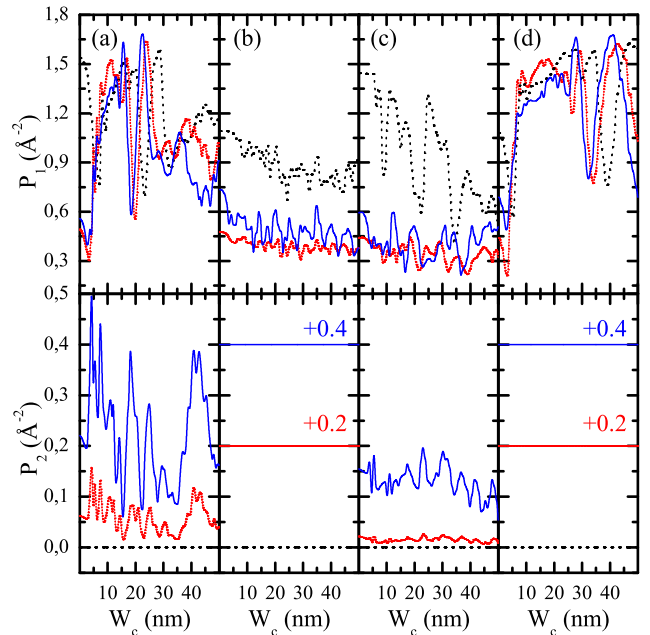


FIG. 5: (Online color) Projection of the wave function on the ground state (top graphics) and first-excited subbands (bottom graphics) as function of channel width W_c , calculated at the output lead. Kinetic energy ε_1 (black dotted line), ε_2 (red short-dot line), and ε_3 (blue solid line). This figure is ordered in the same sequence Fig. 1.

ring has a circular symmetry and the WP propagate in subbands of the top and bottom arms with a phase difference given by π , which leads to an interference that cancels the projection P_2 on the output lead.¹⁸

The contribution $J_x^{(2)}$ of the second subband to the probability density current in Figs. 5(a) and (c) does not vanish, despite of the interference, due to the asymmetry in the potential of these systems. They lead to additional peaks and valleys in the transmission probabilities as a function of the extra channel width for these systems in Fig. 2(a) and (c). Notice that the position of these peaks and valleys are completely independent of the WP energy, whereas the minima observed for $J_x^{(1)}$ are significantly shifted as the energy varies. Therefore, the former minima cannot be interpreted in terms of quantum scattering and interference as done here for the latter, as they are just a consequence of inter-subband scattering by the channel-junctions.

A. Influence of an external magnetic field

Let us now turn our attention to the minima in the transmission probabilities shown in Fig. 2. One may expect that these minima come from interference, and therefore we should be able to change the position of the minima not only by changing the kinetic energy, but also

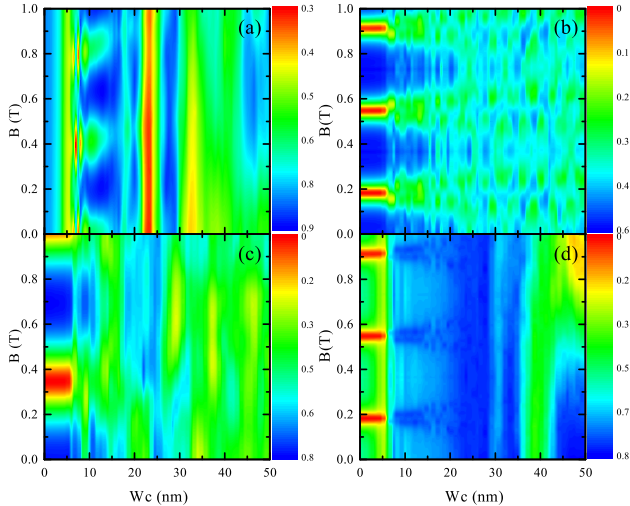


FIG. 6: Contour plots of the transmission probabilities as a function of the extra channel width W_c and magnetic field \mathbf{B} . This figure is ordered in the same sequence as Fig. 1.

by applying an external magnetic field. This magnetic field adds a phase in the wave function through the vector potential \mathbf{A} . If the minima are due to interference, their position will change in the presence of the field, since the vector potential induces an additional phase to the wave function. Fig. 6 displays a color map of transmission probabilities as function of channel width W_c and magnetic field \mathbf{B} . In Fig. 6(a), for $B = 0$, as W_c increases, minima (red and yellow regions) are observed around $W_c = 5$ nm and some intermediate values of $W_c \approx 23$ nm. In these cases, then, enlarging the extra channel reduces the current. As the magnetic field increases, the minima positions are not significantly affected, which indicates that these minima are not related to interference, but rather to pure quantum scattering. For W_c between 5 and 10 nm, there are also other minima (green regions), equally spaced in B , that are affected by the magnetic field, due to the AB effect. In this case, the WP passes through both channels, now connected as a semi-circular ring-like path, which explains the observed AB oscillations. For $W_c < 5$ nm, subband energies are higher than the kinetic energy, and the WP can not propagate through the extra channel. The W_c width and the magnetic field can change the AB period. The system in (a) thus proves to be a good example of the quantum analog of the Braess paradox, where more channels (surprisingly) means less current, and which is not simply due to quantum interference effects.

AB oscillations are evident in Figs. 6(b), (c) and (d), as B increases in the range of small W_c width. As W_c increases, two rings are effectively formed in system (b), and this yields a reduction in the AB period in Fig. 6 (b). In Fig. 6 (c), the minima observed for $B = 0$ are strongly affected by the magnetic field, which indicates that these

minima are a result of destructive interference. In Fig. 6 (d) the minima around $W_c \sim 5$ nm for $B = 0$ do not change with the magnetic field, whereas the next minima, around $W_c \sim 35$ nm, shift to the right as the magnetic field increases, showing that the first minima is due to scattering while the latter is due to WP interference. In order to improve the visualisation of the transmission in Fig. 6(c) and (d), we show the respective transmission as function of W_c width in Fig. 7(a) and (b), corresponding to the systems of Figs. 1(c) and (d), respectively. Each contour (or on-line color) represents a transmission for a specific applied magnetic field, ranging from 0 to 1 T, and reproduce the behaviour of the minima, as discussed above.

B. Effect of extra (obstructing) potentials

In order to test the robustness of the Braess paradox analog, observed here in the context of quantum mechanics, we add a perturbing potential, which can be seen as a model for an AFM tip²⁵, we consider three different configurations for each of the systems of Fig. 1 to analyse the behaviour of the transmissions, see Fig. 8: the tip potential (1) is fixed at the central region $(x, y) = (0, 0)$; the tip potential (2) is placed at $x = 0$ and moved from bottom to top along the y -axis, and the tip potential (3) is placed at $y = 0$ and moved from left to right along the x -axis. This perturbative potential, which depends on the tip position and is assumed to be isotropic, is expressed as a Gaussian distribution centered at (x_p, y_p) ,

$$V_{gau} = V_G \exp \left\{ -\frac{1}{2\sigma_G^2} \left[(x - x_p)^2 + (y - y_p)^2 \right] \right\}, \quad (9)$$

where, V_G is the potential intensity and σ_G ($= 5$ nm) represents the width of the Gaussian potential.

Figure 9 shows transmission probabilities for a WP with kinetic energy ε_1 propagating in the first subband. This figure is spatially arranged in four groups, in the same sequence of geometries as in Figs. 1(a-d), with three panels each: panel (1) shows the transmission probability as function of the tip potential intensity V_G , with the tip potential fixed at the central region of the system; whereas panels (2) and (3) are the transmission probabilities for the tip potential moving from bottom to top side, at $x = 0$, and from left to right at $y = 0$, respectively, as mentioned above. The black solid line represents the transmission calculated for a system with a central channel width $W_c = 10$ nm. The red dotted line represents the transmission probability calculated with W_c given by the respective minima of the transmission, depicted in Fig. 2, *i.e.*, the W_c width is 23 nm in Fig. 9(a), 24 nm in (b), 22 nm in (c), 5.5 nm (related to the minima due to WP quantum scattering), and 39 nm (related to the minima due to WP quantum interference) in (d). For (2) and (3) tips, we use $V_G = 300$ meV, because the red curves (minima) present a large transmission probability

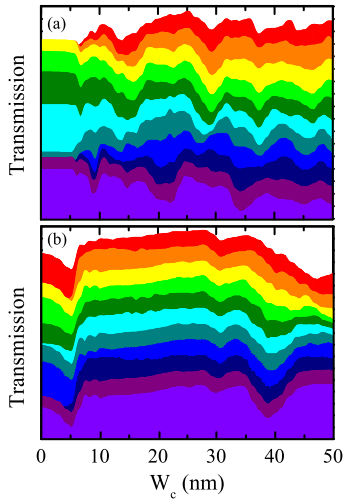


FIG. 7: (Online color) Transmission probability as function of the channel width W_c for quantum rings depicted in (a) Fig. 1(c) and (b) Fig. 1(d), respectively. The kinetic energy used was ε_1 and each color curve represents a transmission probability for a specific magnetic field, ranging from 0 (purple) to 1 T (red).

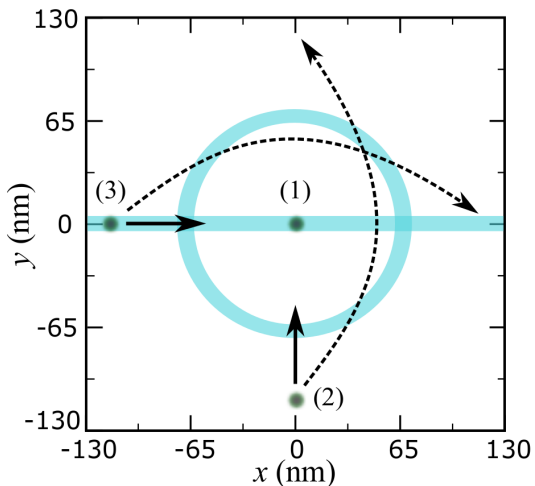


FIG. 8: Schematic diagram for an AFM tip potential over quantum rings represented by the dots (1), (2) and (3). The solid arrows indicate the direction of the tip displacement, while the dash line arrows indicate the final position of the tip. Tip (1) is fixed in the central region for each system.

for this potential, as we can see in Figs. 9 (1) for all four systems investigated.

For all systems investigated here, increasing V_G for the tip in situation (1), i.e. closing the path in the central channel, improves the transmission probability when W_c is chosen as one of the minima mentioned above, as one can see by the red curves in any of the panels labelled as (1) of Fig. 9. In Fig. 9 (a)(1), the minimum of the

transmission (red, dotted line) increases as the potential intensity V_G increases, raising from 0.3 at $V_G = 0$ to around 0.6 at $V_G = 100$ meV and 300 meV. On the other hand, for the solid black line, except for the oscillations around $V_G = 250$ and 500 meV, the transmission has no significant changes. This result reflects the fact that when the transmission in system (a) is in its minimum at $W_c = 23$ nm, a larger part of the WP moves through the extra channel, while for $W_c = 10$ nm, the WP has a large part propagating through the upper arm of the ring, therefore, the tip potential in situation (1) cannot affect much the transport in the latter case. Moreover, this result brings even closer resemblance with the Braess paradox: counter intuitively, the presence of the tip potential, which in practice shuts down the extra channel, raises the overall transmission back to the higher value it had without this channel in the $W_c = 23$ nm (minimum) case. In other words, for this value of channel width, having an extra channel is worse, in terms of conductivity. In Fig. 9 (a)(2) a significant change occurs when the tip is over the bottom edge of the channel, at $(x, y) = (0, 0)$: the minimum of the transmission increases from 0.3 to 0.6, while for $W_c = 10$ nm, the transmission decreases from 0.6 to 0.4. Therefore, if $W_c = 10$ nm, shutting the extra channel decreases the transmission, as expected from a classical point of view, and in contrast with the behaviour observed for $W_c = 23$ nm. Notice that as the tip moves up, the transmission probability minimum for $W_c = 23$ nm (red dotted) decreases to 0.3 at the center of the channel and increases back to 0.6 as the tip moves to the upper edge of the channel. This is due to the fact that, for such larger W_c , the wave packet enters the extra channel through its first excited state subband, whose eigenfunction is zero at $y = 0$, which is not the case for $W_c = 10$ nm (black solid). Out of the central channel, even when the tip is over the upper arm, the potential has no significant effects on the minima transmission, since the largest part of the WP propagates through the extra channel for large W_c . In Fig. 9(a)(3) when the tip potential is over the input or output leads there is no transmission in the ring. Nevertheless, the transmission minimum increases to 0.6 when the tip potential is over the central channel, in accordance with the results discussed above for Fig. 9 (a)(2) and (1).

The time-dependent probability current through the extra channel of the system in Fig. 1 (b) is very small, as depicted in Fig. 3 (b). Therefore, when the tip potential is over the extra channel in this system, the transmission probability has no significant change, as it can be seen in Fig. 9 (b) where the oscillations in the transmission probability exhibit a rather small amplitude ~ 0.2 in the extra channel region. In Fig. 9(b)(3), when the tip is over the extra channel, the transmission presents a small oscillation around $(x, y) = (0, 0)$. The displacement of the tip (2) over the system (c) closes the arm of the squared ring at $y \approx \pm 60$ nm and closes the extra channel at $y \approx 0$ nm. Over the ring arms, the tip potential reduces the

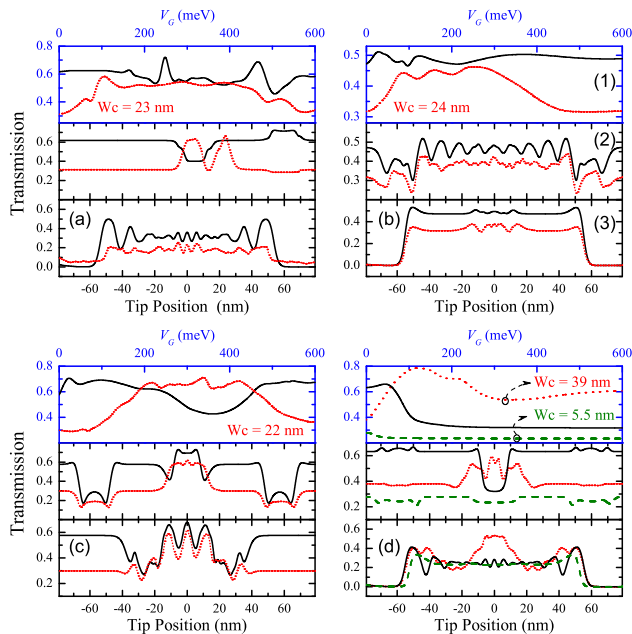


FIG. 9: (Online color) Transmission as a function of (1) intensity of the Gaussian potential, (2) and (3) tip position. The order of the figures refer to the form different depicted in Fig. 1. The curves width black color are for $W_c = 10$ nm, while the curves width red colors are for the minima of the transmission shown in Fig. 2. The WP kinetic energy is ε_1 .

transmission probability to 0.2 for the minimum $W_c = 24$ nm, and to 0.4, for the channel width $W_c = 10$ nm, whereas over the extra channel, the tip potential increase the transmission to 0.3 for the minimum and more than 0.1 for $W_c = 10$ nm, when compared to the case where the tip potential is absent in the system. The displacement of the tip (3) closes the extra channel and the ring arms at $x \approx \pm 30$ nm. When the tip is over the extra channel, the minimum transmission increases, while it decreases when the tip is over the ring arms, as was discussed for the tip (2).

In Fig. 9(d) two minima of the transmission probability are investigated: the first one, red dotted line, is for an extra channel width $W_c = 39$ nm, and the second one, green dashed line, for an extra channel width $W_c = 5$ nm. These minima have their origins in quantum interference and scattering, respectively, as previously discussed. For the minimum coming from interference, the tip potential (1) strongly affects the transmission probability, which changes from ~ 0.4 to ~ 0.8 . On the other hand, for the minimum due to quantum scattering, the tip potential (1) does not significantly change the transmission. For $W_c = 10$ nm, when the tip potential closes the extra channel, it produces interference of the WP that propagate through the ring arms, decreasing the

transmission probability. The tip (2) does not affect the transmission when it is moving over the bottom or top ring arms. When the tip potential is over the extra channel, the minima which came from interference increase to 0.2, while for $W_c = 10$ nm, the transmission decreases from ~ 0.6 to ~ 0.3 . Moreover, when closing the extra channel, the tip (3) increases the minimum 0.6 which comes from interference, but it does not affect either the other transmission minimum, which is due to scattering, and or transmission for $W_c = 10$ nm.

IV. CONCLUSIONS

In summary, we have investigated the WP propagation through rings with different circular and squared shapes, adding an extra channel along their respective diameters, and calculated the transmission probabilities as function of parameters like magnetic field and extra channel width W_c . Contrary to common sense, our results have demonstrated that even when an extra channel is added as alternative path for the WP to pass, the transmission probability through the whole system can be depreciated, when compared to the transmission in a system in the absence of such an extra current path. Such a reduction in the transmission probability can be seen as an evidence for the quantum analog of the Braess paradox in the nanostructures investigated here, and is closely related to transport inefficiency recently demonstrated both theoretical and experimentally for different branched-out mesoscopic networks. In the presence of an external magnetic field, the position of those transmission probability minima owing to quantum interference are clearly shifted, and Aharonov-Bohm oscillations are observed as well. Moreover, a charged AFM tip placed over the systems, acts as an obstruction to some of the quantum pathways, is found to favor enhancement of the transmission probability in its minima under specific conditions. Results shown here, therefore, not only allow us to discuss transport properties of a branched out quantum ring in close resemblance with the Braess paradox, but also provides tools to control the transmission probability minima in such systems.

Acknowledgments

This work was financially supported by PRONEX/CNPq/FUNCAP, Science Without Boards (Cincias Sem Fronteiras) and the bilateral project CNPq-FWO. A. A. Sousa was financially supported by CAPES, under the PDSE contract BEX 7177/13-5. T. A. S. Pereira was financially supported by PRONEX/CNPq/FAPEMAT 850109/2009 and by CAPES under process BEX 3299/13-9.

-
- * Electronic address: ariel@fisica.ufc.br
† Electronic address: andrey@fisica.ufc.br
‡ Electronic address: teldo@fisica.ufmt.br
§ Electronic address: gil@fisica.ufc.br
¶ Electronic address: francois.peeters@uantwerpen.be
- ¹ J. E. Cohen and P. Horowitz, *Nature (London)* **352**, 699 (1991).
 - ² D. Witthaut and M. Timme, *New J. Phys.* **14**, 083036 (2012).
 - ³ M. Rohden, A. Sorge, M. Timme, and D. Witthaut, *Phys. Rev. Lett.* **109**, 064101 (2012).
 - ⁴ M. G. Pala, S. Baltazar, P. Liu, H. Sellier, B. Hackens, F. Martins, V. Bayot, X. Wallart, L. Desplanque, and S. Huant, *Phys. Rev. Lett.* **108**, 076802 (2012).
 - ⁵ A. L. R. Barbosa, D. Bazeia, and J. G. G. S. Ramos, *Phys. Rev. B* **90**, 042915 (2014).
 - ⁶ M. G. Pala, H. Sellier, B. Hackens, F. Martins, V. Bayot, and S. Huant, *Nanoscale Res. Lett.* **7**, 472 (2012).
 - ⁷ D. Braess, A. Nagurney, and T. Wakolbinger, *Transportation Science* **39**, 446 (2005);
 - ⁸ Hai-Feng Zhang, Zimo Yang, Zhi-Xi Wu, Bing-Hong Wang, and Tao Zhou, *Sci. Rep.* **3**, 3292 (2013).
 - ⁹ Hyejin Youn, Michael T. Gastner, and Hawoong Jeong, *Phys. Rev. Lett.* **101**, 128701 (2008).
 - ¹⁰ M. Büttiker, *Phys. Rev. Lett.* **57**, 1761 (1986).
 - ¹¹ A. A. Sousa, A. Chaves, G. A. Farias and F.M. Peeters, *Phys. Rev. B* **88**, 245417 (2013).
 - ¹² S. S. Buchholz, S. F. Fischer, U. Kunze, D. Reuter, and A. D. Wieck, *Appl. Phys. Lett.* **94**, 022107 (2009).
 - ¹³ C. Kreisbeck, T. Kramer, S. S. Buchholz, S. F. Fischer, U. Kunze, D. Reuter, and A. D. Wieck, *Phys. Rev. B* **82**, 165329 (2010).
 - ¹⁴ H. Fehske, J. Schleede, G. Schubert, G. Wellein, V. S. Filinov, and A. R. Bishop, *Phys. Lett. A* **373**, 2182 (2009).
 - ¹⁵ B. Szafran and F. M. Peeters, *Phys. Rev. B* **72**, 165301 (2005).
 - ¹⁶ A. Alvermann and H. Fehske, *Phys. Rev. B* **77**, 045125 (2008).
 - ¹⁷ M. R. Poniedzialek and B. Szafran, *J. Phys.: Condens. Matter* **24**, 085801 (2012).
 - ¹⁸ A. Chaves, G. A. Farias, F. M. Peeters, and B. Szafran, *Phys. Rev. B* **80**, 125331 (2009).
 - ¹⁹ M. H. Degani, *Appl. Phys. Lett.* **59**, 57 (1991).
 - ²⁰ M. H. Degani and M. Z. Maialle, *J. Comp. Theor. Nanosci.* **7**, 454 (2010).
 - ²¹ M. Suzuki, *Phys. Lett. A* **146**, 319 (1990).
 - ²² H. Wang, G. A. Farias, and V. N. Freire, *Superlatt. Microstruct.* **25**, 307 (1999).
 - ²³ J. A. K. Freire, G. A. Farias, and V. N. Freire, *Sol. Stat. Comm.* **106**, 559 (1998).
 - ²⁴ D. E. Manolopoulos, *J. Chem. Phys.* **117**, 9552 (2002).
 - ²⁵ B. Hackens, F. Martins, T. Ouisse, H. Sellier, X. Wallart, A. Cappy, J. Chevrier, V. Bayot, and S. Huant, *Natura Phys.* **2**, 826 (2006).

Quantum tunneling between bent semiconductor nanowires

A. A. Sousa,^{1,2,*} Andrey Chaves,^{1,†} T. A. S. Pereira,^{3,‡} G. A. Farias,^{1,§} and F. M. Peeters^{2,1,¶}

¹*Departamento de Física, Universidade Federal do Ceará,*

Caixa Postal 6030, Campus do Pici, 60455-900 Fortaleza, Ceará, Brazil

²*Department of Physics, University of Antwerp, Groenenborgerlaan 171, B-2020 Antwerp, Belgium*

³*Instituto de Física, Universidade Federal de Mato Grosso, 78060-900, Cuiabá, Mato Grosso, Brazil*

(Dated: May 5, 2015)

We theoretically investigate the electronic transport properties of two closely spaced L-shaped semiconductor quantum wires, for different configurations of the output channel widths as well as the distance between the wires. Within the effective-mass approximation, we solve the time-dependent Schrödinger equation using the split-operator technique that allows us to calculate the transmission probability, the total probability current, the conductance and the wave function scattering between the energy subbands. We determine the maximum distance between the quantum wires below which a relevant non-zero transmission is still found. The transmission probability and the conductance show a strong dependence on the width of the output channel for small distances between the wires.

PACS numbers: 73.63.-b, 85.35.Ds, 73.63.Nm

I. INTRODUCTION

Advances in the fabrication and nanostructuring of semiconductor compounds opens up opportunities for combination of different shapes of devices on a nanometric scale¹⁻⁴. There are numerous experimental methods and techniques of fabricating these semiconductor nanostructures, such as self-organized growth in a MBE chamber⁵⁻⁷, split-gate technique used to fabricate narrow quantum channels for electrons⁸, and AFM lithography, which can be used to create different nanostructures.^{9,10} On a nanometric scale, transport properties of one-dimensional structures are of great interest and a large number of novel phenomena have been predicted and observed in recent years.^{11,12} Here, we shall mention for example investigations on the transport properties through confined states in a 1D wire were performed by Auslaender *et al.*¹³ Tserkovnyak *et al.*¹⁴ gave a detailed experimental investigation and theoretical explanation of a set of interference patterns in the nonlinear tunneling conductance between two parallel wires that were first reported by Auslaender in 2002.¹⁵

From a theoretical point of view, the attempt to model increasingly smaller semiconductor systems that is driven by the miniaturization of technological devices has led to more systematic studies with the aim to describe in more detail the different physical effects, such as tunneling in transistor gate oxides^{16,17} and energy quantization in nanometer scale MOSFETs.^{18,19} In addition, different systems used to calculate the scattering probabilities per unit of time under the effect of perturbative potentials have been proposed and investigated. Some cases of interest here are those when adding an extra path in the system²⁰, an effective potential simulating a Scanning Gate Microscopy tip^{21,22} as well as the effect of a smooth potential in path's connections.²³

In this work, we investigate the wave packet scattering in two L-shaped quantum wires (QW) separated by a distance W_2 , see Fig. 1. The aim is to find the min-

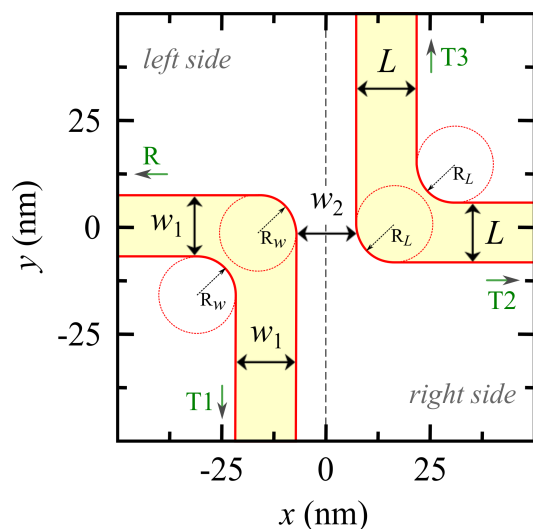


FIG. 1: (Color online) Potential profile scheme for the QWs studied in this work. The two QWs are separated from each other by a distance W_2 , ranging from 0 to 4.8 nm. The smooth connections between vertical and horizontal wire are described by circles of radius $R_W = W_1/2$ and $R_L = L/2$.

imum separation distance between two bent wires with acceptable values for tunneling. For this purpose, we inject a Gaussian wave packet in the left-lead and calculate the transmission into the bottom lead and the tunnelling into the second wire. Our theoretical model is based on the solution of the time dependent Schrödinger equation within the effective mass approach using the split-operator technique.^{23,25} We consider different values of the wave packet kinetic energy and W_2 distances between the quantum wires as well as different width values for the second wire L . We then analyse how the conductivity depends on these parameters (W_2 and L).

This remainder of this organized as follows: In Sec. II, we describe our theoretical model and numerical tech-

nique to solve the time-dependent Schrödinger equation. In Sec. III, we discuss the transport properties of the system and we present our conclusions in Sec. IV.

II. THEORETICAL MODEL

Our model describes electrons in the (x, y) plane moving from left to right in a region with a L-shaped wire (see left side of Fig. 1). The effective-mass approximation was considered and all electrons are confined by a step like potential, i.e., $V(x, y) = 0$ inside the QW and $V(x, y) = V_0$ otherwise. Abrupt interfaces between the confinement region and the potential barrier are assumed. Similarly, in the right side of our set up, another L-shaped QW is considered. The left QW is assumed to have fixed width $W_1 = 10$ nm, whereas for right QW, three different widths L ($= W_1/2, W_1$ and $2W_1$). The smooth edges of the QWs are draw by circles of radius $R_W = W_1/2$ and $R_L = L/2$ for the left and right wire, respectively, in order to approach more realistic systems. The left side is separated from the right by a distance W_2 which ranges from 0 nm to 4.8 nm in this work. In the transverse cross section, the QW behaves as a quasi-one-dimensional channel where an electron confined in this region has a subband energy

$$E_n(k_x) = E_n^{(y)} + \frac{\hbar^2 k_x^2}{2m_e}, \quad (1)$$

where $E_n^{(y)}$ are the y components of the eigenvalues which were obtained numerically for a potential of $V_0 = 600$ meV. These eigenvalues are lower than the corresponding eigenvalues calculated for an infinite potential, $E_n^{(y)} = n^2 \pi^2 \hbar^2 / 2m_e W_1^2$, although this analytical expression can be used for an estimate of energies in a quantum well of W_1 width. A combination of a Gaussian function with a plane wave is injected from the left to the right along the x direction, so that at $t = 0$ the wave packet is given by

$$\Psi(x, y) = \exp \left[ik_0 x - \frac{(x - x_0)^2}{2\sigma_x^2} \right] \phi_0(y). \quad (2)$$

Here, $k_0 = \sqrt{2m_e \varepsilon} / \hbar$ is a wave vector corresponding to the kinetic energy ε , and $\phi_0(y)$ is the ground state wave function of the quantum well in the y direction. The width of the wave packet in the x direction is fixed by σ . The time evolution of the wave packet is studied with the split-operator technique, which allows to separate the kinetic terms for each direction. This separation is important for systems with many degrees of freedom. We follow the approach of Refs. 23 and 25, the details of which will not be reproduced here.

The (x, y) -plane is discretized by a squared grid $\Delta x = \Delta y = 0.4$ nm, and the finite difference scheme is used to solve the derivatives in the kinetic energy terms of the Hamiltonian. To avoid spurious reflection when the wave packet reaches the edges of our set up, we applied

an imaginary potential, as discussed in Ref. 23 and suggested by Manolopoulos.²⁷ The current of the system is given by

$$\mathbf{J} = -\frac{i\hbar}{2m_e} (\Psi^* \nabla \Psi - \Psi \nabla \Psi^*). \quad (3)$$

The transmission T probabilities are calculated in three different positions at vertical (T_1 and T_3) and horizontal (T_2) axis, as shown in Fig. 1. For horizontal axis we fixed a point x_r , localized in the right side and the transmission T_2 is calculated as

$$T = \int_0^\infty dt \int_{-\infty}^\infty dy J_x(x_r, y, t). \quad (4)$$

For vertical axis we fixed a point y_B in the bottom wire and a point y_T in the top wire and calculated the transmission T_1 and T_3 through Eq. (4), changing $J_x(x_r, y, t)$ for $J_y(x, y_T, t)$ and $J_y(x, y_B, t)$, respectively, and the above spatial integral is now evaluated along x -direction. The reflection probability R is calculated in the left side by fixing a point x_l in the left side and evaluating the integrals in dt and dy . More precisely

$$R = -\int_0^\infty dt \int_{-\infty}^\infty dy J_x(x_L, y, t), \quad (5)$$

where J_x is the x component of the probability current.

In order to investigate the scattering of an electron into different subbands of the wires, we project the wave function on the j th eigenstate of the quantum well at a fixed point x_i , using the relation

$$P_j(x_i, t) = |\langle \Psi | \phi_j \rangle|^2 = \left| \int_{-\infty}^{+\infty} dy \Psi(x_i, y, t) \phi_j(y) \right|^2. \quad (6)$$

Eq. (6) is the probability density of finding an electron in the j th subband at position x_i per length in the x direction. Moreover, the contribution of each subband state to the probability current can be calculated by

$$j_x^{(j)}(x, t) = \frac{\hbar}{2m_e i} \left(\bar{P}_j^* \frac{\partial}{\partial x} \bar{P}_j - \bar{P}_j \frac{\partial}{\partial x} \bar{P}_j^* \right), \quad (7)$$

where $\bar{P}_j(x, t) = \langle \phi_j | \Psi \rangle$ gives the time-dependent wave function within the j th subband. Notice that, since $\bar{P}_j(x, t)$ is not normalized, its value can be larger than one. Finally, the time-dependent probability current at x_i is given by

$$J_t(x_i, t) = \int_{-\infty}^{+\infty} J_x(x_i, y, t) dy. \quad (8)$$

Solution of Eqs. (6-8) form the basis to understand the conductivity and the trajectory of the wave packet through the wires.

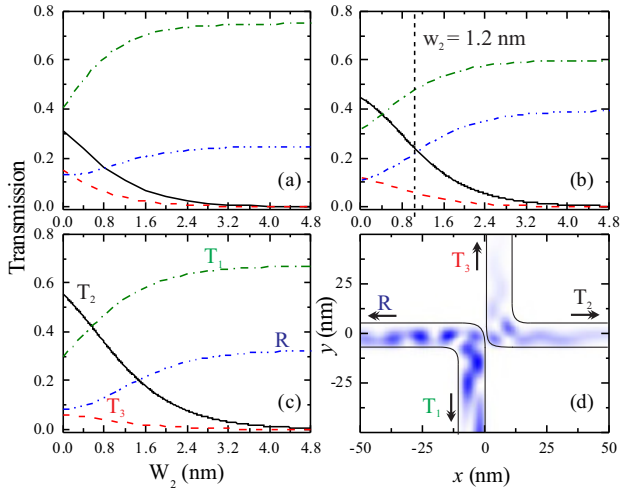


FIG. 2: (Color online) (a)-(c) Wave packet transmissions (T) and reflexion (R) probabilities as function of W_2 for a well width of $L = W_1$. The transmissions are calculated in three different points in the QWs: bottom T_1 (green, dash dot line), top T_3 (red, dash line) right T_2 (black, solid line), while the reflexion R (blue, dash dot dot line) is calculated at the left side, as shown in (d). The wave packet energies used are (a) ε_1 , (b) ε_2 and (c) ε_3 . (d) Snapshot of the wave function calculated at $t = 160$ fs for $L = W_1$ and $W_2 = 1.2$ nm as depicted by the vertical dash line in (b).

III. RESULTS AND DISCUSSION

For all cases considered in this work, we consider material parameters for InGaAs (wire) and GaAs (barrier material), in which the conduction band of the InGaAs/GaAs heterostructure has a band-offset of 600 meV. Moreover, for InGaAs the electron effective mass is $m_e = 0.041 m_0$.²⁶ The wave packets are injected from left to right at $t = 0$, in the lowest subband $\phi_{n=1}(y)$. Three different values of the kinetic energy of the wave packets are considered: $\varepsilon_1 = 70$ meV, $\varepsilon_2 = 140$ meV and $\varepsilon_3 = 200$ meV.

Transmission and reflection probabilities obtained with our method are presented in Fig. 2 and Fig. 3 as function of the distance W_2 for $L = W_1$ and $L = 2W_1$, respectively. The transmission probabilities are calculated on the left-bottom wire T_1 (green, dash dot line), right-output wire T_2 (black, solid line) and right-top wire T_3 (red, dash line). The reflection R (blue, dash dot dot line) is calculated on the input left-wire. We checked numerically that the sum $R + \sum T_i = 1$ is satisfied up to a maximum error of 0.1 %. Figs. 2(d) and 3(d) are snapshots of the wave function with kinetic energy 70 meV, calculated at $t = 160$ fs for $W_2 = 1.2$ nm, as indicated by the vertical dashed-gray line in Fig. 2(b) and Fig. 3(b), respectively. For a wave packet with kinetic energy ε_1 (Figs. 2(a) and 3(a)) the transmission coefficient T_2 decreases faster than the one with kinetic energy ε_3 , (Figs.

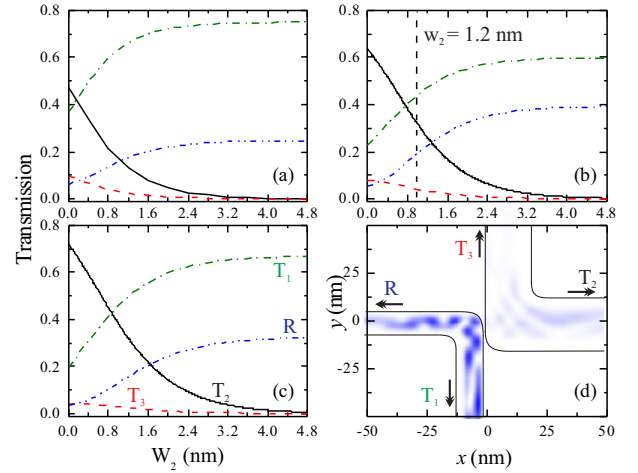


FIG. 3: (Color online) The same result as shows in Fig. 2, but now for $L = 2W_1$.

2(c) and 3 (c)), i.e., the tunnelling through the barrier W_2 is in general larger for higher kinetic energy. Furthermore, the transmission T_2 decreases towards zero with increasing width W_2 , and as a consequence, the transmission T_1 and reflection R increase such that $T_1 + R \simeq 1$ for wide W_2 . The tunnelling T_3 through the top-right side is less than 10%, but nonzero even for high kinetic energy of the wave packet and for different W_2 distance. This behavior is shown in Figs. 2 and 3 by dashed red lines for $L = W_1$ and $L = 2W_1$, respectively, and occurs because the quantum wire shape spreads the wave function around the position $x = 0$, specially for $W_2 = 0$, where the transmission is about 70 % through T_1 and the other 30 % are reflected R or tunnel through T_2 and T_3 , as shown in Fig. 3(c).

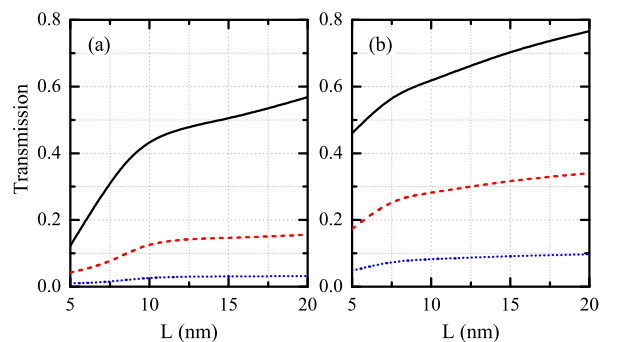


FIG. 4: (Color online) Transmission coefficient ($T_2 + T_3$) as function of the well width L , for wave packet energies (a) ε_1 and (b) ε_3 . Three W_2 distance were considered: 0 nm (black, solid line), 1.2 nm (red, dash line) and 2.4 nm (blue, dotted line).

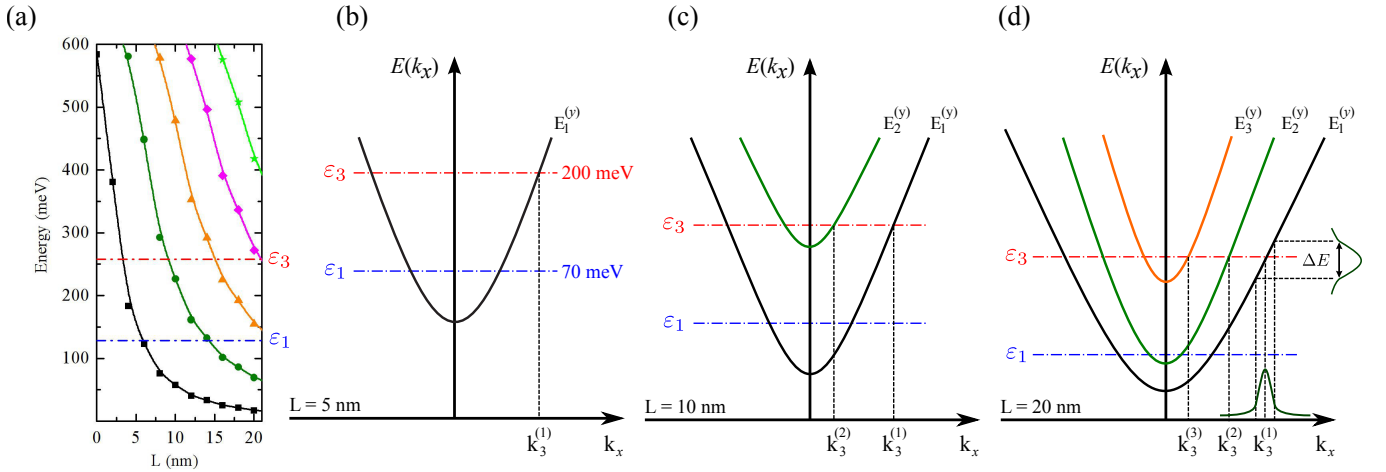


FIG. 5: (Color online) (a) Bottom energy of the different subbands as function of the quantum well width L . Schematic diagrams that represents the subband energies as function of the wave vector k_x in the x direction, for output width of (b) $L = 5$ nm, (c) $L = 10$ nm, and (d) $L = 20$ nm. The horizontal dashed-dot lines represents the average energy of the wave packet, ε_1 and ε_3 .

In order to clarify the role of the well width L in the output lead on the transmission probabilities in Fig. 4 we display the transmission coefficient on the right side ($T_2 + T_3$) as function of L for two different wave packet kinetic energies ε_1 (a) and ε_3 (b). Three different W_2 distances were considered namely, 0 nm (black, solid line), 1.2 nm (red, dash line) and 2.4 (blue, dotted line). The transmission increase with increasing L which is a consequence of the lowering of the subband energy states in the right side over which the tunnelled wave function can be distributed. For a lower wave packet kinetic energy ε_1 the transmission stays below 20 % for W_2 distance above 1.2 nm, and for ε_3 the transmission keep below 40 %.

Let us now discuss the contribution of each subband of the output lead to its overall current. In order to have a better understanding of this problem, we display in Fig. 5(a) the eigenenergies of the output lead as a function of its width. The average wave vector k_x^i of the wave packet is schematically shown in Figs. 5(b) for $L = W_1/2$, 5(c) for $L = W_1$, and in 5(d) for $L = 2W_1$. Here, the highest kinetic energy was chosen to cover the first three subbands in the output lead, where the bottom of the subband is found to be around ε_3 , for an output width of $L = 2W_1$. This kinetic energy allows us to calculate the influence of the subbands on the scattering of the wave packet. The number of k_x values allowed for each kinetic energy ε , at each subband, depends on the width L , which in the case illustrated in Fig. 5 (b) is $k_2^{(1)}$ when $L = W_1/2$. However, it take values $k_2^{(1)}$, $k_2^{(2)}$, and $k_2^{(3)}$ for ε_2 with $L = 2W_1$ (see Fig. 5(d)). As for our Gaussian wave packet, the initial wave functions with distributions of k_x 's around k_x^i , that yields an energy distribution ΔE as illustrated in Figs. 5(d). More details regarding the initial wave package width in k_x -space can be obtained by Fourier transform and this is explained in details in Ref. 23. In the case proposed here, where the

wave function is also Gaussian in reciprocal space, it is possible to determine the energy distribution of the wave packet as $\Delta E = \hbar^2 \Delta k / m_e k_0$, where $\Delta k = 2\sqrt{\ln 2} / \sigma_x$ is the full width at half maximum (FWHM).²³

In Fig. 6 we show the projection of the time-dependent wave packet on the ground (P_1), first-excited (P_2), and second-excited state subband (P_3) of the right-lead. The projections are calculated numerically as function of W_2 at the point $x = 158$ nm in the right side, for output widths $L = W_1$ (a) and $L = 2W_1$ the (b). The results are shown for wave packet kinetic energies of ε_1 (black, solid line), ε_2 (red, dash line) and ε_3 (blue, dotted line). Initially the wave packet propagates in the lowest subband. As expected, all projections decrease towards zero as W_2 increases, since the overall current also exhibits this decreasing behavior. For narrow wells, the packets with kinetic energies ε_2 and ε_3 scatter to the first excited state, while for energy ε_1 this projection is almost zero for any W_2 value. The projection for the second excited state is only possible for wave packets with an energy of ε_3 , as shown in Fig. 5(c). For quantum wells with $L = 2W_1$, the subbands energies get closer to each other such that the wave packet scatter to excited states even for energy ε_1 , Fig. 6(b).

An analysis of the time-dependent current probability for the wave packet as a function of time is illustrated in Fig. 7. The wave packet propagates in the lowest subband from the left to the right side with kinetic energy given by ε_1 (blue, dotted line), ε_2 (red, dash line) and ε_3 (black, solid line). Around $y = 0$ and along the x -axis, the potential is similar to a simple quantum barrier with height of 600 meV. Calculated at $x = 158$ nm across the potential barrier, the time-dependent current probability is a tunnelling current that can give an estimate about the leakage current through the barrier. In Fig. 7 we plot the tunnelling current probabilities for two different

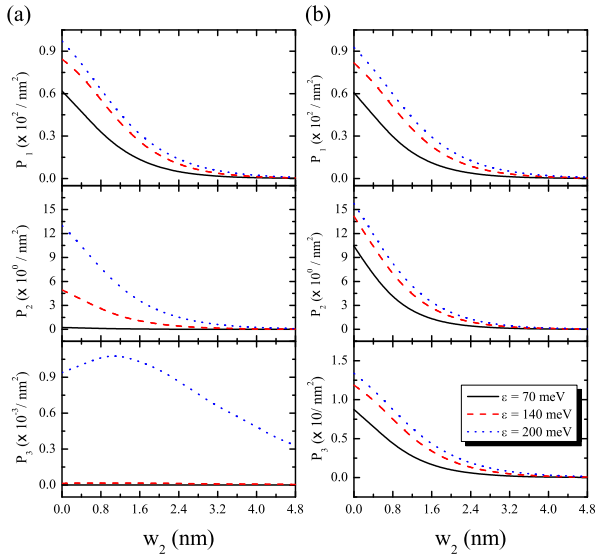


FIG. 6: (Color online) Projection of the wave function on the ground state P_1 , first-excited P_2 and second-excited subbands P_3 integrated in time, for the output width $L = W_1$, panels column (a) and $L = 2W_1$, panels column (b), as function of the distance W_2 calculated at position 158 nm in the right-lead.

W_2 distances: (a) $W_2 = 0$ nm and (b) 2.4 nm. For each W_2 distance we consider three different output widths L , from top to bottom $L = W_1/2$ in the first row, $L = W_1$ in the second, and $L = 2W_1$ in the third row. Clearly, the peak in the probability current is lower at low energies, and it also decreases (increases) with increasing distance (width) W_2 (L). Particularly, in the case of $L = W_1$, Fig. 7 emphasizes the oscillatory behaviour of the probability current for the two distances W_2 used in our calculations. This probability current oscillation is due to wave function scattering in the central region of the wires, as illustrated in Figs. 2 and 3 (d). It is easy to see that the current peak occurs faster as the energy increases, as a consequence of the higher Fermi velocity in this case. Besides, increasing L for fixed W_2 slightly shift the peaks to lower times, which is due to the fact that larger widths lead to lower subband energies and consequently, higher momentum for fixed wave packet energy.

Finally, from a practical point of view, it is important to investigate the behaviour of the conductance for different values of the kinetic energy, W_2 distance and output width L . With this in mind, we express the conductance as a particular case of the multiband Landauer formalism^{28,29}

$$G_l(\varepsilon) = \frac{2e^2}{h} \sum_n T_l^{(n)}(\varepsilon), \quad (9)$$

where the output lead index l is 1, 2 or 3 for conductance calculated with T_1 , T_2 and T_3 , respectively, and

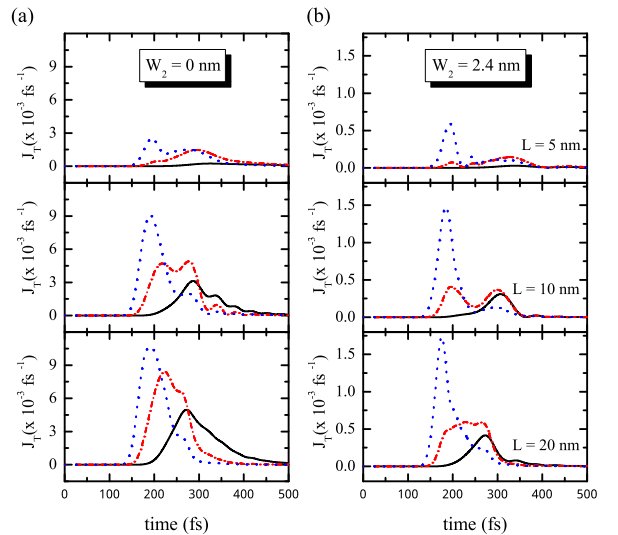


FIG. 7: (Color online) The total time-dependent probability current for wave packet energy of ε_1 (black, solid line), ε_2 (red, dash line) and ε_3 (blue, dotted line). Results for different distances W_2 are plotted in column (a) $W_2 = 0$ nm, and column (b) $W_2 = 2.4$ nm. The output width L is in the first row $L = W_1/2$, second row $L = W_1$, and third row $L = 2W_1$.

the index n account for different occupied subbands in the input lead. The quantum conductance ($G_0 = 2e^2/h$) is used here as unit of electrical conductance, and the transmission coefficients $T_{(x_t, y_t)}^{(n)}(\varepsilon)$ are calculate by setting the wave packet at the initial time in a given subband n , with average energy ε , and integrating the probability current at the axis defined by (x_t, y_t) , as in Eq. (4).

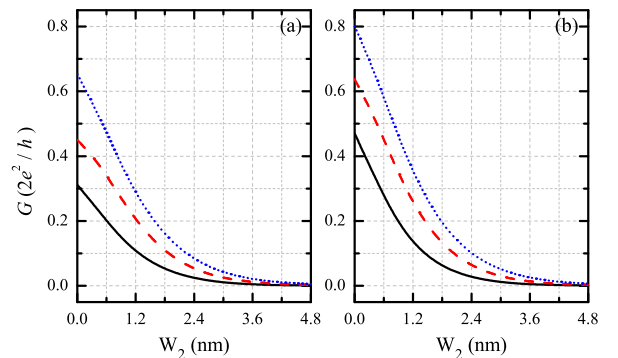


FIG. 8: (Color online) Conductance in the output quantum wire as a function of the distance W_2 . Wavepacket energy is ε_1 (black, solid lines), ε_2 (red, dashed lines) and ε_3 (blue, dotted lines) for quantum well L width of (a) 10 nm and (b) 20 nm.

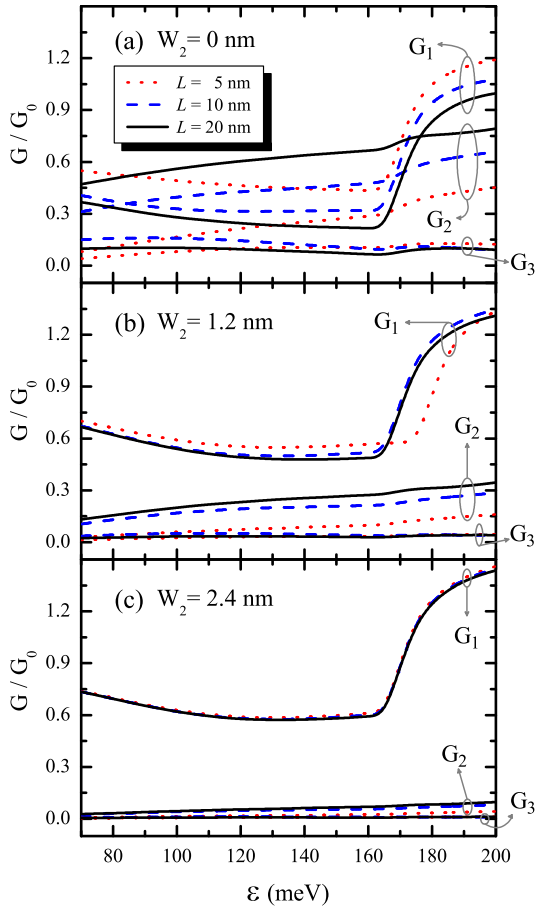


FIG. 9: (Color online) Conductance of the quantum wire as a function of kinetic energy wave packet for the three possible output leads G_1 , G_2 and G_3 , with well widths $L = 5$ nm (dotted red), $L = 10$ nm (dashed blue) and $L = 20$ nm (solid black). The W_2 distance is given by (a) 0 nm, (b) 1.2 nm and (c) 2.4 nm.

Figure 8 displays the conductance versus the distance W_2 calculated for three wave packet kinetic energies ε_1 (solid black), ε_2 (dashed red) and ε_3 (dotted blue). The conductance was computed by taking into account the transmission probability of the first three subbands for the T_2 coefficient at $x = 158$ nm on the output lead, with output width $L = W_1$ in Fig. 8(a) and $L = 2W_1$ in Fig. 8(b). The conductance depends strongly on the distance W_2 . We observe that when the distance W_2 increases the transmission probability decreases, hence decreasing the conductance in the output region. The wave packet scattering is larger for the case where $L = W_1$, resulting in a larger reflection probability, as can be seen in Figs. 2 and 3, which explains why G is higher in 8(b), as compared to Fig. 8(a). Also, the conductance changes with the kinetic energy of the wave function even for $W_2 = 0$ nm, as observed in Fig. 8(a), as a consequence

of quantum scattering at the junction between the wires.

All results presented so far were made for fixed wave packet average energies $\varepsilon = \varepsilon_1$, ε_2 or ε_3 . It is important to discuss how these results relate to possible future experiments aiming to verify the quantum tunnelling effects investigated here. In fact, at temperature $T = 0$ K, Landauer formula for conductance is exactly given by Eq. (9), but with transmission probabilities calculated for a plane wave with energy ε . For non-zero temperature, however, the transmission probability must be multiplied by the derivative of the Fermi's energy distribution and then integrated in energy, so that there will be a temperature dependent range of energies around the Fermi level that effectively contribute to the overall conduction. Notice that in our calculations, since we do not consider plane waves, results are never for a single ε and, consequently, they do not describe a zero-temperature situation. Actually, the Gaussian wave packet considered here yields a Gaussian distribution of momenta or, equivalently, a combination of plane waves with different energies. Therefore, in a sense, our results for conductance are closely related to those for non-zero temperature, where the width of the Gaussian wave packet in reciprocal space is related to the width of the energy distribution and, consequently, plays the role of the temperature. Finding the exact relation between temperature and the wave packet width is, however, a difficult task, which is left for future works, whereas here we restrict ourselves to a more qualitative discussion of this matter.

Having stated that, we now use our method to calculate the steps in conductance as a function of the electron energy, as expected for a quantum channel such as the one considered here. These steps cannot be sharp, since we are dealing with a non-zero temperature simulation. This is shown in Fig. 9 for energies ranging from ε_1 to ε_3 , for three different W_2 width: (a) 0 nm, (b) 1.2 nm, and (c) 2.4 nm. The conductance is calculated between the input lead and the three possible output leads, namely, with G_1 , G_2 and G_3 , showed in Fig. 9 by arrows. Well widths are $L = 5$ nm (dotted red), 10 nm (dashed blue), and 20 nm (solid black). Conductance to the upper lead G_3 is always close to zero and reaches, at most, ≈ 0.15 for $W_2 = 0$, as expected from the low transmission probabilities for this lead observed in previous results in Figs. 2 and 3. Notice that for the widest L width, three subbands are involved in the output lead for a wave packet kinetic energy around ε_3 , as shown in Fig. 5 (d). On the other hand, for narrow widths, one subband is involved for $L = 5$ nm, Fig. 5 (b), and two subbands are involved for $L = 10$ nm, Fig. 5 (c). For this reason, the conductances G_2 in Fig. 9 (a) and (b) are clearly spaced for different values of L . Since G_2 is directly related to the current leak, it is responsible for reducing the conductance through the original channel G_1 . For lower values of energy ε , conductance G_1 is reduced as the energy increases, due to the increasing current leakage G_2 . This effect is reduced either as the distance between wires increases or as the second wire width L is made narrower, thus hindering the

quantum tunnelling between wires. Furthermore, the differences between conductance G_1 for different values of L become negligible as the W_2 distance becomes too large, see Fig. 9 (c). The quantized steps of conductance are also observed in the leakage current G_2 , but much lower than those for G_1 , which suggests that states in the first excited subband of the input lead have lower contribution for the leakage current as compared to those coming from the first subband.

IV. CONCLUSIONS

We have presented a theoretical investigation of the electron transmission between two bent quantum wires that is based on the propagation of a Gaussian wave packet. The two L-shaped semiconductor quantum wires are separated by a distance W_2 . We showed how a changes in the distance between the two QWs W_2 affects the tunneling probability and the time-dependent probability current for different values of kinetic energy wave packet. The wave packet scattered by the potential is re-

flected and transmitted through the barrier. The tunneling current provides an estimate of the leakage current in the system, which becomes larger as W_2 is reduced. It is of fundamental and practical importance to control these undesired leakage currents in miniaturized electronic devices and circuits, thus, we believe the results presented here might contribute to help future experimental investigations of carrier transport in low dimensional circuits and their future applications in nanotechnology.

Acknowledgments

A. A. Sousa was financially supported by CAPES, under the PDSE contract BEX 7177/13-5. T. A. S. Pereira was financially supported by PRONEX/CNPq/FAPEMAT 850109/2009 and by CAPES under process BEX 3299/13-9. This work was financially supported by PRONEX/CNPq/FUNCAP, the Science Without Borders program and the bilateral project CNPq-FWO.

* Electronic address: ariel@fisica.ufc.br

† Electronic address: andrey@fisica.ufc.br

‡ Electronic address: teldo@fisica.ufmt.br

§ Electronic address: gil@fisica.ufc.br

¶ Electronic address: francois.peeters@uantwerpen.be

- ¹ A. B. Balantekin, N. Takigawa, Rev. Mod. Phys. **70** 77 (1998).
- ² R. J. Warburton, C. Schäfflein, D. Haft, F. Bickel, A. Lorke, K. Karrai, J. M. Garcia, W. Schoenfeld, and P. M. Petroff, Nature (London), **405** 926 (2000).
- ³ S. S. Mao, Int. Jour. Nanot. **1** 42 (2004).
- ⁴ C. Y. Hou, A. Rahmani, A. E. Feiguin, and C. Chamon, Phys. Rev. B **86**, 075451 (2012).
- ⁵ J. J. Ramsey, E. Pan, P. W. Chung and Z. M. Wang, NanoScale Res. Lett. **5**, 1272 (2010).
- ⁶ Y. Cohin, O. Mauguin, L. Largeau, G. Patriarche, F. Glas, E. Sondergard, and J. C. Harmand, Nano Lett. **13**, 2743 (2013).
- ⁷ T. Ihn, Quantum states and electronic transport (Oxford University press, Oxford, 2010).
- ⁸ H. U. Baranger, and A. D. Stone, Phys. Rev. Lett. **63**, 414 (1989).
- ⁹ M. D. Seta, G. Capellini, and F. Evangelisti, Phys. Rev. B **77**, 045431 (2008).
- ¹⁰ A. Fuhrer, S. Lüscher, T. Ihn, T. Heinzl, K. Ensslin, W. Wegscheider, and M. Bichler, Nature (London), **413** 822 (2001).
- ¹¹ M. T. Björk, B. J. Ohlsson, C. Thelander, A. I. Persson, K. Deppert, L. R. Wallenberg, and L. Samuelson, Appl. Phys. Lett. **81**, 4458 (2002).
- ¹² T. D. Stanescu, R. M. Lutchyn, S. Das Sarma, Phys. Rev. B **90**, 085302 (2014).
- ¹³ O. M. Auslaender, A. Yacoby, R. de Picciotto, K. W. Bald-

win, L. N. Pfeiffer, and K. W. West, Phys. Rev. Lett. **84**, 1764 (2000).

- ¹⁴ Y. Tserkovnyak, B. I. Halperin, O. M. Auslaender, and A. Yacoby, Phys. Rev. Lett. **89**, 136805 (2002).
- ¹⁵ O. M. Auslaender, A. Yacoby, R. de Picciotto, K. W. Baldwin, L. N. Pfeiffer, and K. W. West, Science **295**, 825 (2002).
- ¹⁶ Y. T. Hou, M. F. Li, Y. Jin, and W. H. Lai, Jour. Appl. Phys. **91**, 258 (2002).
- ¹⁷ W. C. Lee and C. Hu, Trans. Elect. Dev. **48**, 1366 (2001).
- ¹⁸ A. Chaudhry and J. N. Roy, Journ. Elect. Scien. Tech. **9**, 51 (2011).
- ¹⁹ A. Chaudhry and J. N. Roy, Int. Jour. Nanoelect. Mater. **5**, 1 (2012).
- ²⁰ A. A. Sousa, A. Chaves, G. A. Farias, and F. M. Peeters, Phys. Rev. B **88**, 245417 (2013).
- ²¹ B. Szafran, Phys. Rev. B **84**, 075336 (2011).
- ²² H. Sellier, B. Hackens, M. G. Pala, F. Martins, S. Baltazar, X. Wallart, L. Desplanque, V. Bayot, and S. Huant, Semicond. Sci. Techno. **26**, 0644008 (2011).
- ²³ Andrey Chaves, G. A. Farias, F. M. Peeters, and B. Szafran, Phys. Rev. B **80**, 125331 (2009).
- ²⁴ B. A. Z. António, A. A. Lopes, and R. G. Dias, Eur. J. Phys. **34**, 831 (2013).
- ²⁵ M. H. Degani, Phys. Rev. B **66**, 233306 (2002).
- ²⁶ B. Hackens, F. Martins, T. Ouisse, H. Sellier, S. Bollaert, X. Wallart, A. Cappy, J. Chevrier, V. Bayot, and S. Huant, Nat. Phys. **2**, 826, (2006).
- ²⁷ D. E. Manolopoulos, J. Chem. Phys. **117**, 9552 (2002).
- ²⁸ R. Landauer, IBM Journ. Res. Develop. **1**, 223 (1957)
- ²⁹ M. Büttiker, Phys. Rev. Lett. **57**, 1761 (1986).

Appendix B

Publications not related to this thesis

- A. A. Sousa, T. A. S. Pereira, A. Chaves, J. S. de Sousa, and G. A. Farias, *Interfacial confinement in core-shell nanowires due to high dielectric mismatch*, Applied Physics Letters **100**, 211601 (2012), DOI:<http://dx.doi.org/10.1063/1.4720402>

Interfacial confinement in core-shell nanowires due to high dielectric mismatch

A. A. Sousa,¹ T. A. S. Pereira,¹ A. Chaves,² J. S. de Sousa,² and G. A. Farias²

¹*Institute of Physics, Federal University of Mato Grosso, 78060-900 Cuiabá, Mato Grosso, Brazil*

²*Department of Physics, Federal University of Ceará, C.P. 6030, 60455-900 Fortaleza, Ceará, Brazil*

(Received 14 March 2012; accepted 5 May 2012; published online 22 May 2012)

We theoretically investigate the role of the dielectric mismatch between materials on the energy levels and recombination energies of a core-shell nanowire. Our results demonstrate that when the dielectric constant of the core material is lower than that of the shell material, the self-image potential pushes the charge carriers towards the core-shell interface in such a way that the ideal confinement model is no longer suitable. The effects of this interfacial confinement on the electronic properties of such wires, as well as on its response to applied magnetic fields, are discussed. © 2012 American Institute of Physics. [<http://dx.doi.org/10.1063/1.4720402>]

Great attention has been devoted to the investigation of the electronics and optical properties of core-shell nanowires (NW). In particular, the applications of these low dimensional structures in optoelectronic and photonic devices are of interest for the electronics industry, and much effort has been dedicated to their fabrication.¹⁻⁴ In addition, studies of low dimensional systems surrounded by high dielectric constant materials continue to attract attention from many researchers^{5,6} towards a continuation of the Moore's law. Recently, wire diameters of a few nanometers were experimentally achieved,⁷ and carrier confinement effects in these nanowires have been reported with different levels of sophistication.⁸⁻¹⁰

This work aims to investigate the dielectric mismatch effects on core-shell NW, focusing on the possibility of interfacial confinement of the carriers. As for the model structure, we consider a semiconductor cylindrical nanowire (core region) of radius R , surrounded by a different material (shell region). The interface between core and shell regions is assumed to be abrupt, i.e., the materials parameters change abruptly from the core to the shell regions. For the heterostructure materials considered in this paper, the bands mismatch creates a high potential barrier for the charge carriers in the shell, leading to a short penetration of the wave functions in this region. This rules out the role of the shell width on the energy states of the NW since the wave function does not reach the outer edge of the shell. The nanowire electronic structure is obtained by solving numerically a Schrödinger-like equation within the adiabatic approach and the effective mass framework.¹¹ The total confinement potential $V_T^i(\rho_i) = \Delta E_i(\rho_i) + \Sigma_i(\rho_i)$ is given by the sum of band edges discontinuities $\Delta E_i(\rho_i)$ and the self-energy potential $\Sigma_i(\rho_i)$, where $i = e, lh, hh$ represents the carrier types (electron, light hole, and heavy hole, respectively). The latter term appears due to the dielectric mismatch, and its calculation is based on the method of the image charges. The details of this calculation can be seen in our supplementary material.¹¹ In a nutshell, the self-energy potential $\Sigma_i(\rho_i)$ inside the core region, due to a carrier located in the core region, is given by Eq. (19) of Ref. 10, whereas when the carrier is located in the shell region, the self-energy potential inside this region can be obtained using a similar expression, just

by changing the modified Bessel functions of the first type, $I_m^2(k\rho_e)$ and $I_m^2(k\rho_h)$, by those of the second type, $K_m^2(k\rho_e)$ and $K_m^2(k\rho_h)$, respectively.

The electron-hole recombination energy, $E_R^{e-h} = E_G + E_e + E_h$ ($h = lh$ or hh), given by the sum of the band gap energy E_G on the core region with the electron E_e and hole E_h confinement energies, is calculated for the radial ground state quantum number $n = 1$ and zero angular momentum $l = 0$, allowing us to analyze the effects caused by the self-energy potential on the ground state energy of the electron-hole pair. Figure 1(a) shows the role of the dielectric mismatch on the value of the electron-hole recombination energy $\Delta E_R^{e-h} = E_{R,\Sigma_i(\rho_i) \neq 0} - E_{R,\Sigma_i(\rho_i) = 0}$, as a function of the ratio $\varepsilon_r = \varepsilon_1/\varepsilon_2$ between dielectric constants of the core (ε_1) and shell (ε_2) materials, considering several values of nanowire radii R , for different materials. This quantity denotes the difference between the recombination energies with ($E_{R,\Sigma_i(\rho_i) \neq 0}$) and without ($E_{R,\Sigma_i(\rho_i) = 0}$) the self-energy corrections. The analysis of this difference gives us the advantage of excluding the effect of quantum confinement due to the band edge mismatch ΔE_i , remaining exclusively the confinement due to the dielectric mismatch. The material parameters are the same as in Ref. 12.

As in the case of quantum wells, shown by Pereira *et al.*,¹² if the dielectric constant in core region ε_1 is smaller than that of the shell region ε_2 , the potential in the core region is attractive and its contribution to the recombination energy is negative $\Delta E_R < 0$. On the other hand, for a larger dielectric constant in core region, as compared to the one in the shell region, the potential in the core region is repulsive, so that its contribution to the recombination energy is positive $\Delta E_R > 0$, as clearly shown in Fig. 1(a). The resulting ΔE_R^{e-h} for both light and heavy holes are the same, as this quantity only contains the effects of $\Sigma_i(\rho_i)$ on the carrier charge. On the other hand, by plotting E_R^{e-h} , it is possible to observe the difference between $e-lh$ and $e-hh$ pairs, caused by the different light hole and heavy hole effective masses.

Note that the AlGaAs/GaAs heterostructure has $\varepsilon_r \approx 1$, i.e., the dielectric mismatch in this case is negligible. In fact, one can verify in Fig. 1(a) that for AlGaAs/GaAs, $\Delta E_R \approx 0$ for any value of wire radius. AlGaAs/GaAs core-shell wires

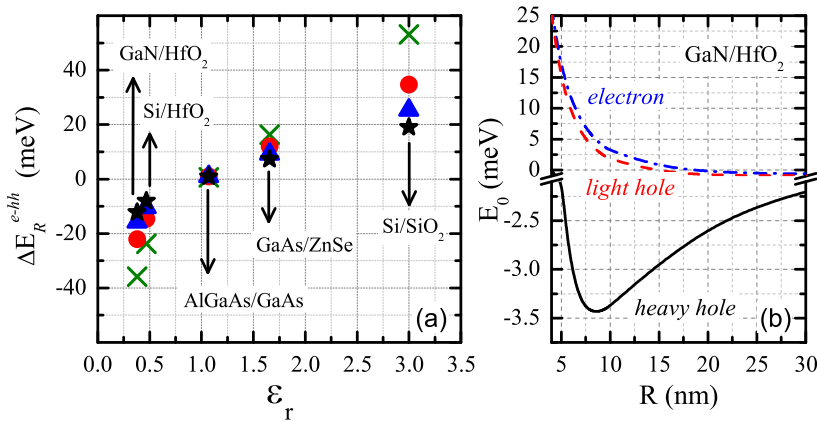


FIG. 1. (a) Effect of the self-energy potential on the recombination energy of an electron-hole pair, for different wire radii: 4 nm (\times), 6 nm (\bullet), 8 nm (\blacktriangle), and 10 nm (\blacksquare). (b) Ground state energies as a function of the core radius for carriers confined in a GaN/HfO₂ core-shell heterostructure.

have been widely experimentally studied for many reasons, e.g., the possibility of obtaining lattice matched defect-free samples, where the AlGaAs shell reduces the surface-related nonradiative recombination, by passivating the GaAs core.¹³ However, the results in Fig. 1(a) suggest that this heterostructure is actually not the best choice for investigating dielectric mismatch effects. As we will demonstrate onwards, the case of GaN/HfO₂ heterostructures is particularly interesting.

The growth of nitride-based cylindrical core wires,⁷ as well as HfO₂ shells,⁶ has been reported recently, which makes us believe that such a structure could be experimentally realized in near future. Figure 1(b) shows the ground state energies E_0 (i.e., for $n=1$ and $l=0$) for each carrier in a core-shell GaN/HfO₂ heterostructure as a function of the core radius. As usual, as the radius increases, the carrier confinement becomes weaker, leading to a reduction in the ground state energy, which is clearly observed for the electron and the light hole in this case. Conversely, the heavy hole energy shows a non-monotonic dependence on the radius, namely, it decreases for smaller radii but starts to increase as the radius becomes larger, suggesting a different confinement regime for this carrier. In fact, such a behavior is analogous to the one reported in the literature for GaN/HfO₂ quantum wells.¹⁴ In the quantum wells case, such a non-monotonic behavior of the confinement energy was demonstrated to be a consequence of the fact that $\epsilon_r < 1$ in this heterostructure, leading to an attractive potential which pulls the carrier towards the interface between the materials. Analogously, this suggests the existence of an interfacial confinement of the heavy hole in the NW. For smaller radii, the quantum confinement due to the bands mismatch is still dominant, but as the radius is enlarged, the energy decreases and eventually enters the negative energy domain, where the hh becomes bound to the core-shell interface due to the self-image potential. Being compressed towards the interface, the hh experiences an increase in its energy as the radius is further enlarged.

Notice that the sign of the confinement energy indicates whether a charge carrier is confined in the core or at the interfacial region. Without dielectric mismatch, or even for $\epsilon_r > 1$, the confinement energy is always positive since the bottom of the confinement potential V_T^c is always either zero or larger. Conversely, the presence of a $\epsilon_r < 1$ mismatch is responsible for negative cusps on the potential at

the interfacial region.^{10,12} Hence, a negative confinement energy suggests an interfacial confinement. In fact, the heavy hole is the only carrier with negative energy in Fig. 1(b), and it is indeed the only one exhibiting non-monotonic behavior of the confinement energy as the radius increases.

The consequences of the interfacial confinement are numerous. For instance, for some combinations of core-shell materials, one might find holes in the interface and electrons in the core. Such an electron-hole spatial separation leads to a reduction of the overlap between their wavefunctions, reducing the oscillator strength and, consequently, the recombination rate. The overlaps between electron and light (lh , top) and heavy (hh , bottom) hole wave functions are shown as a function of the core wire radius R in Fig. 2(a), for the same combinations of core and shell materials in Fig. 1(a). For all the heterostructures shown, the overlap value is slightly lower than unit for small radii. This is just a consequence of the fact that wave functions for different charge carriers penetrate with different depths into the barriers, and this effect is more pronounced when the NW radius is small. In the AlGaAs/GaAs (blue), GaAs/ZnSe (green), and Si/SiO₂ (black) cases, where the dielectric constants ratios are $\epsilon_r > 1$, the overlaps for both $el-lh$ and $el-hh$ pairs simply converge to 1 as the radius increases, which means that electrons and holes are practically equally distributed in space for larger wire radius. However, the overlaps in the $\epsilon_r < 1$ heterostructures exhibit a maximum at moderate R (around 10–20 nm) and decrease after this value, indicating different distributions of electron and holes functions for large R . Although this effect is also present for the Si/HfO₂ heterostructure, it is much stronger in the GaN/HfO₂ case (red), specially for the $el-hh$ pair.

In order to help us to understand the heavy hole interfacial confinement and the consequently different spatial distribution of charge carriers, Fig. 2(b) illustrates the total confinement potential (black solid), along with the normalized ground state wave functions, for electrons (top) and heavy holes (bottom) in a $R=30$ nm GaN/HfO₂ core-shell NW. The electron wave function considering dielectric mismatch effects (black dashed) is still confined mostly in the vicinity of the central axis of the core, even at such a large radius, and its width is wider than that without dielectric mismatch (blue dash dotted). On the other hand, the heavy hole wave functions, depicted in the bottom panel of Fig. 2(b) for different values of the core wire radius R , are clearly

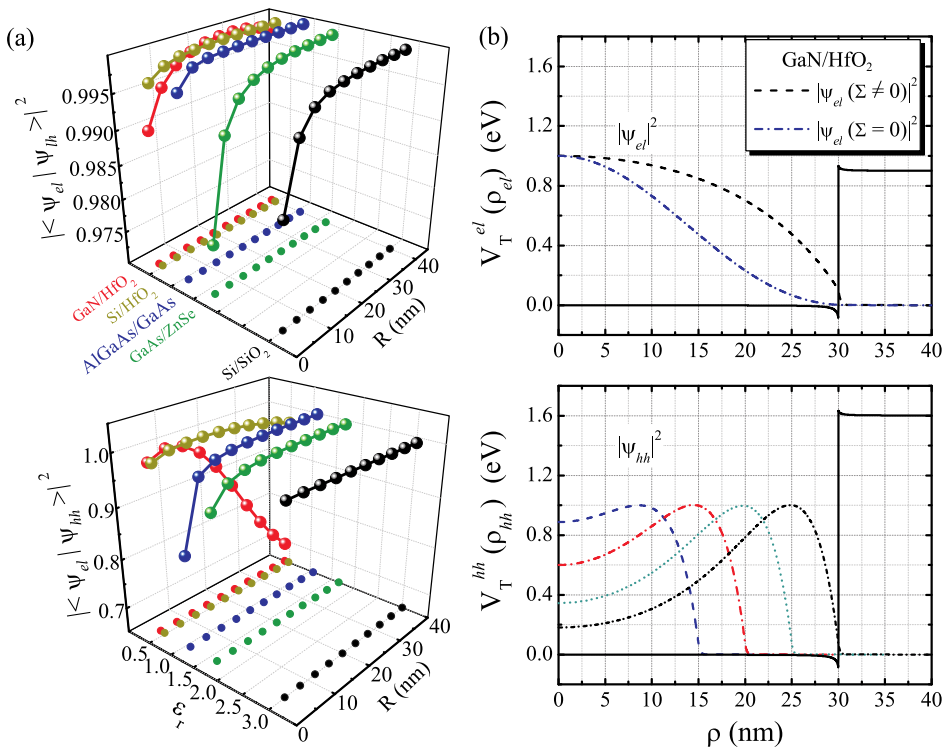


FIG. 2. (a) Overlap between the electron (*el*) and the light (*lh*) and heavy (*hh*) hole wave functions as a function of the core radius R , for several heterostructure materials with different ratios between dielectric constants ϵ_r , represented by different colors. (b) Effective confinement potentials V_T^i (solid) for $R = 30$ nm in the GaN/HfO₂ case for electrons and heavy holes, along with some examples of their wave functions. Electron wave functions are shown with (dashed) and without (dashed-dotted) taking image charge effects into account, for comparison. Hole wave functions (for $\Sigma \neq 0$) are depicted for $R = 15$ nm (blue dashed), 20 nm (red dash dotted), 25 nm (green dotted), and 30 nm (black short dash dotted).

confined at the interface, due to the cusp formed in this region by the self-energy potential (see black solid line). Note that as the radius increases, the *hh* wave function is squeezed towards the interface, explaining the increase of the energy in the heavy hole E_0 curve in Fig. 1(b). Due to its larger effective mass, as compared to that of the other charge carriers, the heavy hole is indeed expected to be more strongly confined in the interfacial cusps. Moreover, heavy holes in GaN/HfO₂ also have larger effective mass as compared to any charge carrier in Si/HfO₂, explaining why the interfacial confinement effect is weaker in the latter case.

Another interesting effect arising from the interfacial confinement in quantum wires comes from their topology: systems where the charge carriers are confined around a core are known to produce an interesting effect when a magnetic field is applied perpendicular to the confinement plane, namely, angular momentum transitions occur, even for the ground state, as the magnetic field intensity increases, which is reminiscent of the Aharonov-Bohm (AB) effect.⁹ In order to illustrate this, the electron and hole energy behaviors under such a magnetic field were numerically⁹ calculated and shown in Fig. 3 as a function of the field amplitude B for the GaN/HfO₂ NW. All the carriers have $E_0 < 0$, suggesting that their ground states are all interfacially confined. A large ($R = 30$ nm) radius is considered, in order to enhance the interfacial confinement effect (see Fig. 2(b)) and reduce the AB period, since this period is inversely proportional to the average radius of the carrier wave function. Indeed, the ground state energy exhibits AB oscillations for all carriers in this case, although they are much more evident for the *hh*. Due to their considerably smaller effective masses,¹⁵ *el* and *lh* are just weakly confined in the interface and still have a large wave function tail spreading inside the core, explaining the large AB period. The first ground state transition for these carriers is not so visible in Figs. 3(a) and 3(b) and

occurs at $B \approx 6$ T. On the other hand, for the *hh*, the AB transitions are quite clear, occurring at smaller magnetic fields, with a period $B \approx 2.5$ T. One easily verifies that the results neglecting the self-energy term in Fig. 3(d) are qualitatively different, showing a more conventional behavior with the magnetic field for a core-shell NW, namely, without angular momentum transitions for the ground state.

The interfacial confinement is also expected to have an important role on the electrons mobility along the core axis since this property depends on the electrons density in the central region of the wire, which is suppressed in the case of interfacial confinement. However, a more detailed investigation on this issue is left for future works.

In summary, we have theoretically investigated the charge carrier confinement in core-shell nanowires with

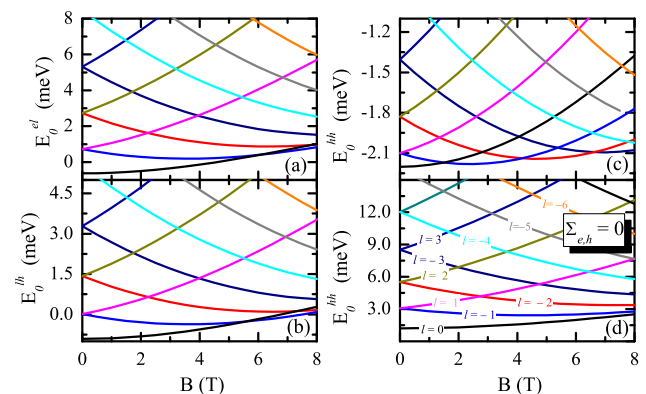


FIG. 3. Confinement energies as a function of the magnetic field for (a) electrons, (b) light, and (c) heavy holes, considering $n = 1$ and different values of angular momentum index l , in a $R = 30$ nm GaN/HfO₂ NW. (d) The results for a heavy hole in the same system, but neglecting image charge effects.

strong dielectric mismatch. Our results predict that, for specific configurations of the system, the carriers may be confined at the core-shell interface. Such interfacial confinement leads to drastic modifications on the electronic properties of the NW, especially under an applied magnetic field, where angular momentum transitions occur for the ground state, due to the AB effect. A decrease in the oscillator strength of the electron-hole pairs in $\epsilon_r < 1$ core-shell quantum wires is also predicted for larger wire radii, which directly affects their recombination rates. We believe that our results will spur on future experimental investigations on core-shell wires made out of high-k materials, contributing for a better understanding of these systems.

This work has received financial support from the Brazilian National Research Council (CNPq), CAPES, PRONEX/CNPq/FUNCAP, and FAPEMAT (Process No. 39788/2009).

¹P. Mohan, J. Motohisa, and T. Fukui, *Nanotechnology* **16**, 2903 (2005).

²A. I. Persson, M. W. Larsson, S. Stenstrom, B. J. Ohlsson, L. Samuelson, and L. R. Wallenberg, *Nano Mater.* **3**, 677 (2004).

³C. Chen, S. Shehata, C. Fradin, R. LaPierre, C. Couteau, and G. Weihs, *Nano Lett.* **7**, 2584 (2007).

⁴D. Tsvion, M. Schwartzman, R. P. Biro, P. Huth, and E. Joselevich, *Science* **333**, 1003 (2011).

⁵D. Jena and A. Konar, *Phys. Rev. Lett.* **98**, 136805 (2007).

⁶X. Zhu, Q. Li, D. E. Ioannou, D. Gu, J. E. Bonevich, H. Baumgart, J. S. Suehle, and C. A. Richter, *Nanotechnology* **22**, 254020 (2011).

⁷X. Jiang, Q. Xiong, S. Nam, F. Qian, Y. Li, and C. M. Lieber, *Nano Lett.* **7**, 3214 (2007).

⁸B. Li, B. Partoens, F. M. Peeters, and W. Magnus, *Phys. Rev. B* **79**, 085306 (2009).

⁹J. C. e Silva, A. Chaves, J. A. K. Freire, V. N. Freire, and G. A. Farias, *Phys. Rev. B* **74**, 085317 (2006).

¹⁰A. F. Slachmuylders, B. Partoens, W. Manus, and F. M. Peeters, *Phys. Rev. B* **74**, 235321 (2006).

¹¹See supplementary material at <http://dx.doi.org/10.1063/1.4720402> for more details about our calculations.

¹²T. A. S. Pereira, J. S. de Sousa, J. A. K. Freire, and G. A. Farias, *J. Appl. Phys.* **108**, 054311 (2010).

¹³J.-H. Kang, Q. Gao, H. J. Joyce, H. H. Tan, C. Jagadish, Y. Kim, Y. Guo, H. Xu, J. Zou, M. A. Fickenscher, L. M. Smith, H. E. Jackson, and J. M. Yarrison-Rice, *Cryst. Growth Des.* **11**, 3109 (2011).

¹⁴T. A. S. Pereira, J. S. de Sousa, G. A. Farias, J. A. K. Freire, M. H. Degani, and V. N. Freire, *Appl. Phys. Lett.* **87**, 171904 (2005).

¹⁵T. A. S. Pereira, J. A. K. Freire, V. N. Freire, G. A. Farias, L. M. R. Scolfaro, J. R. Leite, and E. F. da Silva, *Appl. Phys. Lett.* **88**, 242114 (2006).

Index

- Ab initio, 24
- Adiabatic approach, 25–27
- AFM, ix, 34
- Aharonov-Bohm, xi, 34, 35, 37, 41, 64, 72
- Atom, 24, 25, 31, 33
- Band-off-set, 31
- Bardeen, William Shockley and Walter H. Brattain, 23
- Bloch, 27–29
- Braess paradox, ix, xi, xiii, 37–39, 41, 53, 62–64, 72–74, 102, 103
- Brillouin, 27
- Conductance band, 24
- CVD, 24
- Effective mass, 24, 25, 28–30, 32, 37
- Electrons, 25–37, 40–42
- Energy band, 24, 25, 29–31, 41
- Energy states, 24, 25
- Envelope function, 24
- evolution time operator, 43
- Fermi energy, 25, 88
- Fermi level, 24, 90
- Fermi velocity, 87
- Fermi wavelength, 31
- Frequency cyclotron, 37
- Game theory, 37, 38, 102
- GAP, 24, 25, 28, 31, 33
- Hamiltonian, 24, 27, 28, 30, 36, 37, 43, 51, 54, 66
- Heavy hole, 25, 30
- Impurity, 25, 42, 91–94, 96–100, 102–104
- John Nash, 38, 39
- K.P, 24
- Lattice, 24, 25, 27, 29, 30
- Light hole, 25, 30
- MBE, 24
- MOCVD, 24
- Pauli's Rule, 24
- Poisson equations, 32
- Quantum dot, ix, xi, xiii, 24, 31, 32, 34, 40, 41
- Quantum ring, ix, xi, xiii, 34–36, 41
- Quantum well, ix, xi, xiii, 30, 31, 33, 34, 41, 42
- Quantum wire, ix, xi, xiii, 31–33, 40–42, 78, 79, 83, 88, 89
- Schrödinger, 24–27, 32, 43, 64, 66, 79, 93
- Self energy, x, xii, xiv, 91–95, 97–100
- Semiconductor, ix, 23–25, 28–31, 33, 37, 40, 41

-
- Split-off, [25](#), [30](#)
Split-operator, [ix](#), [xi](#), [43](#), [44](#), [49](#), [54](#), [66](#)
Superlattices, [24](#)
- Time evolution operator, [43–45](#)
Time-dependent Schrödinger, [45](#)
Transport properties, [xi](#), [23](#), [36](#), [37](#), [41](#), [78](#),
[82](#)
Tsu and Esaki, [23](#), [31](#)
- Valence band, [24](#)
VLS, [24](#)
- Wave function, [26–28](#), [33](#), [36](#), [41](#), [42](#)
Wave vector, [25](#)

Appendix C

Curriculum vitae

Ariel Adorno de Sousa



PROFESSIONAL ADDRESS

Av. Fernando Correia da Costa, S/N

Cuiabá - MT - Brazil

ariel@fisica.ufc.br

Born: 28/05/1984

Brazilian citizen

Married

EDUCATION

Year	Graduation Institution	Title of qualification awarded
2005 - 2008	State University of Goiás (UEG)	Undergraduate in Mathematical
2009 - 2011	Federal University of Mato Grosso (UFMT)	Undergraduate in Physics
2010 - 2012	Federal University of Mato Grosso (UFMT)	Master in Physics
2012 - 2015	Federal University of Ceará (UFC)	Ph.D. in Physics
2013 - 2015	University of Antwerp	Ph.D. in Physics

COMPUTER SKILLS

- OS: Windows, Linux (all-dist);
- Microsoft Office, Powerpoint, Word, Excel;
- Programming software: Matlab, C, C++, Fortran, Script-shell;
- Other: Maple, Origin, Octave, Gnuplot, Latex

LANGUAGES

English, Portuguese, Spanish

INTERESTS

Languages, programming, reading, cinema, travels